Development of lithium ferrite-based ceramics for microwave applications

DOCTOR OF PHILOSOPHY

by

PRAJNA PARAMITA MOHAPATRA

DEPARTMENT OF PHYSICS

INDIAN INSTITUTE OF TECHNOLOGY GUWAHATI

GUWAHATI -781039, INDIA

MAY, 2023.

भारतीय प्रौद्योगिकी संस्थान गुवाहाटी
Indian Institute of Technology Guwahati

Development of lithium ferrite-based ceramics for microwave applications

A Thesis submitted in partial fulfillment of the requirements for the

award of the degree of

DOCTOR OF PHILOSOPHY

by

PRAJNA PARAMITA MOHAPATRA

DEPARTMENT OF PHYSICS

INDIAN INSTITUTE OF TECHNOLOGY GUWAHATI

GUWAHATI -781039, INDIA

MAY, 2023.

Dedicated to my Family and friends

INDIAN INSTITUTE OF TECHNOLOGY GUWAHATI
Department of Physics,
Guwahati - 781039

STATEMENT

I hereby declare that the matter embodied in this thesis is the result of investigations carried out by me in the Department of Physics, Indian Institute of Technology Guwahati, Guwahati, India, under the supervision of **Prof. Pamu Dobbidi**. This thesis has not been submitted to any university, institute or elsewhere for the award of the any degree, diploma or associate-ship.

Prajna Paramita Mohapatra

Date 23/01/2023

Prajna Paramita Mohapatra
Department of Physics,
Indian Institute of Technology Guwahati,
Guwahati – 781 039

भारतीय प्रौद्योगिकी संस्थान गुवाहाटी
Indian Institute of Technology Guwahati
Department of Physics
Guwahati-781039, Assam State, INDIA
Phone: +91-361-2582721
Fax: +91-361-2582749
Dr. Pamu Dobbidi
Professor
E-mail: pamu@iitg.ac.in

Date: Jan 23, 2023

Certificate

This is to certify that work contained in the thesis entitled ‘**Development of lithium ferrite-based ceramics for microwave applications**’ by **Prajna Paramita Mohapatra** (Roll no 176121020), a student of Department of Physics, Indian Institute of Technology Guwahati, for the award of degree of Doctor of Philosophy, has been carried out under my supervision and the same has not been submitted elsewhere for the award of any other degree.

(Dr. Pamu Dobbidi)


भारतीय प्रौद्योगिकी संस्थान गुवाहाटी
Indian Institute of Technology Guwahati

Acknowledgment

First and foremost, I would like to thank my thesis supervisor, Prof. Pamu Dobbidi, for giving me the opportunity to work under his supervision and for his constant support, precious advice, and valuable suggestions, which helped me to complete my thesis work. I must acknowledge him for providing the unconditional freedom to work, think and express whatever I have done in my research work by keeping faith in my capabilities. Even during the tough period of the completion of thesis work, he was kind enough and understood the situation and helped to overcome the mental tension.

I am also very grateful to my doctoral committee members, Prof. Perumal Alagarsamy, Dr. U. N. Maiti, Dr. Nageswara Rao Peela, for their timely reviewing and giving me necessary suggestions to improve my work. Their valuable suggestions helped me to improve the work to shape the present thesis.

I am also taking the opportunity to thank the present and former head of the department of Physics, IIT Guwahati, and the head of the central instrumental facility for providing me with the necessary facilities to fulfill my Ph.D. thesis objectives. I sincerely extend my gratitude to all the faculty members of the Department of Physics, who supported me in helping me in several ways during my Ph.D. tenure. I would like to extend my sincere thanks to Dr. Sidananda Sarma, and the technical and non-technical staff of IIT Guwahati for helping me with various instrument operations.

I would like to thank the Indian Institute of Technology Guwahati and the Ministry of Human Resource and Development for providing financial support for this thesis. Also, I would like to express my heartfelt thanks to the Science and Engineering Research Board (SERB)/Department of Science and Technology (DST), New Delhi; Board of Research in Nuclear Sciences (BRNS), Mumbai; Defense Research and Development Organization (DRDO), New Delhi, Indian Space Research Organization, Ahmedabad (Space Applications Centre) for providing various experimental facilities through research projects.

It was a lifetime good experience and pleasure to work with my seniors Dr. Srinivas Pattipaka, Dr. Susmita Rabha, Dr. Apurba Das, Dr. Sasmita Behera, Dr. Pratap Behera, Dr. Aakanksha. I want to thank specially my seniors for their suggestions; they helped me in learning the basics of the instrument and taught me to handle the instruments. I would like to thank my research team members, Shashi Priya, Sunil, Radhika, Anil, Subingya, Karnajit, Somnath, Naphisa, Ganesh, for always being there whenever it is required and making me feel like family.

Friends I have met in IIT Guwahati; Pragya, Dhriti, Subrat, Devender, Madhurima, Ipsita, Juhi, Jayashree, Rohith, Pushpanjali are invaluable to me and made my life enjoyable outside the lab by giving me love and constant support during my Ph.D., whenever I needed. I also met some juniors inside the campus, Sudesna, Alok for their unconditional love, affection, and encouragement.

I am very greatful to my all time friends Namrata, Sweety, Rajib, Subhasmita, Mousumi, Manaswini, Dipti, Nirlipta, Anuradha, Amrita, Mukesh for their constant love and support to push me to move ahead in my life.

My special gratitude goes to my family members; Father (Pramod Kumar Mohapatra), Mother (Rebati Satpathy), Brother (Ashish Mohapatra), Uncles (Prasanna and Prakash), and Nimish for their love and constant support in my life. I don't have any words to express what their support and love mean to me throughout this journey. Finally, I owe my sincere gratitude to Almighty God, who always gives me positive energy to face every problem in my life.

Prajna Paramita Mohapatra

Abstract

Spinel ferrites have gained attention for a long period of time due to their unique electrical, optical, and magnetic properties. They are also very promising for applications such as circulators, phase shifters, memory, magnetic recording devices, gas sensing, etc. The present thesis is focused on the synthesis of lithium ferrite-based ceramics and thin films. Lithium ferrite exhibits high Curie temperature, square hysteresis loop, high saturation magnetization, excellent dielectric properties, high resistivity, etc. The solid-state reaction method is used to prepare substituted lithium ferrites and composites. The effect of alkaline earth elements such as Sr and Mg on the structural, microstructural, dielectric (1 MHz – 1 GHz), and magnetic response is analyzed. Enhanced dielectric response ($\varepsilon_r = 3034$, $\tan\delta = 0.001$ at RT, 1 MHz) is observed for the Mg composition, $x = 0.005$, whereas in the case of Sr series, the best dielectric response is observed for $x = 0.003$ ($\varepsilon_r = 5986$ and $\tan\delta = 1.17$ at RT, 1 MHz). The obtained EA for LMFO and LSFO is 1.39 – 0.35 eV and 0.124 – 0.077 eV, respectively. The LMFO with $x = 0.007$ exhibited the best permeability ($\mu_r = 29$) and magnetic properties (Ms = 55 emu/g) at room temperature. Also, in the LSFO series, $x = 0.007$ showed the highest magnetization among all samples (MS = 61 emu/g). Improved dielectric response with low magnetic as well as dielectric loss is observed for Mg substituted lithium ferrite as compared to Sr. The combined magnetic, dielectric, and permeability response made the Mg substituted lithium ferrite more suitable for circulators and phase shifters. Again, the lithium ferrite/carbon black and Dy substituted lithium ferrite/carbon black composites are prepared, and EMI shielding effectiveness is analyzed in the X (8.2 – 12.4 GHz) and K_u (12.4 – 18 GHz) frequency bands.

Permittivity and permeability are also analyzed. Shielding effectiveness is enhanced with the carbon black as well as Dy content. The maximum shielding effectiveness of 24 dB was obtained for LD10FO/CB ~ 17 – 18 GHz. The Dy substitution enhances the magnetic as well as dielectric loss. Further, 99.68 % of A_{eff} is achieved with 20 wt % of CB reinforcement in LFO, whereas the maximum absorption efficiency of 99.6 % is obtained for LD10FO/CB ~ 17 – 18 GHz.This renders majorly absorption-based shielding rather than reflection-based shielding. The enhancement in the shielding efficiency is attributed to the synergetic effect of the dielectric loss and magnetic loss. Various contributions of magnetic loss, such as natural resonance, domain wall resonance, eddy current loss, hysteresis loss, and spin polarization, are discussed. Further, lithium ferrite and Dy substituted lithium ferrite in the form of thin films are synthesized by PLD having different film thicknesses. The strain-induced structural, microstructural, magnetic, dielectric, and electrical response is analyzed. The magnetization is reduced with the enhancement in film thickness which is explained on the basis of magnetoelastic energy density. The dielectric constant is enhanced, whereas the dielectric loss is reduced with the enhancement in the film thickness. The electrical conduction mechanism is also analyzed, which is in good agreement with Mott's VRH mechanism. The varying thickness of a film is an effective parameter for tuning the physical properties of the film. The observed results suggest that LDFO films are promising for magnetic oxide semiconductor applications.

List of Publications

Journals

1. **Prajna P Mohapatra**, Srinivas Pattipaka, Pamu Dobbidi, The effect of Sr substitution on the electrical, dielectric, and magnetic behavior of lithium ferrite, Ceramics International 45 (2019) 25010-25019.
2. **Prajna P Mohapatra**, Suresh Pittala, Pamu Dobbidi, Temperature dependent broadband dielectric, magnetic and electrical studies on $Li_{1-x}Mg_{2x}Fe_{5-x}O_8$ for microwave devices, Journal of Materials Research and Technology 9 (2020) 2992-3004.
3. **Prajna P Mohapatra**, Pamu Dobbidi, Effect of carbon reinforcement on the EMI shielding response of $LiFe_5O_8$ ceramics, Materials Characterization, 198 (2022) 111985.
4. **Prajna P Mohapatra**, Sagnik Ghosh, Ashish Jain, Suman Aich, Pamu Dobbidi, Dy-substituted lithium ferrite/carbon black composites for shielding electromagnetic radiation, Journal of Magnetism and Magnetic Materials 573 (2023) 170678.
5. **Prajna P Mohapatra**, Pamu Dobbidi, Thickness tuneable dielectric, optical and magnetic response of lithium ferrite thin films deposited by PLD, Thin Solid Films 774 (2023) 139845.
6. **Prajna P Mohapatra**, Pamu Dobbidi, Conduction mechanism, dielectric, and magnetic investigation of lithium ferrite thin films, Applied Surface Science 619 (2023) 156706.

Publications outside the thesis work

1. **Prajna P Mohapatra**, Pamu Dobbidi, Magnetic and broadband dielectric studies of calcium-substituted $LiFe_5O_8$, Journal of Magnetism and Magnetic Materials, 500 (2020) 166354.
2. **Prajna P Mohapatra** and Pamu Dobbidi, Magnetic, Optical, and Impedance Spectroscopy of Barium Substituted Lithium Ferrite, The Journal of Physical Chemistry C, 125 (2021) 14014-14026.
3. **Prajna P Mohapatra**, Hodam Karnajit Singh, Mangalampalli SRN Kiran, Pamu Dobbidi, Co substituted Ni–Zn ferrites with tunable dielectric and magnetic response for high-frequency applications, Ceramics International, 48 (2022) 29217-29228.
4. Hodam Karnajit Singh, **Prajna P Mohapatra**, Somnath Sahu, Pamu Dobbidi, Dielectric and temperature dependent magnetic studies of Al3+ substituted $Ba_{0.4}La_{0.1}Sr_{0.5}Al_xFe_{12-x}O_{19}$ hexaferrite for microwave application, Materials Science and Engineering: B, 284 (2022) 115876.
5. Susmita Rabha, Apurba Das, **Prajna P Mohapatra**, Sunil Gonne, Shashi Priya Balmuchu, Ethi Reddy Radhika, Pamu Dobiddi, Dielectric and leakage characteristics of MTO/STO bilayer films deposited by RF magnetron sputtering technique for optical and electronic applications, Materials Science and Engineering: B, 282 (2022) 115790.

Conference proceedings

1. **Prajna P Mohapatra**, Pamu Dobbidi, Magnetic and dielectric studies of $Li_{1-x}Ca_{2x}Fe_{5-x}O_8$ for RF/microwave applications, AIP Conference Proceedings 2162 (2019) 020029.
2. **Prajna P Mohapatra**, Pamu Dobbidi, Structural and magnetic studies of $Li_{1-x}Ba_{2x}Fe_{5-x}O_8$, AIP Conference Proceedings 2265 (2020) 030530.

Conferences and workshops attended

1. Effect of Sr substitution on the dielectric and magnetic properties of lithium ferrites for RF and microwave applications, Prajna Paramita Mohapatra presented oral presentation in the "International Conference on Advanced Ceramics and Nanomaterials for Sustainable Development" during 19th – 21st September 2018, Christ, Kengeri campus, Bengaluru.
2. Magnetic and dielectric properties of lithium ferrite for microwave applications, Prajna Paramita Mohapatra presented poster in the in the ICMAGMA-2018 during 9 – 13 December 2018, NISER, Bhubaneswar, India.
3. Magnetic and Dielectric Studies of $Li_{1-x}Ca_{2x}Fe_{5-x}O_8$ for RF/Microwave Applications, Prajna Paramita Mohapatra presented poster in the International Conference on Advanced Materials (ICAM-2019), 12 – 14 June 2019, Nirmalagiri College, Kannur, Kerla, India,
4. Structural and Magnetic Studies of $Li_{1-x}Ba_{2x}Fe_{5-x}O_8$, Prajna Paramita Mohapatra presented poster in 64th DAE-Solid State Physics Symposium (DAE-SSPS-2019), 18 – 22 December 2019, IIT Jodhpur, India.
5. Effect of Carbon reinforcement on the EMI shielding response of LiFe5O8 ceramics, Prajna Paramita Mohapatra presented poster in the International Conference On Advanced Materials And Mechanical Characterization (ICAMMC-2021) (virtual mode) 2 – 4 December 2021, SRM Institute Of Science And Technology, India
6. Thickness-tunable Optical, Magnetic, and Dielectric Response of Lithium Ferrite Thin Film Synthesized by PLD, Prajna Paramita Mohapatra given oral presentation in the 6th International Conference on Materials Sciences and Nanomaterials (ICMSN 2022), (virtual mode) 12-14 July, 2022, London, United Kingdom.

Table of Contents

List of Figures

List of Tables

List of Symbols and Abbreviations

m	Meter	ε'	Real part of permittivity
cm	Centimeter	ε''	Imaginary part of permittivity
µm	Micrometer	μ'	Real part of permeability
nm	Nanometer	μ''	Imaginary part of permeability
Å	Angstrom	ε_0	Permittivity of vacuum
°C	Centigrade (degree)	σ_{ac}	AC-conductivity
kHz	Kilo Hertz	M	Magnetization
MHz	Mega Hertz	M_s	Saturation magnetization
GHz	Giga Hertz	H_c	Coercivity
h	Hour	χ	Magnetic susceptibility
F	Farad	E	Electric field
µC	Micro Coulomb	C	Capacitance
N	Newton	d	Thickness
V	Volt	σ	Stress
eV	Electron-volt	η	Strain
g	Gram	P	Polarization
W	Watt	p	Dipole moment
esu	Electrostatic unit	V	Unit cell volume
A	Ampere	Z	Impedance
		Z'	Resistance
ε_r	Relative permittivity	Z''	Reactance
tan δ	Loss tangent	f_0	Resonant frequency
A	Area of the electrodes	τ	Relaxation time

DC	Direct current
AC	Alternating current
E_A	Activation energy
ω	Angular frequency
k_B	Boltzmann constant
ρ_{ac}	AC-resistivity
ξ	Decay length
$N(E_F)$	Density of states
R_H	Hopping length
W_H	Hopping energy

Other parameters

θ	Angle
D	Crystallite size
FWHM	Full width at half maximum
a, b, c	Lattice parameters
χ^2	Chi-square
R_{Bragg}	Bragg factor
R_f	Profile factor

ρ	Density
wt.	Weight
rms	Root mean square
RT	Room temperature
RF	Radio frequency
VRH	Variable range hopping
MIM	Metal-insulator-metal
XRD	X-Ray diffraction
AFM	Atomic force microscopy
SEM	Scanning electron microscopy
FESEM	Field emission scanning electron microscopy
FETEM	Field emission transmission electron microscope
SAED	Selected area electron diffraction
LFO	$LiFe_5O_8$
CB	Carbon black

Chapter 1 : Introduction

Nowadays, the expeditious development in telecommunication and signal processing has enhanced the demand for microwave devices in wireless communication and radar detection system. Ferrites are the most felicitous material for various microwave applications (phase shifters and circulators) owing to their optical, electrical, exciting magnetic, and dielectric properties, very high specific resistance, and remarkable flexibility in tuning the properties.[1][2] With the increasing level of integrated devices for different applications, there is an extensive requirement to develop new microwave materials with desired properties. Especially for operation of non-reciprocal microwave devices like isolators and circulators, there is no alternative rather than ferrites.[3][4][5][6] Apart from that, ferrites' operational frequency range, temperature resistance, and power handling capacity make them unique for application in microwave devices. Further, due to the rapid growth and demand for electronic media and digitalization, electromagnetic (EM) pollution has become a hazardous threat to the operation of devices and the day-to-day healthy human life.[7][8][9] In order to increase the data transfer rate, the dominant frequency regime is shifting towards the high frequency. To minimize electromagnetic pollution, the urge for electromagnetic shields and absorbers increased. So, in the last few years, EM pollution has gained the attention as an exclusive research topic among many researchers and scientist.[10][11][12] The future use of ferrites in such applications will be governed by the specification of the technical problem that requires a solution and the economic considerations. The present study aims to develop the materials suitable for above applications.

1.1 Historical back ground

Ferrites are the class of metal oxides that contain ferric oxides with combined magnetic conductor and electrical insulator properties. The connection between the chemical composition and magnetic response of different ferrites having various elements such as cobalt, copper, manganese, and magnesium was investigated by Hilpert et al.[13] in the year 1909. The primary commercial importance of ferrites came into existence in 1930 through the efforts of Japan's Kato and Takai.[14] The active participation in ferrites for radio frequency applications emerges after the pioneering work by Snoek et al.[15]. Then the superexchange theory was postulated by Yafet and Kittel[16], and Verway and Heilmann explained the distribution of ions over octahedral and tetrahedral positions.[17] After years of research, Globus et al.[18] gave a model that describes the contribution of the domain wall with the permeability. Then, Polder et al.[19] derived the first permeability tensor that laid the foundation to understand the behavior of ferrites in the microwave frequency range. After that, ferrite gained popular interest among microwave engineers and Physicists till now.

1.2 Applications of ferrites as microwave materials

Initially, ferrites as microwave materials gained the interest of researchers due to the requirement for magnetic insulators in high-frequency inductor cores. By taking advantage of the dielectric response of ferromagnetic oxides, ferrites were used for various purposes such as directional coupler, phase shifter, isolator, circulator, etc., as reported earlier.[20][21][22][23] Mainly the focus was laid on the development of magnetic loss of the materials and the ferromagnetic resonance (FMR) linewidths. Another crucial property of ferrites is magnetic anisotropy, which is usually used to bias the materials in microwave regions. Depending upon the materials' performance and requirements, nowadays ferrites are used for various prospective.

1.2.1 Circulator, Isolator, and Phase shifter

The circulator is a multi-port, non-reciprocal passive device that exhibits low insertion loss in the forward direction and high loss in the reverse direction. The main purpose of this device is to control the flow of power. It has the power to regulate the direction of wireless as well as microwave signals where one antenna is needed instead of two for receiving and transmitting at duplex mode.[3] It comprises of a conductor placed over ferrite, which is usually biased by applying an external magnetic field which is perpendicular to the device plane. The graphical representation of a Y-junction circulator in stripline configuration and the magnitude of electric field is shown in **Figure 1-1 (a) and (b)**. One layer stripline circuit with two ferrite discs make the sandwich structure. Port 1 is the input, whereas port 2 is the output port with simultaneously isolated port 3. The transmit-receive (T/R) modules of phased array radar systems are most often used in the Y junction circulator.

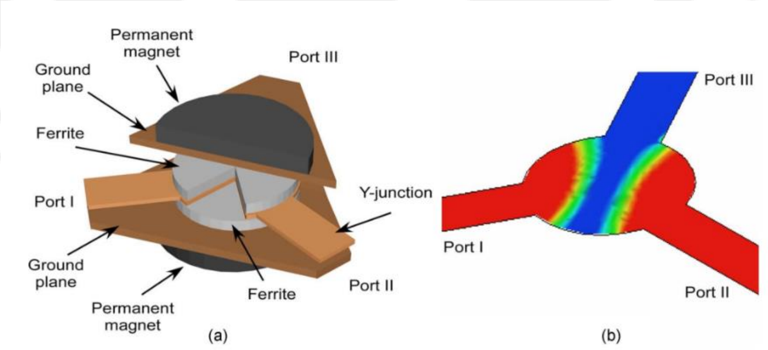

Figure 1-1. *(a) Different parts of a stripline Y-junction circulator. (b) Low insertion loss in the forward direction of propagation (port I–port II). The finite element method is used to deduce the magnitude of the electric field in the stripline Y-junction circulator.[3]*

The nonreciprocity behavior of the circulator can be used to separate received and transmitted waves in communication and radar systems. Initially, barium and strontium hexaferrite were mostly used ferrites for circulators due to their high magnetization, anisotropy, and low loss. As soft ferrites like spinel ferrites render much beneficial low loss, the search for new ferrites for circulators is shifting towards spinel ferrites in recent times.

The isolator comes under two-port devices with nonprocity unidirectional transmission characteristics, as shown in **Figure 1-2**. [24] It is mainly used to block the high reflected power from the damage of the microwave sources. Let's take an example: when plasma is ignited, the impedance of the system changes a lot. The change in impedance will lead to impedance mismatch that causes fatal reflection, which can damage the source. In such cases, an isolator can match or tune the network to absorb the reflected power through the ferrites. The isolators consist of similar essential elements as a circulator, which operates on different principles such as resonance absorption, field displacement, and Faraday rotation.

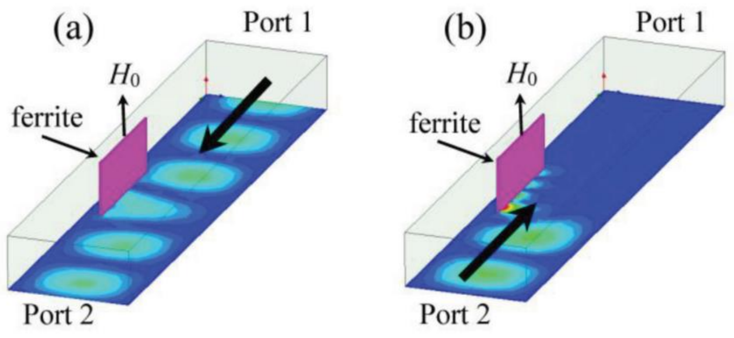

Figure 1-2*. (a) The forward transmission is high from Port 1 to Port 2 : low transmission loss (S21), (b) Reverse transmission is low from Port 2 to Port 1 : high isolation[24]*

The phase shifters also belong to a two-port components system which renders different phase shifts by applying a different bias to the magnetic field, as shown in **Figure 1-3**.[24] The phase shifter is crucially used in phase array antenna to guide the antenna beam in space controlled electronically. The current phase shifter technology with semiconductor and ferroelectrics is suffering operational constraints like power handling capacity and reliability, which limits their use in the military and commercial firms.[25] In contrast, the phase shifters with ferrites show superior microwave handling power and superior insertion loss. Apart from this, it is also rendering radiation-tolerant behavior and reliability. The spinel ferrites substituted with nonmagnetic ions like zinc, magnesium, and lithium are highly suitable for this application.[26][27]

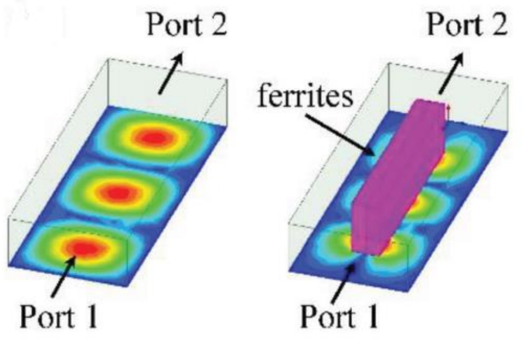

Figure 1-3. *(a)left side of the image refers to the empty wave guide and the right side shows the field strength with ferrites*

1.2.2 Microwave absorber

Microwave absorbers have received wide attention in the last few years due to the increasing demand for telecommunication, wireless electronic devices, and stealth technology.[28][29] Besides, microwave absorbing materials (MAMs) are applied vastly to minimize electromagnetic (EM) reflections on huge bodies like military equipment, tanks, and planes.[30] **Figure 1-4** shows the graphical illustration of the application of microwave absorbers. Majorly the absorbers can be classified into different types, such as dielectric type, resistor type, and magnetic type. In ferrites, the microwave absorption response of absorbent depends upon various factors such as complex permeability (interaction between absorbent and magnetic field), complex permittivity (interaction between absorbent and electric field), dielectric loss (defects), magnetic loss (eddy current effect and domain wall motion).[31][32] Apart from this, there should be effective blending between magnetic and dielectric loss (impedance matching) to achieve effective microwave absorption.[33] Several ferrites such as Ni-Zn, [34][35] barium ferrites, strontium hexaferrite,[36][37] Mn-based spinel ferrites[38] are being used as microwave absorbers as reported earlier.[39]

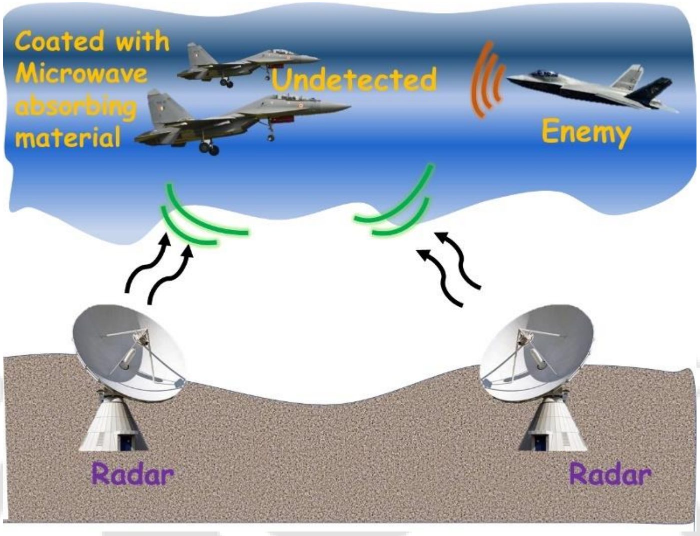

Figure 1-4. *Schematic illustration of the application of microwave absorbing material.*

1.2.3 Electromagnetic interference shielding

In recent days, electromagnetic radiation in gigahertz (GHz) frequency has become an alarming danger for biological systems, commercial applications, high-quality information technology, etc.[10][40] When the EM waves interfere with the signals from different devices, they create noise known as electromagnetic interference (EMI) pollution, which is the consequence of the undesired outcome of modern technology and engineering. Commercial appliances (microwave ovens) and communications devices (bluetooth devices, wi-fi routers, cell phones) are also part of EMI pollution.[41][42] **Figure 1-5** illustrate the various source of EMI pollution around us. EMI pollution is hazardous for the smooth running of the devices and for normal human health, which causes sleeping disorders, headache, nausea, and heart attack.[43][44] The problem of this situation can be solved only by using appropriate EMI-shielded material. So, it is the urgent need of the hour for the whole human community to synthesize high-efficiency EMI shielded material.

The absorption mainly relies on magnetic and electric dipoles present in the shielded materials, whereas to have effective reflections mobile charge carriers are needed.[45][46] The multiple reflections (reflection from various interfaces) are used to be neglected as the re-reflected waves are absorbed in the materials. Earlier, for EMI shielding, metal sheets were considered as an efficient material; however, their heavy weight, processing difficulty, and oxidation-prone nature limit their use in various practical applications.[47] Then the hunt for efficient EMI-shielded material shifted to polymer and polymer-based composites.[48][49][50] But polymer-based composites also have certain limitations like temperature and chemical composition stability. So, currently, the research shifted to ceramics and ceramic-based composites with carbon and polymer.[51] [52][53][54] The shielding effectiveness (SE) of the material depends on several parameters like morphology, conductivity, permeability, permittivity, dielectric loss, and magnetic loss.

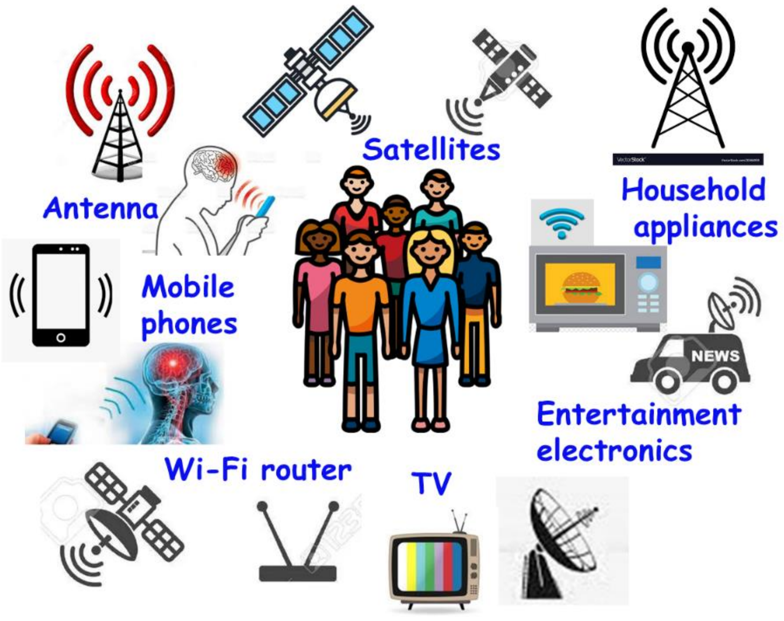

Figure 1-5. *Various sources of EMI pollution/radiation.*

1.3 Theory and fundamentals associated with microwave ferrites

The origin of the magnetic moment of a material arises from the orbital and spin motion of electrons and how they interact. The total magnetic moment of an atom is the combined effect of an individual electron's orbital and spin magnetic moment. According to the magnetic exchange interaction, materials are classified into different categories: diamagnetic, paramagnetic, ferromagnetic, antiferromagnetic, and ferrimagnetic. Materials under the initial two groups do not show any collective magnetic interactions and are not magnetically ordered. The materials under the last three groups show long-range magnetic responses below a specific temperature.

1.3.1 Types of magnetic materials

1.3.1.1 Diamagnetism

Generally, diamagnetic materials are composed of atoms having no net magnetic moment (no unpaired electrons: all orbitals are filled). Diamagnetic nature is a fundamental behavior of all materials. It is because of the non-cooperative behavior of orbiting electrons while exposed to an externally applied magnetic field. According to Lenz's law, when an external magnetic field is applied to a material, a magnetic moment is induced that opposes the direction of the magnetic field.[55] Diamagnetic material shows negative susceptibility, suggesting that the induced magnetization direction is opposite to the direction of the applied magnetic field. Examples of diamagnetic materials are metals (Ag, Au, Cu), polyatomic gas (N_2, H_2), monoatomic rare gases (Ar, Ne, He), etc.

1.3.1.2 Paramagnetic

In paramagnetic materials, the magnetic dipoles are randomly oriented and do not possess any magnetic moment in the absence of a magnetic field. Some atoms and ions in this type of material possess a net magnetic moment due to the presence of unpaired electrons in partially filled orbitals. When the magnetic field is applied, the magnetic dipoles try to align in the direction of the magnetic field, giving rise to positive magnetic susceptibility. The alignment degree increases with an increase in the applied field and a decrease in temperature. As a function of temperature, the susceptibility of paramagnetic materials can be expressed as per the Langevin classical approach, as shown in **Equation 1.1**, known as Curie law.[56][55]

$$\chi = \frac{N\mu_0\mu^2}{3k_BT} \tag{1.1}$$

μ_0, k_B, N are the permeability of free space, Boltzmann constant, and no of magnetic dipoles per unit volume with magnetic moment μ, respectively. In paramagnetic materials, magnetic susceptibility is inversely proportional to temperature. Example of paramagnetic materials are oxides, salts, silicate, carbonate, sulfide, etc.

1.3.1.3 Ferromagnetism

Materials that show spontaneous magnetization even in the absence of magnetic field because of the parallel alignment of magnetic spins. There are two distinct characteristics of ferromagnetic materials: magnetic ordering temperature and spontaneous magnetization. Spontaneous magnetization is confined to small regions in various materials known as the magnetic domain. When an external magnetic field is applied, the multi-domain oriented in a different direction aligns with the direction of the applied field and forms a single domain. Another related term is saturation magnetization (M_s), which is the maximum induced magnetic moment that can be achieved in a magnetic field (H_{sat}). Beyond this, no further increase in magnetization occurs. Although the electronic exchange forces are enormous in ferromagnets, the thermal energy can overcome the exchange and produce randomization of spin. This phenomenon occurs at a particular temperature called Curie temperature (T_c). Below T_c, the ferromagnet is in an ordered state and disordered (paramagnetic) above this temperature. For the region $T>T_c$, these materials follow Curie-Weiss law (**Equation 1.2**):

$$\chi = \frac{C}{T - T_c} \tag{1.2}$$

where C and T_c are Curie constant and Curie temperature, respectively. Some examples of ferromagnetic materials are Co, Ni, Fe.

1.3.1.4 Antiferromagnetism

In this type of material, the magnetic spins nearest to each other are aligned in an antiparallel manner, which results in a net zero magnetic moment. Antiferromagnetic materials exhibit negative exchange interaction. They behaved as ordered material below a certain temperature known as Neel temperature (T_N), above which it acts as paramagnetic.

$$\chi = \frac{C}{T + T_N} \tag{1.3}$$

The known antiferromagnetic materials are NiO, Cr_2O_3, MnO, etc.

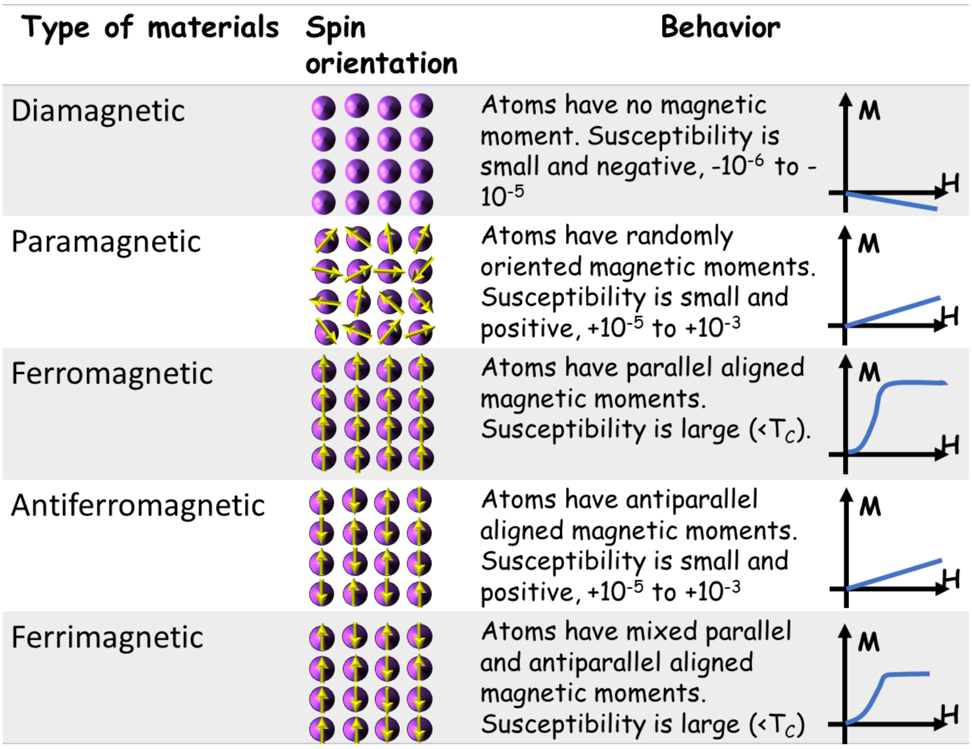

Type of materials	Spin orientation	Behavior
Diamagnetic		Atoms have no magnetic moment. Susceptibility is small and negative, -10^{-6} to -10^{-5}
Paramagnetic		Atoms have randomly oriented magnetic moments. Susceptibility is small and positive, $+10^{-5}$ to $+10^{-3}$
Ferromagnetic		Atoms have parallel aligned magnetic moments. Susceptibility is large ($<T_C$).
Antiferromagnetic		Atoms have antiparallel aligned magnetic moments. Susceptibility is small and positive, $+10^{-5}$ to $+10^{-3}$
Ferrimagnetic		Atoms have mixed parallel and antiparallel aligned magnetic moments. Susceptibility is large ($<T_C$)

Figure 1-6. *Spin alignment and behavior of different types of magnetic ordering.*

1.3.1.5 Ferrimagnetism

Ferrimagnetic materials macroscopically behave like ferromagnetic materials and show similar responses such as spontaneous magnetization, curie temperature, and hysteresis. At the same time, the spin arrangement is antiparallel to each other, like antiferromagnetic microscopically. Like antiferromagnetic materials, ferrimagnetic material exhibits different magnetic sublattices having different magnetic moments. Hence, they do not cancel each other. The magnetic structure comprises two different sublattices (A and B) separated by oxygens, and oxygen anions mediate the exchange interactions. Such interactions are called superexchange interactions. The net magnetization is $M_{net} = M_B - M_A$. Various spinel, garnets, and hexaferrite show ferrimagnetic behavior (Fe_3O_4, $NiFe_2O_4$, $Y_3Fe_5O_{12}$, $BaFe_{12}O_{19}$). A graphical illustration of different types of spin orientation of all the classes of magnetic materials are shown in **Figure 1-6**.

1.3.2 Dielectric polarization

Dielectric materials are very poor conductors, unlike insulators, as they do not have free charge carriers. When an external electric field is applied to a dielectric material, the charge carriers (electrons and holes) do not move. Instead, they slightly shift away from their equilibrium position, which leads to a dipole moment. The positive charge carriers are displaced in the direction of the field, whereas the negative charge carriers are displaced in the opposite direction. But the atoms or molecules will remain neutral as a whole. The dielectric materials can store the electric charge that acts as a capacitor. Depending upon the various contribution of polarization, the storage capability of materials varies from one to another. Mainly polarization ($\vec{P}$) is divided into four different types: space charge ($\vec{P}_{sc}$), dipole/orientational ($\vec{P}_{dp}$), electronic ($\vec{P}_e$), and ionic ($\vec{P}_i$). The schematic illustration of different types of polarization is shown in **Figure 1-7**.

The space charge polarization occurs due to the accumulation of charge carriers at the interface between material and electrodes, grain boundaries, and grains. Generally, it occurs in low frequency range $\leq 10^3$ Hz. The orientational/dipole polarization occurs due to the alignment of the permanent dipole in the direction of the electric field. It occurs in the frequency range of $10^6 – 10^9$ Hz. The relative shift of negative and positive charge carriers with an applied electric field is called ionic polarization, occurring in the range of $10^9 – 10^{12}$ Hz. The distortion of the negative electron cloud around positive nuclei with an applied electric field in the frequency range of $10^{12} – 10^{15}$ Hz is called electric polarization. So, for the high-frequency electric field, ionic and electronic polarization contributes toward net dipole polarization in the dielectric material.[57] The total polarization ($\vec{P}$) is the contribution of all types of polarization (**Equation 1.4**).

$$\vec{P} = \vec{P}_{sc} + \vec{P}_{dp} + \vec{P}_e + \vec{P}_i \tag{1.4}$$

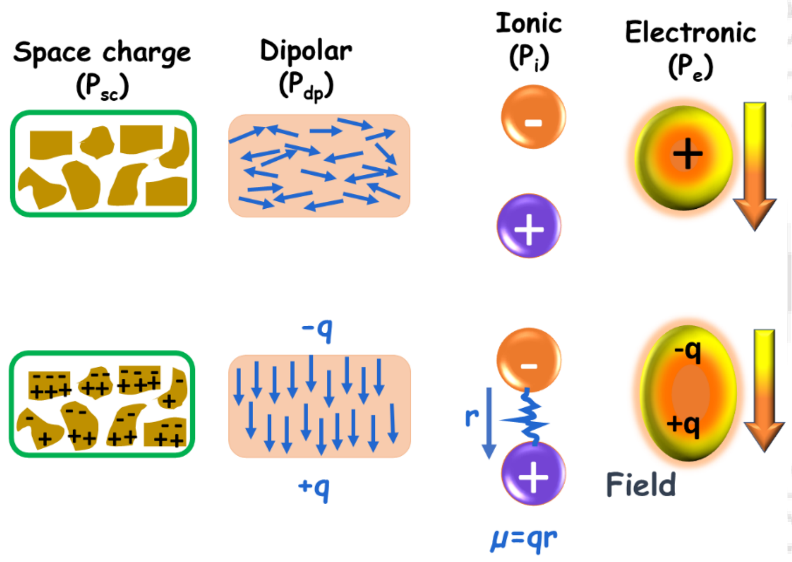

Figure 1-7. Schematic illustration of different types of polarization.

Further dielectric materials can be classified into two types based on the dependency of dipolar polarization with an applied field strength: linear dielectric and nonlinear dielectrics. In linear dielectrics, $\vec{P}$ is directly proportional to the applied electric field. Whereas spontaneous polarization is observed for nonlinear dielectric materials even in the absence of the external applied electric field, which mainly arises due to the non-centro symmetry of crystal structure. The relative permittivity is calculated by the parallel plate capacitor method by using this **Equation 1.5**

$$\varepsilon_r = \frac{\varepsilon}{\varepsilon_0} = \frac{Cd}{\varepsilon_0 A} \qquad 1.5$$

where C, A, d, are the capacitance, area of the sample, and thickness, respectively.

1.3.3 Dielectric loss

It is described as the ratio of the imaginary (ε") and real (ε') part of the permittivity. The high permittivity with low loss materials is the most demanding requirement of ongoing industrial electronics applications. Dielectric loss (tanδ) is the loss of electromagnetic energy inside a dielectric material. Based on the origin, dielectric loss is defined as intrinsic and extrinsic. The dissipation of the electric field due to the interaction with the phonon is known as intrinsic loss. In the presence of an ac electric field, the phonon system undergoes relaxation that dissipates the energy of electromagnetic waves. The intensity of interaction depends on the disorders in the crystal structure. Extrinsic loss arises due to external factors like vacancies, porosity, dislocation, impurities, etc.

1.3.4 Shielding effectiveness

EMI shielding is a mechanism in which conductive or magnetic materials restrict the propagation of EM waves. The shielding effectiveness (SE) is explained as the ratio of the incident and transmitted power of the EM waves, which is described as [58][59]

$$SE_{Total} = 10\,log\left(\frac{P_{input}}{P_{output}}\right) = 20\,log\left(\frac{H_{input}}{H_{output}}\right) = 20log\,(\frac{E_{input}}{E_{output}}) \qquad 1.6$$

where P_{output} and P_{input} are the power of transmitted and incident waves. H and E denotes the intensity of magnetic and electric field, respectively. Transmission, reflection, and absorption occur when EM waves interact with the shielding materials. Total SE is the sum of shielding due to reflection, absorption, and multiple reflections. It is expressed as:

$$SE_{Total}(dB) = SE_A + SE_R + SE_M \qquad 1.7$$

Shielding effectiveness due to reflection, absorption, and multiple reflections are denoted as SE_R, SE_A, and SE_M, respectively. The contribution of multiple reflections can be neglected if SE_A is higher than 10 dB. For efficient reflection, free charge carriers such as electrons and holes should be present in the shielding materials, which interact with the electric and magnetic fields of the imping EM waves. The ratio of E-field to H-field (amplitude) of EM waves is described as the impedance, which is small for a conducting material compared to the impedance of air. The significant mismatch in impedance causes reflection. Reflection loss mainly depends on the shielding material's permeability and conductivity. The reflection coefficient reaches nearly 1 and 0 for ultimately mismatch and matched medium at the interface, respectively. In the case of complete impedance matching, the waves can penetrate the medium. In such a scenario, absorption is crucial in achieving effective shielding. The material must contain electric and magnetic dipoles for better absorption, which will interact with the EM waves. The SE_A is directly related to the product of conductivity and permeability. So, proper conductivity, permittivity, and permeability balance are required to achieve the desired shielding. The coefficient of absorption (A), transmission (T), and reflection (R) are defined in terms of S parameters S_{11} (S_{22}), and S_{21} (S_{12}) such as:[60][61]

$$R = |S_{11}|^2 = |S_{22}|^2; T = |S_{21}|^2 = |S_{12}|^2;\ A = 1 - R - T \qquad 1.8$$

$$SE_R = -10\, log(1 - R)\,;\ SE_A = -10 log\, (\frac{T}{1 - R}) \qquad 1.9$$

According to classical electromagnetic theory, when EM waves interact with the shielding material having a thickness (d), conductivity (σ_{ac}), and magnetic permeability (μ), the EMI shielding effectiveness is expressed as:

$$SE\ (dB) \approx 10 log\left(\frac{\sigma_{ac}}{16\omega\varepsilon_0\mu_r}\right) + 20\frac{d}{\delta} loge \qquad 1.10$$

where skin depth (δ) is proportional to ac conductivity and permeability ($\delta = \sqrt{2/\omega\mu\sigma_{ac}}$), and $\sigma_{ac} = \omega\varepsilon_0\varepsilon''$. The initial term is related to reflection, whereas the latter corresponds to absorption.

$$SE_R(dB) = 10log\left(\frac{\sigma_{ac}}{16\omega\varepsilon_0\mu_r}\right) \tag{1.11}$$

$$SE_A(dB) = 20d\sqrt{\frac{\mu\omega\sigma_{ac}}{2}}loge \tag{1.12}$$

SE_R enhances with a rise in σ_{ac} and reduces with a rise in permeability and frequency of the shielded layer. To interpret the contribution of absorption, the absorption efficiency (A_{eff}) is calculated as follows:

$$A_{eff}(\%) = \frac{(1 - T - R)}{(1 - R)} \times 100 \tag{1.13}$$

1.4 Different Types of Ferrites

Based on the crystal structure, ferrites are classified in to four different types: Hexaferrites, garnet, ortho ferrites, spinel.

1.4.1 Hexaferrite

Hexaferrites exhibit magneto plumbite structure which is hexagonal in symmetry leading to magnetic anisotropy fields energy and magnetocrystalline anisotropy. The most popular hexaferrite is Ba M-type hexaferrite ($BaFe_{12}O_{19}$), having Pb_3/mmc space group.[62][63] The unit cell of $BaFe_{12}O_{19}$ is shown in **Figure 1-8**.

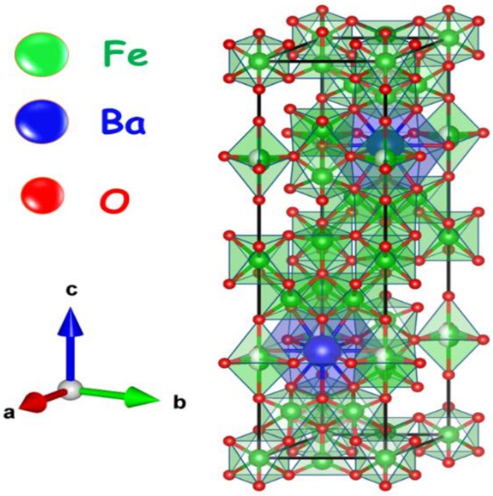

Figure 1-8. *The unit cell of* $BaFe_{12}O_{19}$.

They are highly oriented in the direction of easy magnetic axis (c-axis).[64] The M-type hexaferrite comprises 10 oxygen layers with four successive layers (each contains four oxygen anions followed by a fifth layer having a Ba cation and three anions). The structure is composed of spinel (S) blocks with two oxygen layers separated by an R block containing Ba. Every other R and S rotated by 180° is denoted by R* and S*, respectively.[65][66] The Fe ions occupy the octahedral and tetrahedral sites as well as one trigonal bipyramidal site. The magnetization in hexaferrite originates from superexchange interaction among the cation sublattices. The iron ion located in the R block aligned to the c axis in spin up orientation. In the last few decades, research on various hexaferrite (U, W, X, Y) resulted in properties of many potential applications for microwave applications.[67][68]

1.4.2 Garnet

Garnet is the class of material having a large saturation magnetization, soft ferromagnetic materials with high remanence, and low coercivity with general chemical composition $RE(Fe_5O_{12})$, where RE denotes the rare earth element. It exhibits three different types of crystallographic sites: tetrahedral, dodecahedral, and octahedral. The cationic distribution leads to the fact that garnets possess excellent chemical and structural stability. $Y_3Fe_5O_{12}$ (yttrium iron garnet: YIG) is the most commonly used garnet, the most important garnet for microwave applications due to its small FMR (ferromagnetic resonance) linewidth.[69][70] The unit cell of YIG is illustrated in **Figure 1-9**.

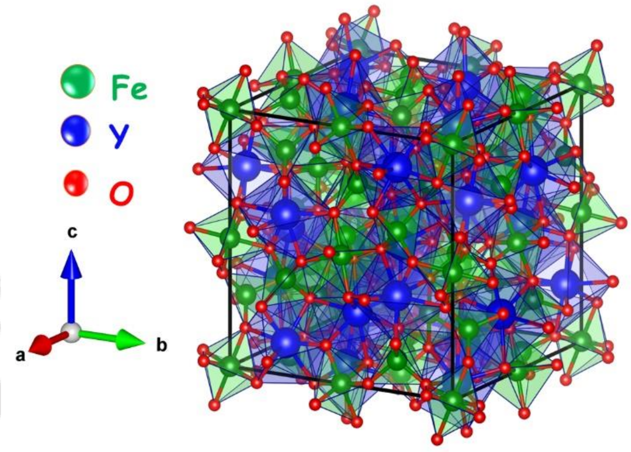

***Figure 1-9**. The unit cell structure of yttrium iron garnet.*

The origin of magnetization in garnet is due to the exchange interaction between Fe^{3+} ions placed at octahedral (a) and tetrahedral (d) sublattices through an oxygen ion. The anti-parallel coupling of $3Fe^{3+}$ in the *d* site with $2Fe^{3+}$ in *a* site leads to ferrimagnetic interaction.[71]

1.4.3 Ortho-ferrites

The Ortho-ferrites possesses ortho-rhombic crystal structure having Pbnm space group. The general chemical formula of these ferrites is $REFeO_3$. The orthoferrites commonly show weak/canted antiferromagnetic behavior with affluent magnetic properties. $DyFeO_3$ and $LaFeO_3$ are examples of ortho ferrite. For example, ortho ferrite exhibits a phase transition from paramagnetic to antiferromagnetic in the range of 620 -750 K.[72][73][74] These types of ferrites possess tunable magnetic behavior where interaction between RE^{3+} and Fe^{3+} ions decide the magnetic response of the ferrites. Also, they possess excellent multi-ferroelectricity. The unit cell structure of $DyFeO_3$ is shown in **Figure 1-10**.

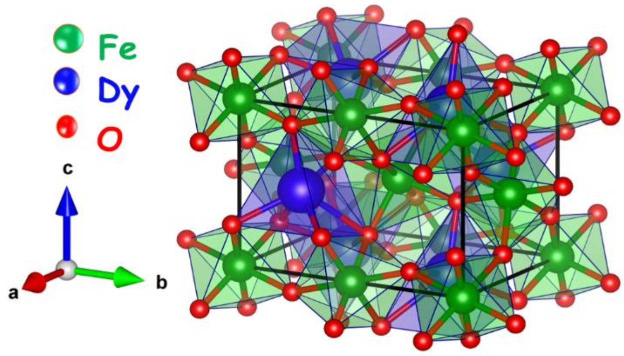

***Figure 1-10**. The schematic illustration of $DyFeO_3$ unit cell.*

1.4.4 Spinel

The spinel ferrites are indicated in the form of AB_2O_4: A denotes the divalent cations that occupy fourfold tetrahedra lattice sites, and B shows the trivalent ions residing at the sixfold octahedral lattice site. B cations occupy 16 out of 32 available octahedral sites, A cations occupy 8 of 64 tetrahedral sites.[75][76] Oxygen anions create a close packed structure of 32 ions that balance the unit cell electrically.[77][78] The most popular spinel is Fe_3O_4. The magnetization in this type of structure arises from superexchange interaction. Superexchange is a negative interaction in the ground state that leads to the antialignment of cation spin. As the B site and A site spins are antiparallel to each other, the magnetization can be enhanced by creating an imbalance between sublattices by substituting a non-magnetic ion like Zn. This idea works up to a certain extent above which the spin in A and B sublattice *cant (twist)* due to the reduction in exchange constant (J_{AB}). So, the amount of substituent elements should be chosen wisely. Spinels are further classified into three different categories: normal, inverse, and mixed. In the case of normal spinel, only divalent cation resides on the 8A sites and trivalent cations on the 16 B sites. $ZnFe_2O_4$ is an example of normal spinel ferrite (Zn resides at the A site and Fe^{3+} at the B site).[79] In the case of the inverse spinel structure, divalent ion resides 8 of 16 B site, and trivalent ions occupy all other B and A sites. $NiFe_2O_4$ comes under inverse spinel as the cationic distribution is as follows: $(Fe^{3+})[Ni^{2+}Fe^{3+}]O_4$. In mixed spinel, different ions of mixed valance state occupy both A and B site.[80] The schematic representation of normal and inverse spinel is illustrated in **Figure 1-11**.

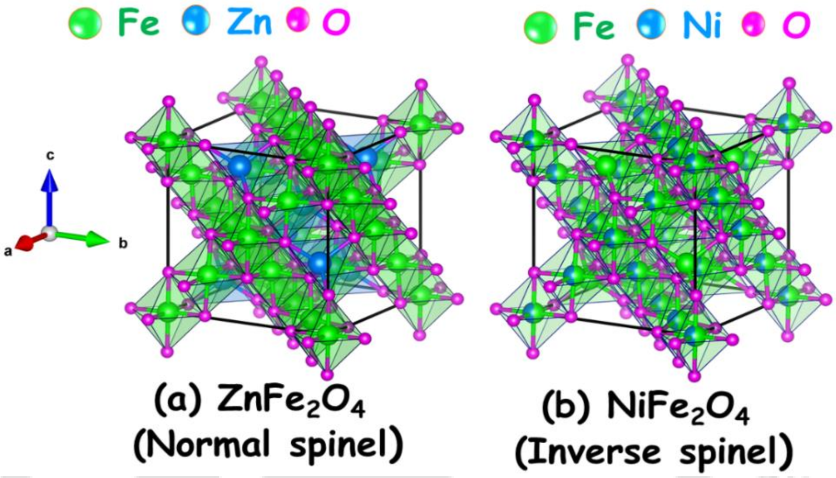

Figure 1-11. *The schematic illustration of unit cell structure of (a) Normal, (b) Inverse spinel.*

1.5 Currently used spinel ferrites for microwave applications

The ferrites have been the subject of research interest due to their use in the broad frequency range domain varies from radio waves (3kHz - 300 GHz) to microwaves (1 GHz-300 GHz).[81][82][83] **Figure 1-12** illustrates the no. of published articles on spinel ferrites for microwave applications in the last few years. Mainly, the behavior of ferrites is divided into two categories: intrinsic and extrinsic. The Curie temperature (T_c), saturation magnetization, and stress sensitivity are intrinsic properties. The microstructure-dependent properties such as coercive force, hysteresis loss, initial permeability, and resonance linewidth come under the extrinsic properties. Spinel ferrites possess high permittivity, moderate magnetic permeability, low loss, low coercivity, high saturation magnetization, and comparatively high curie temperature.[84][85]

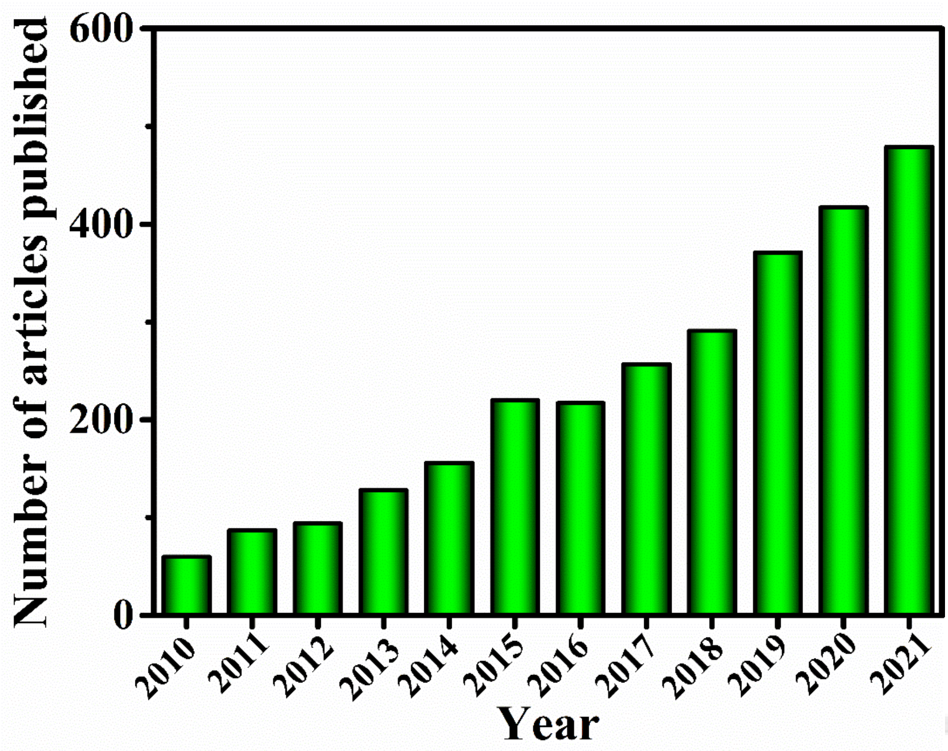

***Figure 1-12**. The number of articles published in the last few years on spinel ferrites for microwave applications.*

As the spinel structure comes under cubic structure, a relatively small effective magnetocrystalline anisotropy energy is observed that corresponds to a low magnetic anisotropy field (H_A). Since the ferromagnetic resonance frequency (FMR) is strongly dependent on H_A, spinel ferrites' zero field FMR frequency falls in lower GHz frequency, typically in the range of X-band, K_u band, or lower.

As the FMR frequency range largely determines the operating frequency range, the spinel ferrites are mainly used in the frequency range of Ku, X, S, and C - bands.[86] Ji et. al.[87] performed FDTD analysis of Y-junction microstrip circulator with Ni-Zn ferrite sphere. They observed the transition loss of 2 dB, the ferrite sphere was operational on the resonant mode in the unmagnetized case, and their resonant standing wave pattern was rotated in the magnetized case. Liu et. al.[88] reported the microwave response of low temperature fired gyromagnetic ferrite (Ni-Cu-Zn) with Bi_2O_3 additive. They reported resonance linewidth (16 kA/m), dielectric loss (5.7E-4), and M_s (337 kA/m) and showed the potential applicability for the passive integrated substrate and microwave chip circulator. Kurlyandskaya et. al.[89] studied the zero field absorption and microwave resonant behavior of pure and dopped Ni-Cu-Zn ferrites. They observed a sizable loss at zero field for the dopped sample and the effect increased with an increase in reaction temperature. Akhtar et. al.[90] reported the magnetic and morphological response of Cu substituted Ni-Zn ferrite. The objective of Cu doping was to check the suitability of the material for various microwave applications such as circulators, phase shifter and multilayer chip inductors. Saha et. al.[91] developed unique metamaterial (Ni-Zn-Cu in polyvinyl fluoride) for enhanced microwave absorption. The soft magnetic behavior modulated by PVDF enhanced the magnetic and microwave properties, which will be useful in designing next-generation devices. The high permittivity of Polyvinylidene fluoride (PVDF) and permeability of Ni-Zn-Cu made it a perfect EMI absorber in the GHz frequency range. Reddy et al. studied the electromagnetic properties of $MnFe_2O_4$ prepared by spark plasma sintering (SPS) and investigated the effect of sintering temperature on the synthesized materials' microwave absorption, M_s, H_c, and particle size.[92] The core-shell structured polythiophene nanofibers layered $MnFe_2O_4/Fe_3O_4$ were synthesized by Hosseni et. al.[93] and microwave absorption, conductive, and magnetic response were investigated. The core-shell structure promoted the interphase interactions at the surface of two ferrite phases. They achieved a minimum reflection loss (RL) of -21 dB at 12 GHz for 1.5 mm thickness. Gong et.al.[94] synthesized the phase transition enabled $MnFe_2O_4$ nanoparticles for enhancing electrical transport properties to be regulated using high pressure. They observed the hybridized enhancement between O–2p and Fe–3d orbitals. Further, they found the increment in interface density that led to an improvement in electrical properties. The enhancement in conductivity of $MnFe_2O_4$ due to the annealing of the pressure cycle provides a new feasible pathway to expand their application in microwave and electronic devices. Mishra et. al.[95] studied the M_s, Ferromagnetic resonance (FMR) linewidth, and Gilbert damping parameters of $MnFe_2O_4$/rGO to check the material's applicability for microwave applications. The composite layer was loaded on the top of a coplanar waveguide transmission line and the experimental values of FMR linewidth was analyzed by different micromagnetic models. They obtained FMR absorption of -28 dB at 22 GHz and suggested the new composite for microwave signal processing devices. Actinomorphic tubular ZnO/$CoFe_2O_4$ composites were synthesized in large scale by Cao and his group.[96] The microwave absorption efficiency was analyzed by the radar absorbing materials reflectivity far field radar cross section method. And, a maximum microwave absorption of -28 dB was obtained at 8.5 GHz which shows that the composite can be used as efficient microwave absorber. Gandhi et al.[97] studied the microwave absorption, dielectric and thermal properties of $CoFe_2O_4$-polyaniline composites synthesized by one step chemical oxidative polymerization. The incorporation of $CoFe_2O_4$ nanoparticles led to high dipolar and interfacial polarization that contributed to high shielding effectiveness. More than 99.99% attenuation of microwaves (Shielding effectiveness due to absorption = 21.5 dB) was achieved in the frequency range of 12.4 – 18 GHz. A high-performance microwave absorber composite ($CoFe_2O_4$/porous carbon nanosheet) was synthesized using instantaneous freezing assisted template by Xu.[98] It possess nanosheet-like pore walls with hierarchical porous structure. The 3D interconnected carbon helps to improve the dielectric loss of absorbers. A broadband absorption bandwidth of 5.36 GHz with RL minimum of -52.29 dB (2 mm thickness) was achieved. Lin et. al.[99] described the EM wave absorption capacity of composites of porous $LiFe_5O_8$ microspheres with reduced graphene oxide. It exhibited outstanding microwave absorbing performance having broad effective bandwidth of 3.5 GHz with minimum reflection loss of -53.4 dB at 12.2 GHz (coating thickness - 2.2 mm). The outstanding absorbing performance was assigned to the magnetic micro flower with multi-interfaces that improved the impedance matching that led to high magnetic, electrical and relaxation loss. They confirmed that this particular composite could be a better choice for lightweight microwave absorbing materials. Li et. al.[100] reported the microwave absorbing performance of tangled $ZnFe_2O_4$@carbon nano tube/PVDF composites. An appropriate combination of magnetic, dielectric and conduction loss led to the excellent absorption. The optimal RL of -54.5 dB was achieved at 10 GHz under a processing temperature of 60 C. Again, Gupta et. al.[101] analyzed the dominant EMI shielding of three-dimensional interconnected graphene aerogels decorated with ZnO nanorods and cobalt ferrite nanoparticles. The addition of magnetic cobalt ferrite enhanced the power absorption from ~ 37.738% to ~ 87.788% and further incorporation of ZnO nanorod enhanced the absorption power to ~ 93.655%. A maximum shielding effectiveness (SE) of 48.56 dB was achieved with a sample thickness of 5 mm.

1.6 A brief overview and literature on lithium ferrite in bulk and thin films

Among the spinel ferrites, lithium ferrite is the most versatile magnetic material used in devices operating at microwave frequency range.[102] Lithium ferrite ($LiFe_5O_8$ or $Li_{0.5}Fe_{2.5}O_4$) (LFO) comes under the soft magnetic materials that exhibit different spinel structures: ordered (α-phase) and disordered (β-phase). In the ordered phase (space group $P4_132$), Li^+ resides at the octahedral 4b positions, whereas Fe^{3+} occupies the octahedral 12d and tetrahedral 8c sites. The rapid quenching of the samples can obtain the disordered phase (space group Fd-3m) from high temperatures (above 800 °C) to room temperature. In the disordered phase, Li^+ and Fe^{3+} occupy 16d octahedral positions, and Fe^{3+} in 8a tetrahedral positions randomly.[103] The unit cell of the ordered and disordered phase of LFO is depicted in **Figure 1-13**. LFO exhibits high resistivity, high saturation magnetization, and low microwave and dielectric losses.[104][105] Further, it possesses a high Curie temperature (~873 K) among all the spinel ferrites. It has gained exceptional attention due to its potential for various technological applications such as gas sensors,[106] magnetically guided drug delivery,[107] ferrofluids,[108] microwave latching,[109] and microwave devices (load, circulators, phase shifters, oscillator, gyrators, and isolators).[110][111][86] It is a revolutionary low-cost magnetic material that replaced the expansive garnets for the application in microwave electronic devices and other ferrites, which are used for write/read heads of high-speed digital tapes, rod antennas, power transformers, etc., due to its chemical stability, mechanical hardness, and high resistivity.[112][113] Again, it is a promising nominee for rechargeable lithium ion batteries electrode material.[114][115]

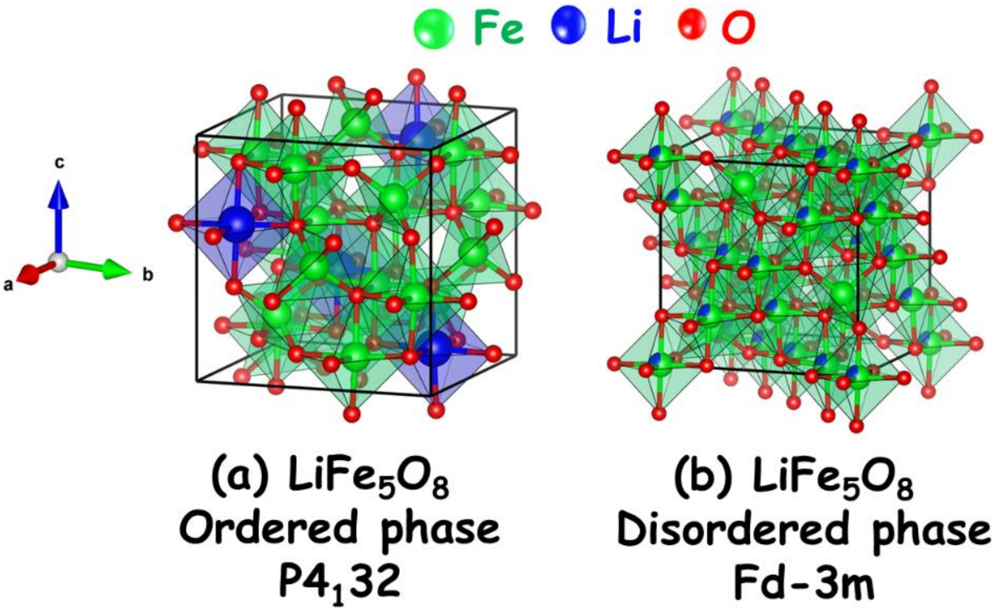

Figure 1-13*. The unit cell structure of ordered and disordered phases of lithium ferrite.*

The ferrimagnetic alignment of magnetic domains arises due to the exchange interaction (Fe^{3+}) between A and B sublattices. Here A and B represent the tetrahedral and octahedral sites, respectively. The exchange interactions in spinel ferrites are A–A, A–B, and B–B, out of which A-B is more prominent than the other two.[116]

The synthesis of LFO with proper stoichiometry is a difficuilt task due to the volatilization nature of Li during the high-temperature sintering process. To minimize the loss of Li and reduce the sintering temperature, Rajesh et al.[117] reported the effect of Bi and Pb, which are used as sintering aids on LFO ceramics. The various physical properties like magnetic and dielectric response can be tuned by substituting suitable metal cations or controlling the synthesis process. Mainly, two important factors affect the properties of substituted LFO: cationic distribution and the magnetic moment of the cation. Mane et al.[118] reported the magnetic and structural behavior of Cr-substituted LFO. The squareness ratio enhanced (as coercivity increased), whereas the saturation magnetization reduced with increased Cr content. A better magnetic and dielectric response is also achieved for Mn-substituted LFO. [119] Again, the substitution of Zn in LFO (both A and B sites) helped achieve relatively high saturation magnetization, comparatively low porosity, and a reduced value of electrical resistivity, as reported by Malyshev et. al.[120]. They also reported that Li-Zn ferrites can be used as a coating layer for EM waves in the microwave range. For such coating layers, high saturation magnetization, large dielectric, and magnetic losses are specific required criteria. Apart from this, the substitution of Ti in LFO can enhance the capability and capacity of electrochemical performance (obtained from cyclic voltammetry (CV) measurements and electrochemical impedance spectroscopy (EIS)) as compared to pure LFO.[121] Thakur et. al.[115] explained the effect of Co on other physical parameters of LFO, such as electrical and structural. By using Mossbauer spectra, they confirmed the presence of two different environments for Fe^{3+}. Due to the Verwey hopping mechanism, the DC resistivity increased with Co substitution. Junaid et. al.[122] reported the impact of Zr^{4+} and Ni^{2+} on the physical properties of LFO synthesized by the microemulsion method. Incorporating heavier ions increased the X-ray density and decreased the dielectric constant and dielectric loss. The ac conductivity and M_s increased, whereas the coercivity decreased. They proposed the nano ferrites for the potential use of high-frequency applications (as they possessed high M_s and low dielectric loss). Ahmed et. al.[123] described the role of Dy and the sintering temperature on the magnetic behavior of Li–Co ferrites prepared by standard ceramics techniques. The insertion of Dy decreased the T_c and increased the effective magnetic moment. The hysteresis loop is only observed concerning magnetic susceptibility in the ferromagnetic region, indicating the first-order phase transition. The microwave absorption, complex permittivity and permeability of Ce substituted LFO – paraffin wax composite was investigated by Sun et al. in the frequency range of 2–18 GHz. They concluded that microwave absorbers over 15 GHz with satisfactory reflection loss (>-20dB for specific frequency) could be obtained by controlling the concentration of Ce. Mohanty et. al.[124] studied the modulus and impedance spectra of Ce-dopped LFO. With the insertion of Ce, the activation energy increased, whereas dc conductivity decreased. Iqbal et. al.[125] explained the effect of Gd on the physical properties of Li-Mg ferrites. Because of the partial solubility of Gd, they observed a lattice stain that enhanced the lattice constant. Magnetization decreased due to the weakening of exchange interaction, whereas coercivity enhanced (the presence of an ultra-thin layer of Gd at the grain boundaries). Further, Manzoor et. al.[126] reported various physical properties like spectral, magnetic, dielectric, and structural properties of Ho-substituted lithium ferrite. They also traced the ortho phase of $HoFeO_3$ for the higher concentration of Ho. Porosity decreased from 44 to 23%. Also, they analyzed dielectric parameters as a function of temperature and composition (ac conductivity enhanced). The coercivity increased, whereas magnetization decreased with the incorporation of Ho. A similar trend of magnetic response is also reported for Tb-substituted Li-Mg ferrites by AsifIqbal et. al.[127] They suggested that the Li-Mg ferrites are suitable for microwave absorption. The dc resistivity linearly decreased with temperature showing the semiconducting behavior of the samples. Recently, Lan et. al.[128] synthesized flexible lithium ferrite nanopillar arrays for bending stable microwave magnetism. The nanopillar arrays exhibited higher M_s and very non-zero coercivity. Their results concluded that tuning the nanostructure of LFO is an efficient way to fabricate future flexible, stable microwave magnetic devices. Morais et al.[129] studied antenna parameters: gain and return loss of LFO for use in the ferrite resonator antennas. The temperature coefficient of resonant frequency was obtained as -482.16 ppm/°C. They explained that the magnetodielectric resonator showed tuning effect in the resonant frequency as a function of an external magnetic field.

For efficient device applications, spinel ferrites in thin films are also highly required. The structural and magnetic properties of LFO thin films that grew epitaxially on the MgO substrate (deposited by PLD) are studied by Oliver et. al.[130] The films deposited at lower oxygen pressures showed cubic anisotropy (close to bulk values) along with high saturation magnetization and narrow ferromagnetic resonance linewidth. Then, Cadieu et. al.[131] studied the microwave and static magnetic properties of highly textured LFO films synthesized by PLD on c-plane sapphire substrates. They reported that LFO films showed the linewidth of 335 Oe with clean symmetric FMR absorption lines for in-plane configuration. In contrast, a highly distorted FMR profile is observed for out-of-plane configuration. The in-plane line widths were significantly larger than for bulk LFO. Boyaraz et. al.[132] investigated LFO thin films as a function of growth temperature and substrate-induced strain. The LFO films grown on the MgO substrate remain coherently strained, whereas films deposited on $MgAl_2O_4$ showed behavior closer to bulk single crystal response. The surface morphology and film texture are enhanced with better lattice match, which indicates different growth modes on various substrates. Further, Zhang et. al.[133] explained the magnetic response of strain-tunable epitaxial LFO thin films deposited on $MgAl_2O_4$ by a sputtering system. They concluded that the in-plane compressive strain could significantly promote in-plane magnetization. In contrast, the out-of-plane tensile strain promotes the reduction of out-of-plane magnetization. Controlling the thickness of the films is an effective method for tuning the magnetic properties and the interface strain of thin films. Chilwar et. al.[134] studied the effect of Al on the optical, magnetic, and dielectric properties of LFO thin films prepared by chemical spray technique on the glass substrate. They reported an optical band gap of 3.36 – 2.04 eV. The saturation magnetization is decreased, and the coercivity increases with incorporating Al. The dielectric constant, as well as dielectric loss, decreased. Further, Zhang et. al.[135] reported another interesting atomic scale investigation of LFO films deposited on $SrTiO_3$ substrate. They described the formation of antiphase boundaries and twin boundaries. The antiferromagnetic coupling occurs across the antiphase boundary. Considering magnetic coupling across twin and antiphase boundaries, the nano-scale twin boundaries have promising applications in nano-spintronic devices such as spin torque magnetic random-access memory. Various research groups have made enormous efforts to optimize the deposition conditions on various substrates and analyze the structural and microstructural response of LFO and substituted LFO thin films.

1.7 Literature gap and motivation of the present thesis

- Based on the literature survey, it is found that most bulk studies are focused either on the low frequency dielectric or magnetic response of the LFO. In order to use the material for practical applications, the combined effect should be appropriately investigated.
- No literature on the temperature variation complex permittivity and permeability in the broadband frequency range (1MHz - 1GHz) is available. These broadband frequency dielectric studies are necessary for microwave device applications.

- However, the ideal material for EMI shielding cannot be obtained using single materials like metal, polymer, and carbon-based compounds. Looking forward to a better perspective of stability, low cost, easy processing, and temperature stability, ceramic composite with carbon-based material is the best option. In this contest to the literature, it is realized that the EMI shielding response of a material mainly originates from the synergistic effect of conduction loss, magnetic loss, and dielectric loss. The spinel ferrite, like lithium ferrite (LFO) based composite, can be a better alternative to be used as a ceramic than polymer composite as LFO possesses high saturation magnetization, high magnetic loss, moderate permeability, and high curie temperature, high temperature resistant.
- It is a known fact that rare (RE) ions possess unpaired 4f electrons, which promotes spin-orbit solid couplings. Incorporating RE ion in spinel ferrite leads to 4f – 3d coupling, which may also modify magnetic and electrical properties. For significant EMI shielding, the shielded material should have magnetic and electric dipoles interacting with the electromagnetic field.
- Very few studies are available on the properties of lithium ferrite thin films, and most of the studies are focused on the films deposited on single crystal substrates. For commercial applications, it is very important to grow the films on low cost substrates such as quartz and silicon, etc. However, reports are only available on the magnetic response of LFO thin films. The dielectric and ac conductivity response of LFO thin films are not yet explored.

Therefore, based on the above literature gaps, the following objectives are formulated.

1.8 Objectives

The objectives that we aim to accomplish in this thesis are as follows,

- ✓ To prepare Mg and Sr substituted LFO and analyze the microstructural, structural response, the variation of complex permittivity and permeability as a function of temperature and frequency, dielectric loss, magnetic loss, magnetic response, and, most importantly, obtain a correlation between the results obtained by different techniques, check the applicability of materials for circulator applications.
- ✓ Synthesize lithium ferrite/carbon black (LFO/CB) with different CB concentrations and Dy substituted LFO/CB composites, Study the effect of CB and Dy on the morphology, structural, magnetic response, permittivity, permeability, and shielding efficiency, analyze the ceramics composite for EMI shielding applications.
- ✓ Develop the thin films of LFO and Dy substituted LFO, optimize the deposition condition with different thicknesses, study the structural, microstructural, magnetic, and dielectric response, and correlate the results.

1.9 Outline of the thesis

In this thesis, the pure LFO and Mg, Sr substituted LFO with different concentrations of Mg and Sr are synthesized. Several physical properties, such as dielectric, magnetic, and conductivity, apart from the structural and microstructural, are explored for the suitability of the material to be used for circulators and phase shifters (low loss with high magnetization and temperature stability). The temperature and frequency-dependent broadband dielectric and permeability response (1MHz–1GHz) is studied. The effect of the incorporation of Mg and Sr on the structural, microstructural, dielectric loss, and magnetic response is investigated systematically. Further, the study is focused on preparing LFO-based ceramic composites with CB to be used as an efficient EMI shielding material. The EMI SE efficiency of LFO/CB composites with different wt% of CB and Dy substituted LFO/CB (10 wt%) are analyzed systematically. Also, the complex permittivity and permeability in the X-band and K_u band, magnetization, and microstructure of all the composites are studied. The synergetic effect of different types of contribution, such as conduction loss, magnetic loss, and dielectric loss, towards the efficient shielding efficiency is obtained. It is found that strikingly excellent efficiency can compete with the recently used materials. Finally, I fabricated our in-house PLD target and developed a series of thin films of LFO by optimizing different deposition conditions. The effect of thickness on the microstructural, magnetic, dielectric, and electrical properties of LFO and Dy substituted LFO is analyzed and correlated. A chronological and brief description of each chapter is included below:

Chapter 1: introduces the different types of applications of microwave materials (circulator, phase shifter, microwave absorber, EMI shielding), the theory and underlying principle associated with it, and different types of ferrites used for microwave applications. The importance of lithium ferrites and their suitability for microwave applications, the literature related to LFO, and the literature gap are also discussed. The research problem and the thesis organization are also included.

Chapter 2: describes the methods of preparation of LFO, LFO-based composites, and the deposition of LFO thin films by pulsed laser deposition system. It also includes experimental details of several characterization techniques such as XRD, Raman, FESEM, dielectric measurement (Impedance analyzer, LCR meter), VSM, VNA, and AFM and the basic details of the working principle associated with it.

Chapter 3: narrates the details regarding the formation of Mg and Sr substituted lithium ferrite and the effect of Mg and Sr on the structural, dielectric, and magnetic response of LFO. The incorporation of Mg and Sr led to lattice distortion that resulted in variations of lattice constant, bond length, and bond angles. The morphology of LMFO and LSFO ferrites exhibited a dense microstructure, and the average grain size is reduced with Mg and

Sr concentrations. The frequency and temperature-dependent permeability and permittivity are analyzed in the broadband frequency range of 1MHz–1GHz. The dielectric constant of lithium ferrite is improved with Mg substitution, x = 0.005 (ε_r = 3034, tan δ = 0.001at 1MHz) showed a maximum value at room temperature. The sample with x = 0.003 showed the best dielectric response (ε_r = 5986, tanδ = 1.17 @1MHZ, at RT) out of all the samples in the LSFO series. The relaxor behavior of the dipoles (the shift in the loss tangent with frequency) is observed in temperature-dependent dielectric response in the broadband. The activation energy of LMFO and LSMO is in the range of 1.39 – 0.35 eV and 0.142 eV – 0.07 eV, respectively. In case of LMFO, maximum permeability ~ 29 is obtained for x = 0.007 at 1 MHz, RT. The magneto-crystalline anisotropy, the thickness and the movement of the domain walls are the main contributers to the variation in permeability. The obtained Curie temperature for LFO is 873K, which is reduced with the substitution of Mg. The highest saturation magnetization (M_s = 54 emu/g) is obtained for x = 0.007 among all the LMFO samples. In the case of the LSFO series, randomness is observed in the values of T_c with respect to the Sr concentration, and a maximum M_s of 61 emu/g is observed for x = 0.007. The magnetic properties are explained by considering Neel's two sub-lattice models. The correlation between variation in structural parameters and the cationic distribution on the dielectric and magnetic response of substituted LFO is also discussed. Further, the applicability of Mg and Sr substituted LFO for microwave applications, such as circulators and phase shifters, is also analyzed (that require low dielectric loss, moderate permittivity and permeability, high magnetization, and high Curie temperature).

Chapter 4: This chapter aims to develop a highly efficient material for EMI shielding. It describes the preparation of LFO/CB (composites with different wt %) and Dy substitute LFO/CB (10 wt %) with varying concentrations of Dy and analyzes the magnetic, structural and microstructural behavior. Further, the addition of Dy caused the inhibition of grain growth and the formation of irregular grains. Though saturation magnetization decreased with incorporating CB, it did not create any considerable decrement. The saturation magnetization is also enhanced with an increase in Dy concentration up to x = 0.1 (LD10FO/CB) and then decreased after that. The complex permittivity, permeability, and EMI shielding efficiency are studied in the X- and K_u band regimes. The 20 wt% of CB with LFO (3 mm thickness) showed highest total SE (28 dB), out of which absorption-based (SE_A) is 23.17 dB and reflection-based shielding effectiveness (SE_R) is 4.58 dB. Both both LFO/CB (15) and LFO/CB (20) exhibited highest absorption efficiency ~ 99.68 % among the composites in the broad frequency range (8.2 – 18 GHz). The maximum shielding effectiveness of 24 dB is obtained for LD10FO/CB ~ 17 – 18 GHz. The Dy substitution enhances the magnetic as well as dielectric loss. Also, it is observed that absorption is the dominant mechanism in EMI shielding. The maximum absorption efficiency of 99.6 % is obtained for LD10FO/CB ~ 17 – 18 GHz. with the incorporation of CB concentration, both real and imaginary parts of permittivity drastically increased (LFO: $\varepsilon' = 4$, $\varepsilon'' = 0.11$; LFO/CB (20): $\varepsilon' = 46$, $\varepsilon'' = 19.05$ @8.2 GHz). Complex permeability is also enhanced with CB content. The values of complex permittivity and permeability for LD10FO/CB are in the range of (20 – 40) and (2 – 6), respectively. Incorporating Dy (rare earth ion) in spinel ferrite led to promoting 4f – 3d coupling along with 3d – 3d, which helped enhance the magnetic and electrical properties. The electron hopping mechanism explains the variation of permeability and permittivity. The synergic effect of dielectric and magnetic loss are the main contributors to the high SE. The above results suggest that LD10FO/CB can be used for EMI shielding applications. The results demonstrate that LFO-based ceramics can be used as a commercial microwave absorber.

Chapter 5: This chapter portrays the successful deposition of single-phase LFO and LDFO thin films using a pulsed laser deposition system. It also reports the various deposition conditions such as background pressure, substrate temperature, the substrate to target distance, etc. The dielectric response is analyzed in the frequency range of (10kHz – 1MHz) and temperature range of (300 K – 523K). The dielectric constant improved, whereas dielectric loss decreased with an increase in thickness. Impedance spectra are studied using the equivalent circuit model, and the associated conduction mechanism is investigated using different conduction models. Conductivity is found to be improved, and the activation energy decreased with the increase in film thickness. A room temperature hysteresis loop with in-plane and out-of-plane configurations is studied. The saturation magnetization is reduced monotonically with an increase in thickness attributed to the decrease in the compressive strain. Coercivity enhanced with the film thickness, possibly due to the grain size enhancement. The influence of film thickness on the physical properties is correlated. Further, it concludes that controlling the film thickness is the easiest and most effective method to tune the dielectric and magnetic response. The observed results suggest that LFO and LDFO films are promising materials for magnetic oxide semiconductor applications.

Chapter 6: summarizes the work done, future work, and the direction we can adopt for further research. The EMI shielding efficiency can be improved further by incorporating other carbon derivatives and nanomaterials of different structures. In the case of thin films, bilayer and multilayer films with dielectric seed layers can be deposited on single crystal and conductive substrates, and the resistive behavior can be studied broadly.

Chapter 2 : Synthesis methods and characterization techniques

This chapter describes the preparation methodology and measurement techniques used in this thesis work. Synthesis methods and a sintering mechanism are implemented to prepare LFO and substituted LFO in bulk form. Then various characterizations are used to study the microstructural, structural, dielectric, magnetic, and EMI shielding efficiency. Later, for depositing thin films, pulsed laser deposition is used. And various characterizations such as optical, microstructural, structural, magnetic, and dielectric are used to study the thin films.

2.1 Synthesis of bulk LFO ceramics

Several methods, such as the sol-gel, wet chemical, co-precipitation, and conventional solid-state reaction, have been developed to prepare the polycrystalline samples with fine particle size, homogeneity, and high purity. In this thesis work, we have used the conventional solid-state reaction method to prepare LFO-based ceramics, which is easy to adopt and cost-effective.

2.1.1 The conventional solid-state reaction method

Synthesis of desired quality material for the required application is the essential requirement for research in the field of experimental condensed matter physics. The conventional solid-state reaction method is the most well-known, widely used, and versatile method for synthesizing polycrystalline samples. The solid-state reaction method is thermodynamically stable, cost-effective, and environment-friendly. Also, it gives a wide selection of starting materials (carbonates, oxides, etc.). This method involves two main steps: uniform mixing of the starting reagents for better homogeneity and heat treatment for phase formation. At room temperature, starting reagents do not react with each other. Proper heating, cooling, and sufficient temperature with optimized time are required for phase formation and densification. Various steps involved in this method are illustrated in **Figure 2-1**.

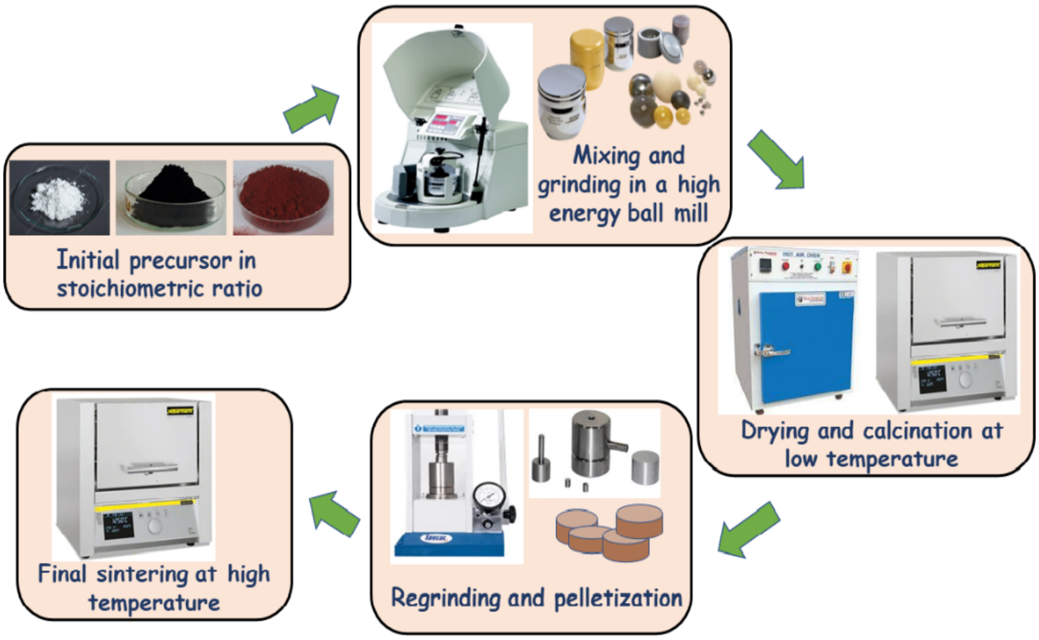

Figure 2-1*: Schematic illustration of solid-state reaction method.*

2.1.1.1 Preparation of ceramic powders

The starting reagents such as Fe_2O_3 (purity 99%, M/s JiangXiHaiTe Advance Material), and Li_2CO_3 (purity 99%, M/s Sigma Aldrich) are used as in stoichiometric ratio and mixed using a planetary ball mill (M/s. Fritsch, Pulverisette 6) for 5h. The reaction is as follows: (**Equation 2.1**)

$$Li_2CO_3 + 5Fe_2O_3 \xrightarrow[800°C]{Calcination} 2LiFe_5O_8 + CO_2 \uparrow \qquad 2.1$$

In the present work, the stoichiometrically weighed reactants are homogeneously mixed by zirconia balls of 5 mm diameter in a 1:5 powder-to-ball weight ratio in a zirconium jar. The obtained slurry was dried for 24 h in a hot air oven (M/s. Optics Technology), and the resulting powders were calcined at 800 °C for 3 h. Generally, the calcination process leads to (1) thermal decomposition, (2) phase transitions, and (3) removes volatile fractions such as carbides, nitrides, etc. In the calcination process, the crystallite growth and formation of larger particles occur by bonding and fusing smaller particles. In addition, the carbonates, nitrides, sulfates, and acetate decompose to form solid or volatile gas. To enhance the density and reduce the initial particle size, the calcined powders are re-milled for 10 h. Compared to the larger particles, the smaller particles possess high chemical reactivity due to a high surface-to-volume ratio. With the decrease in particle size, the sintering temperature reduces, which helps to improve the density of the sample. So, after calcination, it is very much crucial to reduce the particle size of the samples. Structural characterizations such as X-ray diffraction and Raman spectroscopy confirmed calcined ceramic powders' crystallinity and phase purity.

2.1.1.2 High density green cylindrical disc preparation

After the confirmation of phase formation and crystallinity, the powders are pressed into cylindrical discs for dielectric measurement. The physical properties are mainly related to microstructural and structural properties. To get highly densified ceramic discs with minimum defects and uniform smaller particle size is required. The ceramic powders are non-elastic, making it difficult to press into a compact disc. The binding agents, such as clay and polymer, provide appropriate elasticity and mechanical strength to sustain throughout the procedure. Among several binders, polyvinyl alcohol (PVA) is best for dry-pressed ceramics. The use of a low concentration of PVA does not affect the dielectric properties as it evaporates above 400 °C. In this current work, a 5 wt% PVA solution is used as a binder. The PVA is added to the prepared powders, and cylindrical-shaped discs 10 mm in diameter and 1 mm in thickness are prepared using KBr hydraulic press (M/s Technosearch Instruments). The applied pressure is expressed as:

$$P_x = P_a exp^{\frac{-4\mu KL}{D}} \qquad 2.2$$

where, μ, D, L, and K represent the friction coefficient, diameters of the die, length of the die, and a constant, respectively. P_x and P_a are the pressure gradient and the applied pressure.

2.1.1.3 Sintering

Sintering is the heat treatment process where powder of compact discs is treated at high temperatures to achieve grain growth and densification. Mainly there are two types of sintering processes: liquid-phase sintering and solid-state sintering. In the liquid phase sintering process, a liquid phase is present, which is advantageous to hold control over microstructure and improve densification. At the same time, the mechanical properties of ceramics might get affected in the liquid phase sintering. In the present work, solid-state sintering is opted by using a conventional furnace (M/s Nabertherm, GmbH). The timeline of the sintering process can be divided into three different stages. (a) initial stage: Surface polishing and connections between different particles or grains take place to form neck structure. By the end of this stage, 60-65% relative density can be achieved. (ii) intermediate stage: the neck formed between the different particles and grains grows rapidly through surface diffusion, lattice diffusion, and grain boundary diffusion, and relative density improved from 65% – 90% at the end of the intermediate stage. (iii) final stage: densification is much slower in this stage than in the initial and intermediate stages. The maximum porosity can be removed when the void space is connected to short diffusion paths. The schematic representation of three different phases is depicted in **Figure 2-2**.

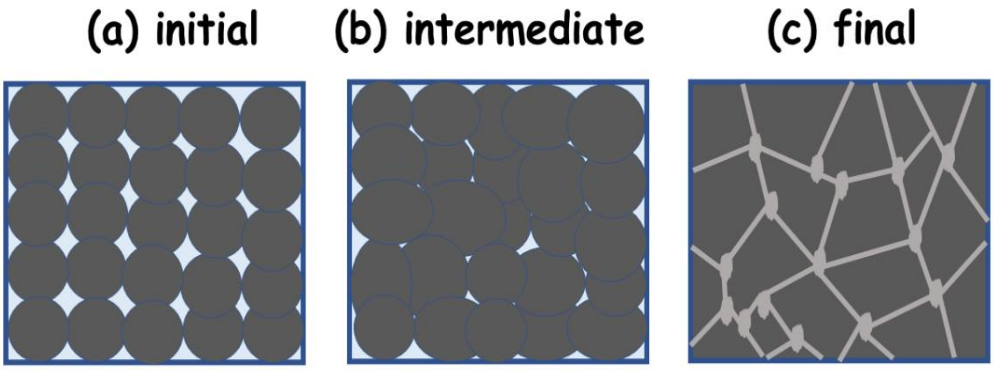

Figure 2-2. *Different stages of the sintering process.*

2.2 Deposition of thin films

2.2.1 Preparation of LFO target

The LFO target is synthesized by the conventional solid-state route. High purity (99.99%) powders of ferric oxide (Fe_2O_3; (M/s JiangXiHaiTe Advance Material) and lithium carbonate (Li_2CO_3)(M/s Sigma Aldrich; 99%) are mixed by using a planetary ball mill (Pulverisette 6, M/s. Fritsch). The obtained powders are calcined at 800 °C for 3 h. Then, the calcined powders are reground for 5 h to reduce particle size and to enhance the densification process. After that, PVA is added to the fine powder and pressed into a cylindrical shape having 20 mm diameter and 4mm thickness by using a KBr press (M-20, M/s Technosearch Instruments). Then the target was sintered at 1000°C for 10 h with a heating rate of 5°/min.

2.2.2 Pulsed laser deposition (PLD)

Several techniques and methods exist to deposit thin films, such as physical and chemical vapor deposition methods. Pulsed laser deposition, sputtering, thermal evaporator, etc., come under physical deposition methods. Among them, PLD is a widely used versatile tool for the deposition of complex oxide thin films due to stoichiometry control of the film composition, chemical homogeneity, film thickness, control over film crystallinity, and excellent adhesion. In PLD, a high-energy pulsed laser beam is focused on a target of the deposited material placed in a high vacuum chamber. The ejected material from the target occurs after laser irradiation, i.e., ablation plume that consists of the particulate component, gas, and plasma. The flux of material impinges on a substrate. The block diagram of the PLD reaction chamber is depicted in **Figure 2-3**. The view of the PLD system available in our laboratory is shown in **Figure 2-4**.

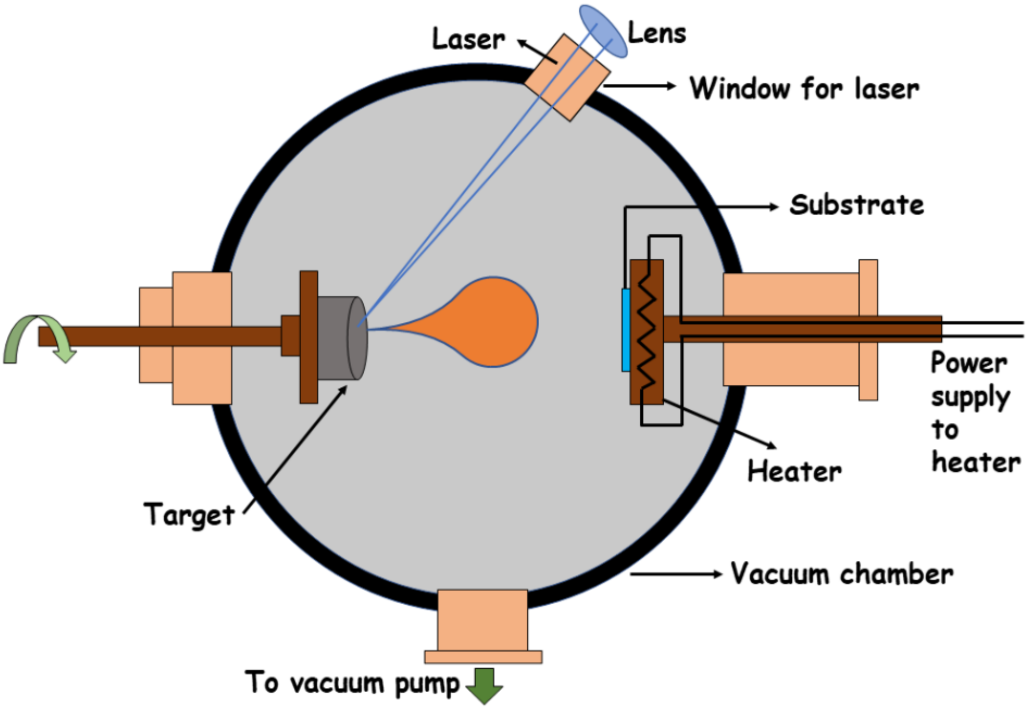

Figure 2-3*. Block diagram of PLD reaction chamber.*

The PLD chamber is made up of stainless steel (SS) spherical vessel of 16″ chamber equipped with multiple viewports, target holder carousel stage having the microprocessor-controlled facility, substrate holder along with provision for the programmable heater to elevate the substrate temperature, pressure gauges, gas inlet port and a molecular turbo pump (M/s Pfeiffer, Hi Pace 300 C) backed by a rotary pump (M/s Pfeiffer, DUO 10MC). The sufficient laser energy density on the surface of the target causes the ejection of ionized and neutral material via thermal, chemical, and mechanical mechanisms.

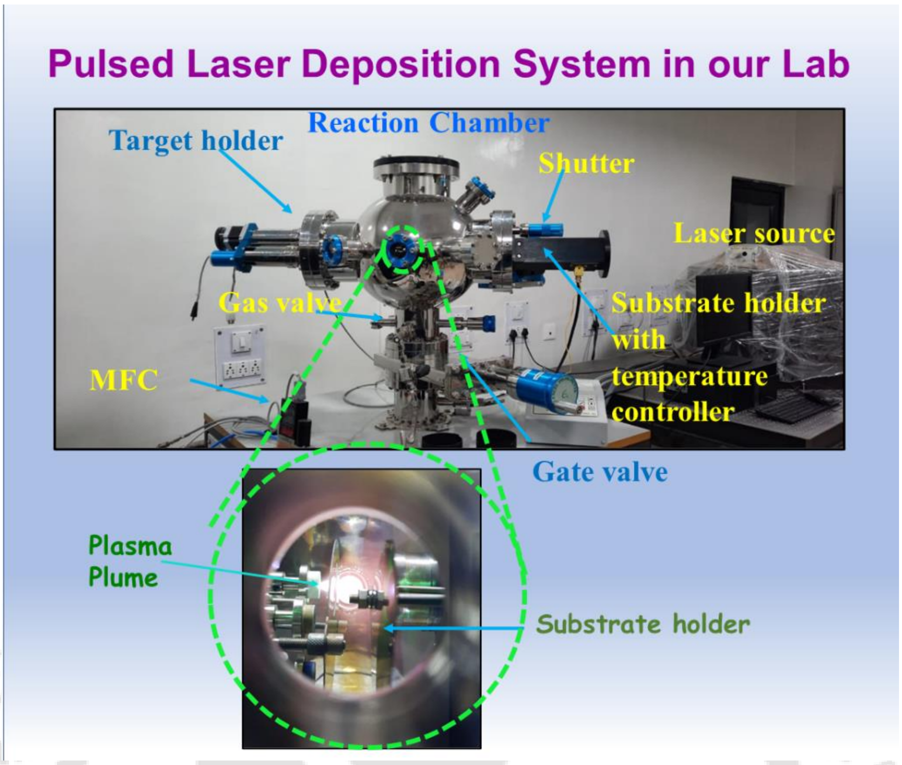

Figure 2-4. *Pictorial view of PLD system in our Lab.*

The gas line from the oxygen cylinder is connected to the chamber via a gas flow controller. The pressure inside the chamber is monitored by a compact penning gauge and Pirani gauge working in the low-pressure regime (10^{-2}–10^{-7} mbar) and high-pressure regime (10^{3}–10^{-3} mbar), respectively. The substrate holder uses resistive heating to maintain the desired temperature during deposition. Before deposition, the chamber is evacuated in the range of 10^{-5} to 10^{-6} mbar base pressure using a molecular turbo pump backed by a rotary pump and then pressurized with background oxygen gas at the required pressure for the deposition of LFO and Dy substituted LFO films.

2.2.3 Film growth

The quality and growth of the film depend on several parameters, such as substrate temperature, vacuum quality, and kinetic energy of the deposition flux. The substrate temperature is the crucial parameter that influences morphology, crystallinity, and phase formation. In the prior stage of the film growth, the flux deposited on the substrate may reevaporate by forming the clusters or be trapped on a surface defect side. These surface rearrangements are probable at high temperatures but inhibited at low temperatures. The growth models are mainly divided into the island (Volmer-Weber), layer-by-layer, and mixed growth. When the cohesive energy of the atoms within the film is greater than the cohesive energy between the film and atoms on the surface, it forms an isolated island structure. When the cohesive energy between film and substrate is greater than the cohesive energy of the film atoms, it gives rise to a layer-by-layer structure (Frank-van der Merwe). In this type of growth, the deposition of the monolayer at the time of growth gives rise to a very smooth epitaxial film. With the addition of each layer, the cohesive energy will be decreased monotonically. In such a situation, the island's growth is formed successfully after the first monolayer. When other factors like strain due to lattice mismatch override energetically, binding energy decreases monotonically. This situation favors the formation of a mixed growth structure. The schematic illustration of different growth is shown in **Figure 2-5**.

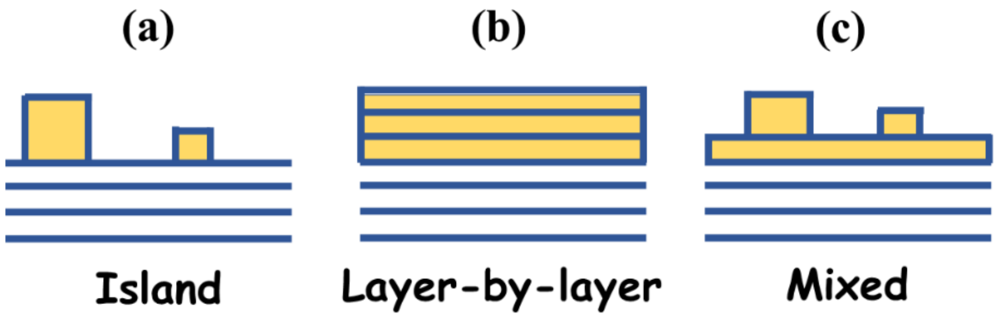

Figure 2-5. *Different growth modes in the thin film deposition.*

2.2.4 Deposition parameters

Especially for the oxide thin films, the introduction of background gas is most important. The presence of oxygen controls the kinetic energy of deposited flux. If high kinetic energy is not there in the deposition flux, the flux will be scattered by collisions with the gas. In such conditions, the film thickness drops dramatically. In this present thesis, all the films are deposited at a fixed laser fluence of 4.5 J/cm^2 from high power, 3rd harmonic (λ =355 nm), of Nd: YAG laser (SpitLight compact 400, M/s InnoLas Laser GmbH) of pulse width ~ 10 ns and repetition rate of 10 Hz. The rate at which the material impinges upon the surface is known as the deposition rate, mainly dependent on the deposited material. A very high deposition rate deteriorates the quality of the film as it provides much less opportunity for the relaxation of the film. Also, a meager rate of deposition leads to unavoidable long-run deposition. The deposition rate is also related to the quantity and quality of the chamber pressure.

2.3 Characterization techniques

2.3.1 X-Ray diffraction

X-ray diffraction is a non-destructive technique to determine materials' crystal structure, crystallinity, and phase purity. As the wavelength of an X-ray is comparable to the size of atoms (~0.1Å), so X-ray is more suitable for investigating the structural arrangement of atoms in different materials. The X-ray diffraction phenomena can be explained through Bragg's law. When an X-ray is an incident on the powder sample having several lattice planes with interplanar spacing d, it gets diffracted with an angle θ.[136] The diffracted ray from the surface of the lattice plane undergoes constructive and destructive interference depending upon the interplanar distance. Constructive interference obeys Bragg's law:

$$2d\sin\theta = n\lambda \tag{2.3}$$

where, *n* and λ represent the order of spectrum and the wavelength of the incident X-ray beam, respectively. The ray diagram related to Bragg's law is depicted in **Figure 2-6**. In this work, an X-ray diffractometer (TTRAX-III 18kW, M/s Rigaku) having CuK$_\alpha$ radiation (λ=1.5406Å) is used to characterize the LFO-based ceramics and thin films. The XRD patterns are scanned in the 2θ range of 20° – 70° with a step size of 0.03° and scanning rate of 3°/min. The 2θ calibration is performed using a standard Si sample to suppress the instrumental line broadening approximately equal to 0.15°.

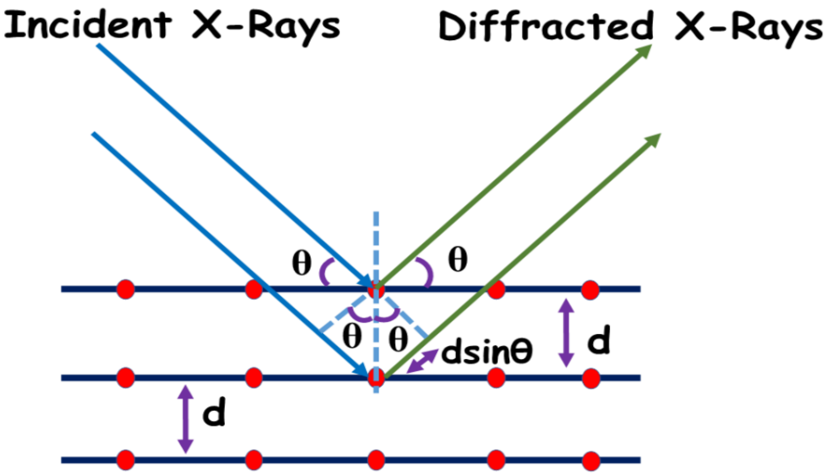

Figure 2-6. *Ray diagram of Bragg's law for X-ray diffraction.*

The depth of analysis was enhanced in 1969 due to the development of the Rietveld refinement technique by Fullprof software. It verifies the phase purity of the crystal structure along with structural parameters such as atomic position and experimental factors. Polynomial function and Pseudo–Vogit functions are used to refine the background and peak shape in the least-squares approach. The half-width parameters (u, v, w,), background polynomial, scaling factor, and lattice parameters are varied in the refinement. In this, occupancy is the chemical occupancy normalized to the diversity of the general position of the group. The oxygen occupancy was taken as 1 for all refinements. The quality of refinements is based on the values of reliability factors such as R_{exp} (expected weight factor), R_p (Profile factor), R_{wp} (weighed profile factor), and χ^2.

2.3.2 Density measurement

Archimedes' principle is employed to determine the relative density of sintered LFO discs. According to this principle, when an object is partially or fully immersed in a fluid, there is an upward force (buoyance force) exerted by the fluid on the object. The weight of the fluid displaced by it equals the upward force. The object's apparent weight is equal to the difference between the magnitude of the buoyance force and the actual weight of the object. The following expression calculates the apparent density of the sintered pellets.

$$\rho_a = \left(\frac{w_1}{w_2 - w_3}\right) \times \rho_w \quad g/cm^3 \qquad 2.4$$

where, w_1, w_2, w_3, ρ_w are the weight of the pellet in air immersed in the liquid after being removed from the liquid medium and the density of the liquid used, respectively. The relative density of the sample in percentage is estimated using the below expression:

$$relative\ density(\%) = \frac{\rho_a}{theoritical\ density} \times 100 \qquad 2.5$$

2.3.3 Raman spectroscopy

Apart from XRD, Raman spectroscopy is a versatile technique to study the crystal structure and is the measurement of the wavelength and intensity of inelastically scattered light from molecules that detect the molecular vibration of the sample. Sir Chandrasekhara Venkata Raman first discovered this phenomenon in 1928. It does not require any specific sample preparation. When the monochromatic radiation interacts with the specimen, inelastic scattering of the laser light leads to a change in the frequency of the scattered light. Usually, the scattered radiation possesses three different frequencies: less than the incident radiation (Stokes radiation), higher than the incident beam (Anti-Stokes radiation), and unchanged frequency. The unchanged frequency is due to the elastic scattering (Rayleigh scattering) **Figure 2-7**. The intensity of the Stokes line is more than the anti-stokes lines.[137] So, the Stokes lines are used to measure the conventional Raman spectroscopy, whereas the Anti-Stokes radiation is used for fluorescing samples. In this thesis, the Raman measurements are carried out using an Ar-ion laser of wavelength 488 nm (Jobin Yvon

LabRAM, M/s Horiba). This instrument has a dedicated cooling/heating sample stage (THMS6000, Linkam).

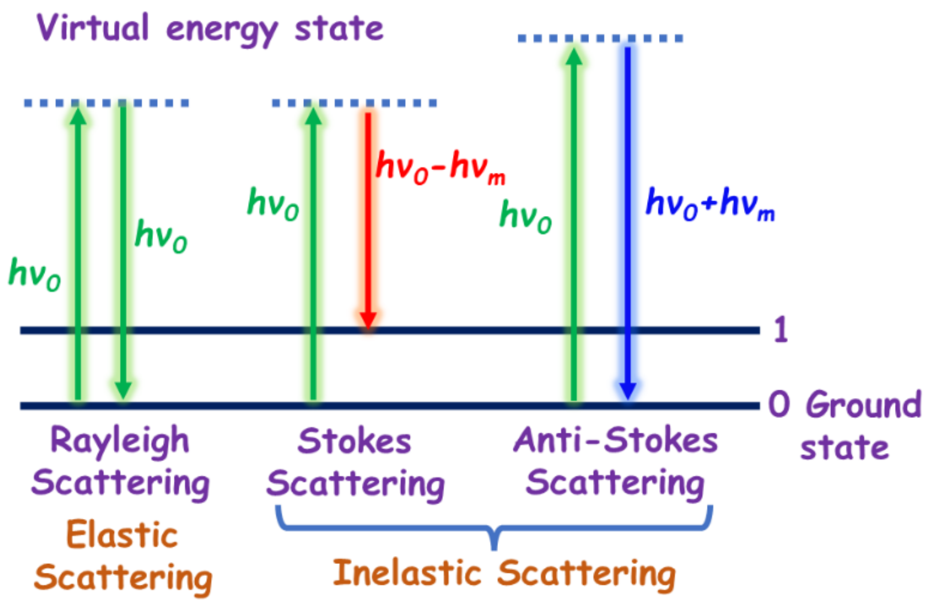

***Figure 2-7**. Energy level diagram of Rayleigh and Raman Scattering.*

2.3.4 Field emission scanning electron microscopy

Field emission scanning electron microscopy (FESEM) provides information about the surface morphology of various samples (biological, material and chemical, etc.). FESEM works with a field emission source known as a cold cathode field emitter. The source consists of a zirconium oxide-coated tungsten (ZrO_2/W) emitter that operates in a thermally assisted Schottky emission anode. The gun probes narrow beams with high electron energy, which helps to minimize sample damage and improve spatial resolution. The electrons liberated from the field emission source are accelerated in a high vacuum condition and electrical field gradient. The high vacuum allows the electrons to move in a linear motion without scattering assist to block the discharge in the instrument. The pictorial diagram of FESEM is shown in **Figure 2-8**.

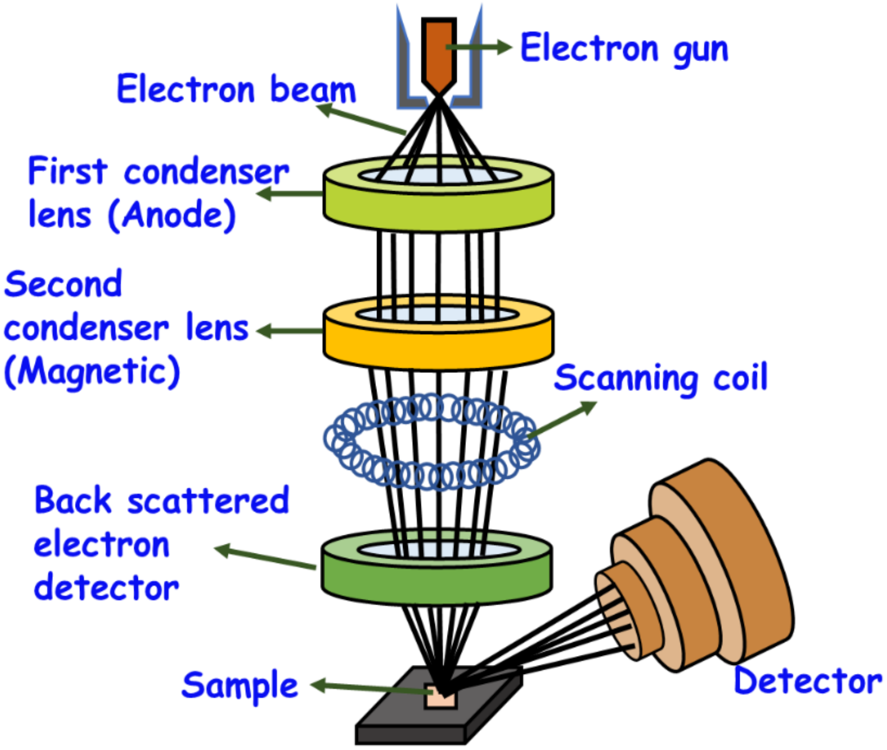

***Figure 2-8**. Pictorial diagram of FESEM.*

The primary electrons are focused and deflected by the second condenser lens. The bombardment leads to different types of emitted electrons. Along with secondary electrons, transmitted electrons, and characteristic X-rays, the backscattered electrons are also emitted from the specimen surface. A highly efficient detector receives the secondary electrons and produces an electronic signal. The signal is amplified and transferred to the digital image. In this work, SIGMA 300 (M/s ZEISS) studies the surface morphology of samples. The sample preparation part is exciting as our samples are semiconducting. To get the FESEM images, a thin layer of gold (~10 nm) is coated by sputtering over the surface that will be exposed to the source.

2.3.5 Dielectric measurements

The dielectric constant in the frequency range of 1MHz – 1GHz is measured by an impedance analyzer (4991A, M/s Agilent Technologies,). The impedance analyzer provided the advantage of measuring 133 K – 523 K in the temperature range. The temperature variation is carried out by a temperature control system (BDS 2300, M/s Novocontrol), where liquid nitrogen is used to regulate the temperature. The frequency variation spectra are measured once the temperature stabilizes after an interval of 10 K. For the measurement, a compact cylindrical disc is prepared, as mentioned above. The compact disc is converted to a metal-insulator-metal (MIM) configuration by coating a silver layer on both sides of the disc. Then the capacitor is loaded into the sample holder for the measurement. The schematic representation of the impedance analyzer is shown in **Figure 2-9**. The low-frequency dielectric measurement of thin films is carried out by an LCR meter (1J43100, M/s Wayne Kerr Electronics Pvt. Ltd.) in the temperature range of 300 K – 523 K.

Impedance spectroscopy is a widely used technique to understand the electrical properties of the material. The ac current and voltage of an electrical network can be expressed as:

$$V(t) = V_0 exp(jwt) \tag{2.6}$$

$$I(t) = I_0 exp(jwt + \varphi) \tag{2.7}$$

where, j=√-1, φ and w represent phase angle and angular frequency, respectively. The representation of complex impedance (Z*) in terms of phase angle and magnitude is as follows:

$$Z(w) = |Z| exp(-j\varphi) \tag{2.8}$$

$$Z(w) = |Z| cos\varphi - j|Z| sin\varphi \tag{2.9}$$

$$Z^*(w) = Z'(w) - jZ''(w) \tag{2.10}$$

where Z"(*w*) and Z'(*w*) are the imaginary and real part of impedance.

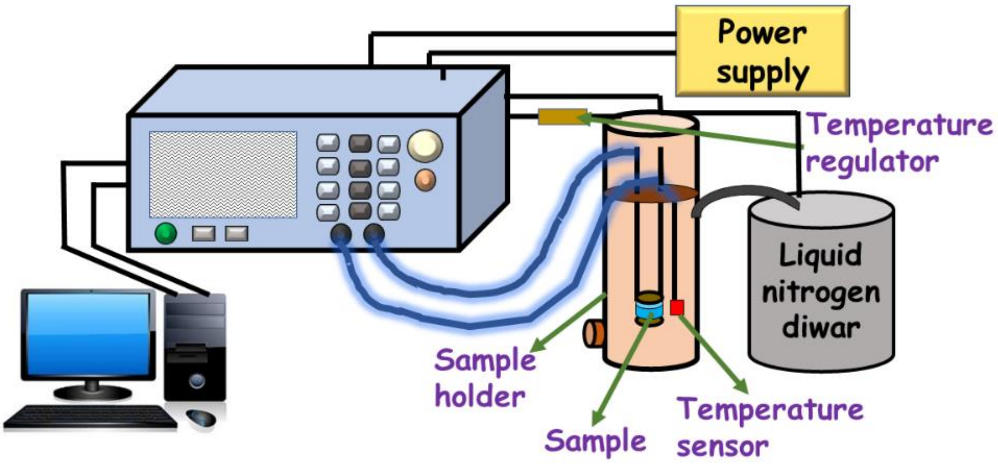

Figure 2-9. *Block diagram of Impedance analyzer measurement set-up.*

2.3.6 Vibrating sample magnetometer

The vibrating sample magnetometer (VSM) is the most successful and widely used instrument to measure the magnetic response of various materials in different temperatures range (low and high) and magnetic fields. Foner developed it. It can measure the magnetic moment with a precise accuracy of 5×10^{-6} emu. The working principle is based on Faraday's law, which states that the magnetic flux changes through coil-induced electromotive force. When a sample/pickup coil is placed under the magnetic field generated by an electromagnet, it will experience a change in magnetic flux that will induce a voltage in pickup coils. This induced voltage is proportional to the magnetic moment of the sample. The block diagram of the VSM measurement setup is shown in **Figure 2-10**. In this work, field and temperature variation measurements (300 K – 1173K) are done by VSM (7401, M/s Lakeshore) attached to a high-temperature oven (74034). The temperature is measured by the K-type thermocouple attached to the oven. The samples vibrated at a frequency of 50 Hz by a mechanical vibrator attached to the head drive. Before starting the measurement, the instrument is calibrated by a standard Ni spherical sample (moment 6.92 emu/g at 5kOe).

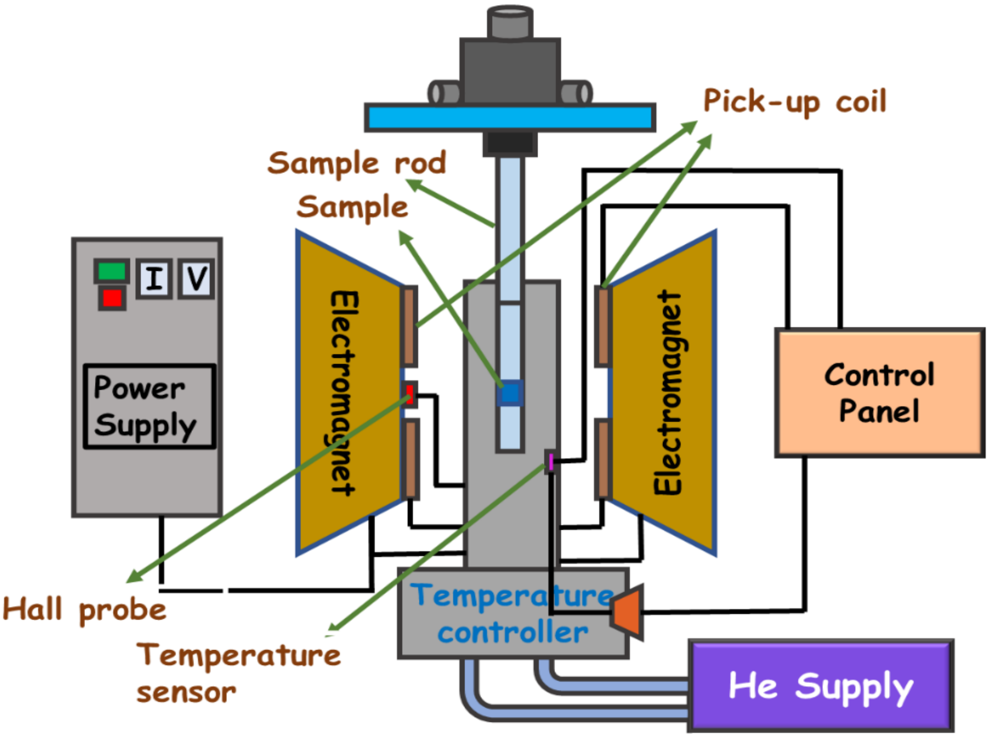

Figure 2-10*. Block diagram of VSM measurement set-up.*

2.3.7 Vector network analyzer

A Vector network analyzer (VNA) is an efficient and widely used device to analyze electromagnetic waves. A network Analyzer is a swept frequency measurement equipment to completely characterizes the complex network parameters in comparatively less time without any degradation in accuracy and precision. Two types of network analyzers are available: scalar and vector network analyzers. Scalar network analyzer measures only the magnitude of reflection and transmission coefficients, while the vector network analyzer measures both the magnitude and phase. Note that the magnitude and phase of a component can be critical to the performance of a communication system. A vector network analyzer can provide information on a wide range of these devices, i.e., from active devices such as amplifiers and transistors to passive devices such as capacitors and filters. VNA consists of a signal source, receiver, and display. The source generates the signals at the required frequency range that pass through the device or material under test. At the same time, the receiver is tuned to a similar frequency range to detect the transmitted and reflected signal.

The obtained response shows the phase and magnitude of the transmitted and reflected signal. The fundamental principle of VNA is to measure the phase and magnitude of the reflected, incident, and transmitted waves at various ports.

Two port VNA is used to measure four elements named scattering parameters: S_{11}, S_{12}, S_{22}, and S_{21} (S_{12}: coefficient at port 2 due to the source at port 1). The present study uses the PNA-L network analyzer (N5232A, M/s Keysight) and material parameters kit to measure S-parameters. The waveguide and the sample holder are connected to VNA by coaxial cables. Shot-Open-Load-Thru (SOLT) method is employed to calibrate up to the port of the waveguide setup before measurement associated with the calibration kit (X11644A, P11644A). The required rectangular waveguides are used according to the required frequency range (X- band: 8.2 – 12.4 GHz, K_u band: 12.4 – 18 GHz). The rectangular waveguide dimensions used for X are the K_u band (22.86 × 10.16 mm) and (15.79 × 7.89 mm), respectively. The schematic representation of the experimental set-up is depicted in **Figure 2-11**.

Further, the N1500A- Materials measurement suite is also used to take care of the signal loss at the interface of the sample and waveguide. This software is based on the transmission line and free space method, which includes an algorithm that corrects the effects of the air gap between the sample holder and the sample. Then, the Nicolson-Ross-Weir method calculates the complex permittivity and permeability, which provides an algorithm to derive the real and imaginary permittivity and permeability from the S-parameters in the measured frequency range. The equations are as follows:[138][139]

$$\mu_r = \frac{1+R}{(1-R)\Lambda\sqrt{(1/\lambda_0^2)-(1/\lambda_c^2)}} \tag{2.11}$$

$$\varepsilon_r \mu_r = \lambda_0^2 \left(\frac{1}{\Lambda^2} + \frac{1}{\lambda_c^2}\right) \tag{2.12}$$

$$where, \frac{1}{\Lambda^2} = -\left[\frac{1}{2\pi D} ln\left(\frac{1}{T}\right)\right]^2 \tag{2.13}$$

where, λ_0 is the free space wavelength and Re $(1/\Lambda) = 1/\lambda_g$, λ_g is the transmission line guide wavelength, λ_c is the cutoff wavelength of the transmission line.

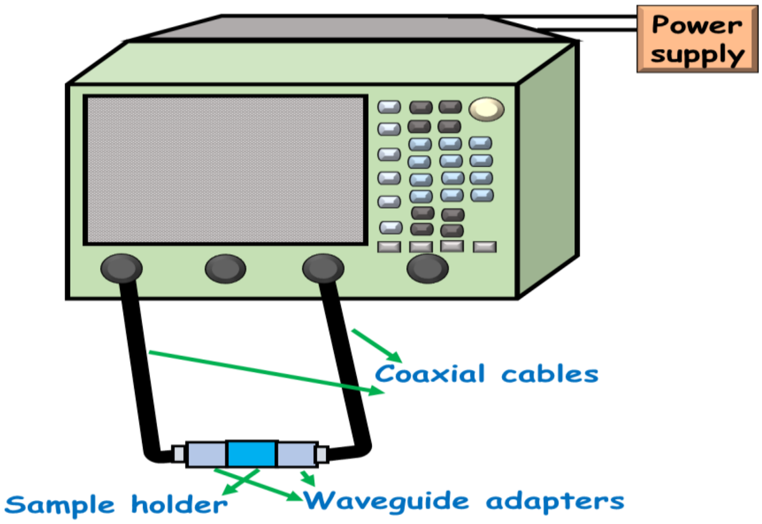

Figure 2-11. *Schematic representation of VNA measurement set-up.*

2.3.8 X-ray photoelectron spectroscopy

X-ray photoelectron spectroscopy (XPS) is a surface science technique used to reveal information regarding empirical formula, elemental composition, chemical valance state, and electronic state of the elements present on the surface of the material. It is one of the most prominent and versatile techniques for detecting elements. In this process, x-rays are bombarded on the material's surface, and the emitted electron's kinetic energy is measured. Except for hydrogen and helium, all other elements can be detected by XPS. It can study materials ranging from plastic to textiles to soil to semiconductors. The working principle is based on the photo-electric effect. Soft X-rays (energy less than 6keV) is incident on the material, and the kinetic energy of the emitted electron is measured. The emitted photoelectron is the consequence of the transfer of X-ray energy to a core-level electron. Mathematically, it can be expressed as:

$$BE = h\nu - KE - \varphi_{spec} \qquad 2.14$$

where hν, BE, KE, and φ_{spec} are X-ray energy, binding energy, kinetic energy, and spectrometer work function (a constant), respectively. The ray diagram is shown in **Figure 2-12**. The energy of the ejected electrons is analyzed by the detector. Electrons of different energies follow different paths through a detector that helps to computer to distinguish the electrons. Since electrons are in orbitals farther from the nucleus, less energy is required to eject them. Hence, higher orbitals possess lower binding energy.

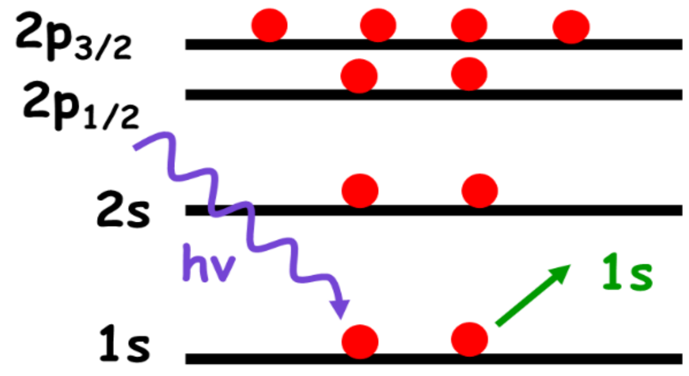

***Figure 2-12**. Emission of photoelectrons that come out due to the X-ray bombardment of a surface.*

There are different types of peaks are observed in any XPS spectra:

a) Sharp peaks: photo electrons created within the first few atomic layers (corresponding to a particular element)

b) Satellites: a sudden change in Coulombic potential as the photo-ejected electron passes through the valence bond

c) Multiplet splitting: when an unfilled shell contains unpaired electrons in an atom

d) Auger peaks: produced by X-rays (transitions from L to K shell)

In this thesis work, the XPS (PHI5000 VersaProbe III, M/s ULVAC-PHI, Inc.) is used to study the valance state of constituent elements of the deposited thin films.

2.3.9 Atomic force microscope

Atomic force microscopy (AFM) is a powerful imaging technique to analyze the topographical view that quantifies surface roughness, size, and surface morphology. The 3D profile of the sample surface can also be obtained from AFM. It consists of a flexible cantilever with a sharp tip, controller, scanner, and signal processing unit. The tip scans the sample surface and provides the surface topography based on the interaction between the surface atom of the films and the tip atom. According to Hooke's law, the Van der Waals forces between atoms at the tip and the sample surface lead to a deflection of the cantilever, measured using a laser and photodetector. The signal processing unit processes the collected signal to produce a topographical image along with phase and amplitude. In this study, the atomic force microscope (Cypher, M/s Oxford) is used to obtain AFM images of the LFO-based thin films, and further, the surface roughness, 3D and 2D image processing were done using WSxM 4.0 Beta software.[140]. The block diagram of AFM is depicted in **Figure 2-13**.

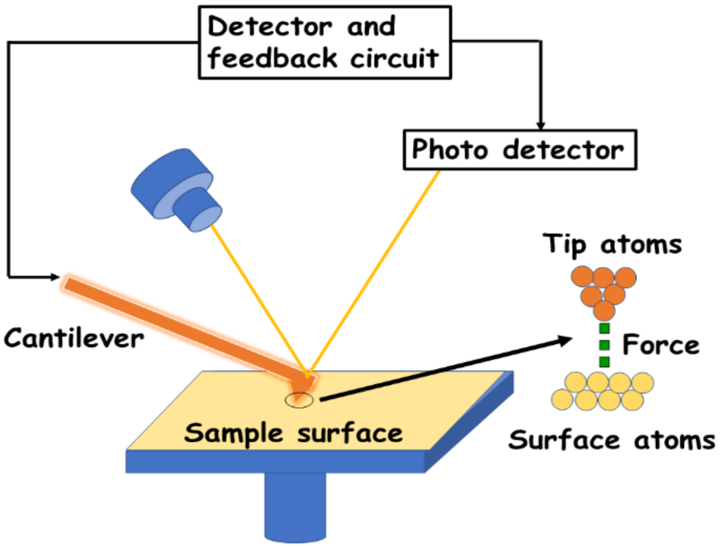

***Figure 2-13**. Block diagram of AFM.*

Chapter 3 : Broadband dielectric and magnetic studies of Mg and Sr substituted LFO for microwave applications

This chapter deals with the structural, microstructural, temperature, and frequency dependent dielectric response of *Mg* and *Sr* substituted *LFO* for low loss microwave applications. Apart from that, magnetic and permeability response is also analyzed.

3.1 Introduction

Recently, the spinel-structured lithium ferrite ($LiFe_5O_8$) has been extensively investigated for microwave devices (load, gyrators, oscillators, circulators, phase shifters, and isolators) due to its low loss at microwave frequencies coupled with superior magnetic properties.[20] It also exhibits excellent properties such as a hysteresis loop, high dielectric constant, high saturation magnetization (M_S), low dielectric loss, and relatively high Curie temperature (T_C).[141] This material is a better substitution for expensive yttrium iron garnet (YIG) for microwave applications. Further, LFO-based ferrites can also be used as a cathode in lithium-ion batteries [103],[114], and many magneto-mechanical applications.[142] Various researchers have focused on the different preparation methods of *LFO*, such as the sol-gel process,[143] solid-state reaction method,[144] auto-combustion method,[145] solvothermal,[146] microemulsion, etc. The solid-state reaction method provides the unique advantage of having a low cost of starting reagents, high yield, and a straightforward preparation methodology compared to other techniques. Moreover, considerable studies have been done on substituting dopants in either Li or Fe-site of *LFO* to enhance the dielectric and magnetic properties. Baba et al.[147] reported that the substitution of *Zn* in *LFO* benefits coercive force, magnetic loss, and densification. *Co* and *Sr* substitution enhance DC resistivity[115] and AC conductivity[148]. Hilli et al.[149] studied the electromagnetic properties of Sm-doped *LFO* nanoparticles. The resistivity of *Sm*-doped *LFO* increased with *Sm* concentration. Bamme et al.[150] reported the dielectric properties of *Cd* substituted *LFO* using the microwave-induced combustion method. The dielectric constant degraded with *Cd* substitution, and the quality factor shows cusps in the frequency range of 80 – 400 kHz. The citrate precursor method was used to prepare nanosized *Zr*, and *Mn* substituted *LFO*.[151] With an increase of *Zr* and *Mn* content, DC electrical resistivity is enhanced, which follows the polaron hopping mechanism. Similarly, with the increase in *Zr–Co* concentration, coercivity increases, but saturation magnetization decreases.[152] Nutan et al.[110] studied the complex permittivity and permeability of *Co*-substituted LFO for microwave applications. Argentina et al.[102] reported that *LFO* is better than the magnesium and nickel ferrites used at the microwave frequency region due to its relative effectiveness. El-Shaarawy et al.[153] studied structural, dielectric behavior, and ac conductivity in the lower frequency range (20Hz–10MHz) of *Mg*-doped *LFO* powders and found that AC conductivity increased with *Mg* concentration.

It is known that substituting a small amount of divalent ions in spinel ferrites may modify their electromagnetic properties and microwave absorption. In this respect, it is interesting to investigate the doping of a divalent atom on the electrical and magnetic properties of *LFO*. Different factors can affect the properties of doped spinel ferrites, such as the magnetic moment of cations and the moment distribution between sites with tetrahedral and octahedral coordination, etc. The doping with Mg^{2+} and Sr^{2+} at both Li^{+} and Fe^{3+} sites would be attractive due to its dissimilar ionic radii compared to Li^{+} and Fe^{3+}, which can introduce structural distortions, eventually modifying the *Fe–O*, *Li–O* bond lengths and *Fe–O–Fe* bond angles. Thus, it can alter the magnetic and dielectric properties, though *Mg* and *Sr* carry no magnetic moment. Moreover, the charge compensation due to the different valance states of *Li* and *Fe* compared to *Mg,* and *Sr* can create oxygen vacancies. The fluctuation of the iron valency can effectively alter the electrical properties. Hence, it is worth investigating the dielectric and magnetic properties of *Mg* and *Sr*-doped *LFO* ceramics. Most of the available studies are on low-frequency dielectric or magnetic responses of *LFO*. The combining effect of magnetic and dielectric response in the required frequency range should be studied to use the material for a particular application.

3.2 Materials and method of preparation

The polycrystalline samples of $Li_{1-x}Mg_{2x}Fe_{5-x}O_8$; x = 0, 0.003, 0.005, 0.007, and 0.01 (*LMFO*) ceramics are synthesized by the solid-state reaction process. Fe_2O_3 (M/s JiangXiHaiTe Advance Material, 99.99%), *MgO* (M/s Sigma Aldrich, 99.99%), and Li_2CO_3 (M/s Sigma Aldrich, 99%) are used as starting reagents. For the synthesis of $Li_{1-x}Sr_{2x}Fe_{5-x}O_8$; x = 0, 0.003, 0.005, 0.007, and 0.01 (*LSFO*), similar precursors are used as of *LMFO,* and $SrCO_3$ (M/s Sigma Aldrich, 99.99%) is used instead of *MgO*. All the solid-state reaction methods steps are used to synthesize the specimen, as described in Chapter 2. The resulting powders are calcined at 800 °C for 3 h. To enhance the density and to reduce the particle size, the calcined powders were re-milled for 10 h. The powders were pressed into two different shaped discs (1 mm thickness and 10 mm diameter) and toroids (outer diameter = 16 mm, inner diameter = 8 mm and height = 1.5 mm) for electrical and permeability measurements, respectively. Then the specimen are sintered at 1050 °C.

3.3 Results and discussion

3.3.1 Structural analysis

The X-ray diffraction patterns of *LMFO* ceramics are shown in **Figure 3-1.(a)**. The observed XRD revealed the formation of cubic ferrite phase (JCPDS Card No. 82-1436), without the presence of any other secondary phases. The enlarged view of the predominant diffraction peak (311) around 2θ ~ 35° is depicted in **Figure 3-1.(b)**. As the concentration of *Mg* increased, Bragg's reflections shifted towards lower angles, which resulted in an increase in the lattice parameters and cell volume (see **Table 3-1**) associated with the structural distortion due to dissimilar ionic radii of the Mg^{2+} (0.71 Å) with Li^{+} (0.76 Å) and Fe^{3+} (0.64 Å). Further analysis is carried out using the Rietveld refinement method to estimate the crystal phase, space group, and atomic positions by using FullProf Suite. **Figure 3-1.(c)** shows the representative refined XRD pattern for $x = 0.005$. It is noted that Mg substituted lithium ferrite is in a single-phase cubic structure with (space group - $P4_132$).[153] The goodness of the fit is estimated by the *R*-values, as listed in **Table 3-1**.

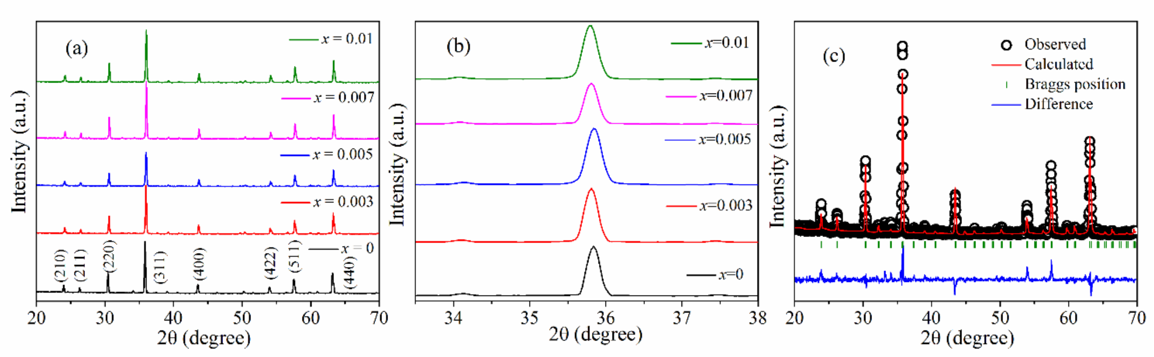

Figure 3-1. *(a) X-ray diffraction pattern of* $Li_{1-x}Mg_{2x}Fe_{5-x}O_8$ *samples. (b) Zoomed portion of the XRD around 35°. (c) Refinement pattern of LMFO (x = 0.005)*

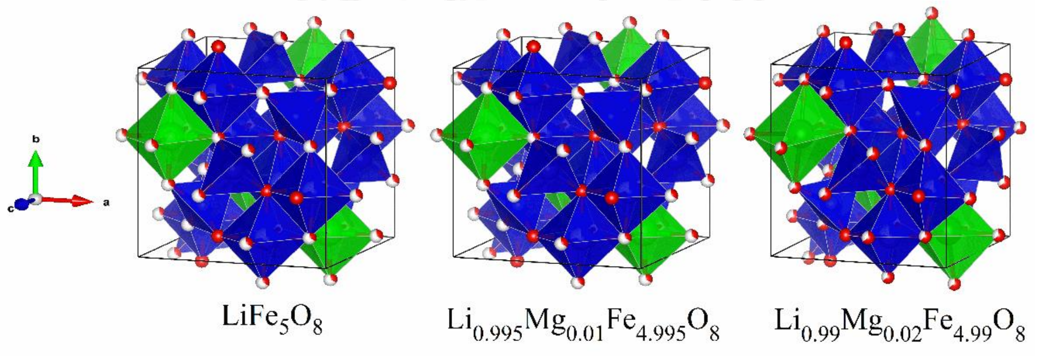

Figure 3-2. *Schematic representation of unit cells of LMFO. The green color and the blue color show the Li/Mg trigonal bipyramids and Fe/Mg trigonal bipyramids, respectively.*

To observe the cell distortion due to *Mg* substitution in *LFO*, the illustrative unit cells are generated by the Vesta software, as shown in **Figure 3-2**. It is observed that the trigonal bipyramids of iron and lithium showed a tilt as the Mg content increases. These tilts eventually affect the magnetic as well as electric properties.

Table 3-1. *Unit cell parameters calculated from the XRD pattern of the LMFO ceramics.*

Composition	**x = 0**	**x =0.003**	**x =0.005**	**x =0.007**	**x =0.01**
a = b = c (Å)	8.3259(6)	8.3344(4)	8.3293(2)	8.3358(4)	8.3506(7)
V (Å^3)	577.15	578.92	577.87	579.22	582.31
D (nm)	70.11	82.16	70.31	90.14	95.11
Strain	0.009	0.0011	0.0014	0.0014	0.0015
χ^2	1.76	2.89	2.53	2.92	2.62

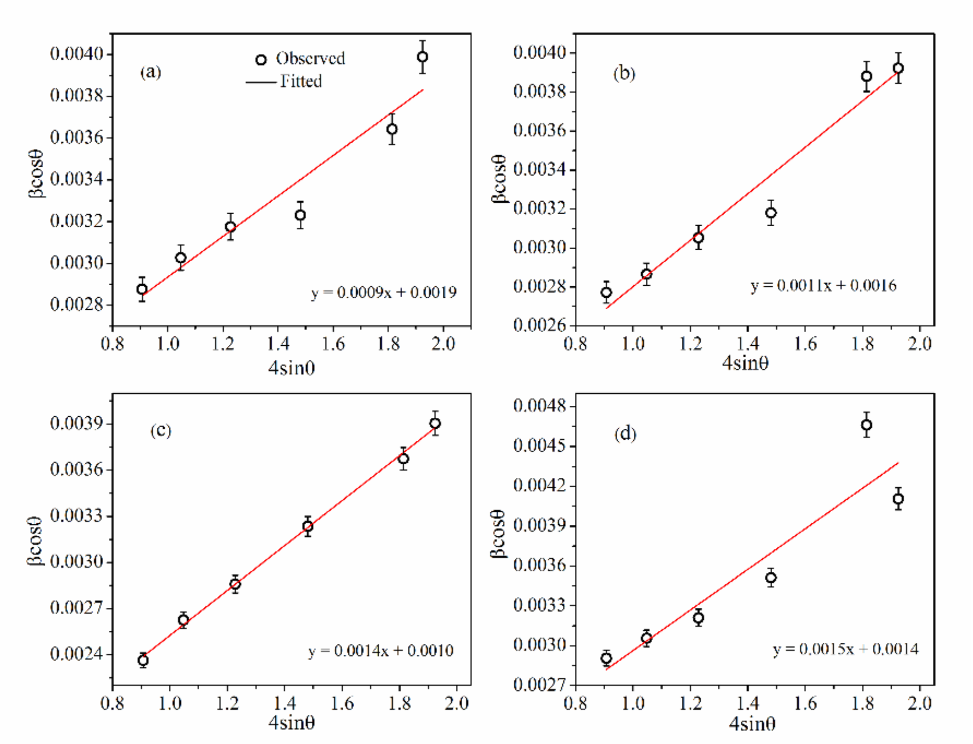

Figure 3-3. *W-H plot of LMFO ceramics (a) x = 0, (b) x = 0.003, (c) x = 0.005, (d) x = 0.01.*

The lattice strain and crystallite size in the *LMFO* ceramics are estimated by using the Williamson-Hall plot method (**Equation 3.1**):

$$\beta cos\theta = \frac{k\lambda}{D} + 4\varepsilon sin\theta \qquad 3.1$$

where k is the shape factor, β the full-width half maxima (FWHM) of the diffraction peak, λ the incident X-ray wavelength, θ is the Bragg angle, D is the crystallite size, and ε is the strain.[154] **Figure 3-3.** shows the plots between $\beta cos\theta$ and $4sin\theta$. Strain and crystallite size is calculated from the fitted line and listed in **Table 3-1**. The crystallite size and strain range between 70–95 nm and 0.09 %–0.15 % for x = 0–0.01, respectively. The crystallite size and strain are enhanced with increased Mg content.

Figure 3-4.(a) shows the XRD pattern of *LSFO* ceramics. As the concentration of Sr increases, it is observed that the diffraction peaks shifted towards the lower Bragg angles (see **Figure 3-4.(b)**), indicating the structural distortion caused by the dissimilar ionic radii of the dopant and parent elements.

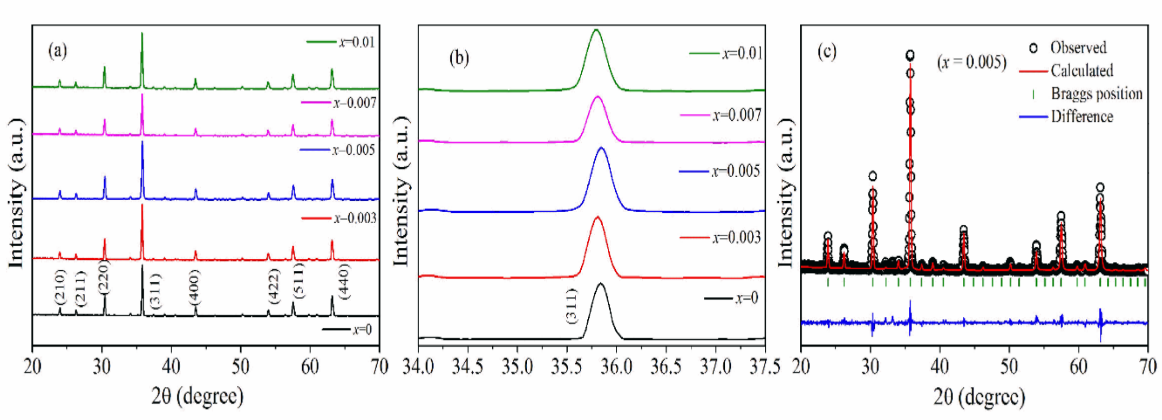

Figure 3-4. *(a). XRD Pattern of* $Li_{1-x}Sr_{2x}Fe_{5-x}O_8$ *samples. (b). The zoomed portion of the XRD ~ 35°. (c). Rietveld refinement pattern of LSFO for x = 0.005.*

Further, the Rietveld refined XRD patterns of sintered *LSFO* samples are carried out to estimate the lattice parameters, the volume of the unit cell, atomic positions, and crystal structure by using Full-prof software by considering the pseudo-Voigt function. **Figure**

3-4.(c) shows the Rietveld refined pattern of the *LSFO* sample for x = 0.005. The lattice parameters are enlisted in **Table 3-2**. It is found that the lattice constants and unit cell volume are enhanced with Sr concentration due to the larger ionic radii of (Sr^{2+} ~1.18Å) as compared to Li^{+} (0.76Å) and Fe^{3+} (0.64 Å). The shift of the predominant (311) peak of *LSFO* towards the lower Bragg angle (2θ) with *Sr* substitution confirmed the lattice expansion.

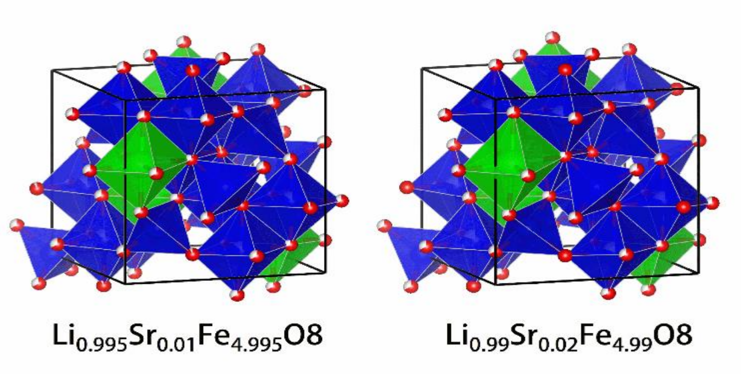

Figure 3-5. *Schematic representation of unit cells of LSFO.*

Table 3-2. *XRD parameters calculated from the XRD pattern of LSFO ceramics.*

composition	**x = 0**	**x =0.003**	**x =0.005**	**x =0.007**	**x =0.01**
a = b = c (Å)	8.3259(6)	8.3491(3)	8.3492(4)	8.3514(6)	8.3502(5)
V (Å^3)	577.15	582	582.02	582.48	582.2
D (nm)	70.11	64.37	58.34	59.88	63.6
Fe-O (Å)	1.9236	1.9233	1.8695	1.9455	1.92357
Fe-O-Fe (°)	121.20	122.46	122.33	126.35	127.21
Strain	9.6E-4	0.00105	0.00118	9.9E-4	0.00125
χ^2	1.76	3.29	2.9	2.57	2.91

Costa et al.[155] also observed similar values (a = b = c = 8.3257 Å, α = β = γ = 90°) in *LSFO* prepared by solid-state reaction method. The Vesta software draws the schematic unit cell structures to show the cell distortion upon Sr doping. **Figure 3-5** shows the unit cells for x = 0, 0.005, and 0.01, and it is clear that the trigonal bipyramids of lithium and iron showed a tilt with an increase in the Sr concentration. The crystallite size and lattice strain of the *LSFO* sample are calculated by the Williamson-Hall plot method by using **Equation 3.1**, as shown in **Figure 3-6**. The obtained crystallite size and the strain are in the range of 58.34 nm – 70.11 nm and 0.096 % – 0.125 % for x = 0 – 0.01, respectively.

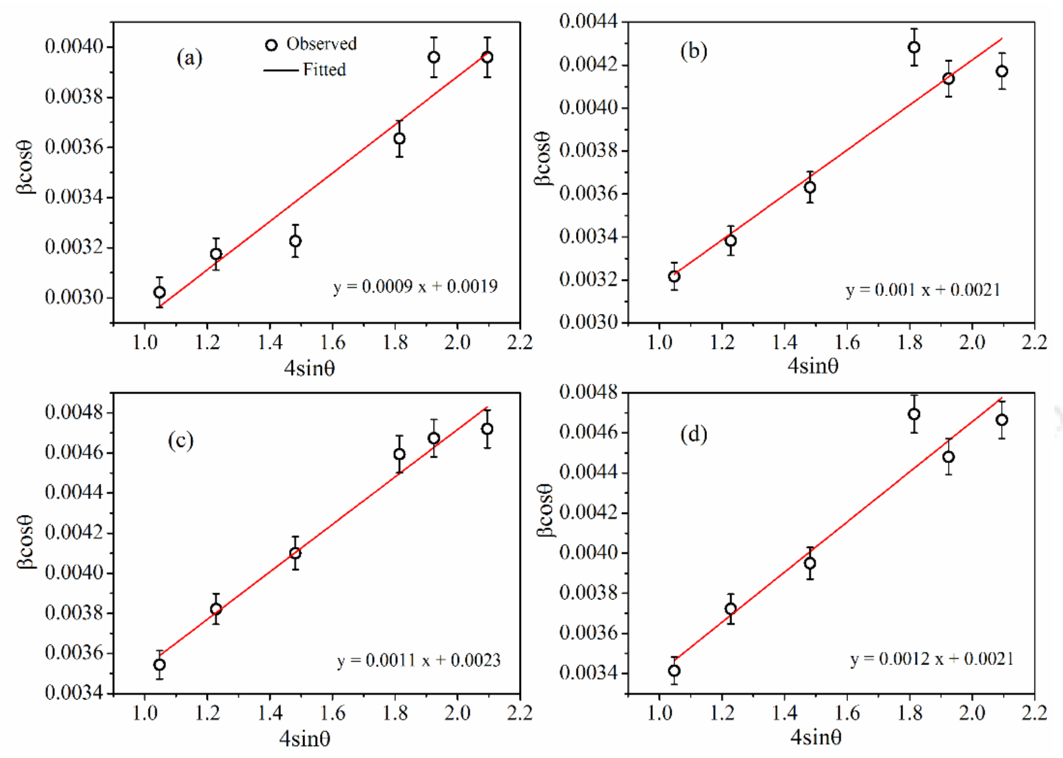

Figure 3-6. *W-H plot of LSFO ceramics (a) x = 0 (b) x = 0.003 (c) x = 0.005 (d) x = 0.007 (e) x = 0.01.*

The larger crystallite size (70.11 nm) is obtained for pure *LSFO*, which is approximately equal to the reported values [156], and further, it decreases to 58.34 nm for the x = 0.005 sample. The crystallite size and strain variations are attributed to the substitution of larger Sr^{2+} ions at Li^{+} and Fe^{3+} sites of the *LFO* matrix.

3.3.2 Surface morphology

The surface morphologies of the *LMFO* and *LSFO* ceramics are shown in **Figure 3-7** and **Figure 3-8**,respectively. It is observed that the *Mg* and *Sr*-doped *LFO* samples exhibit uniform grain distribution with dense microstructure as compared to pure *LFO*. The microstructure and grain size are strongly affected by *Mg* and *Sr* substitution. The density of *LMFO* and *LSFO* ceramics is calculated by Archimedes's principle and is around 95% of the theoretical density. The smaller initial particle sizes, which enhance the sintering velocity at lower temperatures, are attributed to higher relative densities. The grain size is a crucial parameter influencing the ferrite's dielectric and magnetic properties. The density of the *LMFO* and *LSFO* is found to increase with *Mg* and *Sr* concentrations. The average grain size is measured by Image J software (linear intercept method), and the obtained grain sizes for *LMFO* and *LSFO* are between 1.26–0.97 µm and 1.26 – 1.1 µm, respectively.

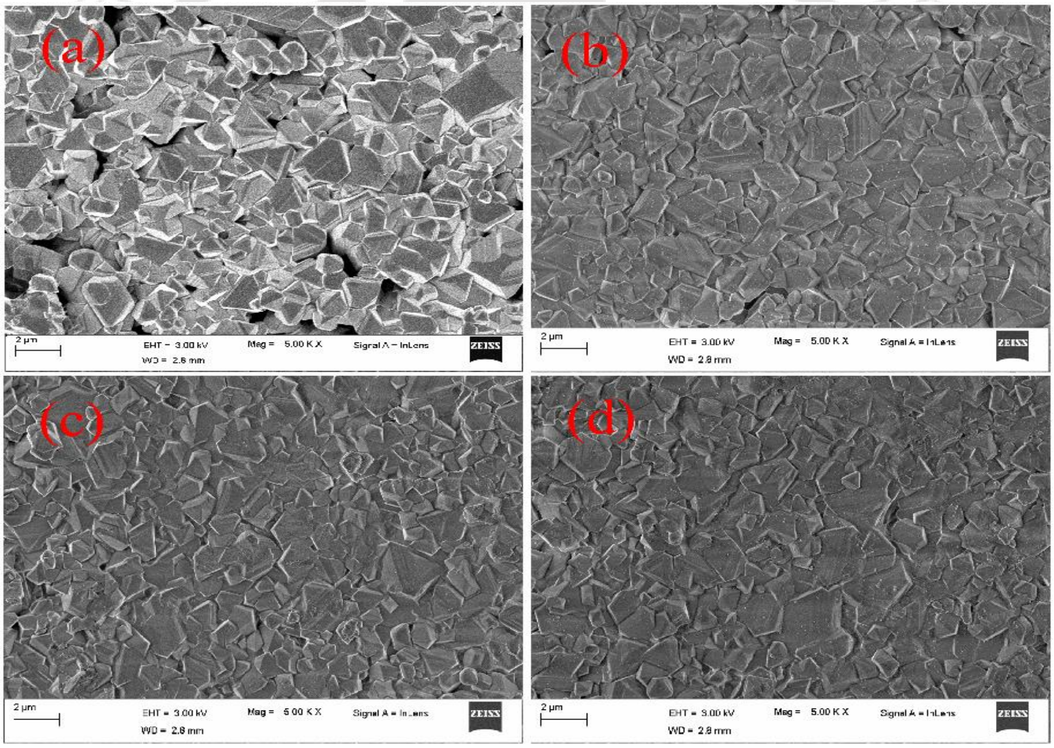

Figure 3-7. *FESEM micrograph of the LMFO samples (a) x = 0, (b) x = 0.003, (c) x = 0.005, (d) x = 0.01.*

Different parameters, such as the concentration of various ions and diffusion coefficient, can explain the variations in the grain size.[112] The grain size of the ferrites is highly influenced by the domain wall contributions in the low-frequency regime [157], which can also be seen in permeability. The flexibility of the grain boundary causes grain growth.

Further, grain growth and re-crystallisations are related to the mobility of grain boundaries.[158]

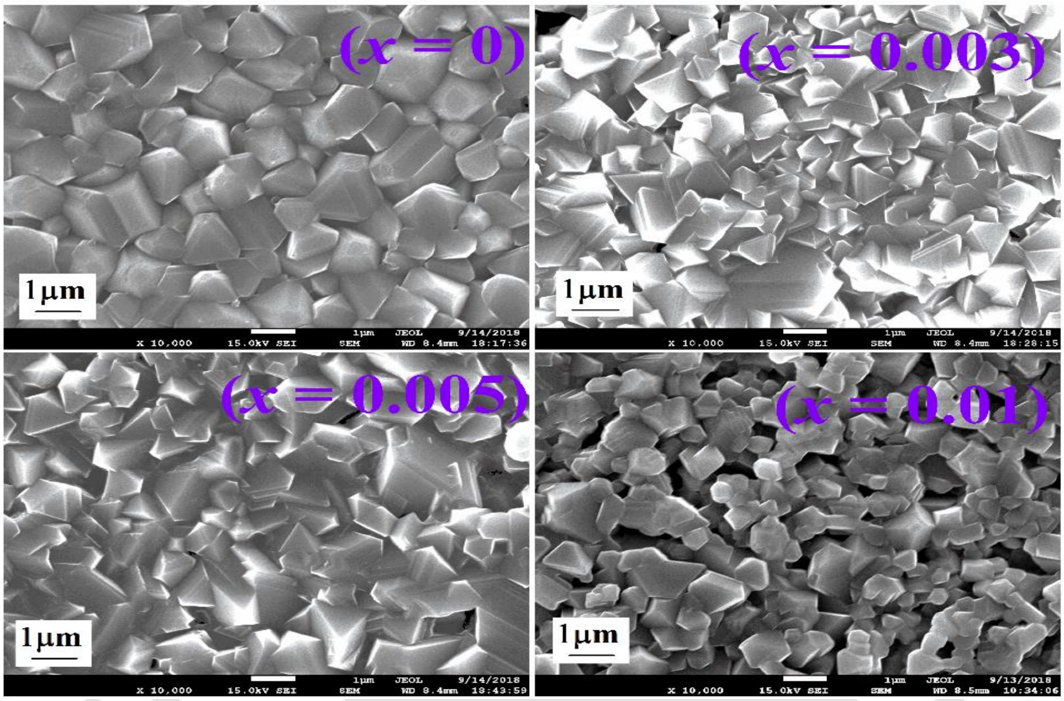

Figure 3-8. *FESEM micrograph of the LSFO samples (a) x = 0, (b) x = 0.003, (c) x = 0.005, (d) x = 0.01.*

3.3.3 Dielectric response

3.3.3.1 Dielectric dispersion with frequency

The frequency-dependent dielectric constant measured in the temperature range of 133 K – 523K is shown in **Figure 3-9**. The dielectric constant of the *LMFO* samples decreases with applied frequency, which is a typical linear dielectric response. The contribution to the dielectric constant comes from different polarization mechanisms, such as ionic, electronic, interface, and dipole polarization, which influence the frequency-dependent dielectric response. In the high-frequency regime, the dielectric response is mainly affected by dipole, ionic, and electronic polarization. The frequency-dependent dielectric constant may also be explained based on the electron hopping mechanism and dipole relaxation. The reduction of dielectric constant till 100 MHz can be due to the relaxation of dipoles. In applying the external electric field, the interchange of electrons between $Fe^{3+} \leftrightarrow Fe^{2+}$ builds up local displacement of charges that causes polarization. Polarization reduces with an enhancement in frequency.

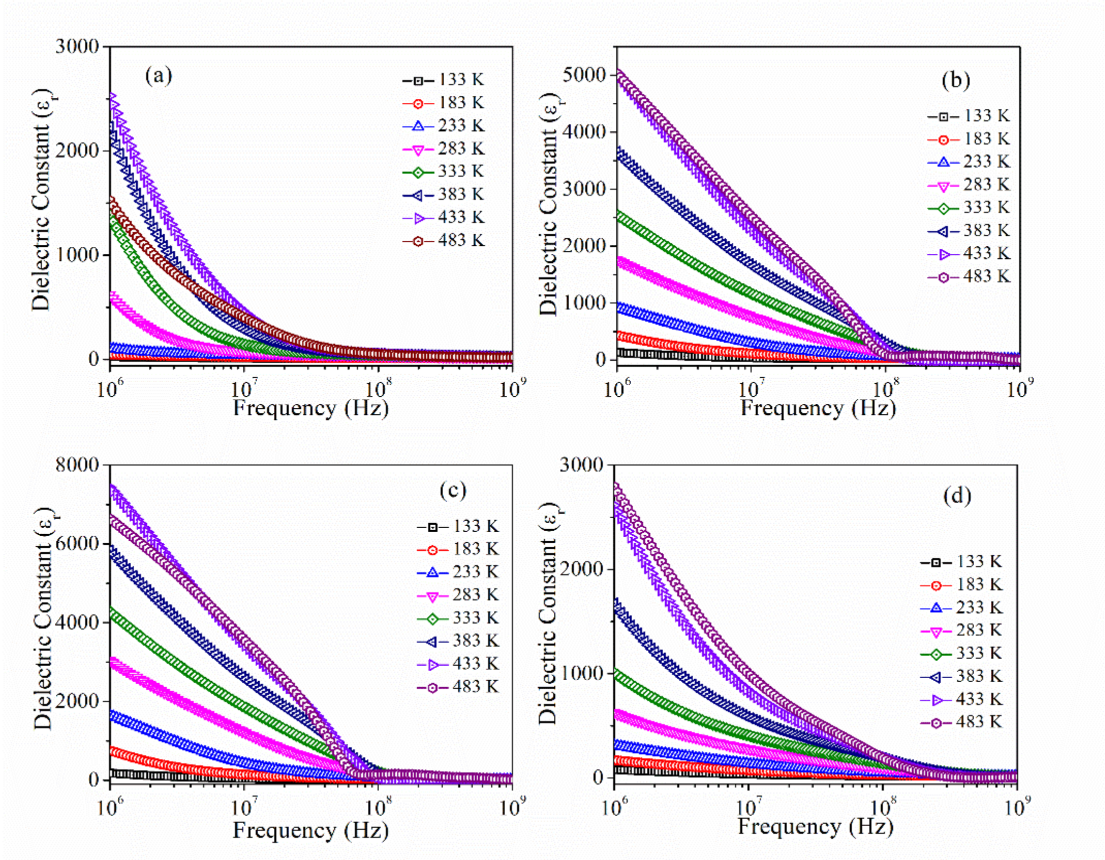

Figure 3-9. *Frequency dependent dielectric constant of LMFO ceramics, measured at different temperatures (a) x = 0, (b) x = 0.003, (c) x = 0.005, (d) x = 0.01.*

Table 3-3. *The obtained permittivity and dielectric loss tangent values of LMFO ceramics.*

Composition		**x = 0.00**		**x = 0.003**		**x = 0.005**		**x = 0.007**		**x = 0.01**	
		ε_r	tanδ	ε_r	tanδ (10^{-2})	ε_r	tanδ (10^{-2})	ε_r	tanδ (10^{-2})	ε_r	tanδ (10^{-2})
133 K	1MHz	26	0.63	134	0.3	181	0.42	121	0.27	80	0.18
	1GHz	11	0.09	17	0.05	18	0.06	18	0.05	16	0.06
300 K	1MHz	619	2.87	1759	0.15	3034	0.16	1670	0.16	626	0.20
	1GHz	16	0.70	17	0.98	12	0.93	21	1.03	19	0.55
513 K	1MHz	143	22.8	4857	1.85	6056	1.89	6738	0.90	2830	1.31
	1GHz	19	2.62	3	1.6	14	1.6	10	2.32	20	1.61

The hopping of electrons is occurred up to a particular frequency, beyond which it gets relaxed. Hence, ε_r becomes constant.[159],[160],[161] Whereas the more considerable dielectric constant value at a lower frequency regime may be ascribed to grain boundary defects and the predominance of Fe^{2+} ions. A similar kind of response is reported by Iqbal [151] and Surzhikov.[160] It is noted that the dielectric constant of the samples enhanced with Mg substitution up to $x = 0.005$ compositions and reduced further with the addition of *Mg*. This can be attributed to the higher polarizability of *Mg*, uniform grain size, and maximum relative density. The dielectric constant improves with temperature, as seen in **Figure 3-9**. At higher temperatures, the dipoles align easily, leading to a higher dielectric response. The dielectric response is enhanced with *Mg* substitution. The earlier studies found that Li^{+} ions reside only at octahedral sites, whereas Mg^{2+} prefers both octahedral and tetrahedral sites. Hence, it replaces the Fe^{3+} ions with B-site from A- site. Consequently, more Fe^{2+}–Fe^{3+} ion pairs accumulate at B-site, thus increasing the hopping mechanism.[153] Further, another factor such as oxygen vacancy which is created by the substitution of Sr^{2+}/ Mg^{2+} also plays a role in the dielectric response. The single ionization of oxygen vacancies ($V_{\dot{O}}$) is use to be created over grain boundaries. The natural oxygen vacancy (V_O) is created due to the heating of the LMFO/LSFO samples at high temperatures. By losing an electron ($V_o = V_{\dot{O}} + e'$), the natural vacancy in the Fe^{3+}–O–Fe^{2+} network can be transferred to a singly ionized ($V_{\dot{O}}$) positive charge. Interestingly, $x = 0.005$ samples exhibited the best dielectric response at the measured temperature range, and all other samples displayed better dielectric response than pure *LFO*. The reduction in the dielectric constant in higher concentration of Mg can be attributed to the presence of oxygen vacancies that degrades both dipole and ionic polarizations through domain-wall clamping. The values of dielectric loss and dielectric constant obtained at some frequencies and temperatures are listed in **Table 3-3**. Very low dielectric loss is achieved with *Mg* substitution when compared to previous reports. [162],[151] **Figure 3-10** shows the variation of dielectric constant with frequency at different temperatures for *LSFO* ceramics. A similar response is observed for *LSFO* as for *LMFO*. The dielectric constant of the *LSFO* ceramics diminishes with a rise in frequency except for $x = 0.01$. As temperature rises, the dielectric constant of the sample is enhanced drastically. At lower temperatures, the dielectric constant values are lower as compared to the samples measured at higher temperatures. It can be due to the freezing of dipoles at cryogenic temperatures. But with a temperature rise, the dipole alignment occurs quickly. Interestingly, the sample with $x = 0.003$ displayed the best dielectric response. The sample with $x = 0.01$ revealed an inferior dielectric response, which may be attributed to the porous microstructure and lower relative density.

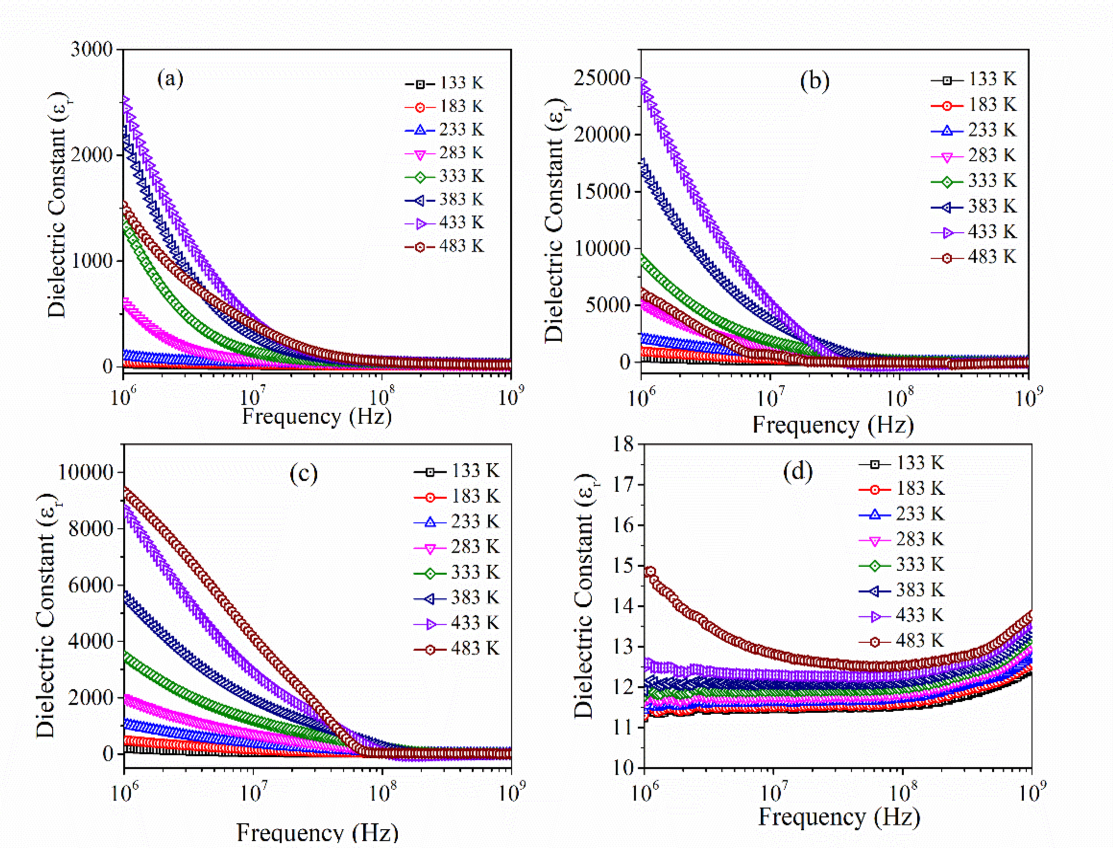

Figure 3-10. *Frequency variation of the dielectric constant of LSFO ceramics, measured at different temperatures for (a) x = 0, (b) x = 0.003, (c) x = 0.005, (d) x = 0.01.*

3.3.3.2 Variation of dielectric response with temperature

The temperature-dependent dielectric constant (ε_r) and dielectric loss (*tanδ*) of LMFO obtained at different frequencies are shown in **Figure 3-11** and **Figure 3-12**, respectively. As the temperature increased from 133K, the dielectric constant of *LFO* initially increased, exhibited a hump at around 433K, and then decreased for a further rise in temperature.

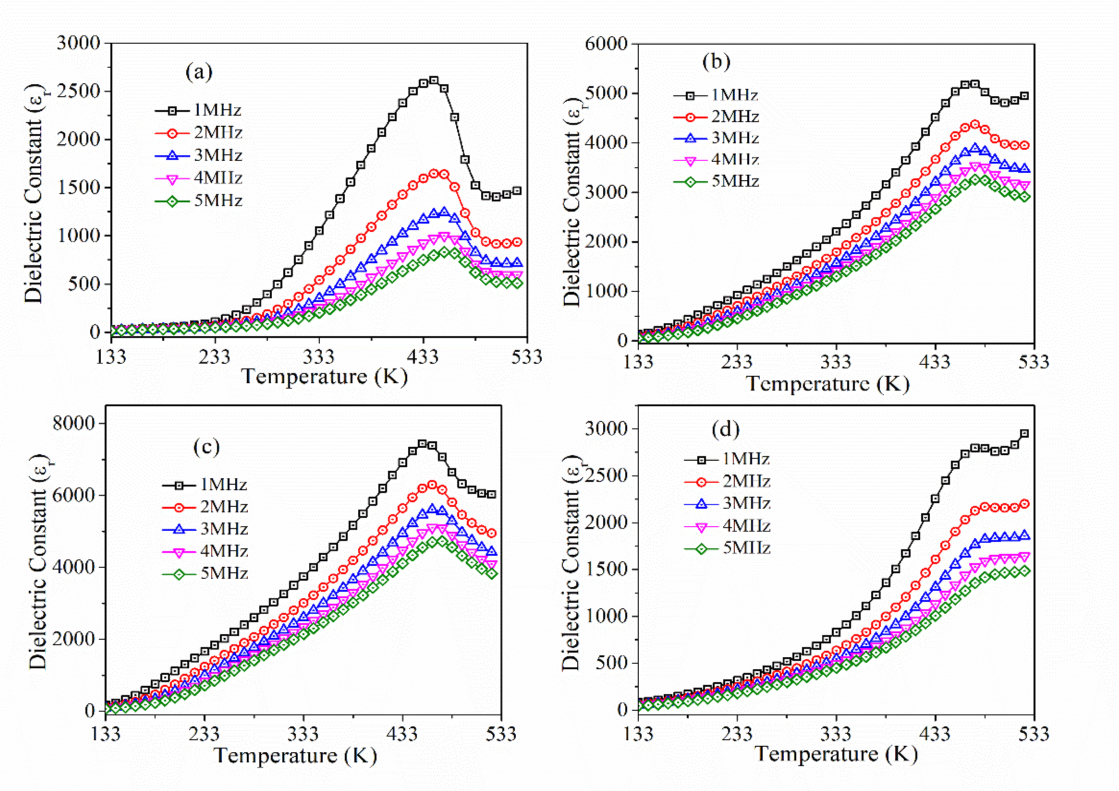

Figure 3-11. *Temperature variation dielectric constant of LMFO ceramics, measured at different frequencies for (a) x = 0 (b) x = 0.003 (c) x = 0.005 (d) x = 0.01.*

This trend is also actual for the other compositions; *x* = 0.003, 0.005, and 0.007. However, the hump in the dielectric constant shifted towards higher temperatures with an increase in the Mg concentration till *x* = 0.007. In contrast, the dielectric constant for the *x* = 0.01 sample increased continuously with temperature without any hump or reduction in the values. The value of the dielectric constant increased from 619 to 3034 while the dielectric loss reduced remarkably from 2.87 to 0.001 as the *Mg* concentration increased from *x* = 0 to x = 0.005 at 300 K. For *LFO*, as the temperature increased, *tanδ* enhanced initially exhibiting a cusp at 233K and again increased sharply above 433K at 1 MHz. The same trend is followed for all frequencies. The samples with x = 0.003, 0.005, and 0.007 followed the same trend, but the hump shifted toward a lower temperature range. The shift in the hump is attributed to the relaxation of dipoles. For x = 0.01, the values of *tanδ* increased smoothly with temperature, accompanied by a sharp rise above 453K. The surge in dielectric response is attributed to the higher relative density, and the lattice distortion of the *Mg*-substituted compounds.

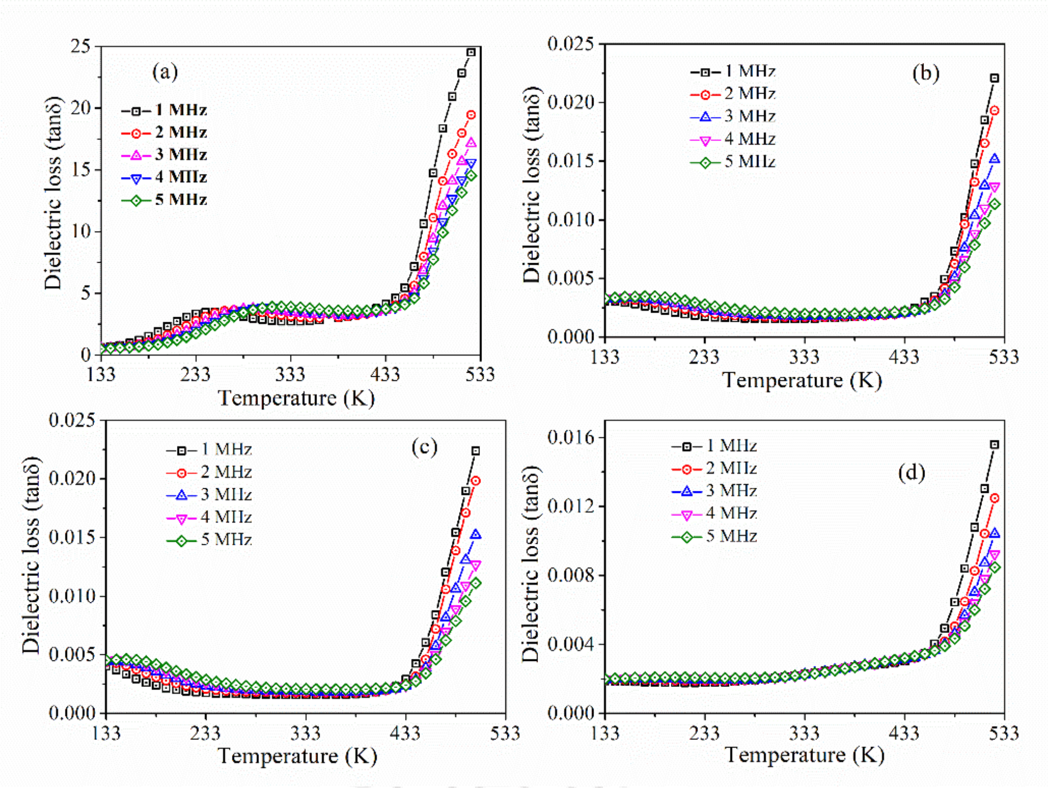

Figure 3-12. *Temperature variation dielectric loss tangent of LMFO ceramics, measured at different frequencies for (a) x = 0 (b) x = 0.003 (c) x = 0.005 (d) x = 0.01.*

Further, it is found that the dielectric constant and dielectric loss are improved with an increase in temperature due to the displacements of localized charge carriers. However, the enhancement in the conductivity of the samples may be attributed to the increasing mobility of charge carriers due to applied thermal energy. The observed high dielectric constant and low loss (order of 10^{-3}) in the high-frequency regime makes *LMFO* a better candidate for microwave applications.[102],[109] At lower temperatures, both the dielectric constant and loss tangents are lowered, and it is due to the lower thermal vibrations and the freezing of dipoles. Further, substituting *Mg* effectively minimized the dielectric loss in these ceramics.

Table 3-4. *The dielectric constant and tanδ at different frequency and temperatures of LSFO ceramics.*

Composition		**x = 0.00**		**x = 0.003**		**x = 0.005**		**x = 0.01**	
		ε_r	tanδ	ε_r	tanδ	ε_r	tanδ	ε_r	tanδ
133 K	1MHz	26	0.63	363	0.89	190	0.81	11	0.001
	1GHz	11	0.09	23	0.28	18	0.25	12	0.08
300 K	1MHz	619	2.87	3863	1.09	1760	0.67	11	0.002
	1GHz	16	0.70	12	6.85	15	1.96	12	0.09
513 K	1MHz	143	22.8	116	16.7	7149	3.82	17	0.78
	1GHz	19	2.62	10	1.6	15	5.25	13	0.12

Figure 3-13 and **Figure 3-14** show the variation of the ε_r and *tanδ* versus temperature of LSFO ceramics measured at different frequencies from 1 MHz – 1 GHz. A similar type of response is observed for LSFO ceramics as for LMFO. The dielectric constant and the dielectric loss tangent measured for LSFO ceramics at different temperatures and frequencies are listed in **Table 3-4**. The dielectric constant and loss tangent of *LSFO* is ε_r = 619 and *tanδ* = 2.87 @ RT at 1MHz. The enhancement in dielectric constant and loss (ε_r = 24647, *tanδ* = 1.73 @ 433K, 1 MHz) are obtained for x = 0.003 and further decreased (for $x \geq 0.005$). The enhancement in ε_r is attributed to the maximum relative density and incorporation of *Sr* into the *LFO* system. Additionally, it is observed that with a temperature rise, the dielectric constant and loss tangent are both enhanced due to the orientation of

dipoles at the temperatures. Still, at the same time, the conductivity of the samples also improved, which caused the high-loss tangents. In addition, as the measurement frequency increases, the dielectric constant reduces, which can be ascribed to the relaxation of dipoles. Moreover, the maximum dielectric constant (ε_{rmax}) at critical temperature gradually shifted to higher temperatures with a rise in the frequency from 1 MHz to 1 GHz.

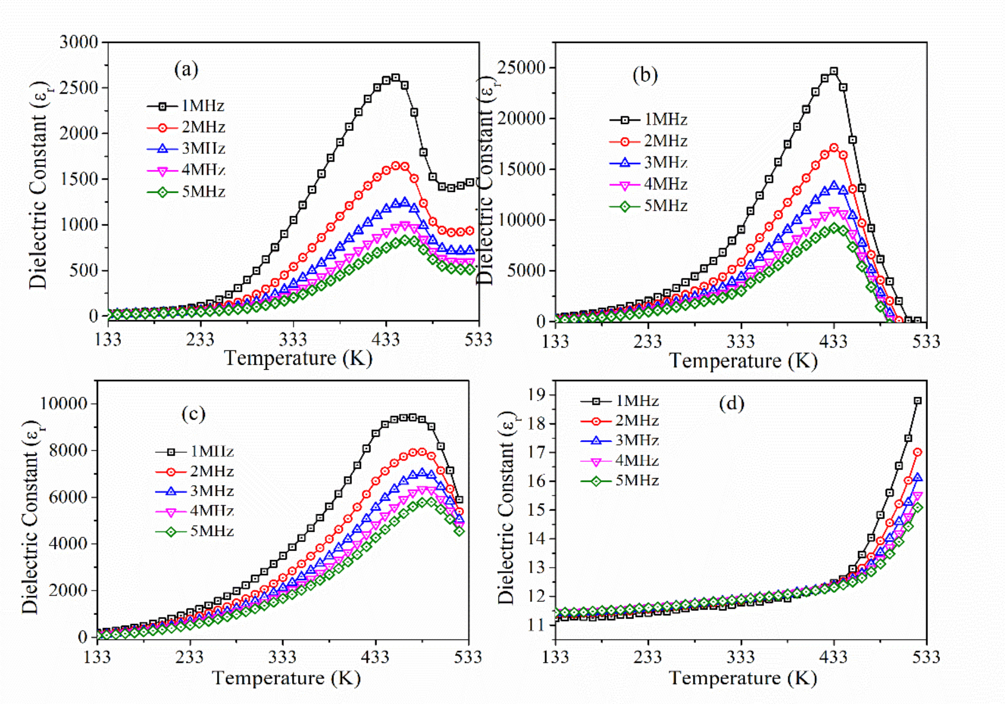

Figure 3-13. *Temperature dependent dielectric constant of LSFO ceramics, measured at different frequencies for (a) x = 0 (b) x = 0.003 (c) x = 0.005 (d) x = 0.01.*

The frequency dispersion with diffuse transition is a typical signature of relaxor behavior presented in the system.[163] According to the observed results, *LMFO* showed a better dielectric response (high dielectric constant with magnificent low dielectric loss) than *LSFO*.

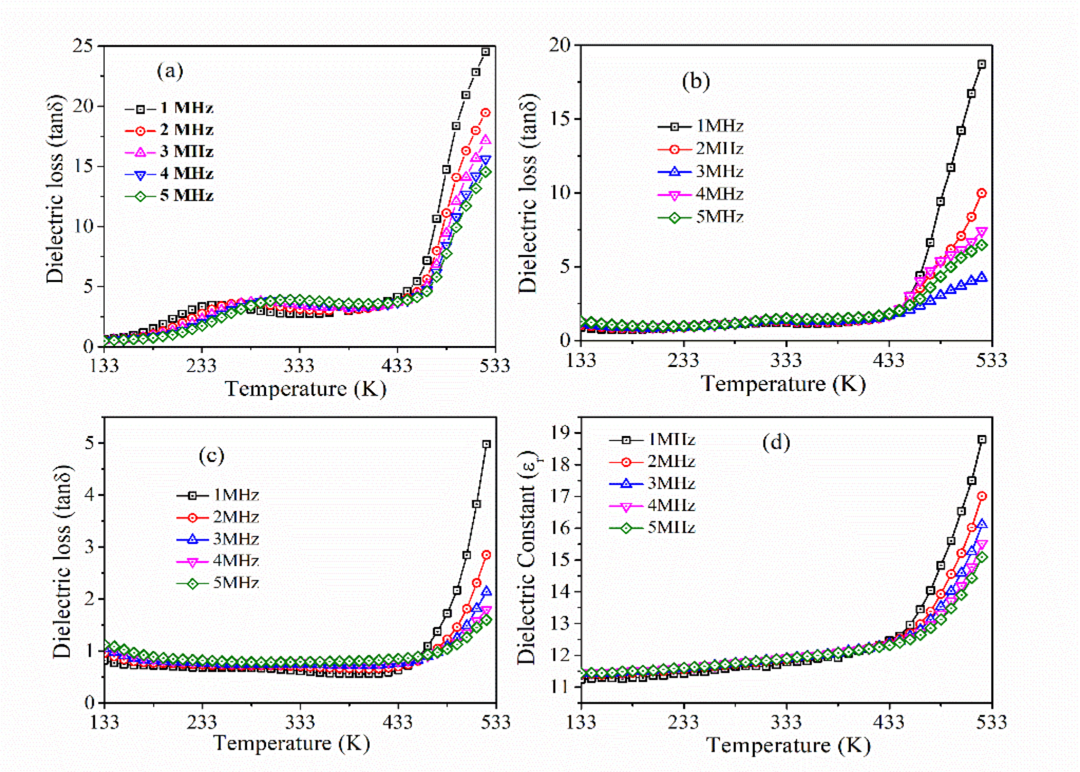

***Figure 3-14.** Temperature dependent dielectric loss of LSFO ceramics, measured at different frequencies for (a) x = 0 (b) x = 0.003 (c) x = 0.005 (d) x = 0.01.*

3.3.4 Electrical conductivity

The activation energy (E_A) of all the specimens is calculated from the temperature-dependent ac conductivity (σ_{ac}) by using the Arrhenius equation (**Equation 3.2**):

$$\sigma_{ac} = \sigma_0 exp(\frac{-E_A}{k_B T}) \qquad 3.2$$

where, σ_0 is the pre-exponential factor, k_B is the Boltzmann constant, and T is the absolute temperature. The logarithmic variation of σ_{ac} is plotted against 1000/T at 1 MHz for *LMFO* and *LSFO* ceramics, as shown in **Figure 3-15 (a)** and **(b)**. The activation energy is estimated from the slope of the plot. The conductivity is found to increase with temperature and *Mg^{2+}* ion concentration. The principle of the electrical conduction mechanism can be understood by the dielectric polarization mechanism. The conductivity increase with a concomitant temperature increase is because of the thermally activated interchange of the charge carriers among Fe^{2+} and Fe^{3+}. Further, the increase in the conductivity due to the Mg^{2+} ion is attributed to the concentration ratio of Fe^{3+}/Fe^{2+} ions on the B site. The activation energy is found to be 1.39 eV for $x = 0$, which is decreased to 0.35 eV for $x = 0.005$ for *LMFO* ceramics. However, it shoots up again with an increase in Mg concentration. In the case of *LSFO* ceramics, E_A is decreased to 0.077 for $x = 0.005$ specimens. The variation in activation energy can be attributed to the redistribution of oxygen vacancies and other charge carriers such as electrons, holes, and defects. When an atom with a different valence state is substituted on the lattice, charge vacancies are formed to maintain local charge neutrality. Since Sr^{2+} ions replace Fe^{3+} ions, oxygen vacancies or negative valences are created, which reduces activation energy.[164]

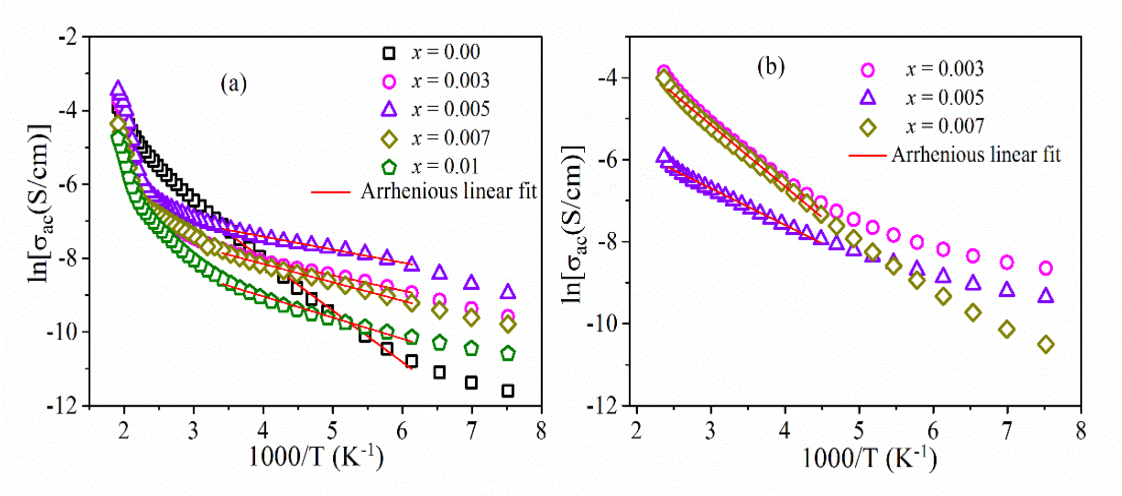

Figure 3-15. *Logarithmic variation of ac conductivity as a function of 1000/T for (a) LMFO, (b) LSFO.*

3.3.5 Permeability analysis

The frequency (1 MHz to 1 GHz) and temperature (133 K – 523 K) dependent real part of permeability is plotted for *LMFO* ceramics, as shown in **Figure 3-16(a)** and **(b)**. The obtained permeability for pure *LFO* is $\mu_r = 27.88$ at 1 MHz frequency, comparable to previously reported data [56]. Permeability is strongly influenced by *Mg* concentration. For $x = 0.003$, the permeability decreases to 23.94. However, for $x = 0.005$ and $x = 0.007$, the permeability raised to 28.56 and 29. The variation in permeability mainly depends on the thickness of the domain walls (δ), magneto-crystalline anisotropy (k_1), the average grain size (D_m), and inner stress (σ), which can be well understood by **Equation 3.3**:

$$\mu \propto \frac{\mu_0 M_s^2 D_m}{[k_1 + (3/2)\lambda_s \sigma]\beta^{1/3}\delta} \qquad 3.3$$

where M_s, λ_s, and β are the saturation magnetization, saturation magnetostriction constant, and volume concentration of impurity, respectively.

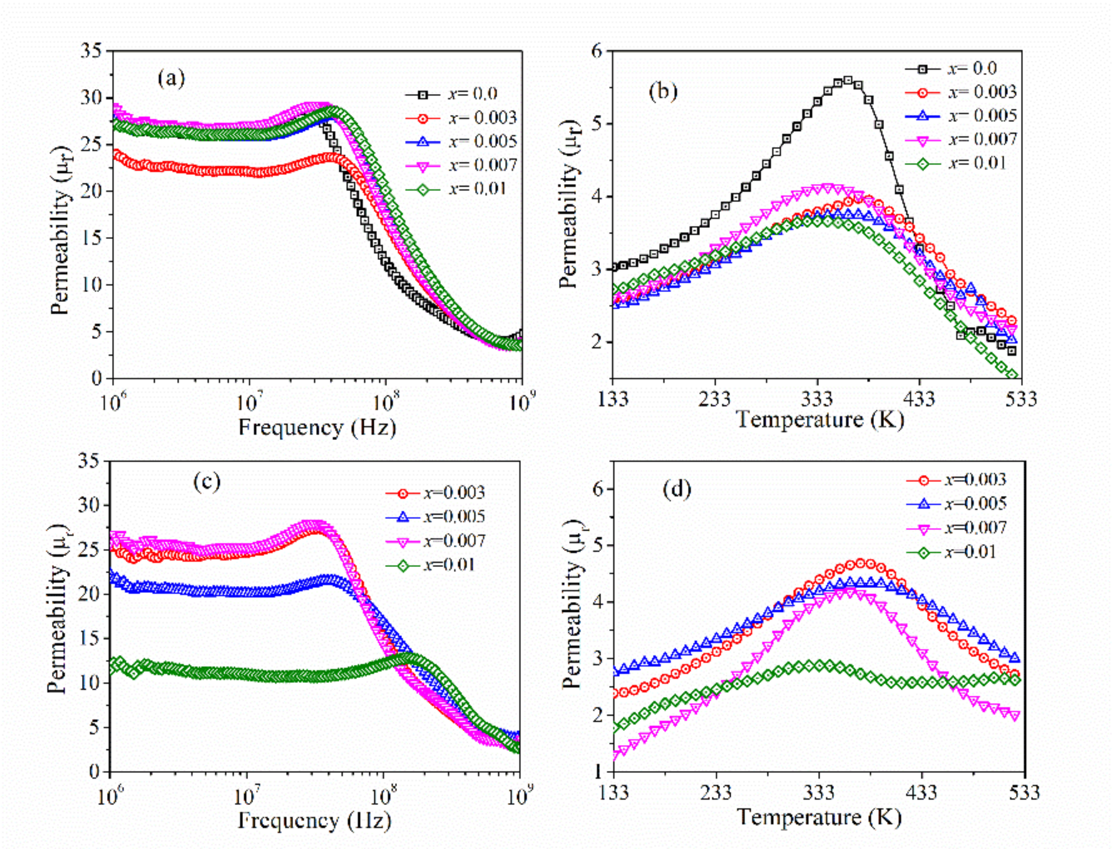

Figure 3-16. *Frequency and temperature dependent permeability of (a), (b) LMFO, and (c), (d) LSFO ceramics.*

In this case, the variation in μ_r can be attributed to the variation in magnetization and the average grain size. A 343 – 363 K transition is observed from the temperature-dependent permeability for all the *LMFO* ceramics. **Figure 3-16 (c)** and **(d)** shows the μ_r as a function of frequency and temperature for *LSFO* ceramics. It is noticed that the Sr content strongly influenced the permeability. The permeability value decreases with an increase in *Sr* content. For the sample with $x = 0.007$, μ_r is approximately the same as that of pure *LFO*, which is attributed to the significant variation in the grain size.

3.3.6 Magnetic studies

Figure 3-17 shows the variation of magnetization curves as a function of temperature (M–T) for *LMFO* samples. Magnetization decreases with an increase in temperature, which can be because the iron spins at octahedral and tetrahedral sites are sealed in the direction of the applied magnetic field at low temperatures. With a temperature rise, spins get randomized due to thermal energy, resulting in a decrease in magnetization. Above a specific temperature, the magnetization becomes zero, which indicates a paramagnetic state. According to **Figure 3-17**, the Curie temperature (T_c) of *LMFO* is shifted to lower temperatures as Mg concentration changes. The T_c for the pure *LFO* is 873K, and the decrease in T_c with an increase in Mg substitution is not monotonous. The substitution of non-magnetic Mg^{2+} ions in place of iron ions in both *A* and *B* sites of AB_2O_4 lithium ferrite inverse spinel causes the *A–B* interaction to be weak, which leads to a reduction in magnetization and the Curie temperature. The room temperature M–H loop of *LMFO* ceramics is shown in **Figure 3-18(a)**. The values of coercivity (H_C), saturation magnetization (M_S), and remanent magnetization (M_r) are illustrated in **Figure 3-18(b)**.

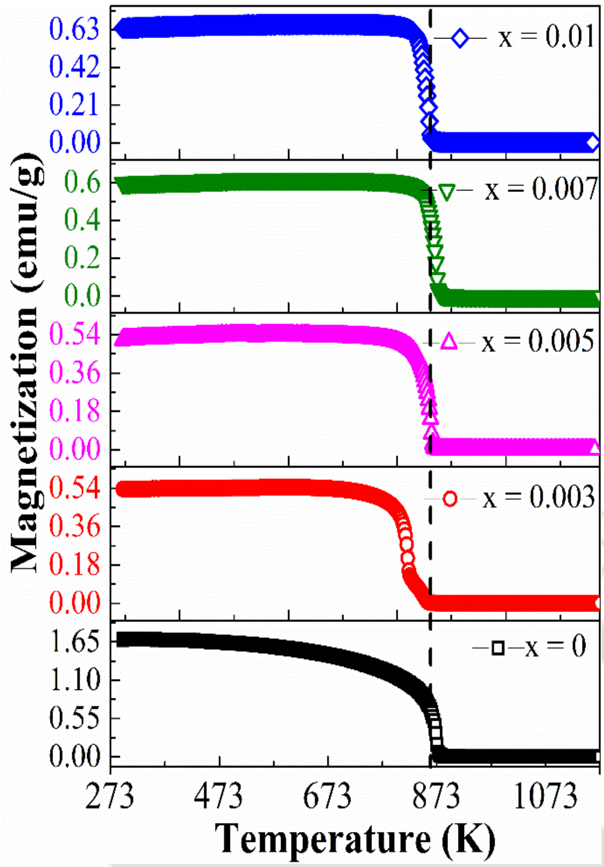

Figure 3-17. *Temperature dependent magnetization curve of LMFO samples.*

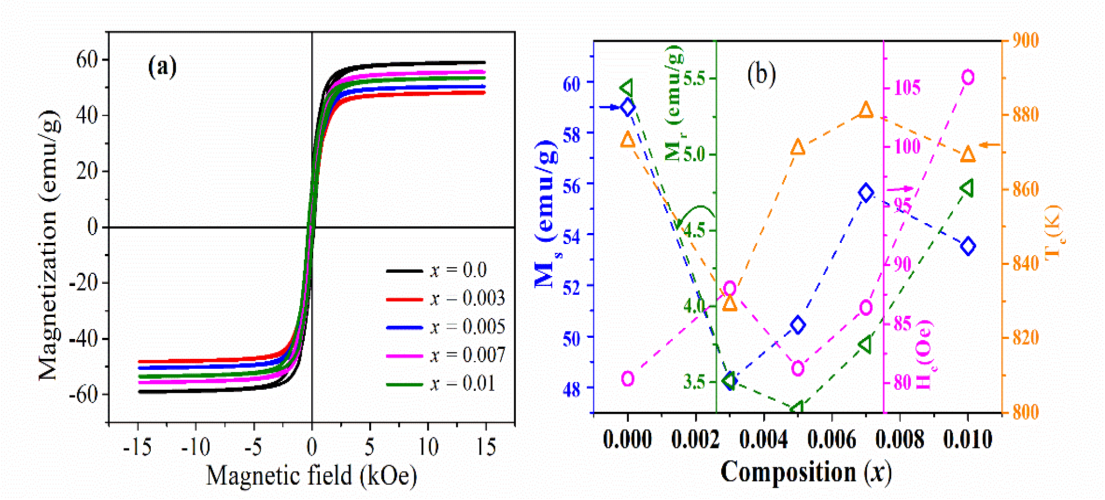

Figure 3-18. *(a) Room temperature M-H curves of the LMFO, (b) Variation of magnetic parameters with Mg composition.*

It is observed that saturation magnetization is reduced as a function of *Mg* concentration. Nevertheless, the sample with *x* = 0.007 exhibited the highest saturation magnetization among all the other substituted samples. The observed magnetization could be due to several factors, such as *A–B* exchange interaction, cation distribution, anisotropy, density, and grain size.[165],[166],[167] This can be better understood by Neel's two-sublattice model. According to this model, the magnetic moment per formula unit $n_B^N(x)$ in units of Bohr magneton (μ_B) is expressed as:

$$n_B^N(x) = M_B(x) - M_A(x) \qquad 3.4$$

where M_B and M_A are the *B* and *A* sub-lattice magnetic moment in μ_B, respectively; according to Neel's model, three types of interactions exist *A–A*, *B–B*, and *A–B*. Among these, the exchange *A–B* interaction is the strongest one. The resultant magnetization arises from a vector sum of two sublattices, *A* and *B*.[168] In order to accommodate the Mg^{2+} ions at the A-site, Fe^{3+} ions get transferred from the *A* site to the *B* site, which caused the initial decrease in M_s. Hence, Fe^{3+} ion content increased at B–site, causing the antiparallel spin coupling, which eventually resulted in the reduction of *A–B* exchange interaction strength, and consequently, decreases the magnetization. The increase in M_s for $x = 0.007$ may be due to Mg^{2+} ions, which are substituted for Li^+ and occupy the tetrahedral *A* site with an analogous transfer of Fe^{3+} from the *A* to *B* site. This enhanced the magnetization in the *B* site. The random behavior of H_C is attributed to the variation in grain size.[169],[170] The *Mg* substitution on *LFO* leads to structural distortion, as depicted in **Figure 3-2**, which modifies *Fe–O–Fe* bond angles at both the tetrahedral and octahedral positions and the *Fe–O* bond length.

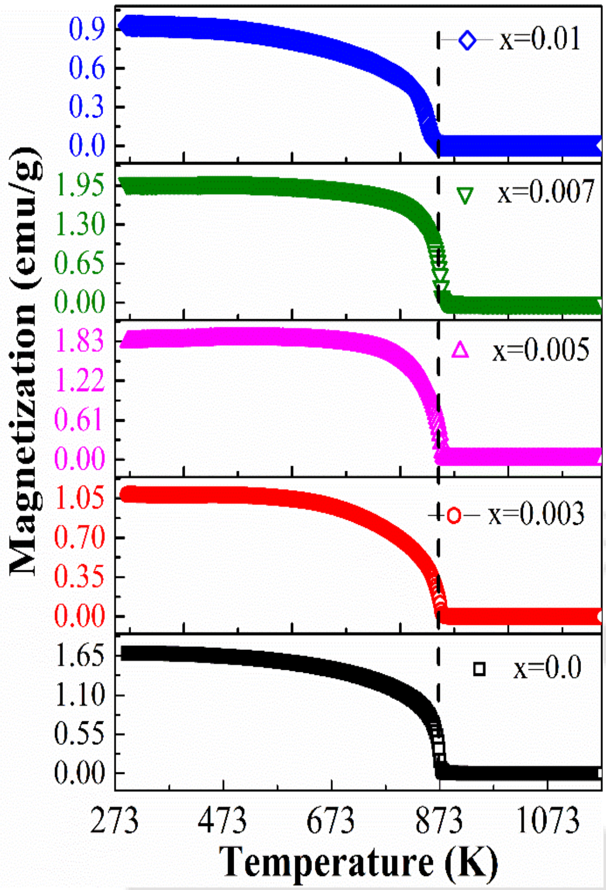

Figure 3-19. *Variation of magnetization as a function of temperature for LSFO ceramics.*

Figure 3-19 shows the temperature-dependent magnetization curve of *LSFO* samples. It is clear that the T_C of *LSFO* shifted to lower temperatures as *Sr* content changed. The value of T_C for the undoped *LFO* is 873K, whereas it reduced to 849K for $x = 0.01$ sample. The room temperature hysteresis loop of *LSFO* ceramics is depicted in **Figure 3-20(a),** and the variation of M_s, H_c, T_c as a function of Sr composition is illustrated in **Figure 3-20(b)**. However, all the samples are saturated at low fields of the order of 10 kOe. Thus, all the samples exhibited a soft ferrimagnetic behavior. Unlike the behavior observed in *M–T* curves, the saturated magnetization values in *M–H* curves decreased for $x = 0.003$. They attained a maximum value for $x = 0.007$; further, it declined for $x = 0.01$.

In undoped *LFO*, magnetization arises from the iron ions. The Fe^{3+} ions occupy both tetrahedral and octahedral sites, while Fe^{2+} ions occupy only the octahedral sites forming the two sublattices, leading to ferrimagnetism. The magnetic moment of the Fe^{3+} ion is lesser ($4\ \mu_B$) than the Fe^{2+} ions ($5\ \mu_B$), leading to a net magnetization in *LFO* samples. Any changes in the population of magnetic ions in the octahedral and tetrahedral sites effectively change the net magnetization. Also, it is believed that the occupancy of the Fe^{3+} and Fe^{2+} ions in the tetrahedral and octahedral sites changes with the *Sr* doping, leading to the increment in magnetization values. Nevertheless, this change in the occupancy is not linear with the *Sr* content, due to which a non-linearity in the M_s is observed with Sr content.

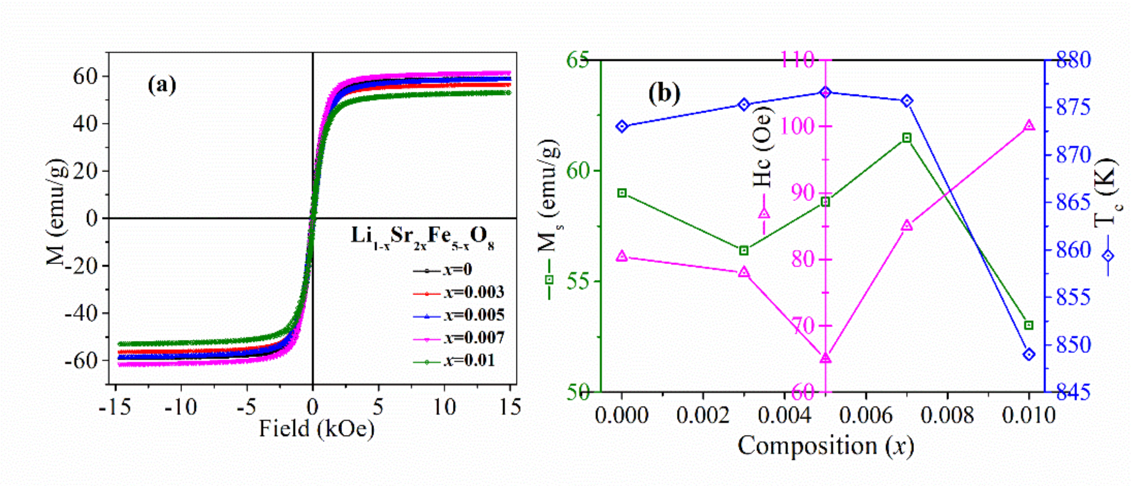

Figure 3-20. *(a) Room temperature M-H curves of the LSFO, (b) Variation of magnetic parameters with Sr concentration.*

The variations in H_c can also be understood in terms of grain size. The reduction in the grain size with the *Sr* substitution led to an increase in the surface-to-volume ratio between the atoms. As a result, the surface effects become prominent and produce vacancies in *LSFO* structure.[171] Thus, we can conclude that the structure, grain size, porosity, lattice imperfections, concentration of cations, and morphology can influence the magnetic properties of the spinel ferrites.[172][173]

3.4 Conclusions

Two series of substituted *LFO* with different Mg and Sr concentrations are synthesized successfully. The microstructure, structural, dielectric, and magnetic response variations are correlated. The substituted samples showed dense microstructure as compared to pure *LFO*. Enhanced dielectric response (ε_r = 3034, $tan\delta$ = 0.001 at RT, 1 MHz) is observed for the *Mg* composition, x = 0.005, whereas in the case of *Sr* series, the best dielectric response is observed for x = 0.003 (ε_r = 5986 and $tan\delta$ = 1.17 at RT, 1 MHz). The variations in the dielectric properties are explained on the basis of the electron hopping mechanism. AC conductivity increased with an increase in temperature as well as Mg^{2+} concentration due to the exchange of electrons among Fe^{2+} and Fe^{3+} ions. The activation energy is decreased by incorporating both *Mg* and *Sr* in *LFO*. The obtained E_A for *LMFO* and *LSFO* is 1.39 – 0.35 eV and 0.124 – 0.077 eV, respectively. The *LMFO* with x = 0.007 exhibited the best permeability (μ_r = 29) and magnetic properties (M_s = 55 emu/g) at room temperature. Also, in the *LSFO* series, x = 0.007 showed the highest magnetization among all samples (M_S = 61 emu/g). The change in magnetic behavior is explained by exchange interactions and Neel's two sub-lattice models. Looking into the combined response of dielectric and magnetic properties, *Mg*-substituted *LFO* showed a better response as compared to *Sr*-substituted *LFO*. A combination of high dielectric constant, low loss tangent (order of 10^{-3}), high permeability, and magnetic properties of *LMFO* make x = 0.005 specimens a good candidate for microwave applications such as phase shifters and the circulator.

Chapter 4 : Permittivity, permeability, and EMI shielding effectiveness of LFO-based ceramics composites

This chapter deals with the magnetic, structural, microstructural, permittivity, and permeability response of lithium ferrite/carbon black (different wt %) and *Dy* substituted *LFO/CB* (10 wt %). The EMI shielding efficiency in the X–and K_u band is also analyzed.

4.1 Introduction

Day by day, special gadgets and electronic devices are becoming a necessary part and part of our lives. There are advantages and disadvantages associated with these devices, such as EMI, which are of deep concern for the smooth functioning of the devices. The EMI created at microwave frequencies causes severe threats not only to military equipment and commercial communication systems but also to normal human health. [174][175][99][176] With emerging 5G technology, the complications associated with the EMI are expected to enhance. The EMI shield can be achieved by attenuating electromagnetic radiation by absorption or reflection. The EM reflection from various metallic bodies such as ships, aircraft, and the walls of the anechoic chamber can be reduced by tailoring the dielectric and magnetic loss. Absorption, reflection, transmission, and multiple reflections occur when EM waves strike the shielding materials. The absorption depends on electric and magnetic dipoles of the shielded materials, whereas mobile charge carriers are required in order to have efficient reflections. Reflection from various interfaces is termed as multiple reflections, which is neglected in most cases since the re-reflected waves used to be absorbed in the materials. Metal sheets used to be considered an efficient material for EMI shielding; however, oxidation prone nature, processing difficulty, and heavyweight restrict their use in various practical applications [44]. Again, carbon-based polymer composite emerged as an alternative to metals due to its lightweight, large surface area, and high electrical conductivity. Carbon-based materials such as carbon nanotubes (CNT), carbon nanowires, and reduced graphene are extensively studied as filler components. [177][178][179][180] The unstable nature of polymer with temperature limits its use in EMI applications. Further, the ceramic-based composite attracted attention in the last few years due to its better temperature stability, hardness, and easy processing methodology.[181][182] Among carbon-based materials, carbon black (CB) is a well-explored and suitable material due to its low cost, easily available, stable and easy processing criteria. Also, it helps to enhance the electrical conductivity of the material. Sang et al.[183] synthesized the carbon nanotubes/alumina@ nickel ceramic composites by hot press sintering. The EMI SE and electrical conductivity of $9CNTs/Al_2O_3$ ceramic composites were found to be 33.6 dB and 103.1 S/m, respectively. Huang et. al. [52] developed reduced graphene oxide/silica ceramics that are mechanically reliable and lightweight for EMI application. They mainly analyzed the toughness and flexural strength that enhance the balanced interfacial interaction and hierarchical structure. They achieved 33 dB SE in the X-band regime. Yuchang et. al.[184] prepared $BaTiO_3$/*graphene nanosheets* (GN) ceramics, and they reported the total SE was achieved greater than 40 dB for this composite. They also reported that the complex permittivity was enhanced with GN content. Qing reported the complex permittivity, permeability, and SE of $BaTiO_3/NiFe_2O_4$. With the two ceramics (one soft magnetic component), they achieved an SE of 34 dB in X-band.[54] $BiFeO_3$ nanowire-rGO having absorption bandwidth of 2.2GHz and RL_{max} of -28.68 dB were observed by Ghosh et al.[185] The exceptional absorbing performance is ascribed to the unique microstructure of the absorber and impedance matching. The ferrite-based materials such as Fe_3O_4, $CoFe_2O_4$, and $NiFe_2O_4$ for EMI shielding and microwave absorber have been reported. [186][187][188] The spinel ferrites exhibit high saturation magnetization, high Curie temperature, low resonance line width, moderate dielectric, and magnetic loss. A combination of carbon-based filler with magnetic material as the matrix can be a better replacement for polymer-based composites as it can result in high magnetic and dielectric loss, better temperature stability, high eddy current loss, and interfacial polarization. Various rare earth substitutions like *Y*, *Pr*,[189] *Nd*[190], *Er*[191] and *Dy*[192] in the spinel ferrites are also reported recently to enhance the EMI efficiency.

However, the ideal material for EMI shielding cannot be obtained using single materials like metal, polymer, and carbon-based compounds. Looking forward to a better perspective of stability, low cost, easy processing, and temperature stability, ceramic composite with carbon-based material is the best option. In the contest to the situation mentioned above, It is realized that the EMI shielding response of a material mainly originates from the synergistic effect of conduction loss, magnetic loss, and dielectric loss. Spinel ferrite, like lithium ferrite, can be a better alternative to be used as a ceramic. *LFO* possesses high saturation magnetization, high magnetic loss, moderate permeability, and high curie temperature. Further, It is a known fact that rare (RE) ions contain unpaired *4f* electrons, which promotes spin-orbit solid couplings. Incorporating RE ion in spinel ferrite leads to $4f-3d$ coupling, which may also modify magnetic and electrical properties. For significant EMI shielding, the shielded material should have magnetic and electric dipoles interacting with the electromagnetic field. Most of the researchers focused either on the magnetic or dielectric perspective. But the cumulative effect of electrical, magnetic, and dielectric loss mechanisms is essential to understand the performance of the material for this type of application which is lacking in the literature and hence this study. In this work, It is intended to achieve high EMI shielding efficiency by incorporating CB into lithium ferrite and *Dy* substituted lithium ferrite matrix. The *Dy* substitution is expected to promote polarization, magnetic loss, and microstructure, enhancing the EMI efficiency.

4.2 Methods of preparation

Lithium ferrite (*LFO*) is prepared by the solid-state method, as reported in Chapter 2. The ceramic powders are calcined at 800 °C for 3 h. The used *CB* is obtained from M/s JiangXiHaiTe Advance Material in its pure form. To prepare composites, *LFO* and *CB* are mixed using a ball mill with different weight ratios of *CB* (5, 10, 15, 20 wt%). The composites are symbolized as *LFO/CB (5)*, *LFO/CB (10)*, *LFO/CB (15)*, *LFO/CB (20)*. Propanol is used as a grounding medium. Then the homogeneous slurry is dried in a hot air oven. The *Dy* doped lithium ferrites ($LiFe_{5-x}Dy_xO_8$) are prepared for five different compositions of dysprosium: $x = 0$, 0.05, 0.1, 0.15, and 0.2. The 10 wt % of *CB* is added to all the prepared compositions. The composite corresponding to $x = 0$ is termed as *LFO/CB* (undoped lithium ferrite-carbon composite), whereas the other composites corresponding to $x = 0.05$, 0.1, 0.15, 0.2 were termed as *LD5FO/CB*, *LD10FO/CB*, *LD15FO/CB*, and *LD20FO/CB*, respectively. The structural, microstructural, magnetic, shielding efficiency, complex permittivity, and permeability studies are carried out for all the compositions. The results are presented and discussed simultaneously.

4.3 Results and discussion

4.3.1 Surface micrograph and structural analysis

The surface morphology of prepared samples is shown in **Figure 4-1**. It is clearly visible from **Figure 4-1(a)** that the well-defined and uniform distributed grains are in the case of pure *LFO*. The average grain size obtained for *LFO* is 0.72 µm. For *LFO/CB* composites, additional sheet-like structures are noticed. The dimension of sheet-like structures is in the range of 1 - 4 µm. The *CB* particles are agglomerated and form a sizeable sheet-like structure. The flat sheet-like structure of *CB* provides a pathway for the first migration of electrons. With an increase in *CB* concentration, more sheet-like structures are observed. Also, some flexes are quite large (10 μm). The *CB* is agglomerated and assembled on the grain boundary of *LFO*. With an increase in *CB* content, a more disturbed grain structure is observed.

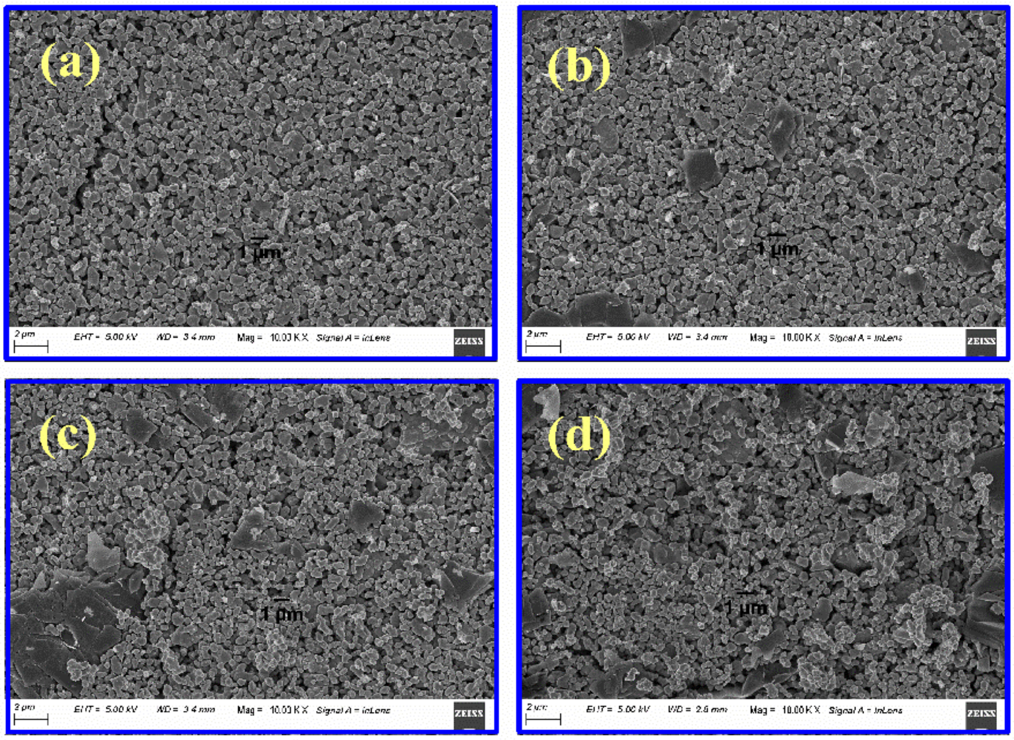

***Figure 4-1**. Surface morphology of (a) LFO, (b) LFO/CB (5), (c) LFO/CB (10), (d) LFO/CB (20).*

Figure 4-2 shows the surface morphology of the composites of Dy substituted samples. The irregularly shaped grains with well-defined grain boundaries are observed. The carbon sheets have an average size of 1- 4 μm. However, a few are much more prominent, within the range of 4 - 8 μm. It is observed that the average grain size decreases slightly from 1.19 μm (*LFO/CB*) to 0.92 μm (*LD15FO/CB*). This decrease in grain size with an increase in Dy^{3+} concentration is because of the large size of Dy^{3+} ions, which hinders grain growth by diffusing to the grain boundaries and forming the $DyFeO_3$

secondary phase.[193] The obtained irregular grains with porous structure facilitate microwaves' absorption, leading to better SE.

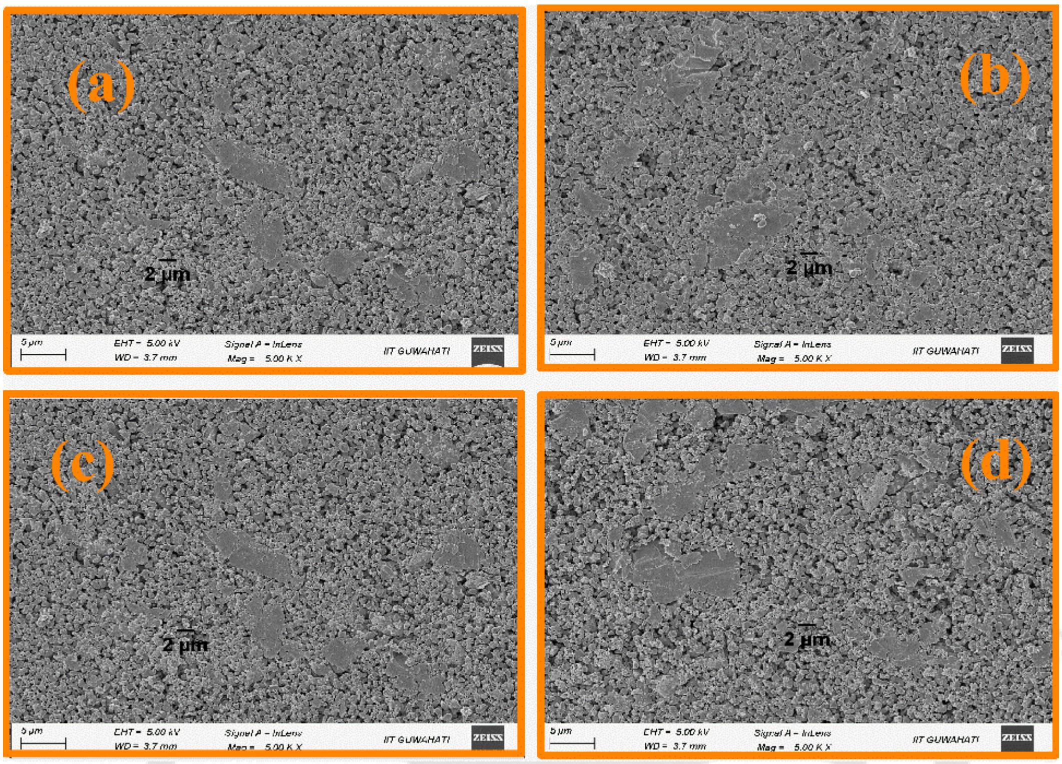

***Figure 4-2**. FESEM micrograph of (a) LFO/CB, (b) LD5FO/CB, (c) LD10FO/CB (d) LD15FO/CB.*

The typical XRD pattern of *LFO*, *CB*, and composite materials is depicted in **Figure 4-3(a)**. Two prominent peaks are observed for CB at 2θ of 26.43, 54.51correspond to (002) and (004), respectively (hexagonal, P63/mmc, JCPDS # 00-060-0053), confirming the pure phase formation. All the observed peaks of LFO are appropriately matched with the ordered cubic phase ($P4_132$, JCPDS # 82-1436)[194]. Interestingly, no additional peak for any other undesired phases has been observed in the composites apart from *LFO* and *CB*. The intensity of *LFO* is suppressed with an increase in *CB* content. The predominant peak of *LFO* (311) shifted towards the lower 2θ, which is attributed to the addition of *CB* that led to the generation of strain (**Figure 4-3(b)**). For further clarification about lattice parameters, Rietveld refinement is carried out by Fullprof software. The refined pattern is shown in **Figure 4-3(c)**. For *CB* lattice parameters are : a= b= 2.4616 Å, c= 6.7226 Å, α = β = 90°, γ

= 120° and for LFO: a= b= c= 8.3452 Å, α = β = γ = 90°. Also, the presence of two phases is examined through refinement, where we can get information regarding volumetric concentration (percentage contribution of individual phase).

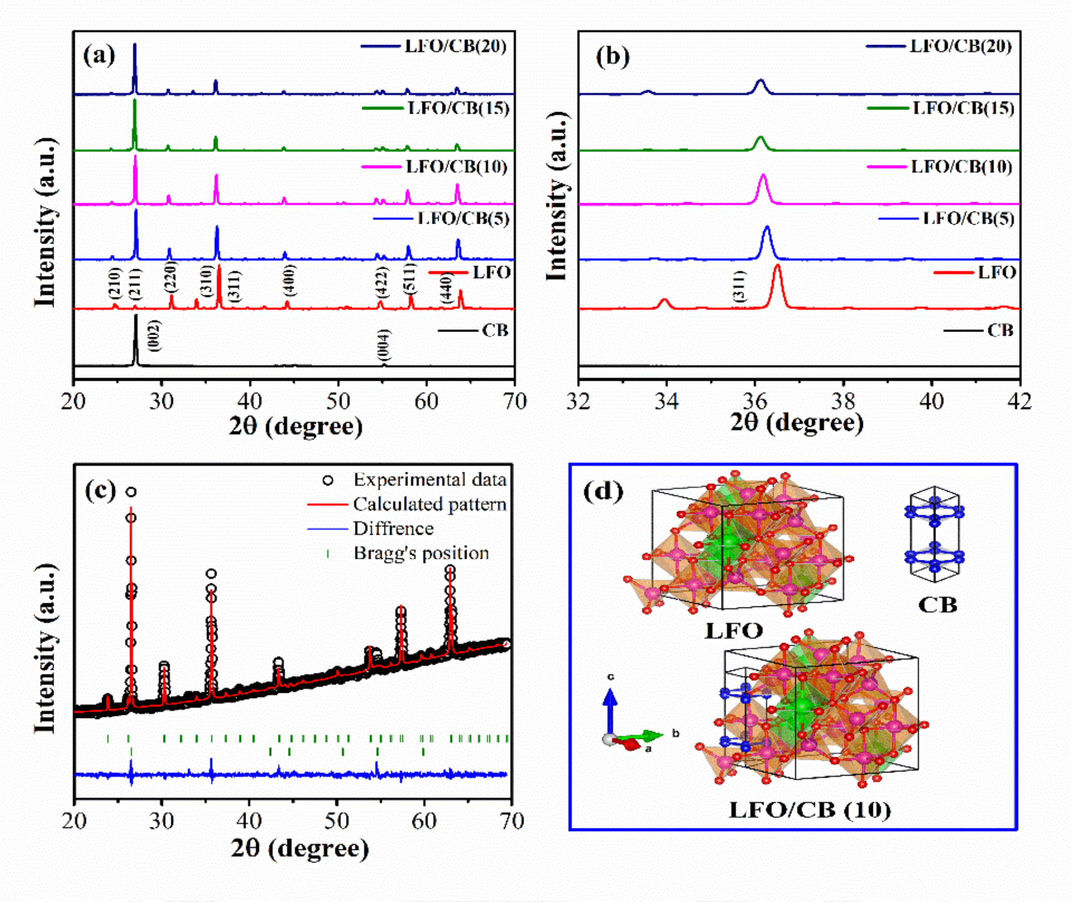

__Figure 4-3__. (a) XRD pattern of LFO, CB, and composites, (b) Relative shift of predominant peak (311), (c) Rietveld refinement pattern of LFO/CB (10), (d) Schematic illustration of the Unit cell of LFO, CB, and LFO/CB.

The Scherrer equation estimates the average crystallite size (D) of *LFO* and composites (all the intense peaks are considered).

$$D = \frac{k\lambda}{\beta cos\theta} \qquad 4.1$$

here, β, λ, θ, k is Full width at half maximum (FWHM), the wavelength of incident X-ray, Bragg’s angle, and shape factor (0.98), respectively. The calculated D for pristine *LFO* is

33.98 nm, whereas it varies from 35.85 to 35.19 nm for composites. The unit cell image of *LFO*, *CB*, and composites are shown in **Figure 4-3(d)**. *Li*, *Fe*, *O*, and *C* atoms are represented in green, magenta, red, and blue, respectively.

The XRD patterns of pure *CB*, *LFO/CB*, and *LDFO/CB* composites are depicted in **Figure 4-4(a)**. For the *LFO/CB* and *LDFO/CB* composites, intense peaks are observed for (220), (311), (400), (422), (511), and (440) planes, thereby confirming the spinel phase formation of lithium ferrite. The shift of the peaks indicates the substitution of Dy^{3+} cations in the matrix (**Figure 4-4(b)**). The most intense peak (311) gets shifted towards higher 2θ values with an increase in Dy^{3+} doping up to $x = 0.15$. For $x = 0.2$, the (311) peak shifted to the left concerning the peak positions of other composites. Fullprof software is used to perform Rietveld refinement of the XRD patterns (**Figure 4-4(c)**). The various lattice parameters are enlisted in **Table 4-1**.

Table 4-1*. Structural parameters of LDFO.*

	LFO	**LD5FO**	**LD10FO**	**LD15FO**	**LD20FO**
a (Å)	8.3452	8.3415	8.3392	8.3374	8.3397
Volume (Å^3)	581.17	580.40	597.92	579.55	580.03
χ^2	1.24	1.32	1.26	1.44	1.47

The highest lattice constant is observed for the *LFO/CB* composite, whereas it is the lowest for *LD15FO/CB*. With an increase in Dy concentration, the lattice constant is found to be decreased up to *LD15FO/CB*. On doping, the larger Dy^{3+} (0.91 Å) ions in place of the smaller octahedral Fe^{3+} (0.64 Å) ions, the lattice strain, and disorder may arise due to ionic radii mismatch of the dopant and host ions, resulting in an increase or decrease of the lattice parameter.[195][196] Here, the substitution of Dy^{3+} cations has reduced the lattice constant initially. A similar trend has been observed in other rare-earth-doped spinel ferrites like dysprosium doped cobalt-zinc ferrite,[197] Dy^{3+} doped nickel-cobalt ferrite,[165] *Ce-Dy* substituted cobalt ferrite,[198] and Gd^{3+} doped cobalt ferrite[195]. For a high amount of Dy-doping (x = 0.15, 0.2), extra peaks are also found around 2θ ~ 33° corresponding to $DyFeO_3$ phase formation.[199] The large Dy^{3+} ions cannot completely replace all the Fe^{3+} ions in the octahedral positions at high doping concentrations. This results in distortion of the spinel structure, and the excess *Dy*-ions move to the grain boundaries resulting in the $DyFeO_3$ impurity phase.[200][201] The composites' average crystallite sizes (D) are calculated using **Equation 4.1**. For the *LDFO/CB* composites, the *D* values ranged from 30.05 to 42.39 nm.

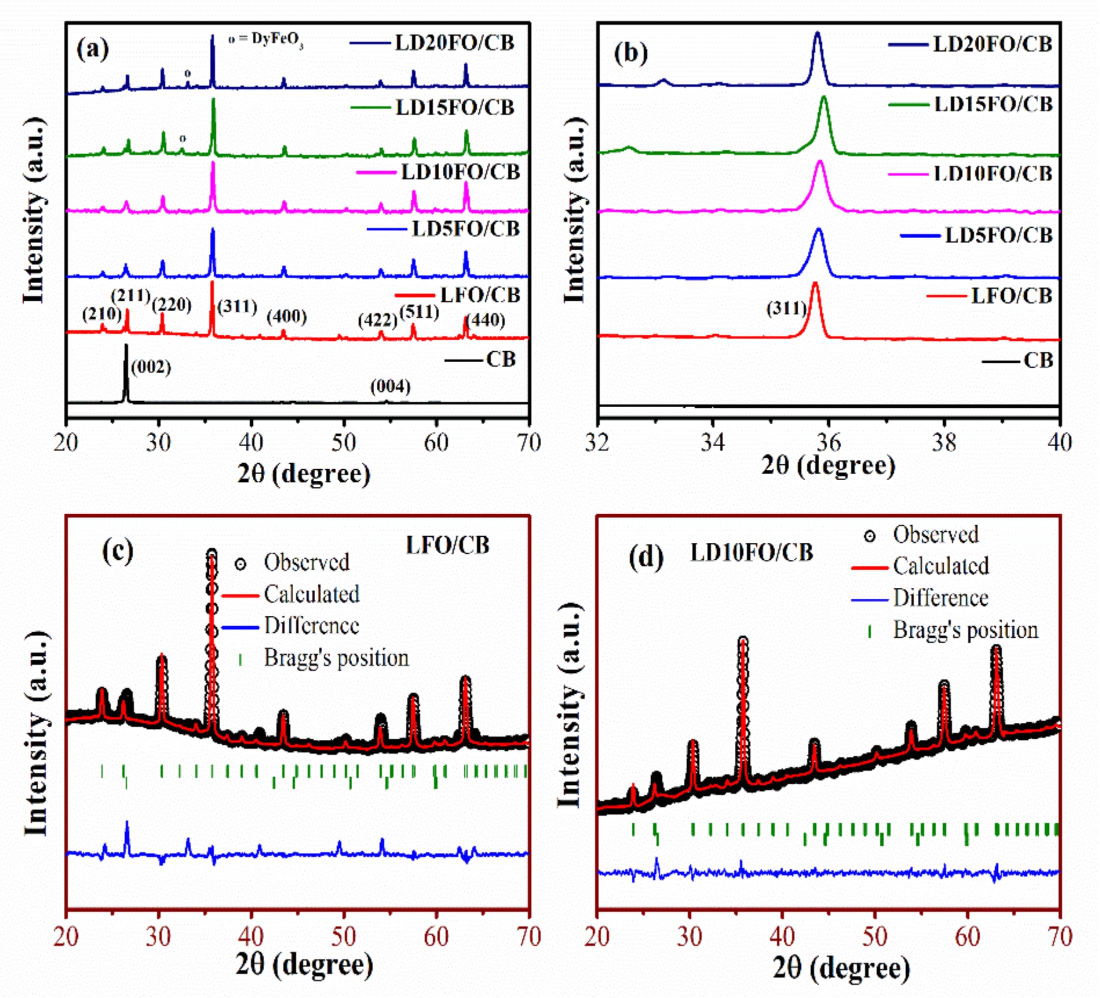

Figure 4-4. *(a) XRD pattern of all the composites, (b) Relative shifting of the predominant peak, (c) Reitveld refinement pattern of LFO/CB, (d) LD10FO/CB.*

4.3.2 Magnetic response

The room temperature magnetization is recorded up to 15 kOe as a function of the magnetic field of *LFO/CB* composites, as shown in **Figure 4-5(a)**. All the samples exhibited a typical ferrimagnetic behavior, and M_s, H_c is obtained from the M-H loop (**Table 4-2**). *LFO* attained a saturation magnetization of 64 emu/g, which is well compared with the available literature[202],[160]. Magnetic properties of spinel ferrites are governed by several parameters, including synthesis methods, homogeneity, crystallite size, grain size, defects, porosity, morphology, and distribution of cations between octahedral (B) and tetrahedral (A) sites. The magnetization in LFO is due to the cationic distribution of Fe ions. *LFO* exhibits inverse spinel structure where Li^+ occupies the octahedral (B site) 4b position and Fe^{3+} occupy tetrahedral (A site) 8c and octahedral 12d sites. This can be well governed by Neel's two sublattice models and exchange interaction[168].

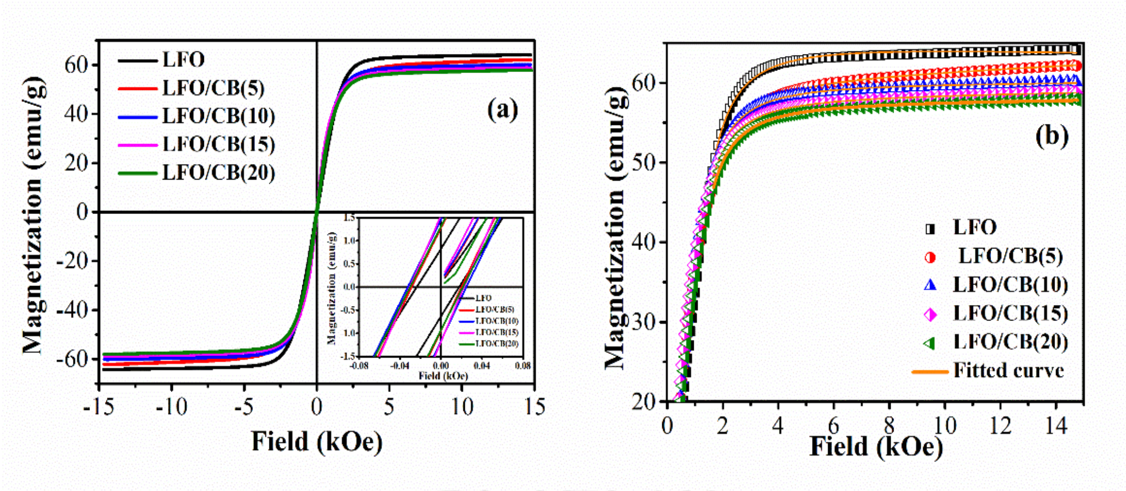

***Figure 4-5**. (a) Magnetization as a function of magnetic field for all the samples, (b) Initial experimental data fitted with LAP.*

Total magnetization is obtained from the difference between the net magnetization in octahedral and tetrahedral sites. Again, mainly three types of interaction occur between sublattices: *A–A*, *B–B*, and A–*B*, where *A–B* predominates the other. With an increase in *CB* concentration, M_s slightly decreased compared to pristine *LFO*, which indirectly confirms the proper *CB* dispersion in *LFO*. The obtained M_s for *LFO/CB(5), LFO/CB(10), LFO/CB(15), LFO/CB(20)* is 62, 60, 58, and 57 emu/g respectively. Also, there is not much variation observed for H_c. All the magnetic parameters are enlisted in **Table 4-2**. Further, the effective magnetocrystalline anisotropy (k_1) is evaluated by fitting the initial magnetic curve data with the law of approach to saturation magnetization (LAP):[203]

$$M = M_s\left(1 - \frac{8}{105\mu_0^2 M_s^2}\left(\frac{k_1}{H}\right)^2\right) + \gamma H \tag{4.2}$$

where γ and 8/105 are the susceptibility and cubic anisotropy of polycrystalline specimens. The fitted curve with experimental data is shown in **Figure 4-5(b)**. The obtained value of k_1 is 1.88 ×10^5 erg/cm^3, found to be decreased with enhancement in *CB* concentration. The k_1 is crucially dependent on M_s, H_c, domain wall motion, and crystallite size. In the present case, the decrement can be due to the change in M_s value as not much difference is observed in all other parameters.

***Table 4-2**: Magnetic parameters of all the composites.*

Sample name	M_s (emu/g)	H_c (Oe)	k_1 (erg/cm^3)
LFO	64	21	1.88 ×10^5
LFO/CB (5)	62	25	1.70 ×10^5
LFO/CB (10)	60	27	1.52 ×10^5
LFO/CB (15)	58	30	1.43 ×10^5
LFO/CB (20)	57	28	1.39 ×10^5
LD5FO/CB	62	60.9	1.10 × 10^5
LD10FO/CB	70	67.0	1.28 × 10^5
LD15FO/CB	68	54.8	1.24 × 10^5
LD20FO/CB	60	66.1	1.10 × 10^5

The M-H loops shown in **Figure 4-6(a)** confirm the ferrimagnetic nature of the *LDFO/CB* composites. The saturation magnetization is enhanced up to *LD10FO/CB* and then decreased. The values of H_c, M_s, and k_1 are listed in **Table 4-2**. The M_s monotonically increased with increasing dysprosium content up to $x = 0.1$ (as *Dy*-ions with $\mu_{eff} = 10.50\ \mu_B$ possess higher magnetic moment as compared to Fe $\mu_{eff} = 5.85\ \mu_B$). [201] This increases the μ_{eff} (effective magnetic moment), which explains the increase in magnetization of the composites. However, from $x = 0.15$ onwards, a decrease in saturation magnetization is observed. Due to their large size, the *Dy*-ions prefer to occupy the bigger octahedral sites, thereby replacing the Fe-ions. Therefore, the paramagnetic Dy^{3+} ions rapidly substitute the ferromagnetic Fe^{3+} ions at higher doping concentrations. The replacement of *Fe* by *Dy* at the octahedral sites reduces the exchange interaction and hence the saturation magnetization. When RE^{3+} ions substituted in place of Fe^{3+} in spinel ferrite, the possible exchange interactions are: $RE^{3+} – RE^{3+}$ ($4f – 4f$ interaction) and $Fe^{3+} – RE^{3+}$ ($3d – 4f$ interaction). However, these interactions are weaker than $Fe^{3+} – Fe^{3+}$ ($3d – 3d$) interactions. Like other rare earth cations, in Dy^{3+} $4f$, electrons remain highly localized in the solid lattice, attributed to the orbital screening effect. Hence, the 4f electrons remain shielded from the crystal field by $6s$ and $5d$ electrons, leading to weak interactions with neighboring cations. The existence of indirect $4f – 5d – 4f$ electron coupling between $Dy^{3+} – Dy^{3+}$ and weak interactions in $Fe^{3+} – Dy^{3+}$ ($3d – 4f$ coupling) resulted in the reduction of net magnetization. Another reason for the decrease in magnetization could be the formation of the non-magnetic $DyFeO_3$ impurity phase. $DyFeO_3$ possesses a distorted perovskite structure where the Fe^{3+} spins exhibit antiferromagnetic ordering.[204] Also, the *Dy–Fe* interaction is weaker than the *Fe–Fe* interaction, which results in a decrease in saturation magnetization at high doping concentrations. Although no clear trend is visible between doping concentration and coercivity, it is observed that all the doped composites' coercivity

(*Hc*) is lesser than the undoped one. Adding Dy^{3+} cations increased the number of magnetic domains, leading to easy demagnetization and lowering coercivity.[205] The LAP fitted curves for *LDFO/C*B composites are depicted in **Figure 4-6(b)**. LFO/CB (10) composite has a k_1 value of 1.02×10^5 erg/cm^3, which increased with Dy^{3+} addition up to $x = 0.15$. This trend in k_1 value is almost similar to the variation of magnetization (M_s) with Dy^{3+} concentration. The schematic illustration of the effect of *Dy* substitution is shown in **Figure 4-7**.

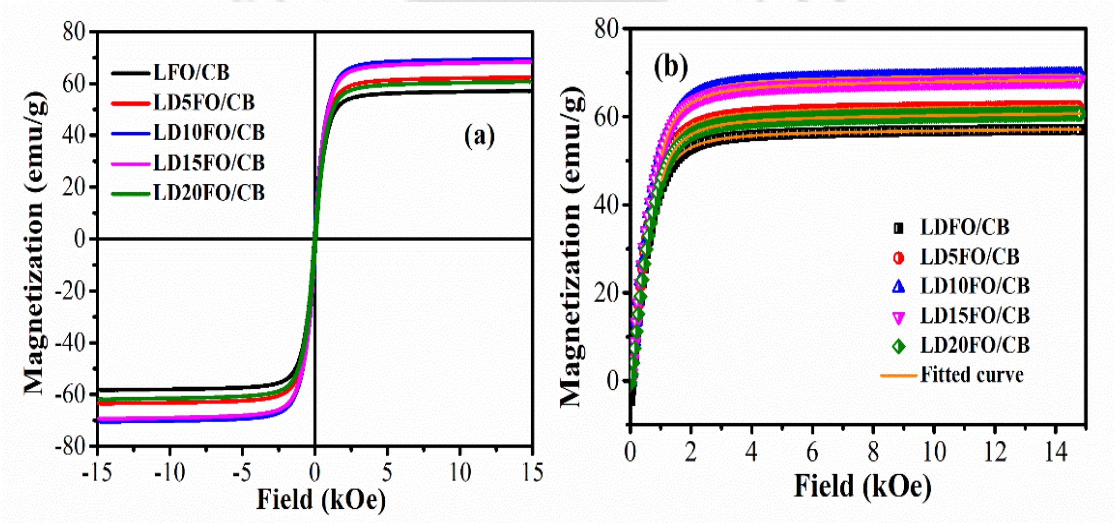

Figure 4-6. *(a) Room temperature Hysteresis loop of LDFO/CB composites, (b) Fitted curve of virgin magnetization loop with Law of approach to saturation of LDFO ceramics.*

The insertion of Dy^{3+} favours $3d - 4f$ coupling ($Fe^{3+} - RE^{3+}$) and $4f - 4f$ coupling ($RE^{3+} - RE^{3+}$) along with $3d - 3d$ coupling ($Fe^{3+} - Fe^{3+}$). The interlink between magnetization and anisotropy is evident from **Equation 4.2**. Also, the increase in magneto crystalline anisotropy is due to dysprosium's high negative anisotropy value.[206] Magnetization, coercivity, crystallite size, and domain wall movements affect the k_1 value.

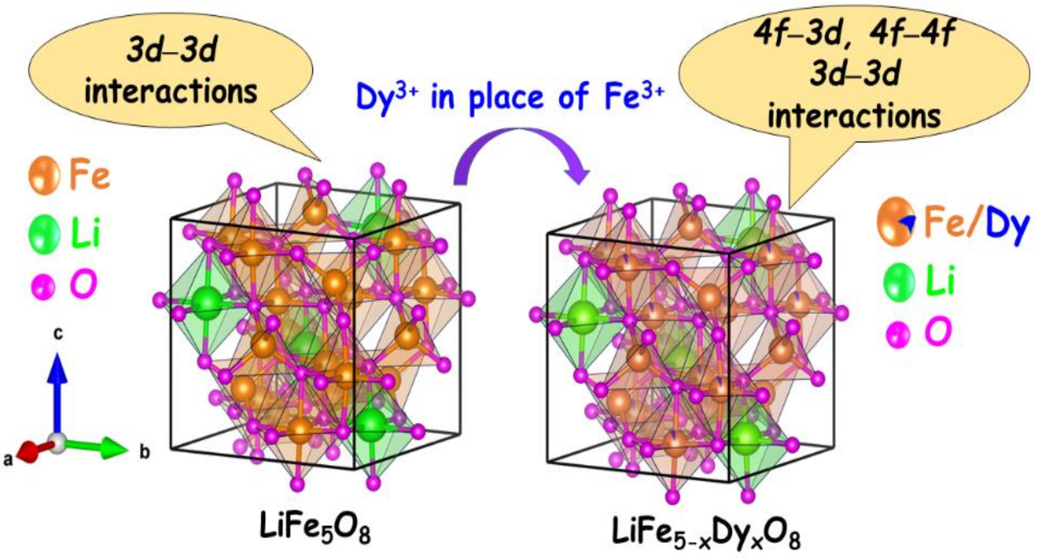

Figure 4-7. *The schematic illustration of the effect of Dy substitution on lithium ferrite.*

4.3.3 EMI shielding studies

The SE_R, SE_A, and SE_T variation with frequency of *LFO* and composites with CB is shown in **Figure 4-8**. **Figure 4-8(a)** shows that SE_R decreased up to 15GHz (0.2 dB) with increased frequency and then expanded for pristine *LFO*. More or less, all other composites followed the same trend (decrease up to a specific frequency). But with an increase in the content of *CB*, SE_R increased to 5.36 dB for *LFO/CB (20)* at 15 GHz. The values of SE_R represent that a tiny amount of EM power is reflected in the case of *LFO* and composites. Similarly, SE_A enhanced drastically with *CB* content (**Figure 4-8 (b)**). The obtained values of SE_A at 15 GHz are 1.5, 2.38, 15.21, 21.3, and 21.8 dB for *LFO*, *LFO/CB (5)*, *LFO/CB (10)*, *LFO/CB (15)*, *LFO/CB (20)*, respectively. Though both SE_R, SE_A increased with an increase in *CB* content, SE_A still increased much faster as compared to SE_R. **Figure 4-8(c)** depicts the SE_T as a function of frequency. The observed value of SE_T is ~ 5 dB for pristine *LFO*, whereas ~ 26 dB for *LFO/CB (20)* for the broad frequency range (8.2–18 GHz). The rapid enhancement in SE_A above 10 wt % of *CB* may be attributed to the conductivity, which usually increases intrinsically with *CB* content[207]. The enhancement mechanism of EMI SE of the composites may be interpreted in two ways: primarily uniform dispersion of *CB* in *LFO* ceramics (evident from **Figure 4-1**).

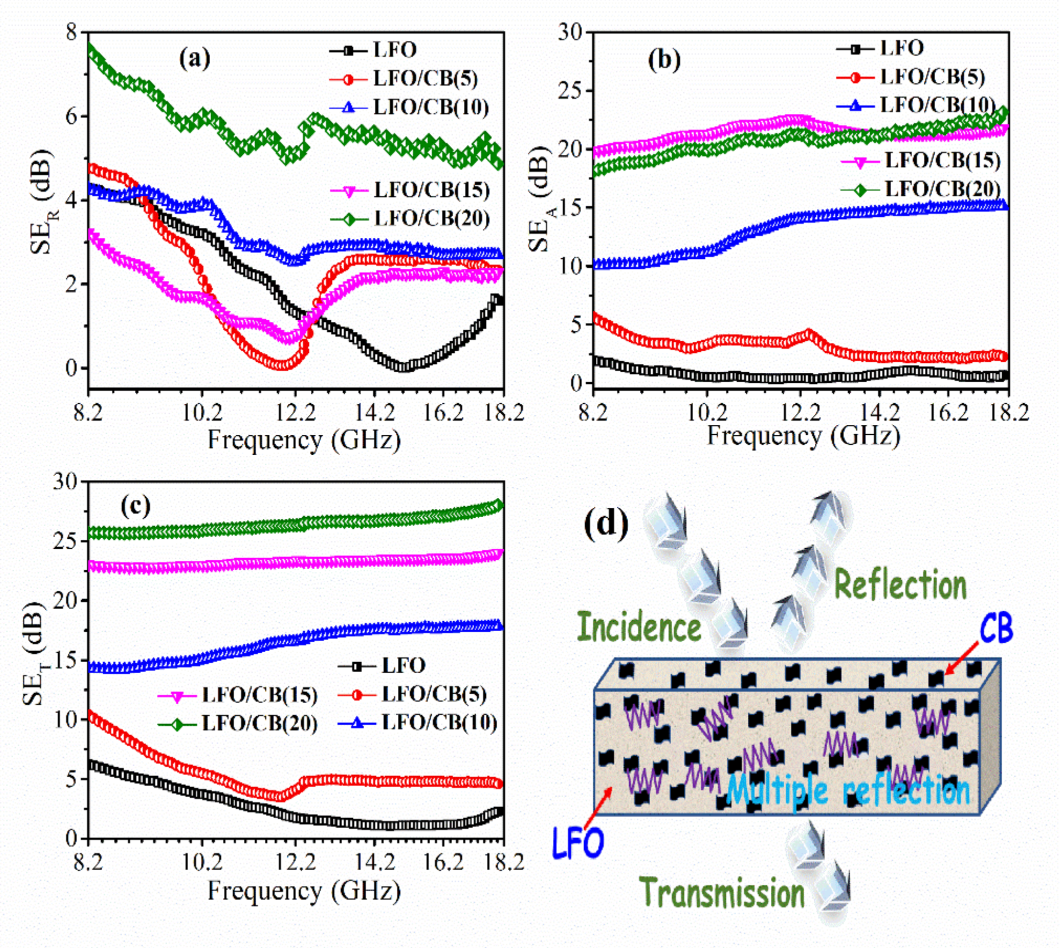

Figure 4-8*. EMI Shielding effectiveness of composites (a) Reflection, (b) Absorption, (c) Total, (d) Schematic illustration of EMI mechanism.*

Uniform distribution in ceramic matrix ensures conductivity enhancement due to *CB* and *SE*. Secondly, the permittivity and permeability of the ceramic matrix play a crucial role in EMI shielding (discussed in the next section). The values of SE_A and SE_R at different frequencies are given in **Table 4-3**. **Figure 4-8(d)** shows the schematic diagram of EMI phenomena. To further understand the absorption contribution in the SE mechanism, absorption efficiency (A_{eff}) is calculated by using **Equation 1.13**. The absorption efficiency of all the specimens for the whole frequency range 8.2 – 18 GHz is depicted in **Figure 4-9(a)**. The observed A_{eff} is in the range of 25 – 30 % for pristine *LFO*. With 5 wt % of CB, it increased to 65 – 45 %. A_{eff} of material has to be more than 96 % for practical use in daily life. *LFO/CB (10)* showed $A_{eff} > 96$ % in the higher frequency range only (12 – 18 GHz). Further, *LFO/CB (15)* and *LFO/CB (20)* exhibited almost the same A_{eff} varying from 98.8 – 99.68 % in the broad frequency. Hence, it is evident that *LFO/CB (15)* and *LFO/CB (20)* can be used as potential microwave absorbers. The A_{eff} of the composites at 15 kHz is shown in **Figure 4-9(b)**.

***Table 4-3**: SE, Permittivity, and permeability of LFO/CB composites at different frequencies.*

Sample name → **Parameters**		**LFO**	**LFO/CB (5)**	**LFO/CB (10)**	**LFO/CB (15)**	**LFO/CB (20)**
SER (dB)	8.2 GHz	4.29	4.75	4.28	3.21	7.61
	18 GHz	1.60	2.33	2.69	2.28	4.85
SEA (dB)	8.2 GHz	1.98	5.67	10.06	19.79	18.06
	18 GHz	0.88	2.26	15.17	21.73	23.17
ε'	8.2 GHz	4.81	9.54	23.22	24.91	46.52
	18 GHz	2.40	1.77	7.91	18.22	22.83
ε''	8.2 GHz	0.11	0.86	3.12	13.55	19.50
	18 GHz	1.15	0.42	5.75	3.11	9.42
μ'	8.2 GHz	0.86	0.67	0.49	0.36	0.09
	18 GHz	1.16	1.14	1.10	0.28	0.24
μ''	8.2 GHz	0.15	0.09	0.54	0.45	0.52
	18 GHz	0.07	0.16	1.17	1.02	0.88

The frequency variation of SE_R, SE_A, and SE_T for all the LDFO/CB composites are shown in **Figure 4-10**. SE_R values are less than 10 dB for all the composites but show slight improvement with increasing Dy^{3+} concentration.

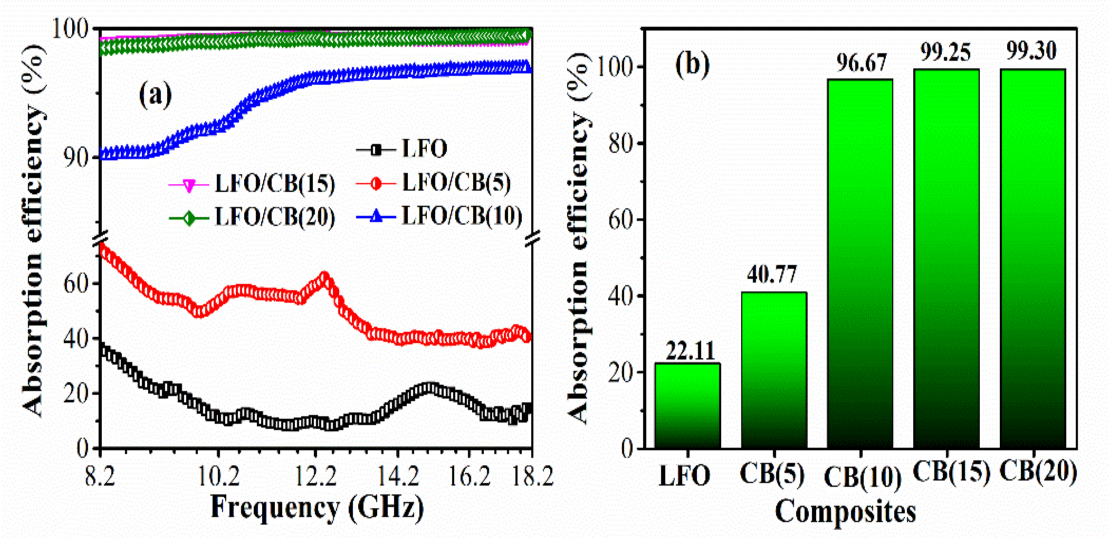

Figure 4-9*. (a) Variation of absorption efficiency with frequency, (b) Absorption efficiency at 15 GHz.*

For *LFO/CB* composite, the SE_R value ranges from 4.28 dB at 8.2 GHz to 2.69 dB at 18 GHz. For *LD15FO/CB* composite, the SE_R value was enhanced to 6.64 dB at 8.2 GHz and 5.44 dB at 18 GHz. *Dy* doping has enhanced the shielding due to reflection and improved magnetic and dielectric properties. However, the low SE_R values indicate that only a tiny portion of the incoming EM radiation is reflected. The SE_A attains a maximum of 23.7 dB at 17.3 GHz for *LD10FO/CB* composite. The SE_A values at different frequencies are tabulated in **Table 4-4**. SE_A has improved with Dy^{3+} substitution with maximum shielding effectiveness corresponding to *LD10FO/CB*. Introducing Dy^{3+} cations enhances the magnetic losses, leading to increased absorption. Relaxation and conductance loss are the main contributors to the high absorption efficiency of the doped composites.[58] Figure 4-10(c) showed that the SE_T value is greater than 10 dB (90% shielding efficiency) for all the composites over the entire range of X and K_u bands. *LD10FO/CB* exhibited the highest

SE_T value of 25 – 26 dB, corresponding to 16.9 – 18 GHz frequency. The trend is similar to the variation in saturation magnetization.

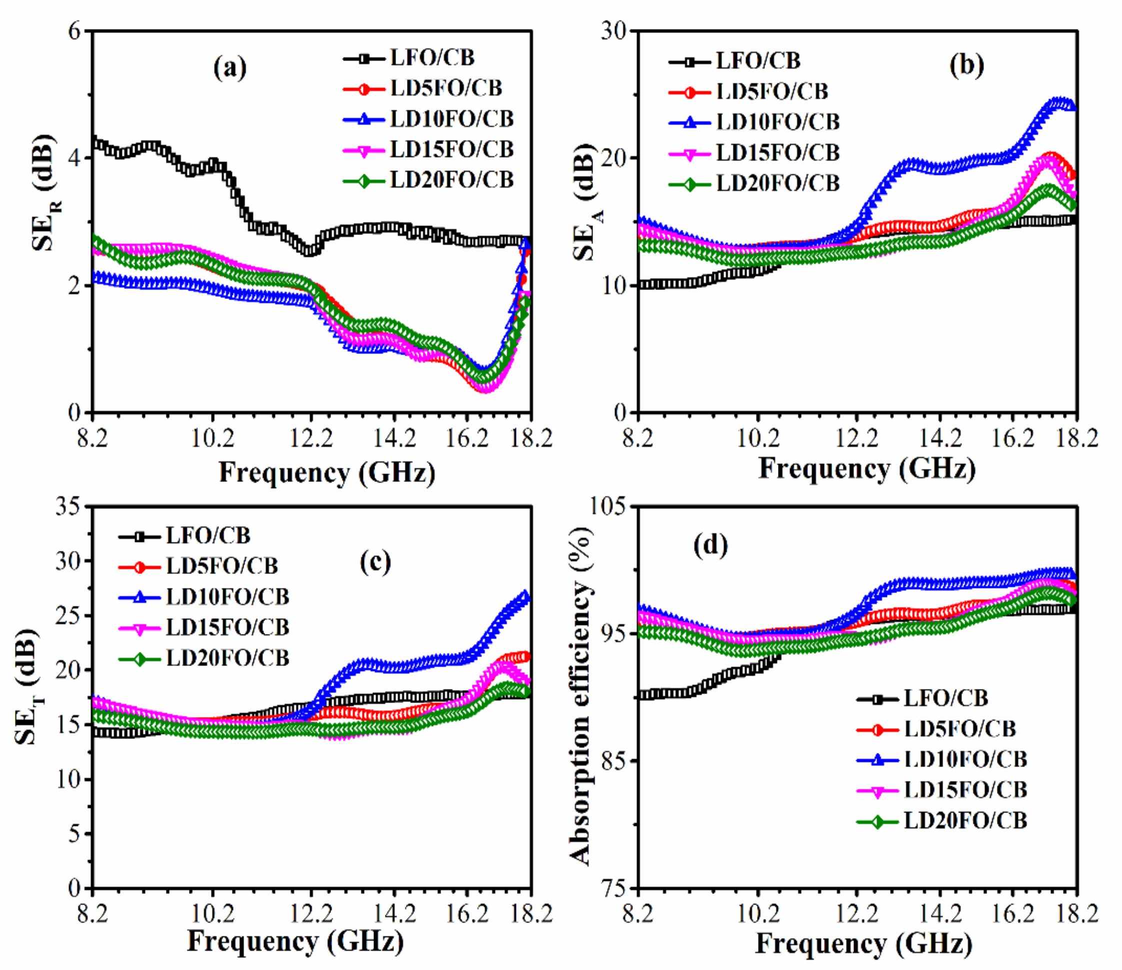

Figure 4-10. *EMI shielding effectiveness of all the LDFO/CB composites (a) SE_R, (b) SE_A, (c) SE_T, (d) Absorption efficiency.*

Like saturation magnetization, the peak values of SE_T and SE_A also increased with *Dy*-concentration up to x = 0.1 and then decreased with a further increase of doping concentration. This indicates a strong correlation between magnetization and shielding performance. *Dy*-doping enhances magnetic loss, further improving absorption and total shielding effectiveness. It must be noted that throughout the X and K_u bands, SE_A is the primary contributor to total shielding effectiveness.

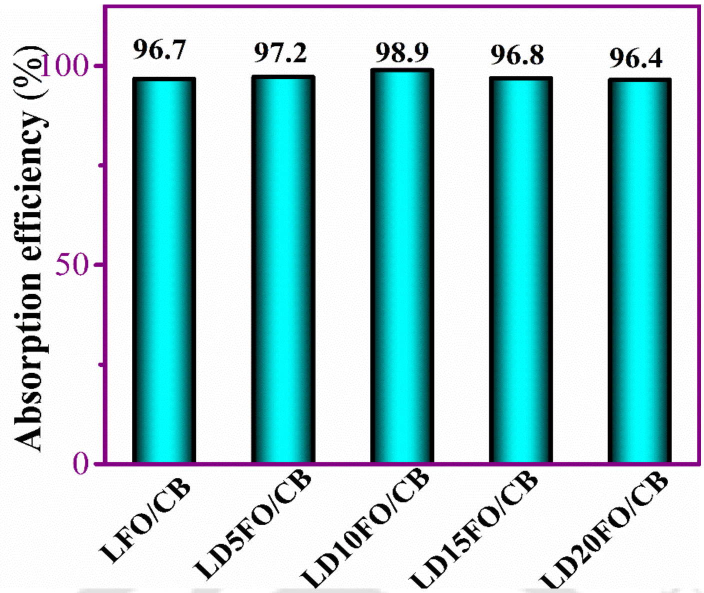

Figure 4-11. *Absorption efficiency of all the LDFO/CB composites at 15 GHz.*

Table 4-4: *SE parameters, complex permittivity, and permeability of LDFO/CB composites at different frequencies.*

	Frequency	**LD5FO/CB**	**LD10FO/CB**	**LD15FO/CB**	**LD20FO/CB**
SE_R (dB)	8.2 GHz	2.58	2.13	2.58	2.71
	18 GHz	2.53	2.64	1.84	1.73
SE_A (dB)	8.2 GHz	13.97	15.03	14.51	13.16
	18 GHz	18.70	24.05	17.04	16.34
ε'	8.2 GHz	27.38	38.44	34.23	33.58
	18 GHz	24.59	27.34	30.44	27.44
ε''	8.2 GHz	20.78	22.56	18.39	19.64
	18 GHz	28.35	37.11	32.51	30.79
μ'	8.2 GHz	0.87	1.06	1.09	1.14
	18 GHz	1.43	2.18	1.99	2.10
μ''	8.2 GHz	1.13	1.00	0.99	0.99
	18 GHz	0.89	0.64	0.63	0.66

This establishes the fact that for lithium ferrite and Dy-doped lithium ferrite-carbon black composites, absorption is the dominant shielding mechanism. **Figure 4-10(d)** depicts the frequency variation of absorption efficiency of all the composites within the 8.2–18 GHz range. *LD10FO/CB* showed 91.50 – 99.6% absorption efficiency in the 12–18 GHz frequency range (shown in **Figure 4-11**). *LD10FO/CB* showed the best shielding and highest absorption efficiency over the K_u band. Therefore, it can be used as a commercial microwave absorber.

4.3.4 Complex permittivity

The real part of permittivity (ε') depends on the polarization that takes place in the material, whereas the imaginary part (ε'') is dependent on the energy dissipation. The variation of complex permittivity as a function of frequency is depicted in **Figure 4-12**. It is observed from the figure that *LFO* showed ε' varying from 5 – 2 in the frequency range 8.2 – 18 GHz. With an increase in frequency, ε' decreased, which is a natural tendency of a dielectric material. This occurs due to the reduced capability of the dipoles to align with the direction of the rapid electric vector of applied electromagnetic waves. Generally, permittivity depends on interfacial, ionic, electronic, and dipole polarization [60],[208],[209]. At a high-frequency regime (GHz range), mainly dipole and electronic polarization play a vital role. It depends on electron hopping between cations of different valances (Fe^{3+} and Fe^{2+}). A similar trend is also observed for the composites with frequency variation. But with an increase in *CB* content in composites, ε' increased to 46 for *LFO/CB(20)* at 8.2 GHz. Further, ε'' is also enhanced drastically with an increase in *CB* concentration from 0.11 (*LFO*) to 19.70 (*LFO/CB(20)*) at 8.2 GHz. Variation in ε" directly affects the microwave absorption of the material. According to the above discussion, both the real and imaginary parts of complex permittivity dramatically increased with the *CB* weight ratio. This can be attributed to the enhancement in the electrical loss of *CB*. It is well known that carbon-based materials, including carbon nanotubes and graphite, promote conductivity and dielectric loss[210],[211]. The obtained results imply that microwave absorption is substantially enhanced by increasing *CB* loading in *LFO/CB* composite.

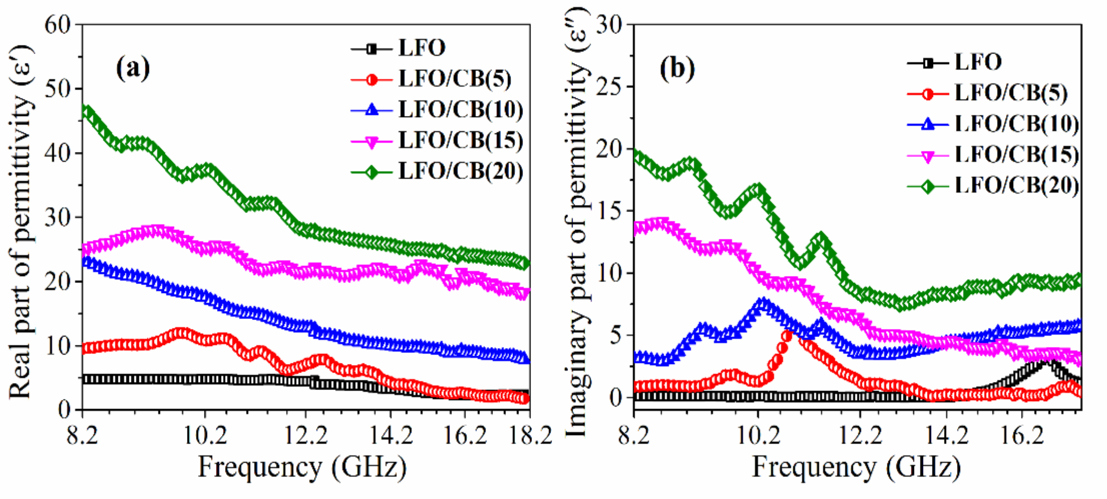

***Figure 4-12**. Complex permittivity of LFO/CB composites in the frequency range (8.2–18 GHz) (a) Real part, (b) Imaginary part.*

Figure 4-13 shows the frequency variation of complex permittivity of *LDFO/CB* composites in the X and K_u bands. It is evident from **Figure 4-13** that *Dy*-doping has enhanced the real and imaginary parts of permittivity. When lithium ferrite is doped with dysprosium, Dy^{3+} ions replace the Fe^{3+} ions from the octahedral sites. This reduces the relative concentration of Fe^{3+} ions concerning Fe^{2+} ions. At 8.2 GHz frequency, *LD10FO/CB* has ε' value of 38.10, much higher than that of *LFO/CB*. The ε'' value also increases from a mere 3.14 (*LFO/CB*) to 22.89 (*LD10FO/CB (10)*) at around 8.2 GHz. The mismatch of ionic radii between Dy^{3+} and Fe^{3+} causes lattice strain which may also be responsible for the increase in dielectric loss (ε''). Also, the introduction of Dy^{3+} in the lattice causes an increase in bond lengths of *Fe–O* and *Dy–O* at the octahedral positions. This leads to higher polarizability and increased permittivity.[212] However, for higher concentrations of Dy-doping (x = 0.15, 0.20), the excess Dy^{3+} ions migrate to the grain boundaries to form the secondary $DyFeO_3$ phase. This decreases the availability of Dy^{3+}

ions, thereby weakening the electron hopping mechanism. The Dy^{3+} ions also replace the octahedral Fe^{3+} ions, which further diminishes the electron exchange between $Fe^{2+} \leftrightarrow Fe^{3+}$. Hence, $x = 0.15$ onwards, both ε' and ε'' decreased.

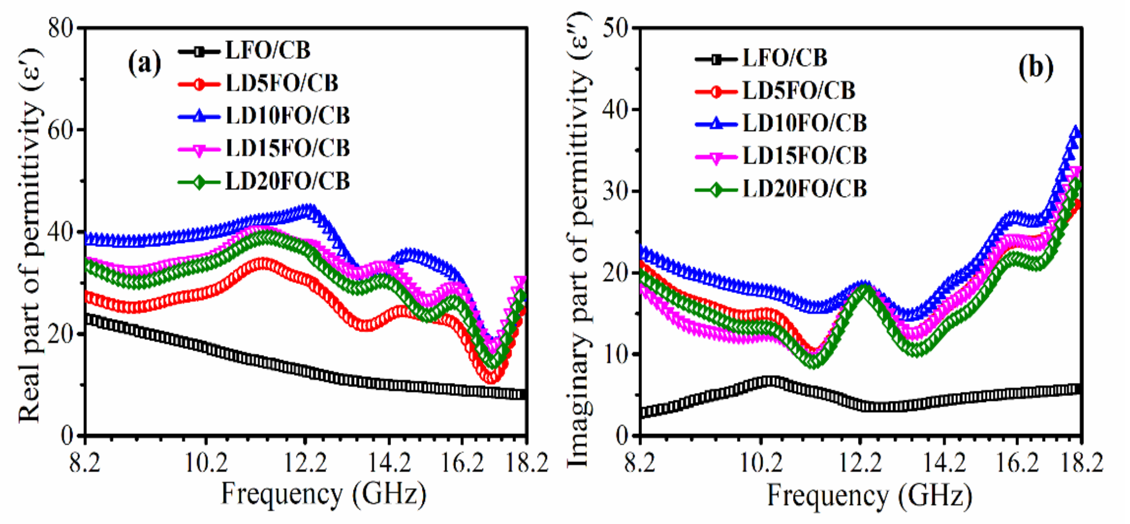

Figure 4-13. *Complex permittivity of LDFO/CB composites in the frequency range (8.2–18 GHz) (a) Real part, (b) Imaginary part.*

The observed fluctuations in ε' and ε'' at higher frequencies (> 13 GHz) is attributed to the dipole relaxations. When the electric field is applied to dielectric material, re-orientation of dipoles takes place, leading to the relaxation of polarized dipoles afterward. More energy is required to reorient the dipoles in case of dielectric relaxation, which causes the higher dissipation of electromagnetic energy at high frequencies. The dielectric relaxation can induce dielectric loss, which is responsible for the enhancement of SE. The variation in dipole polarization also helps to generate small microcurrents induced due to the free electrons' local movement, which also favours the dielectric loss and SE.[213] In order to get more clarity in the relaxation process, the complex permittivity is analyzed in terms of the Cole-Cole plot (**Figure 4-14**). On the basis of Debye dipole relaxation, complex permittivity is expressed as [214]

$$\varepsilon_r = \varepsilon' + i\varepsilon'' = \varepsilon_\infty + \frac{\varepsilon_s - \varepsilon_\infty}{1 + i2\pi f\tau} \qquad 4.3$$

$$\varepsilon' = \varepsilon_\infty + \frac{(\varepsilon_s - \varepsilon_\infty)}{1 + (2\pi f\tau)^2} \qquad 4.4$$

$$\varepsilon'' = \varepsilon_\infty + \frac{2\pi f\tau(\varepsilon_s - \varepsilon_\infty)}{1 + (2\pi f\tau)^2} \qquad 4.5$$

where τ, f, ε_∞, and ε_s are the relaxation time for dielectric polarization and frequency, dielectric constant at infinite frequency, and static dielectric constant, respectively.

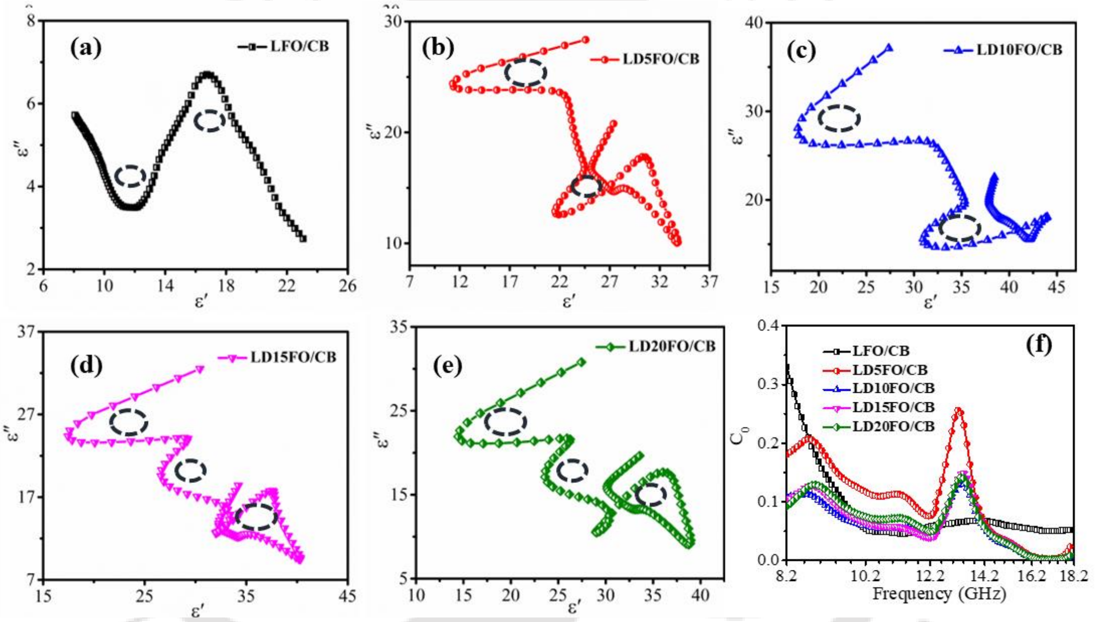

Figure 4-14. *Cole-Cole plot of all the composites (a) LFO/CB, (b) LD5FO/CB, (c) LD10FO/CB, (d) LD15FO/CB, (e) LD20FO/CB, (f) Frequency variation eddy current loss of all the samples.*

Figure 4-14 shows the Cole-Cole plot of all the composites. Ideal Debye behavior shows the semi-circular response between ε' and ε'', where each semicircle corresponds to one Debye relaxation process. In this present case, a mixed response of semicircle and linear behavior is observed that can be related to conduction loss generally developed from microcurrent at the interface (heterostructure of composites), electron hopping between Fe^{3+} and Fe^{2+}.[213] Further, conductivity is deduced by using the equation: $\sigma_{ac} = \omega\varepsilon_0\varepsilon''$ and found to be increased with the incorporation of *Dy*. The obtained conductivity for

LFO/CB and *LD10FO/CB(10)* is in the order of ~10^{-2} and 10^{-1} S/cm, respectively. This confirms the presence of higher conduction loss in *Dy*-substituted composites. Conductivity also plays a significant role in enhancing SE.

4.3.5 Complex permeability

Figure 4-15(a), (b) depicts the frequency variation of the real (μ') and imaginary (μ'') parts of the permeability of all the specimens. μ' decreased with an increase in *CB* content in the composites. The obtained μ' is 0.86, 0.67, 0.49, 0.36, 0.09 for *LFO*, *LFO/CB(5)*, *LFO/CB(10)*, *LFO/CB(15)*, *LFO/CB(20)*, respectively at 8.2GHz. This decrease in μ' can be attributed to the reduced saturation magnetization with increasing *CB* content. However, the μ'' increased with different *CB* wt % in the composites. It increased to 0.52 for *LFO/CB(20)* from 0.15 for *LFO*. The values of complex permittivity and permeability at different frequencies are given in **Table 4-3**.

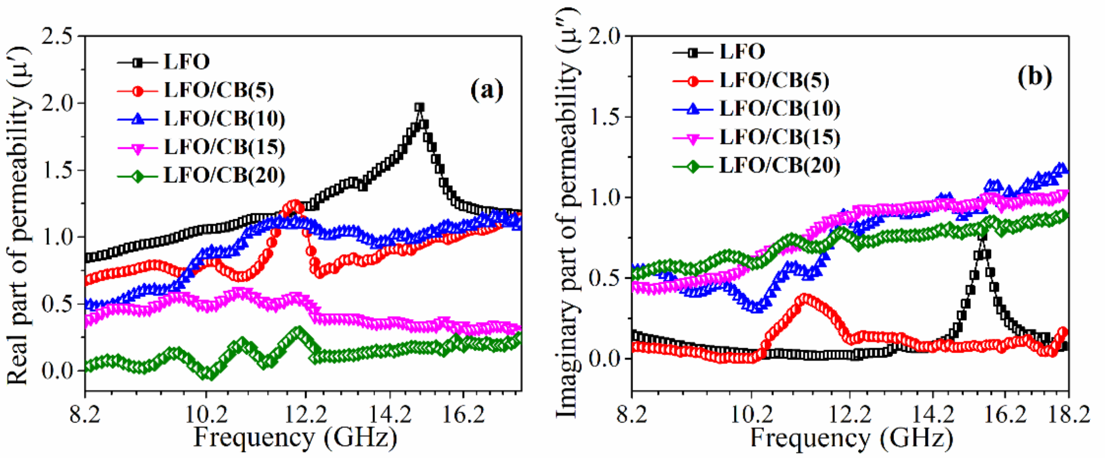

***Figure 4-15**. Variation of complex permeability of LFO/CB composites in the frequency range (8.2–18 GHz) (a) Real part, (b) Imaginary part.*

On the other hand, in terms of shielding efficiency, the magnetocrystalline anisotropy is related to the magnetic loss (μ''), which comes from the domain wall motion, spin resonance in the microwave frequency band. A smaller anisotropy field improves the absorption bandwidth. For an efficient microwave absorber, magnetic shielding requires the conservation of its magnetic permeability over the GHz range. With the addition of CB, though the magnetocrystalline anisotropy decreased, the μ" increased, which enhanced the EMI shielding efficiency. The variation of μ' and μ" of LDFO/CB composites as a function of frequency is shown in **Figure 4-16**. The μ' showed almost constant value in the X-band range for all the compositions, and a variation is observed in the K_u band regime. LD10FO/CB composite exhibited the highest value of μ' (7.75) at around 17 GHz. The values of the complex permeability and permittivity at different frequencies are enlisted in **Table 4-4**. The highest saturation magnetization and SE_T value are also observed for the same composition. The increase in the peak values is linked with the increase in magnetization due to Dy-doping. The substitution of Dy^{3+} (10.50 μ_B) for Fe^{3+}(5.85 μ_B) results in an increase in M_s up to x = 0.1. A similar trend is also observed in the values of μ' and μ''. An increase in magneto-crystalline anisotropy and lattice distortion due to Dy^{3+} doping is also responsible for the enhancement of μ'' peaks in the LD10FO/CB composites. Also, higher magnetic losses resulted in improved absorption efficiency in the doped composites.

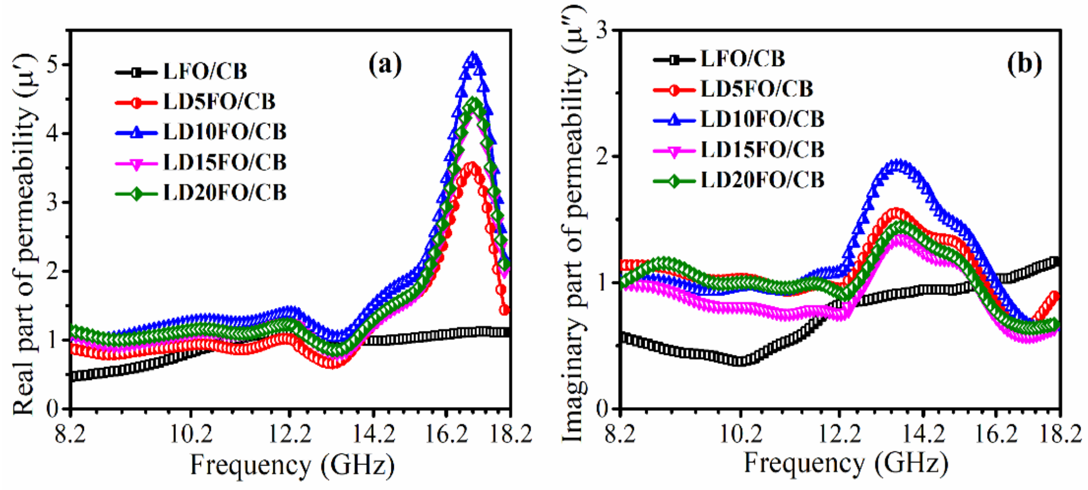

Figure 4-16. *Variation of complex permeability of LDFO/CB composites in the frequency range (8.2–18 GHz) (a) Real part, (b) Imaginary part.*

In the microwave frequency regime, the magnetic loss is mainly related to natural resonance, domain wall resonance, eddy current loss, and magnetic hysteresis loss. Out of these, domain wall resonance occurs in the 1 – 100 MHz regime, and hysteresis loss can be neglected in a weak external field.[215] The eddy current loss is connected with conductivity and the thickness of the shielded material, which can be expressed as: $C_0 = \mu''(\mu')^{-2}f^{-1} = 2\pi\mu_o\sigma d^2/3$. The value of C_0 must remain constant with respect to frequency if the materials' magnetic loss originates from eddy currents loss. In this present case, C_0 is observed to be varied with frequency (as observed in **Figure 4-14 (f)**). So, eddy current loss is not the reason for the magnetic loss of the shielded material. According to the Kittel equation, the natural resonance frequency can be calculated as: $f_r = \frac{\gamma}{2\pi}H_{K,}$ where γ is the gyromagnetic ratio. For cubic systems, the magnetocrystalline anisotropy field (H_K), $H_K = \frac{4|K_1|}{3\mu_0 M_S}$. The natural resonance frequency of the samples is in the range of 1.5 – 3 GHz. The peaks observed in μ' and μ'' are at ~ 16.9 GHz and 13.52 GHz, which are very far from the range of natural frequency.[216] In this study, the observed resonance peak may be observed due to exchange resonance, spin relaxation, and domain wall rotation which generally occurs at a higher frequency than the resonance frequency.[217] According to the above analysis, it is concluded that both dielectric and magnetic loss are responsible for efficient EMI shielding.

A comparison table is given with other previously reported data used for this purpose with the present work (**Table 4-5**). Most of the reported work with high SE are polymer-based composites, whereas we tried to enhance the SE with ceramics only.

Table 4-5. *EMI shielding effectiveness of reported other materials and present work.*

Material Name	**Total EMI SE (dB)**	**Reference**
Barium ferrite with reduced graphene oxide composite	30	[8]
NiMgZn ferrite	12.13	[60]
Polythiophene/$Ni_{0.5}Zn_{0.5}Fe_{2-x}Ce_xO_4$	24.5	[218]
Polyaniline barium ferrite composite with aromatic sulphonic acid	28.9	[219]
Graphene-$MnFe_2O_4$-Multiwalled Carbon Nanotube Hybrids composites	34	[220]
Mesoporous strontium ferrite/polythiophene composite	29	[221]
Cobalt Ferrites and Coal-Fly-Ash Based Polymer Nanocomposites	32	[222]
Polyaniline doped with paratoluene sulphonic acid and cobalt ferrite	26	[223]
Lithium ferrite - Carbon black composite	28	**Present work**
Dy substituted LFO/carbon black	26	**Present work**

4.4 Conclusions

Two series of ceramics composites of lithium ferrite/carbon black (different wt % of carbon black), and *Dy* substituted lithium ferrite/carbon black (with different concentrations of Dy) are synthesized successfully. Morphology, structure, magnetic, permittivity, permeability, and shielding efficiency is analyzed. The lattice constant and volume were found to be initially decreased with an increase in *Dy* concentration. The high electrical properties of *CB* and the rich magnetic and dielectric properties of *LFO* contributed to achieving high EMT shielding. Though saturation magnetization is decreased with the incorporation of *CB*, high saturation magnetization is still observed. The maximum saturation magnetization is obtained for *LD10FO/CB*. SE due to reflection as well as absorption enhanced with the incorporation of *CB*. A total SE of 28 dB is obtained for *LFO/CB(20)* at 18 GHz. The maximum shielding effectiveness of 24 dB was obtained for *LD10FO/CB* ~ 17 – 18 GHz. The *Dy* substitution enhances the magnetic as well as dielectric loss. Further, 99.68 % of A_{eff} is achieved with 20 wt % of *CB* reinforcement in *LFO*, whereas the maximum absorption efficiency of 99.6 % is obtained for *LD10FO/CB* ~ 17 – 18 GHz. The electron hopping mechanism explains the variation of permittivity. The synergic effect of dielectric and magnetic loss are the main contributors to the high SE. Out of all synthesized samples, LD10FO/CB showed the best EMI shielding response. The obtained results suggest that LD10FO/CB can be used for EMI shielding applications in the commercial aspect.

Chapter 5 : Deposition and characterization of $LiFe_5O_8$ and $LiDy_{0.1}Fe_{4.9}O_8$ thin films

This chapter investigates the structural, surface morphology, dielectric and magnetic response of $LiFe_5O_8$ (*LFO*) and $LiDy_{0.1}Fe_{4.9}O_8$ (*LDFO*) thin films having different thicknesses. The involved electrical conduction mechanism is also studied.

5.1 Introduction

Due to miniaturizing technology, various devices such as spintronics, memory, and multifunctional devices have rapidly developed. Ferrite thin films have gained more attention due to their high electrical resistivity, magnetoelectric coupling, resistive switching, magnetic response, and application in high-frequency devices.[224],[225],[226] Ferrites are mainly well-known for gyrators, circulators in microwave devices, insulators, and integrated microwave circuits that are supposed to replace the surface-mounted device shortly.[227] The emerging spintronics technology (integration of electron's spin into conventional electronics) has increased the imposition of a new material: ferromagnetic semiconductors. Previously, the focus was on the semiconducting host material where ferromagnetism was induced by substituting magnetic ions. Now hunt for such material has shifted to another possible way: causing semiconductivity by electronic doping in an insulating ferromagnet.[228] Among various ferrites, lithium ferrite is known for high Curie temperature, high resistivity, high magnetization, moderate dielectric permittivity, and permeability.[229],[105],[230] The magnetic and dielectric response of *LFO* thin films is strongly thickness-dependent. So, it is fascinating to tune the magnetic and dielectric response by controlling various properties like lattice strain, choice of substrate, grain size, microstructure, film thickness, etc.[231],[232]. Several deposition techniques, such as spray pyrolysis,[134] sputtering,[233] and PLD[130], have been used to deposite *LFO* thin films. PLD is more suitable for depositing complex oxide films, including rare earth iron garnets,[234] hexaferrite,[235] and spinel ferrites.[236] This provides better control to maintain the stoichiometry and the high quality of films.

Moreover, the deposition of single-phase *LFO* is difficult due to the volatility of *Li* and the formation of the impurity phase of $LiFeO_2$ and Fe_2O_3. Cadieu et al. [131] synthesized highly textured (311) oriented *LFO* films on c plane sapphire substrate that showed peak-to-peak linewidth of 355 Oe for in-plane static configuration. The out-of-plane FMR profile was completely distorted. They obtained the saturation flux density of the films same as bulk LFO materials. Boyraz et al. [132] reported the structural properties of *LFO* films grown at different temperatures and on other substrates (MgO, $MgAl_2O_4$ (MAO), $SrTiO_3$). They provided evidence of partial ordering of *Fe* and *Li* at the octahedral site of the *LFO* films fabricated on *MAO* substrate, whereas complete octahedral site disorder of the films grown on *MgO* substrate. Zhang et al. [133] fabricated *LFO* films in the high-pressure sputtering system on an *MAO* substrate. It was reported that more significant out-of-plane tensile and in-plane compressive strains could be achieved by reducing the film thickness. Controlling thickness is an effective method to tune the interface strain and improve the magnetic response of the films. The structural, optical, and dielectric response of Al-substituted *LFO* films is reported by Chilwar et al. [134]. The saturation magnetization, dielectric constant, and dielectric loss decreased with the substitution of Al. Oliver et al.[130] reported the structural and magnetic properties of lithium zinc ferrite thin films. They also mentioned that film grown at lower oxygen pressure showed cubic anisotropy, the highest magnetization, and the narrowest resonance line width. Zhang and his group discussed the epitaxial film growth and magnetic response of *LFO* thin films with different thicknesses grown on $MgAl_2O_4$ substrate deposited by a high-pressure sputtering system.[133] They found that the in-plane compressive strain can be achieved by decreasing thickness. It can also enhance magnetization and decrease coercivity.

Nowadays, interface engineering has become a widespread technique in tuning the physical properties of thin films and nanomaterials. In this instance, the optical, magnetic, and electrical responses can be tailored by interface modification. The most effective and easiest way to tune the interface strain is to control the film thickness. The dependence of the thickness on the magnetic and structural response of $BiFeO_3$ thin films was reported by Rana et al.[237] and they displayed a weak improvement in magnetization. Kale et al.[238] studied the temperature and film thickness-dependent magnetic properties of Fe_3O_4 films. They observed notable differences between magnetization and magnetocrystalline anisotropy. Moreover, synthesizing single-phase *LFO* thin film is difficult due to the volatility of *Li* and the formation of the impurity phase of $LiFeO_2$ and Fe_2O_3. The pulsed laser deposition (PLD) technique provides the advantage of depositing high stoichiometry film quickly. So, PLD is used for the deposition of *LFO* films. This work aims to deposit high-quality (high magnetization, compact microstructures, and high dielectric constant with low dielectric loss) *LFO* films that can be used for microwave and magnetic devices. According to the available literature, vital interest was laid on the magnetic response and the structural modification of the LFO thin films. In order to include the *LFO* thin films in the electronic and microwave applications, it is required to systematically investigate the dielectric, impedance, and morphology response of the films. In this work, we synthesized $LiFe_5O_8$ and $LiDy_{0.1}Fe_{4.9}O_8$ thin films are deposited with different thicknesses on Pt(111)/Ti/SiO_2/Si substrate. We have systematically investigated the structure, morphology, and magnetic and dielectric response. The effect of thickness on the dielectric, electron hopping, and magnetic properties are also analyzed and correlated.

5.2 Materials and method of deposition

$LiFe_5O_8$ powder is prepared by the solid-state method, as described in Chapter 2. After calcination, the powder is milled for 6 h. Then, the powder is pressed into a 4 mm thickness and 20 mm diameter cylindrical disk and sintered at 1000 °C for 6h. The prepared target is used for further deposition thin films on Pt(111)/Ti/SiO_2/Si substrate by pulsed laser deposition (PLD). Initially, the reaction chamber is evacuated to a base pressure of $\sim 10^{-6}$ mbar. Then the films of different thicknesses (160 nm, 200 nm, 240nm, 300 nm) are deposited at 0.01 mbar. The distance between the substrate and target is kept around 4 cm while the laser pulse repetition rate to 10 Hz. Before deposition, the substrate is preheated to 700 °C for 1h, and after deposition, it cooled down slowly.

5.3 Results and discussions

5.3.1 Structural analysis

Figure 5-1 (a) shows the XRD pattern of the deposited *LFO* films with different thicknesses (160, 200, 240, and 300 nm). It revealed the polycrystalline growth of thin films having a cubic spinel structure with the $P4_132$ space group. Again, a slight shift is observed in the predominant peak (311) towards the right with an increase in thickness. The full-width half maxima (FWHM) also decreases with a rise in film thickness. For further analysis, Rietveld refinement is performed using Fullprof software. The refined pattern of 240 nm film is shown in **Figure 5-1**. The lattice constant, volume, and goodness of fit are enlisted in **Table 5-1**. The lattice constant is decreased from 8.342 Å for 160 nm to 8.3312 Å for 240 nm and enhanced after that. This can be attributed to the compressive strain generally arising from the lattice mismatch of the substrate and the deposited samples. The intensity of the XRD peaks also increased with the film thickness, indicating the film's crystalline nature. The crystallite size (D) and lattice strain (ε) is determined by using **Equation 3.1** (shown in **Figure 5-2**). The calculated crystallite size and microstrain are enlisted in **Table 5-1**.

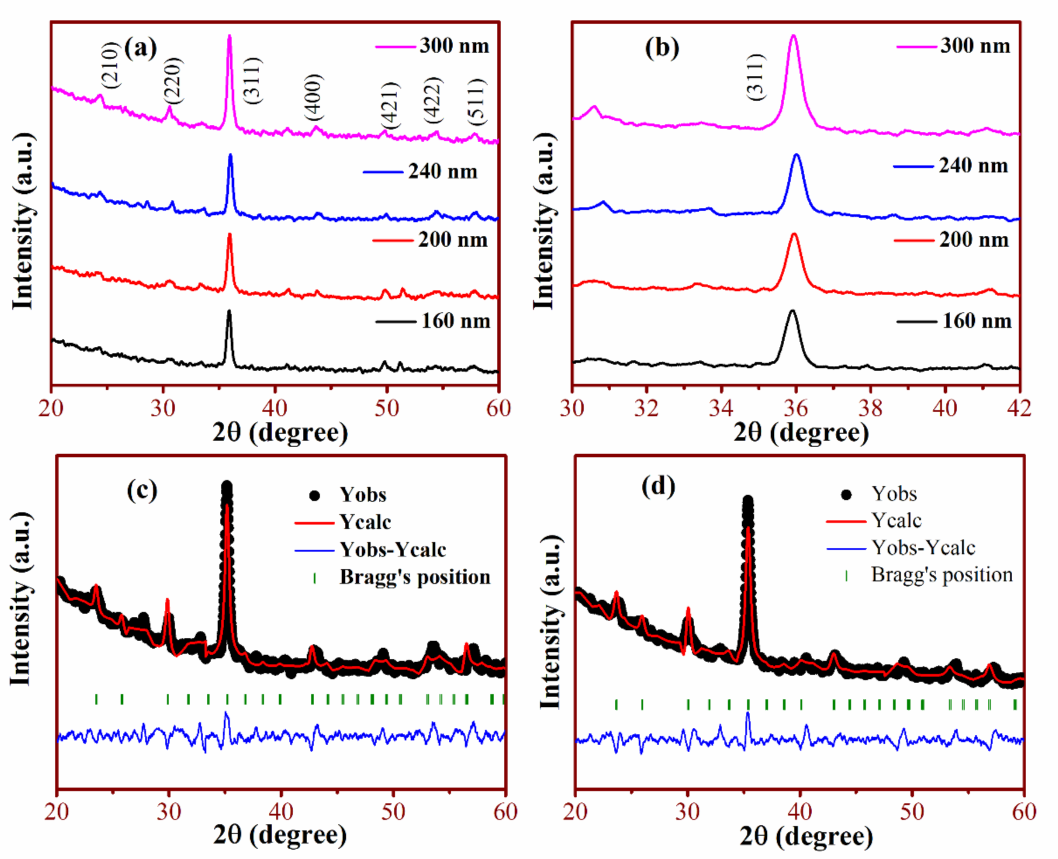

***Figure 5-1**. (a) XRD pattern of all LFO films, (b) Zoomed view of (311) peak, Rietveld refinement pattern of (c) 240 nm, (d) 300 nm.*

With the enhancement in the film thickness, both crystallite size and strain are decreased. In the initial stage of film growth, there is a considerable lattice mismatch between the *LFO* and substrate. Since the substrate's lattice parameter is about half that of bulk LFO, one *LFO* lattice unit can fit on four lattice units of the substrate. The theoretical lattice misfit is calculated as -6.06% (a_{sub} = 0.3925nm, $a_{LFO/2}$ = 0.4163nm). So, the compressive strain arises at the interface. With the gradual increase in film thickness, the strain gets released. The number of grain boundaries per unit area in the low film thickness will be significant [14]. That results in an increase in strain in the low-thickness films.

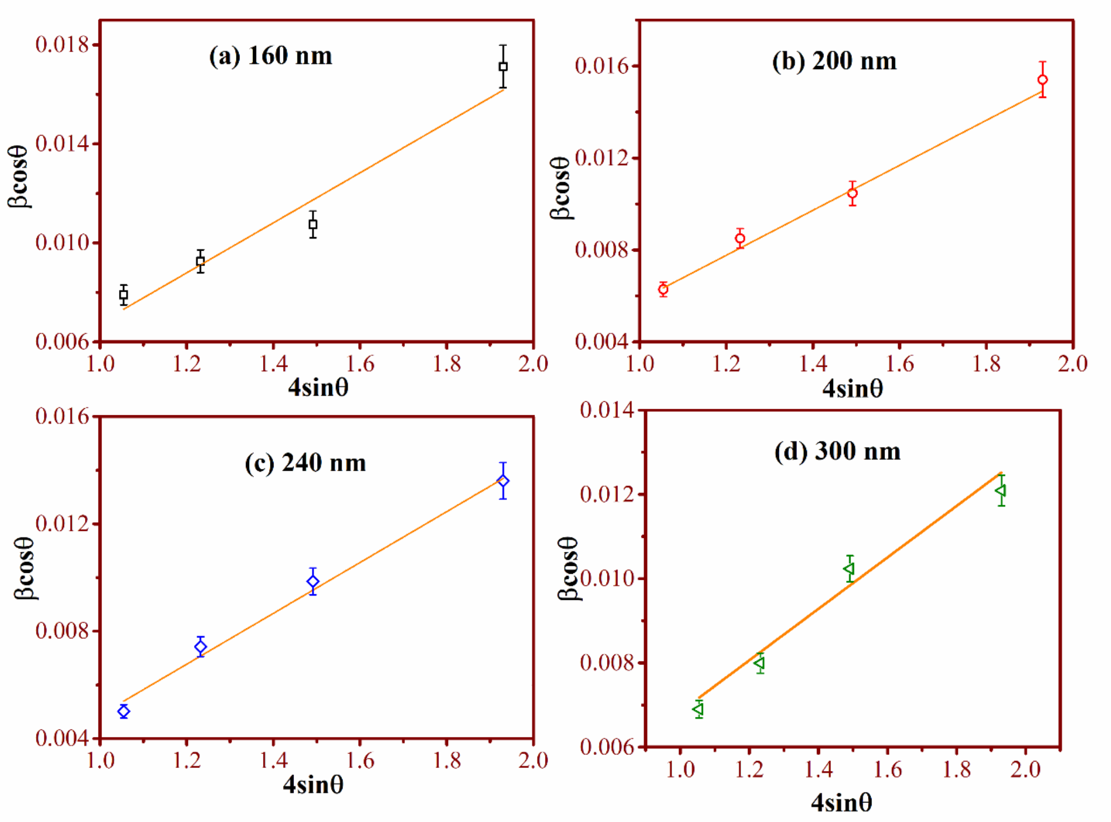

***Figure 5-2**. Williamson -Hall plot of all the LFO thin films.*

***Table 5-1**. Different structural parameters of LFO films.*

Parameters	160 nm	200 nm	240 nm	300 nm
Lattice constant (Å)	8.3424 (3)	8.3336 (2)	8.3312 (3)	8.3372 (3)
Volume (Å^3)	580.594	578.759	578.259	579.509
Crystallite size (nm)	41.51	35.12	30.44	34.23
Strain	0.0101	0.0097	0.0064	0.0072

Figure 5-3(a) shows the XRD pattern of LDFO thin films having different thicknesses of 160 nm, 200nm, 240 nm, and 300 nm, deposited at an oxygen partial pressure of 10^{-2} mbar and substrate temperature of 700 °C. All the films exhibited cubic ordered phase with a space group *$P4_132$*. It shows that *Dy* is appropriately incorporated in place of

Fe in *LFO*. No secondary phase of $DyFeO_3$ is detected.[199] As Dy^{3+}(0.91 Å) possesses higher ionic radii than Fe^{3+} (0.64 Å), it tends to occupy the octahedral position. With the incorporation of *Dy*, it occupied the octahedral position by shifting the *Fe* ions from the octahedral sites to the tetrahedral site. Again, a shift in the predominant peak (311) is observed towards higher 2θ from 160 nm to 240 nm and decreased afterward with an increase in film thickness (depicted in **Figure 5-3(b)**).

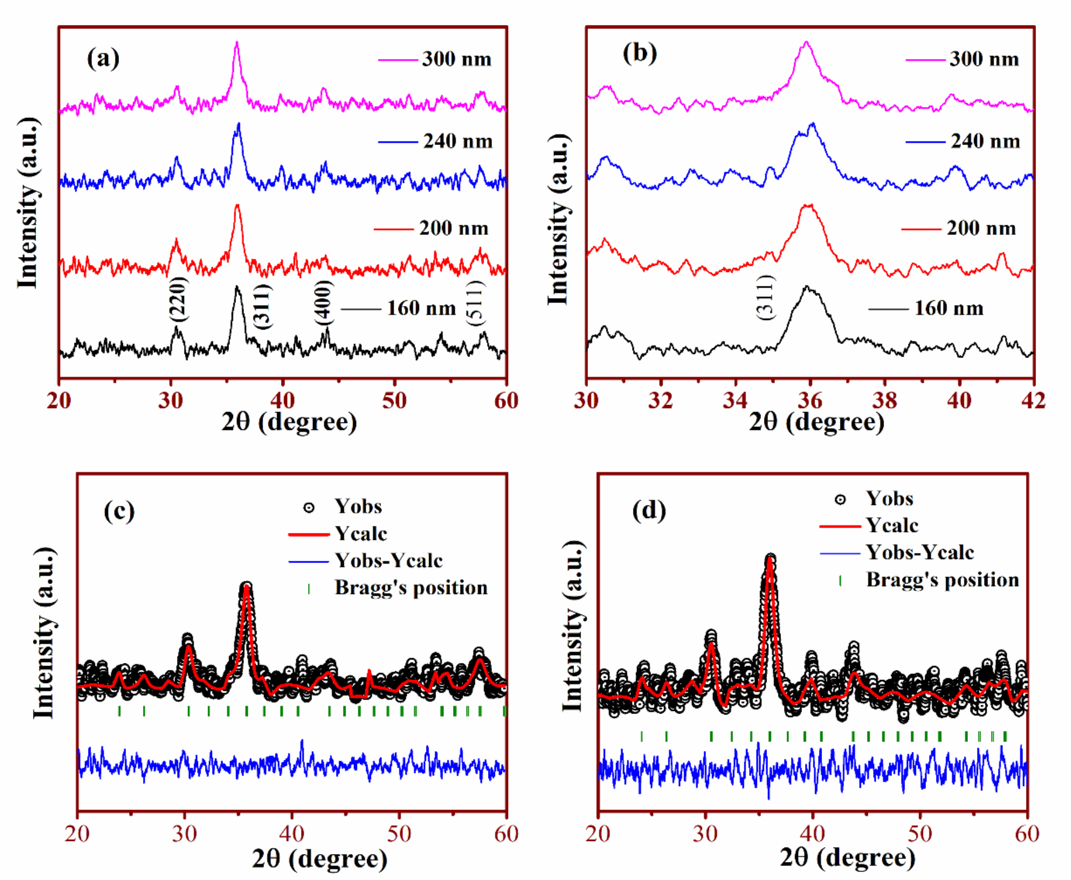

Figure 5-3*. (a) XRD pattern of all the LDFO films, (b) Predominant peak, Rietveld refinement pattern of (c) 200 nm, (d) 240 nm.*

The full-width half maxima (FWHM) is found to be decreased with an increase in film thickness. The extracted lattice constant, volume, and goodness of fit (χ^2) values are enlisted in **Table 5-2**. The refinement pattern of 200nm and 240 nm are shown in **Figure 5-3** (**c and d**). The obtained values of the lattice constant of *LDFO* thin films agree with previously reported *LFO* thin films.[134],[132] The lattice constant and volume are decreased up to a film thickness of 240 nm and enhanced with a further increase in film thickness. The decrease and increase in constant lattice volume are ascribed to the compressive and tensile strain of the films, respectively, which usually arises due to the lattice mismatch between the substrate and the deposited layer. The calculated lattice mismatch for *LDFO* films is ~ -6.21%.

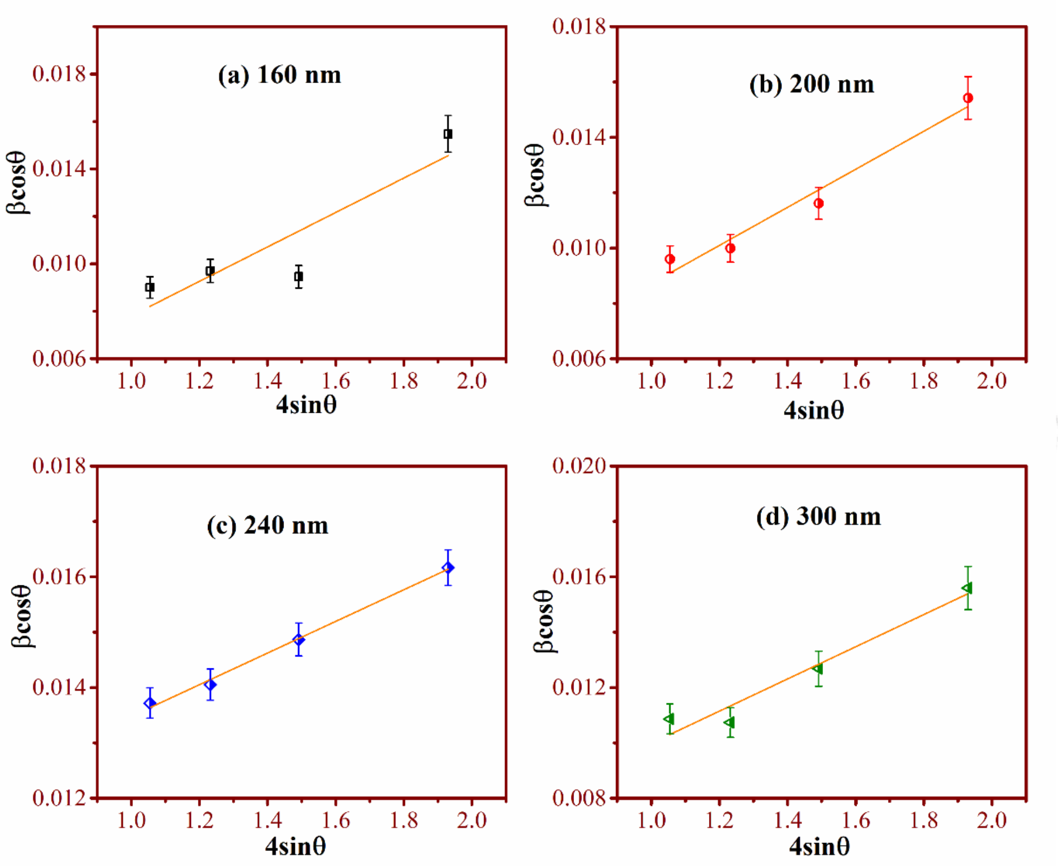

Figure 5-4. *Williamson – Hall plot of all the LDFO films.*

The W–H plot (βcosθ as a function of 4sinθ) is shown in **Figure 5-4** for all the *LDFO* films. The crystallite size and microstrain are deduced from the intercept and slope, respectively, and enlisted in **Table 5-2**. It is observed that the film with the lower thickness (160 nm) showed the highest lattice strain, which is reduced with increasing thickness up to 240 nm and then enhanced with a further increase in thickness. Wang et al. [242] also reported a similar type of response for GdBCO films synthesized by sputtering. In the initial stage of film growth, there is a lattice mismatch (~ -6.21%) between the substrate and the deposited film. This results in compressive strain. With the rise in thickness, the strain is used to release. The lowest strain is observed for 240 nm. After reaching an optimum thickness, the tensile strain plays a significant role that further promotes strain enhancement. The crystallite size is found to be decreased.

Table 5-2. *The extracted structural parameters of LDFO films.*

	160 nm	**200 nm**	**240 nm**	**300 nm**
Lattice constant (Å)	8.3284 (2)	8.2775 (3)	8.2611 (3)	8.2809
Volume (Å^3)	577.6769	567.1440	563.7814	567.8506
Crystallite size (nm)	37.61	32.71	31.44	32.52
Strain	0.007	0.005	0.001	0.004

5.3.2 Raman analysis

Further, Raman spectra are recorded in the wavenumber range of 330 - 930 cm^{-1} to confirm the phase for all the films, as depicted in **Figure 5-5**.

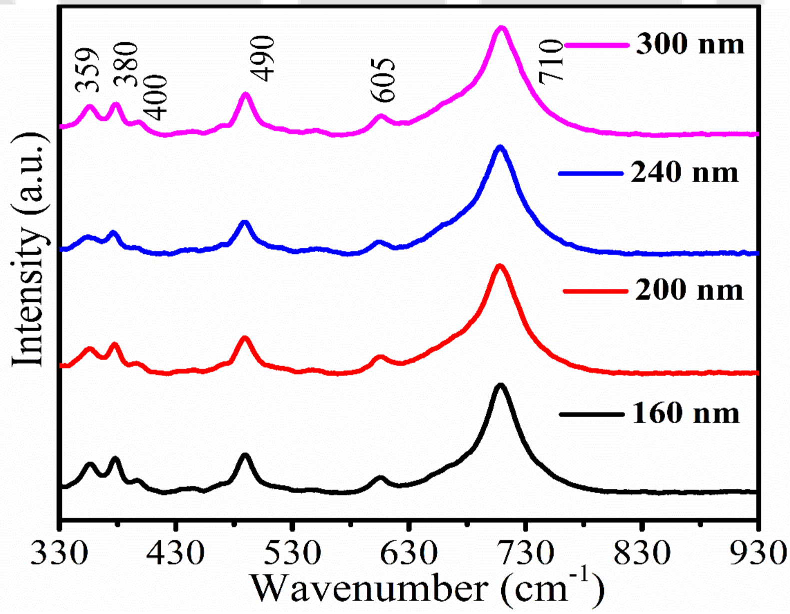

Figure 5-5. *Room temperature Raman spectra of all the deposited LFO films.*

According to the group theory analysis, 40 Raman active modes are present in the ordered *LFO* ($P4_132$ space group) phase. In the present case, we have observed six modes ($2E+2A_1+2F_2$) in the measured wavenumber range.[239] The modes observed at 359 and 380 cm^{-1} correspond to *E* mode, whereas 400 and 710 cm^{-1} belong to A_1. F_2 modes are observed at 490 and 710 cm^{-1}. A shift in the predominant peak is observed toward the lower wavenumber with the increase in thickness up to 240 nm film and towards higher for 300 nm films which can be ascribed to the change in the lattice constant.

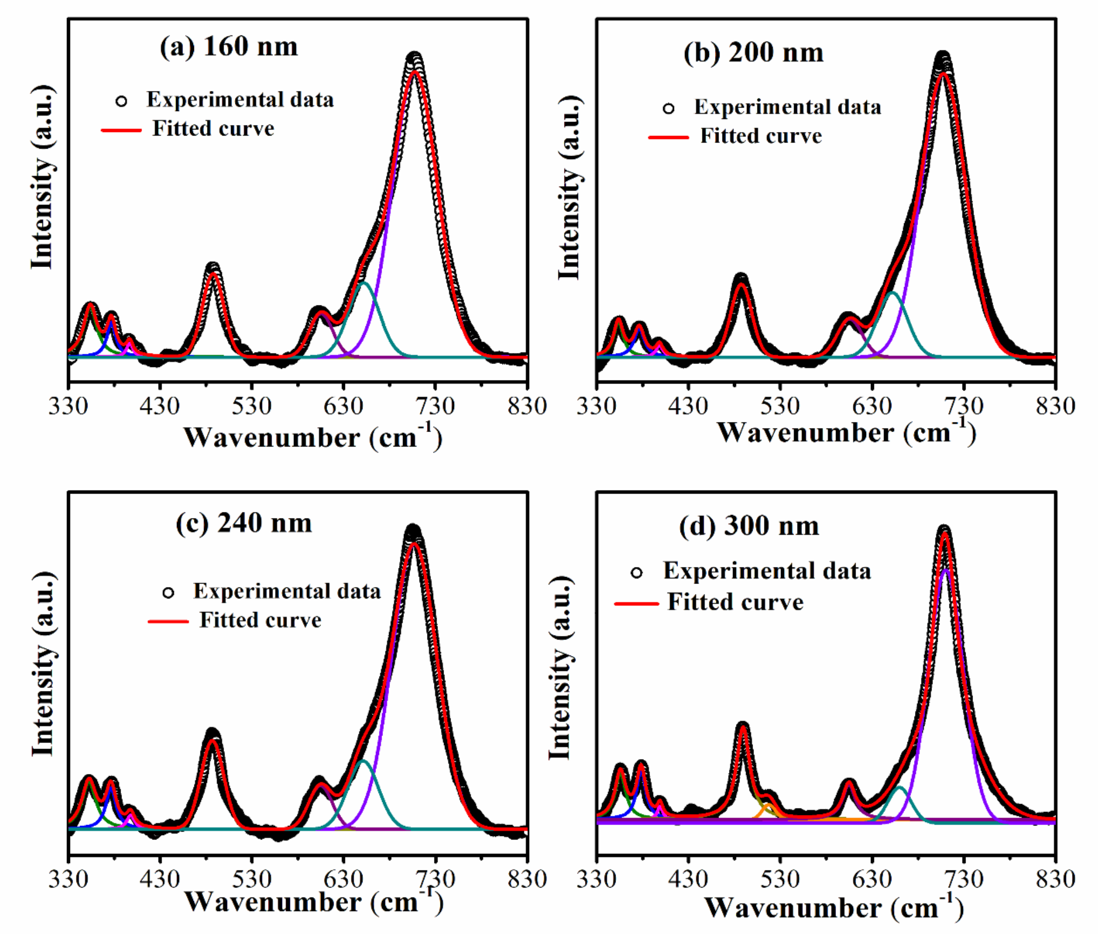

***Figure 5-6**. Room temperature Raman spectra of all the deposited LDFO films.*

Similarly, Raman spectra of *LDFO* films with the deconvoluted peaks are shown in **Figure 5-6**. In this case, seven modes ($2E + 2A_1+3F_2$) are observed in the measured wavenumber range for 160, 200, and 240 nm films. The peak observed at ~ (353, 376), (396, 707), and (487, 605, 651) cm^{-1} correspond to *E*, A_1, and F_2 modes, respectively. The observed modes in 472 – 714 cm^{-1} are attributed to the *Fe–O* bands in the octahedral and tetrahedral sites.[240] With the increase of film thickness up to 240 nm, a shift towards lower wave number is observed and then shifted towards higher wavenumber with further increase in thickness. All the deconvoluted peak positions and the *FWHM* of each peak are enlisted in **Table 5-3**. The variation in the *FWHM* of a particular peak implies the lattice distortion and crystallinity caused by the lattice mismatch between the deposited layer and the substrate that causes strain. For 300 nm film, an extra peak is observed at ~ 514 $cm^{-1,}$ generally observed for the bulk lithium ferrite samples. The observed result of Raman spectra provided the complementary response to the XRD response.

Table 5-3*. Raman deconvoluted peak profiles of all the LDFO films.*

Modes	**160 nm**		**200 nm**		**240 nm**		**300 nm**	
	Raman shift	**FWHM**	**Raman shift**	**FWHM**	**Raman shift**	**FWHM**	**Raman shift**	**FWHM**
1	353.9	17.67	353.5	12.63	352.3	18.63	356.1	15.37
2	376.9	11.79	376.1	13.55	376.2	13.69	378.0	12.83
3	396.8	8.82	398.3	9.23	397.7	10.54	397.1	6.42
4	487.7	27.53	487.3	26.94	486.7	29.05	489.2	18.19
5	-	-	-	-	-	-	514.5	13.46
6	605.2	30.00	605.5	31.71	604.6	30.26	605.3	16.90
7	651.7	39.60	651.8	38.09	650.9	39.62	659.6	29.50
8	707.4	57.71	707.4	57.46	706.7	58.07	710.0	45.04

5.3.3 XPS analysis

Figure 5-7 and **Figure 5-8** show the high-resolution XPS spectra of all the constituent elements of 240 nm film of *LFO* and *LDFO*, respectively, which gives better clarity regarding the presence of the valance state of the present elements. For *Li 1s*, the prominent peak is observed at ~ 55 eV, further deconvoluted to two different peaks, 49.5 and 50.5. eV.

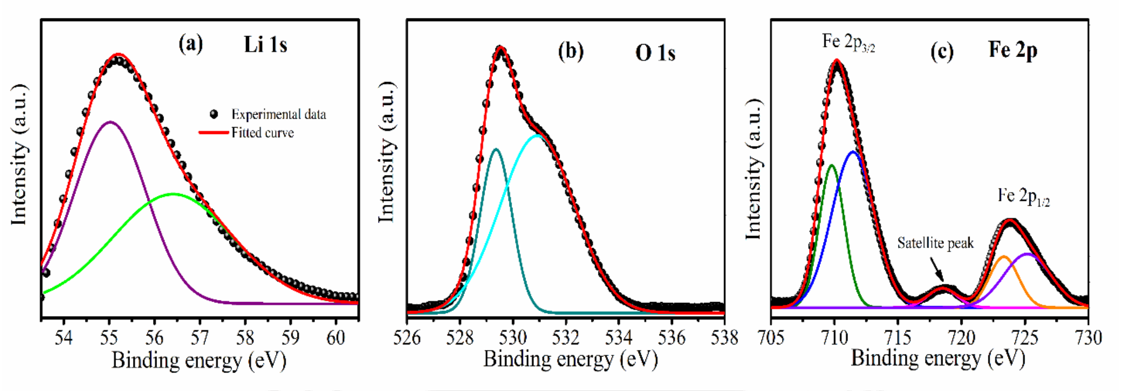

Figure 5-7. *High-resolution XPS spectra of 240 nm LFO film (a) Li 1s, (b) O 1s, (c) Fe 2p*

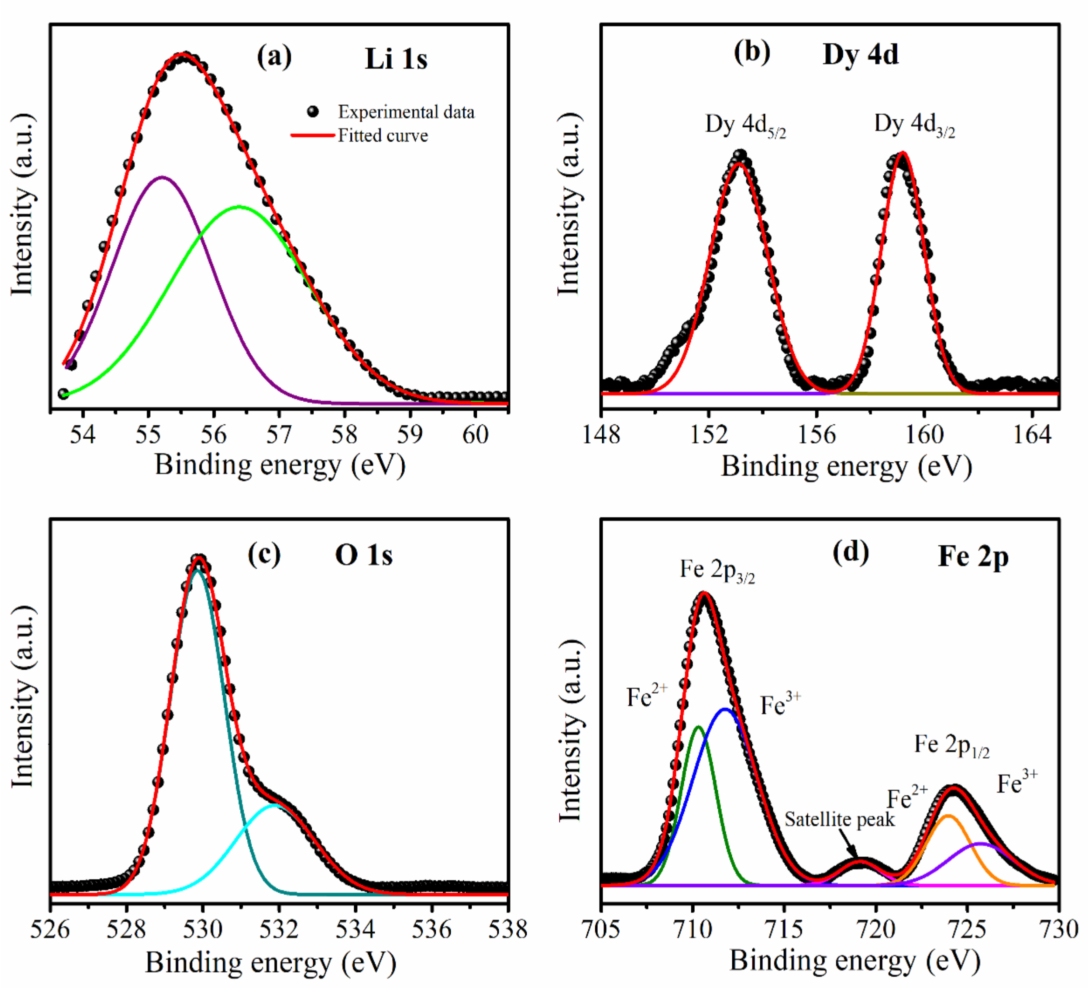

Figure 5-8. *XPS spectra of 240 nm LDFO film having different constituent elements (a) Li, (b) Dy, (c) O, (d) Fe.*

A broad peak is observed for *O 1s* spectra at 529 eV and further deconvoluted to 529.3 (O_i) and 531 eV (O_{ii}), associated with metal – oxygen bond (octahedral and tetrahedral bonded cations) and dangling bond, respectively. The dangling bond is mainly associated with oxygen vacancy on the films that can be roughly estimated from the area ratio (O_{ii} / O_i) of the observed peak. The observed area ratio for LFO and LDFO film is 1.5, 0.4, respectively. LDFO film showed lower oxygen vacancy as compared to the LFO films. Further, two measure peaks are obtained for *Fe 2p* spectra at ~710 and 723 eV, which correspond to $Fe2p_{3/2}$ and $Fe2p_{1/2}$, arising due to the spin-orbit coupling among *2p* and *3d* orbitals.[241] The significant peaks are further deconvoluted to 709, 711, and 723, 725 eV, where the higher binding energy deconvoluted peaks correspond to the Fe^{3+} ions and the lower ones with Fe^{2+}. A similar response is observed for Li, O, and Fe in the case of *LDFO* film (240 nm). **Figure 5-8(b)** shows the XPS spectra of *Dy 4d* core level of *LDFO* film with doublet components at 153 and 159 eV, which is attributed to the electrostatic interaction of *4f* electrons and *4d* holes of *Dy* along with the spin-orbit splitting ($4d_{5/2}$ and $4d_{3/2}$). These two states have a difference of 6eV.[242],[243]

5.3.4 Microstructural

The FESEM images recorded for *LFO* and *LDFO* films with different thicknesses are shown in **Figure 5-9** and **Figure 5-10,** respectively. The morphology of the thin films mainly depends on the deposition condition, like chamber pressure and substrate temperature. The grain size is calculated by image-J software, and the histogram is plotted in order to get precise information regarding the average grain size. The average grain size for *LFO* films ranges from 11 nm to 16 nm and is found to be increased slightly with the increase in thickness. Similarly, the average grain size for *LDFO* films is found to be 24 nm – 28 nm. The average grain size is increased from 24 nm for 160 nm to 28 nm for 300 nm film. Forming uniform and compact grains requires optimized conditions like oxygen partial pressure and substrate temperature.

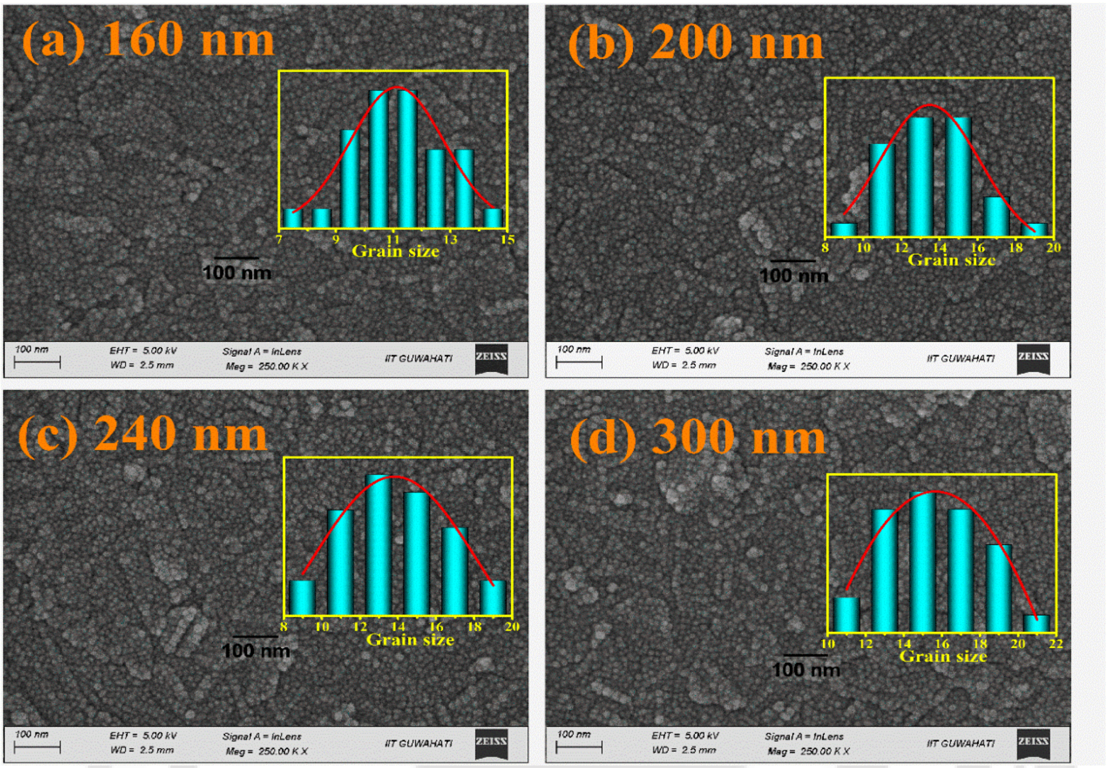

__Figure 5-9__. FESEM surface micrograph and the histogram of grain size for all the LFO films.

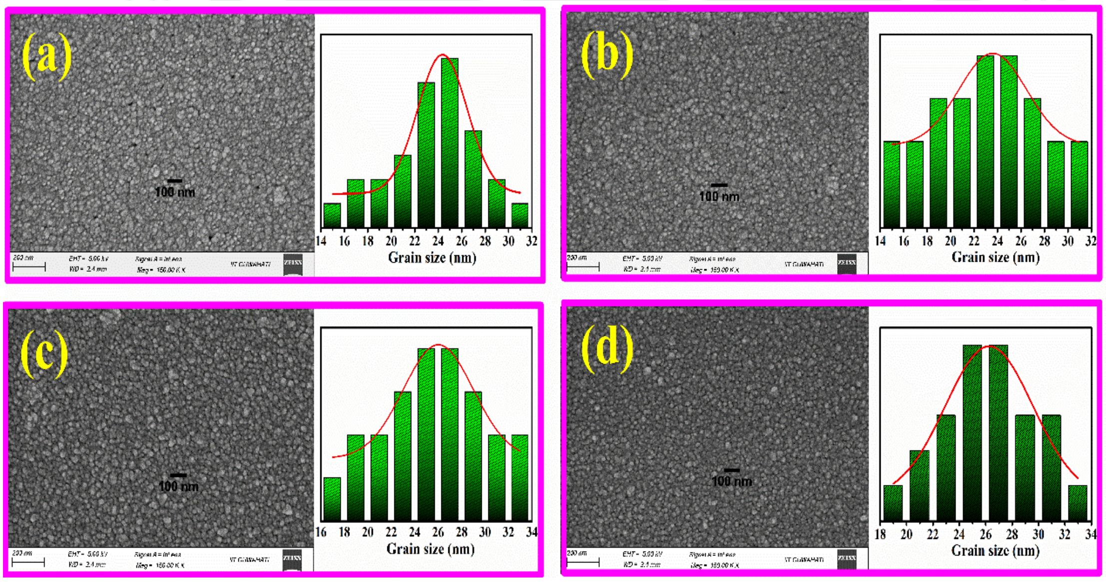

__Figure 5-10__. FESEM surface micrograph with the histogram of LDFO films (a) 160 nm, (b) 200 nm, (c) 240 nm, (a) 300 nm.

At high temperatures such as 700 °C, the atoms get sufficient thermal energy to accommodate and acquire a particular place in the lattice crystal of the substrate. All the films exhibited uniform microstructure with spherical shapes. As the film thickness increases, the layer's density increases, so the film's porosity decreases, indicating the film's dense and compactness with the increase in film thickness.

The AFM 2D and 3D images of *LFO* and *LDFO* films with different thickness over a scan area of 5µm × 5µm is shown in **Figure 5-11** and **Figure 5-12,** respectively. The root-mean-square (RMS) roughness is also analyzed by Gwyddion software. As the thickness increases, the grains are clearly visible with uniform structure. The obtained RMS roughness for all the *LFO* and *LDFO* films is in the range of 5 nm to 12 nm, increasing with the increase in thickness. The increase in roughness can be due to the formation of abrupt large particles with the increase in thickness.

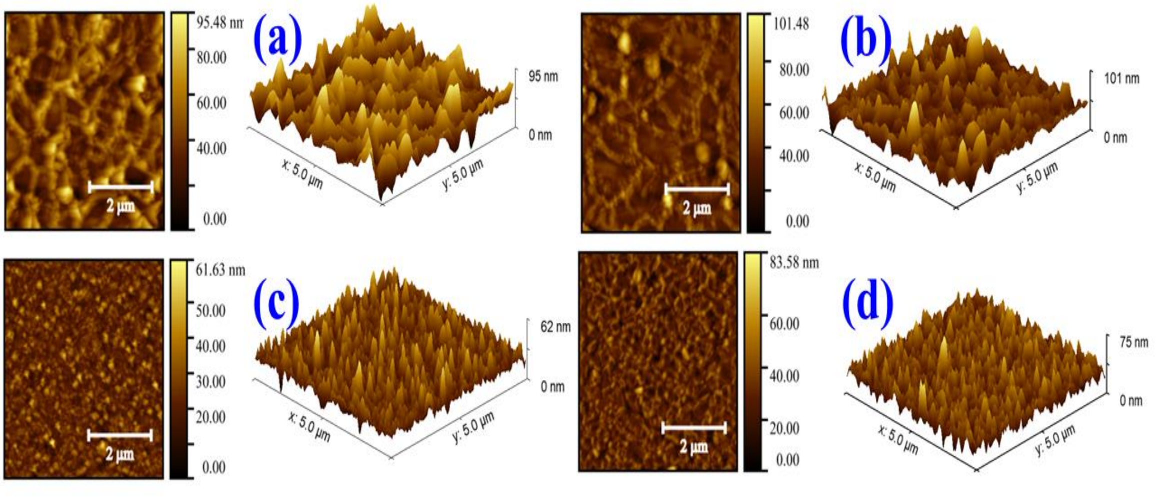

Figure 5-11*. The 2D and 3D representation of AFM images of all the LFO films (a) 160 nm, (b) 200 nm, (c) 240 nm, (d) 300 nm.*

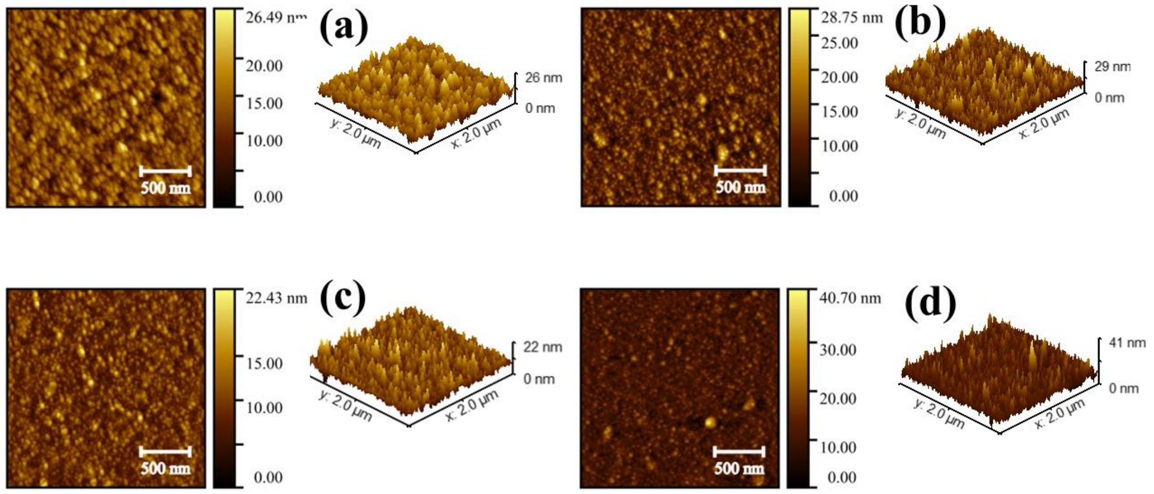

Figure 5-12*. AFM images with 2D and 3D view of LDFO films (a) 160 nm, (b) 200 nm, (c) 240 nm, (a) 300 nm.*

5.3.5 Magnetic study

To analyze the influence of thickness on the magnetic response, room temperature in-plane (IP) and out-of-plane (OP) hysteresis loop is measured up to a maximum field of 1 T. **Figure 5-13,** and **Figure 5-14** show the M-H loop of all the *LFO* and *LDFO* films, respectively. All the samples exhibit a hysteresis loop that indicates the existence of the ferrimagnetic order of the thin films. As the substrate exhibits assertive diamagnetic behavior, it cannot be ignored for magnetic measurements. So, we have subtracted the substrate contribution from the films. In the case of *LFO*, magnetization mainly arises due to the distribution of Fe ions in the tetrahedral and octahedral sites. The net magnetization is the difference between the total magnetization at B and A sublattices. The saturation magnetization is found to be decreased with an increase in film thickness. The obtained values of the saturation magnetization for IP and OP are 178, 142, 118, 100 emu/cm^3 and 122, 102, 96, and 87 emu/cm3 for 160, 200, 240, and 300 nm, respectively. A similar type of response is reported in the literature.[244] In *LDFO*, magnetization arises due to *Fe* and *Dy* ions at the octahedral and Fe at the tetrahedral position. The net magnetization is a result of exchange interaction that involves several contributions like $Fe^{3+} – Fe^{3+}$ ($3d – 3d$), Dy^{3+}–Dy^{3+} ($4f – 4f$), and $Fe^{3+} – RE^{3+}$ ($3d – 4f$) interactions. The magnetization of both IP and OP configuration decreased, whereas the increase in film thickness enhanced coercivity. The maximum in-plane magnetization of 250 emu/cc is observed for 160 nm film (*LDFO*), reduced to 125 emu/cc for 300 nm film.

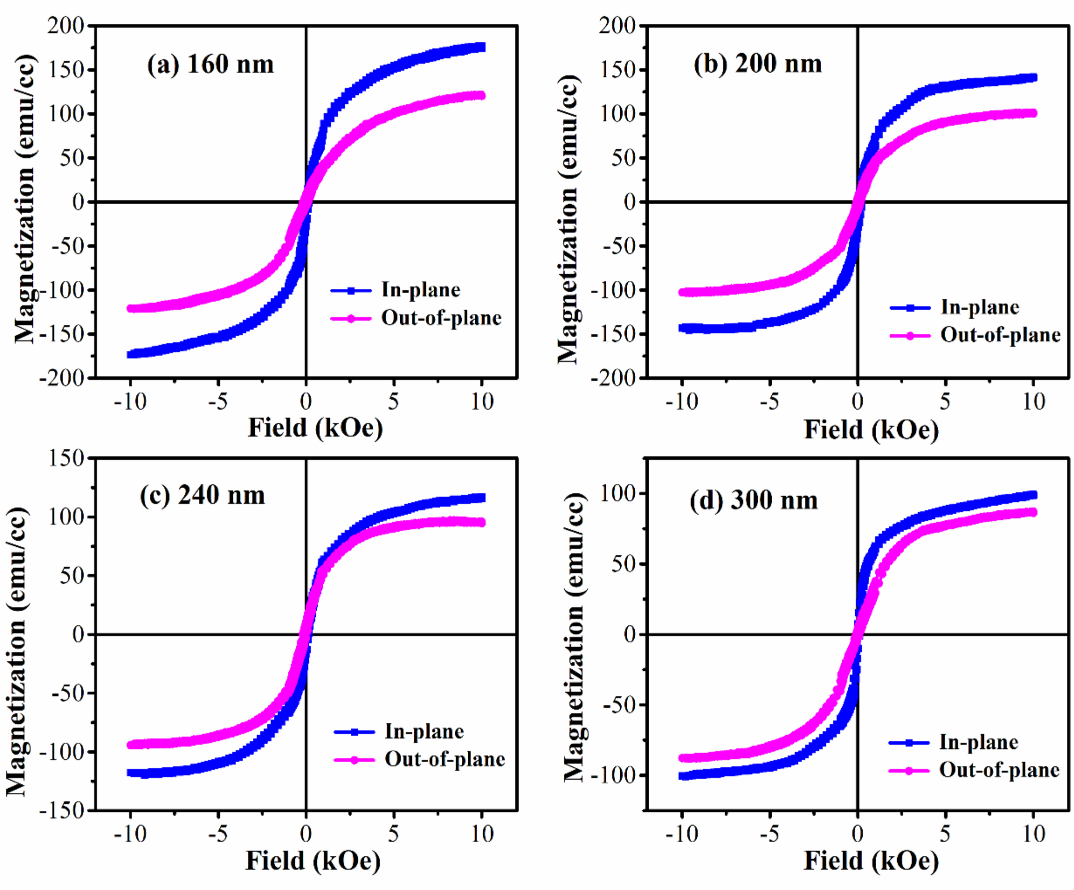

Figure 5-13*. Hysteresis loop of all the LFO films measured at 300 K.*

Various factors influence the magnetization of thin films, such as film orientation, structural transition, and cationic redistribution. It can be excluded the possibility of cation redistribution among the A and B sites as no change is observed in the chemical composition as observed from the XRD results. Another crucial factor in tuning the magnetic response is interface strain that arises due to lattice mismatch between film and substrate. Generally, the in-plane compressive strain enhances the magnetization, while the tensile strain decreases the magnetization. Further, to understand deeply, we considered the in-plane magnetoelastic energy density that can be expressed as [245]

$$E = -\frac{1}{2}\mu_0 H_{eff} M_s cos^2\theta = \frac{3}{2}\lambda_s \sigma cos^2\theta \qquad 5.1$$

where σ, θ, λ_s, H_{eff}, are stress, the angle between stress and magnetization (zero for IP), saturation magneto restriction, and effective magnetic anisotropy induced by strain, respectively. Since *LFO* belongs to negative magnetostrictive material (-27.8 ppm), the compressive strain will enhance the magnetization by changing the effective magnetic anisotropy. The compressive strain helps to align the spin along the film plane. A similar response is observed by Zang et al. [133] for *LFO* and Monsalve et al. [246] for $ZnFe_2O_4$.

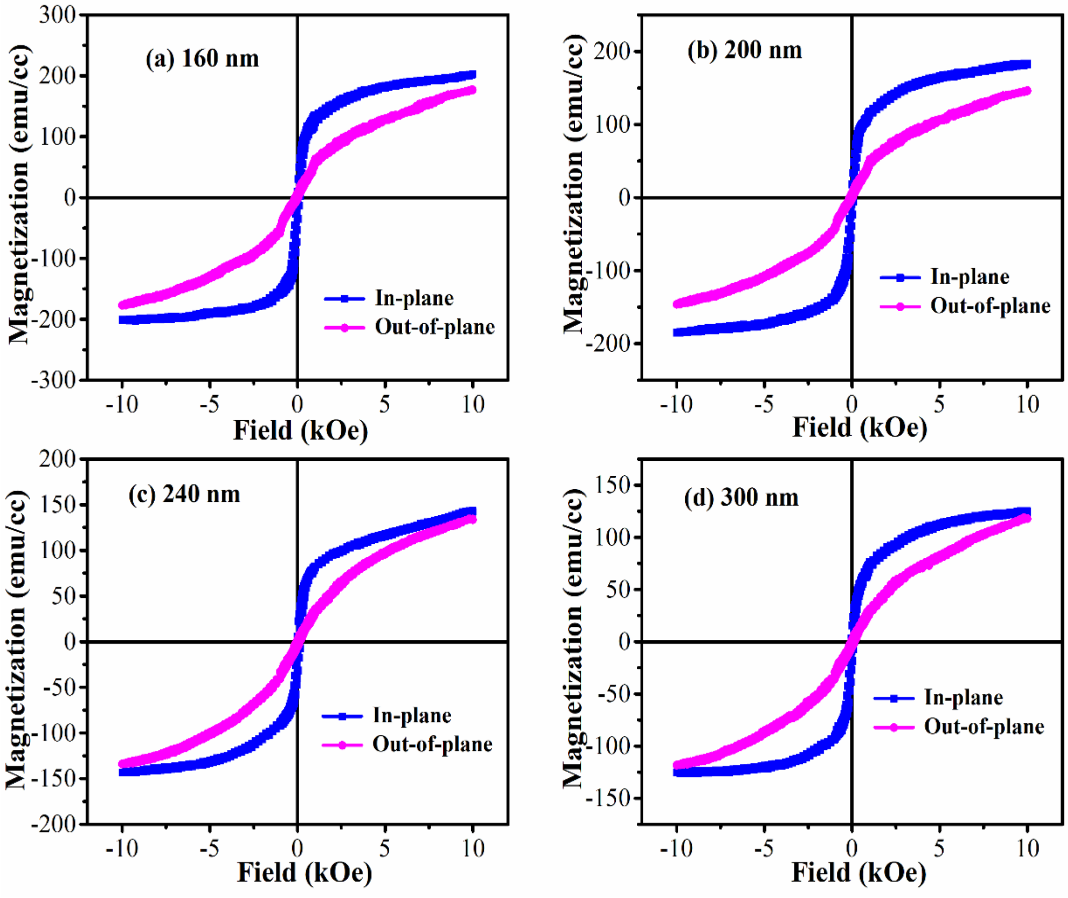

Figure 5-14. *The room temperature hysteresis loop of all the LDFO films in IP and OP configuration.*

Coercivity is considered an extrinsic property of thin films that depends on various factors such as dislocation, grain size, grain boundaries, and inhomogeneities. The coercivity is observed to be increased with film thickness (75, 85, 120, 140 Oe, for 160, 200, 240, and 300 nm in IP orientation) for *LFO* films. For *LDFO* films, the IP coercivity for 160,200, 240, and 300 nm are 85, 95, 110, and 150 Oe, respectively. The dislocations may play a part in pining centers and trap domain wall motion. Apart from that, the enhancement in coercivity can also be attributed to the increase in grain size with thickness. The obtained films with higher magnetization and compact microstructure films with comparatively higher thicknesses than previously reported studies.[133]

5.3.6 Dielectric response

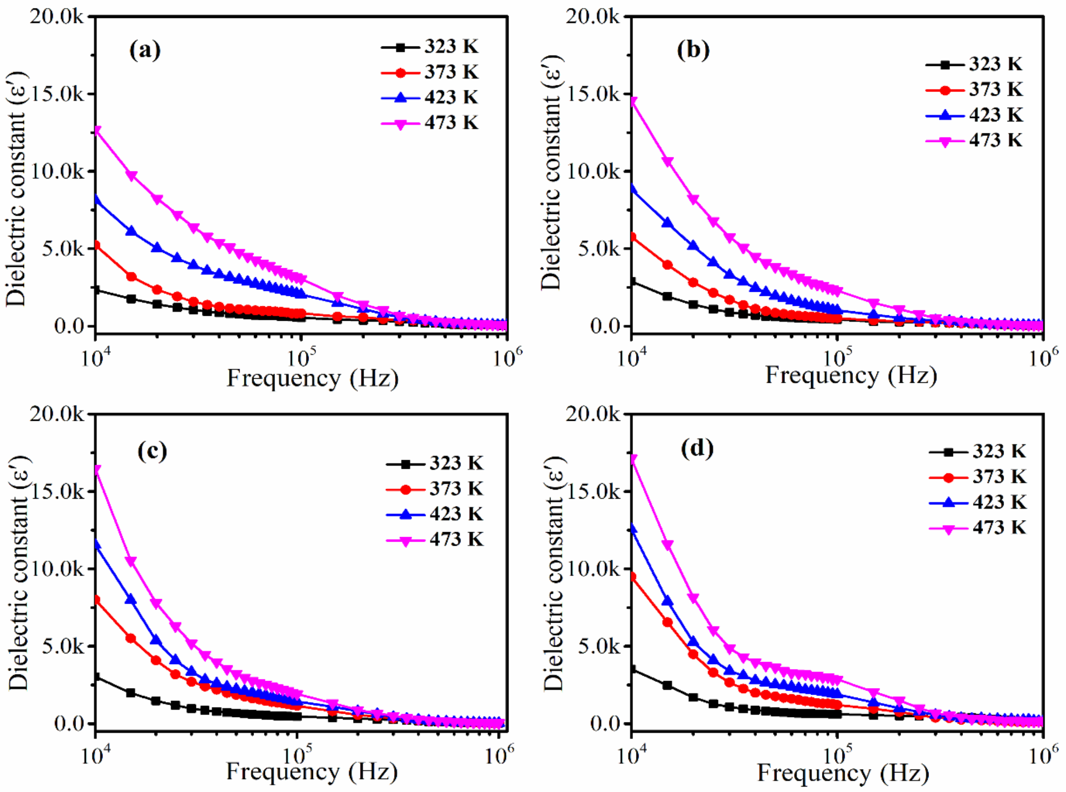

Figure 5-15. *Variation of the dielectric constant of LFO films at different temperatures (a) 160 nm, (b) 200 nm, (c) 240 nm, (d) 300 nm.*

The dielectric response of *LFO* and *LDFO* films with different thicknesses is measured in the frequency range of 10^4 Hz to 10^6 Hz at different temperatures (300K – 473 K). **Figure 5-15** and **Figure 5-16** show the dielectric spectra of all the thin films at different temperatures for *LFO* and *LDFO*, respectively. The dielectric constant (ε') decreased sharply up to 10^5 Hz and then became constant with an increase in frequency. A similar response is observed for all the films. Basically, the dielectric response of the films depends on various extrinsic and intrinsic factors such as grain growth, film orientation, porosity, etc. In the case of thin films, grain boundaries play a dominating role because of the reduced size of grains. The grain boundaries and grains are larger in numbers in thin films than in bulk.[247]

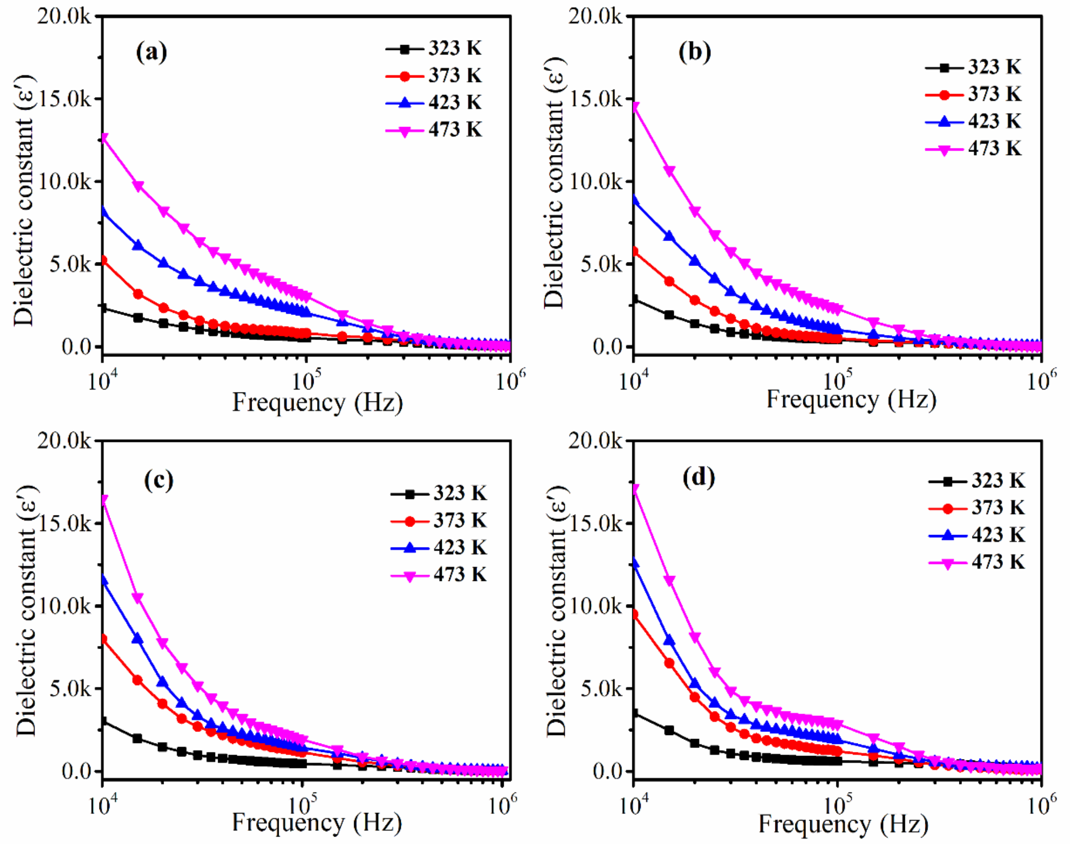

Figure 5-16. *Variation of the dielectric constant of LDFO films at different temperatures (a) 160 nm, (b) 200 nm, (c) 240 nm, (d) 300 nm.*

Various researchers have proposed several models to understand the dispersion in dielectric constants such as electrode barrier effect, inhomogeneity, and electron hopping conduction mechanism due to Debye-type relaxation. The Maxwell-Wagner model can well understand this in accordance with Koop's phenomenological theory.[248][249] The variation in the ε' can be attributed to the co-existence of two different valance states of *Fe* (2+ and 3+). The electron hopping between Fe^{2+} and Fe^{3+} gives rise to polarization. After a certain frequency, the hopping of electrons between Fe^{2+} and Fe^{3+} can not align along the applied electric field. So ε' become stable above 10^5 Hz.

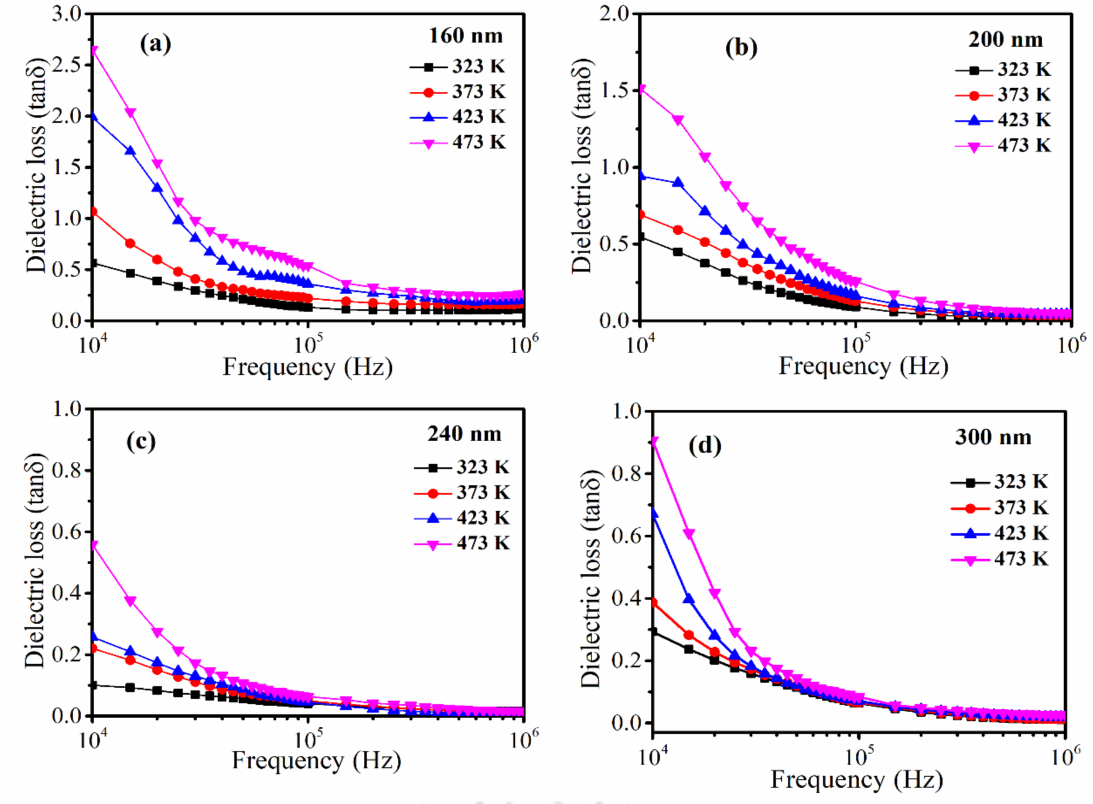

Figure 5-17. *Variation of dielectric loss at different temperatures of LFO films at different temperatures (a) 160 nm, (b) 200 nm, (c) 240 nm, (d) 300 nm.*

Further, ε' is increased with an increase in thickness and temperature. The ε′ increased to 1120 for 300 nm from 125 for 160 nm at 10kHz for *LFO* films. Similarly, for *LDFO* films, ε′ is enhanced from 320 for 160 nm to 1430 for 300 nm at 300 K with the increase in film thickness. This can be ascribed to dense microstructure and uniform grain size with an increase in the thickness of the films. Further, the giant dielectric response with temperature can be due to the thermally activated dipole orientations. At high temperatures, the dipoles aligned faster in the applied field direction.

The frequency variation dielectric loss (*tanδ*) at different temperatures for *LFO* and *LDFO* are shown in **Figure 5-17** and **Figure 5-18**, respectively. It also showed a similar behavior as ε' with the increase in frequency, whereas it decreased with the increase in thickness up to 240 nm. The values of tanδ observed at 10kHz are 0.42, 0.36, 0.01, 0.1 for 160, 200, 240, and 300 nm, respectively, for *LFO* films. The values of tanδ for *LDFO* films are 0.42, 0.25, 0.05, and 0.59 for 160, 200, 240, and 300 nm films at 10 kHz, respectively. The decrement in the tanδ can be attributed to the compactness of the thin films with the increase in thickness. The abrupt enhancement in tanδ for 300 nm film may be due to the rise of lattice strain and the formation of particulates.

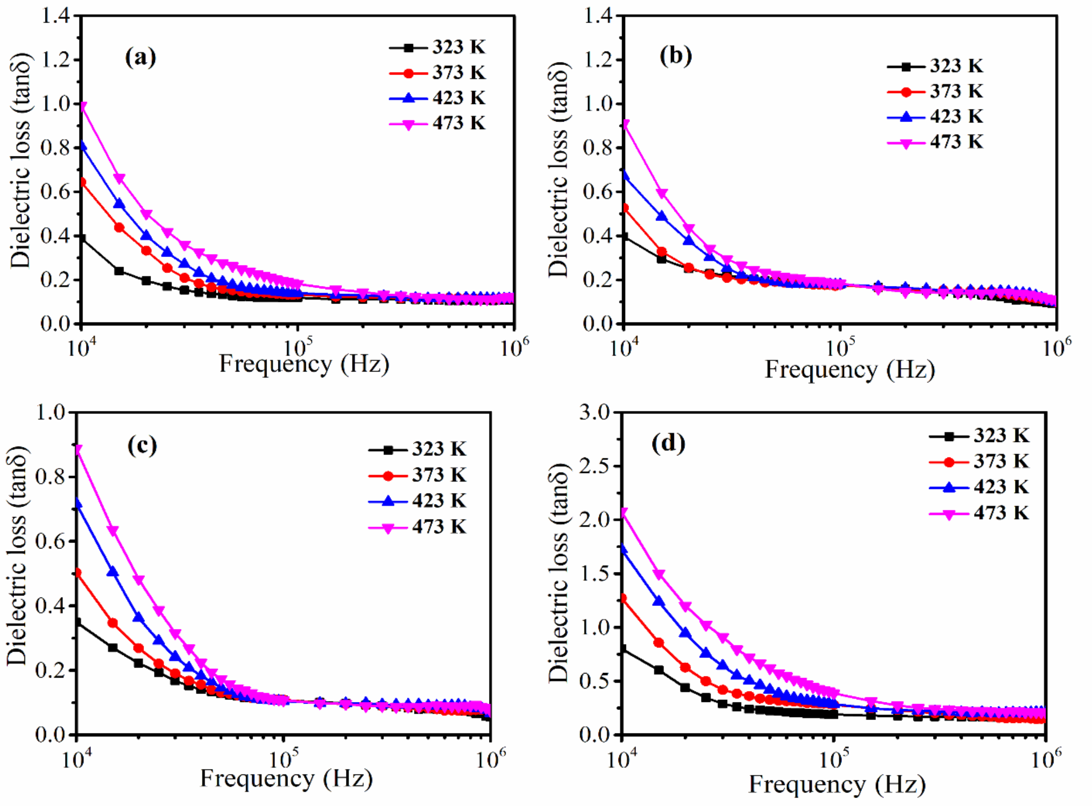

Figure 5-18*. Variation of dielectric loss at different temperatures of LDFO films at different temperatures (a) 160 nm, (b) 200 nm, (c) 240 nm, (d) 300 nm.*

5.3.7 Impedance spectroscopy

In order to have a deep understanding of the contribution of grains, grain boundaries, and electrode interface, we have studied the impedance spectra at different temperatures in the frequency range of 10^4 Hz to 10^6 Hz for all the samples. Impedance spectroscopy is a powerful tool to characterize the electrical properties of materials and their interface, which can better estimate electrically active regions.[250] **Figure 5-19(a,b,c)** shows the Nyquist plot (Z' vs. Z") of the *LFO* films with thicknesses 160, 200, and 240 nm. The decrease in the diameter of a semicircle with the increase in temperature shows the NCTR behavior (negative temperature coefficient of resistance), that is, the decrease in impedance with an increase in temperature.[251]

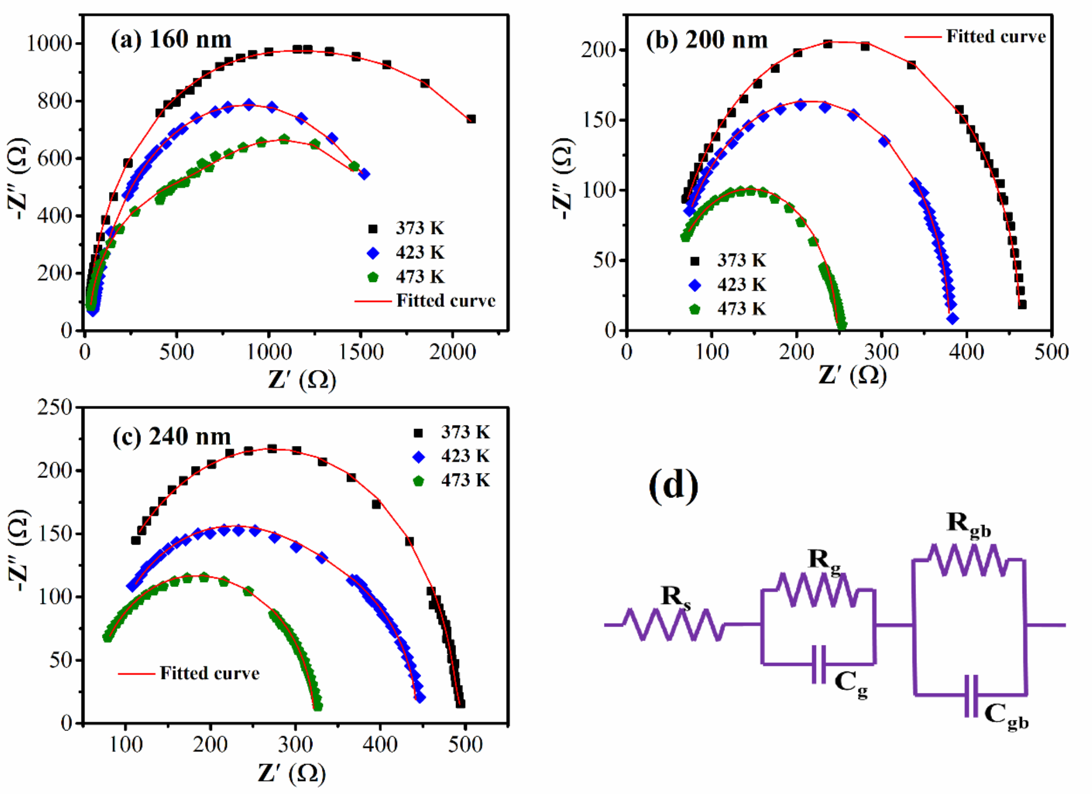

***Figure 5-19**. Nyquist plot of LFO films (a) 160 nm, (b) 200 nm, (c) 240 nm, (d) Equivalent circuit diagram.*

The impedance spectra are fitted with equivalent circuit model R(CR)(CR) by employing least-square fits using ZSimpWin software. The initial R denotes the series

***Table 5-4**. Extracted parameters from the fitted equivalent circuit for LFO films (473 K)*

Parameters	160 nm	200 nm	240 nm	300 nm
R_s (Ω)	23	44	52	50
C_g (F)	2.051E-9	2.032E-9	2.148E-9	2.128E-9
R_g (Ω)	199	209	264	264
C_{gb} (F)	1.819E-6	3.184E-7	6.167E-8	6.367E-8
R_{gb} (Ω)	1738	1634	1521	1123

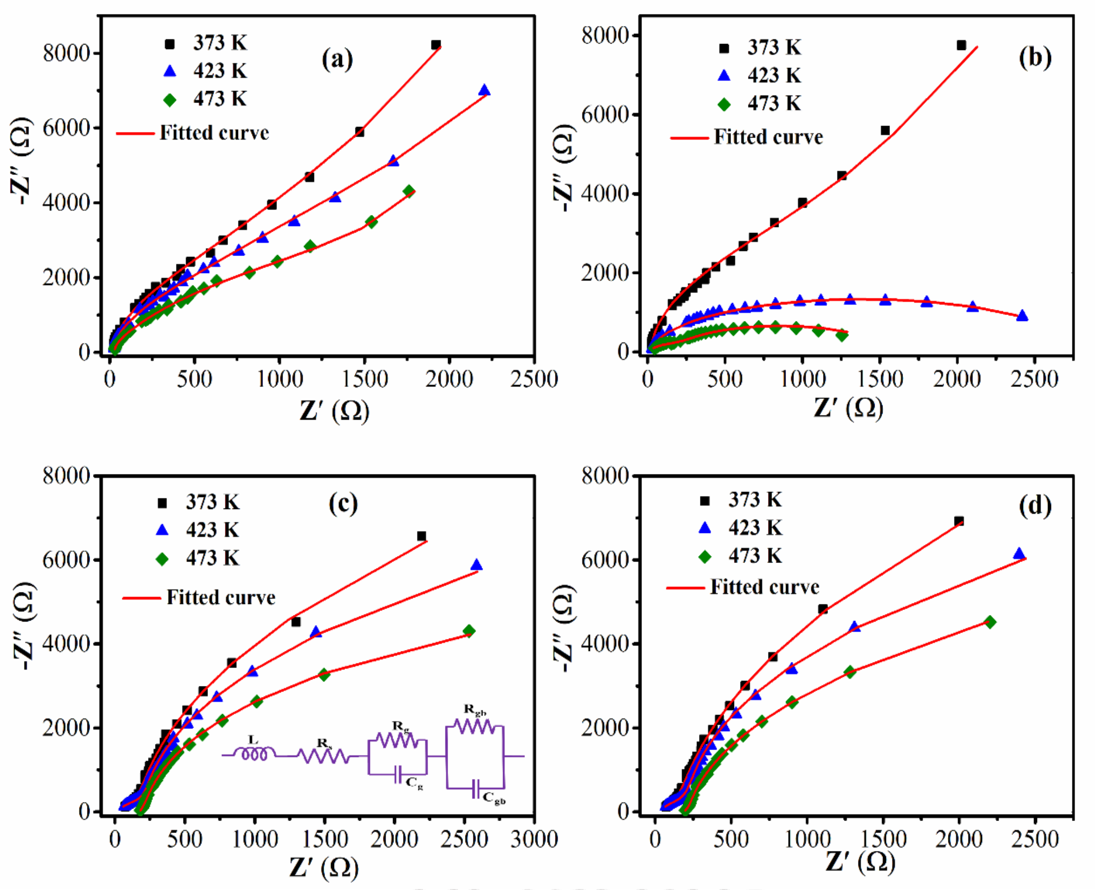

***Figure 5-20**. Nyquist plot of all the samples of LDFO films at different temperatures (a) 160 nm, (b) 200 nm, (c) 240 nm, (a) 300 nm.*

resistance required to overcome the mismatch between the Fermi level of deposited thin film and the electrode [252], and the other R and C denote the resistance and capacitance due to grains and grain boundaries. The values of R_s, R_g, C_g, R_{gb}, C_{gb} of the fitted circuit for 473 K are enlisted in **Table 5-4**. The equivalent circuit diagram is shown in **Figure 5-19(d)**.

The grain boundary resistance is decreased, whereas the grain resistance increases with the thin film's thickness. **Figure 5-20** shows the imaginary complex impedance spectra as a function of real impedance spectra (Nyquist plot) of all *LDFO* films measured at different temperatures. The impedance spectra are fitted with an equivalent circuit model of $LR_s(R_gC_g)(R_{gb}C_{gb})$. Here, L denotes inductance due to measuring leads, R_s – resistance due to the mismatch between the fermi level of deposited thin film and the electrode. All the extracted values of circuit components fitted for 473 K of *LDFO* film are enlisted in **Table 5-5**. With the rise in film thickness, the grain resistance and inductance are increased, whereas the resistance due to grain boundaries is degraded.

Table 5-5*. Extracted parameters of equivalent circuits for all the LDFO films measured at 473 K.*

	160 nm	**200 nm**	**240 nm**	**300 nm**
L (H)	1.539E-6	2.132E-6	3.912E-6	4.193E-6
R_s (Ω)	16	23	26	32
C_g (F)	3.944E-9	2.57E-9	2.877E-9	1.57E-9
R_g (Ω)	201	509	1967	8030
C_{gb} (F)	8.349E-7	2.352E-7	8.932E-6	3.462E-6
R_{gb} (Ω)	6830	2670	1121	723

5.3.8 Electrical conduction mechanism

Figure 5-21 shows the temperature variation conductivity (σ) of *LFO* and *LDFO* films with different thicknesses. The σ decreased with the film thickness up to 240 nm and enhanced for 300 nm film. This variation can be related to the variation in $tan\delta$. The Arrhenius equation can explain the dependence of σ on temperature. The activation energy is calculated using **Equation 3.2**. At high temperatures, the increase of σ corresponds to electron hopping conduction arising due to regular band-type conduction in the extended state. As depicted in **Figure 5-21**, the electrical conductivity is varied with temperatures for *LFO* thin films having different thicknesses of 160, 200, 240, and 300 nm. The activation energy is calculated from the slope of the fitted curve. And found to be 0.092, 0.087, 0.062, and 0.066 eV for 160, 200, 240, and 300 nm *LFO* films, respectively.

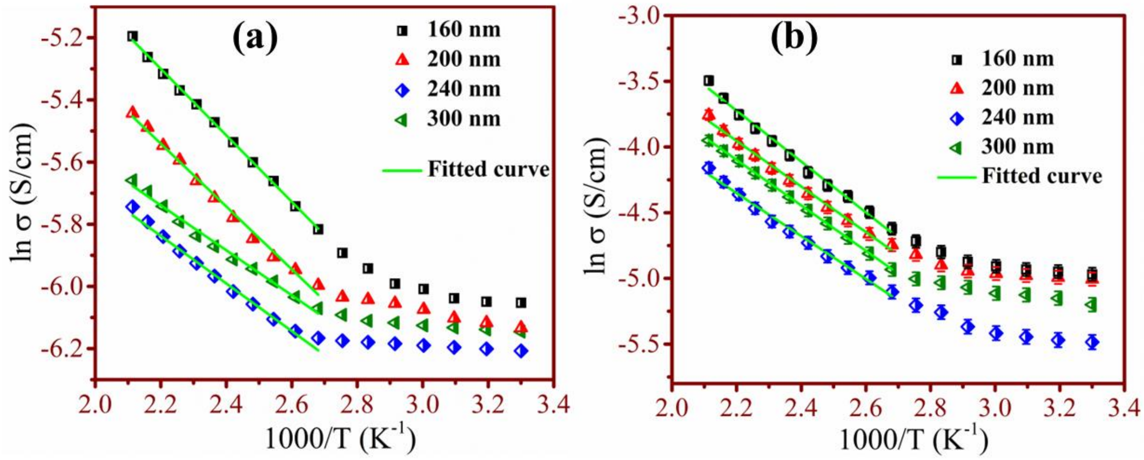

Figure 5-21. *Variation of conductivity as a function of temperature for all the films (a) LFO, (b) LDFO.*

The obtained values of E_A for *LDFO* films are 0.162, 0.152, 0.142, and 0.150 eV for 160, 200, 240, and 300 nm films, respectively. With the substitution of *Dy* on *LFO*, the σ enhanced. *Dy* preferably occupies the octahedral site due to the larger ionic radii that led to converting Fe^{3+} to Fe^{2+} and hence improved the conductivity by enhancing the hoping mechanism of single spin state t_{2g} electron at the octahedral site. Above that, with the increase in film thickness, σ decreases up to 240 nm.

It is observed that an increase in σ with temperature is the typical behavior of dielectrics. In ceramics, the trapping center of electrons, impurities, and density of defects is relatively higher. So, hopping is the primary conduction mechanism in this case. Mainly two types of hopping mechanisms take place: Variable range hopping conduction (VRH) and nearest neighbor hopping conduction (NNH).[253] In the case of the NNH mechanism, the hopping occurs between the nearest neighbor empty sites, and in such a conduction process, the E_A value should be constant in a particular range as reported. However, In this case, E_A depends on temperature, as depicted in **Figure 5-21**. The variable nature of E_A indicates the existence of the VRH mechanism.

Investigating the hopping phenomena from the perspective of resistivity can provide a better understanding of the conduction mechanism. The conclusion derived from the conductivity or resistivity plot is equally applicable. In the case of the VRH mechanism, the charge carriers hop between the energy levels nearer to the Fermi level without depending on their spatial distribution[254]. Generally, two kinds of VRH phenomena occurred, such as Mott's 3D VRH and Efros - Shklovskii (ES-VRH). The equation explaining the model is as follows:

$$\rho = \rho_0\, exp\left(\frac{T_0}{T}\right)^p \qquad 5.2$$

where ρ_0 and T_0 are the pre-exponential factors and characteristic temperature, respectively, the value of p is 1/4 or 1/2 depending on the density of states at the Fermi level. Considering Coulombic interaction among the final and initial states with p = 1/2 gives the ES-VRH mechanism. p=1/4 without considering Coulomb interaction indicates Mott's VRH mechanism that works on the assumption that VRH remains constant near the Fermi level in the disorder system. Identifying the dominant conduction mechanism depends on fitting the appropriate model with the experimental data is crucial. The best fit of the value of p indicates the dominant conduction mechanism in the provided temperature range. The linear plot between ln (ρ_{ac}) vs. $T^{-1/4}$ and ln[ln(ρ_{ac}/ρ_0) vs. ln(T) is shown in **Figure 5-22** and **Figure 5-23** for LFO films that reconfirms the presence of Mott's 3D VRH mechanism.

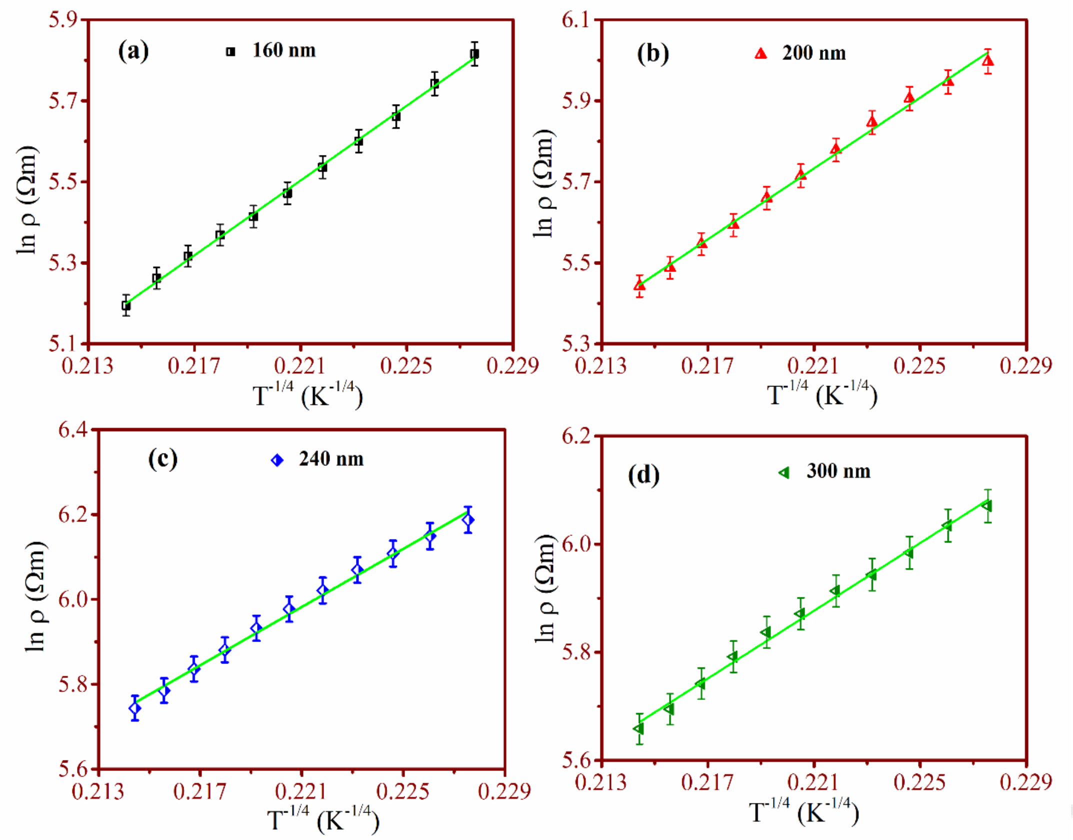

***Figure 5-22**. Variation of ln (ρ_{ac}) vs. $T^{-1/4}$ for all the LFO films.*

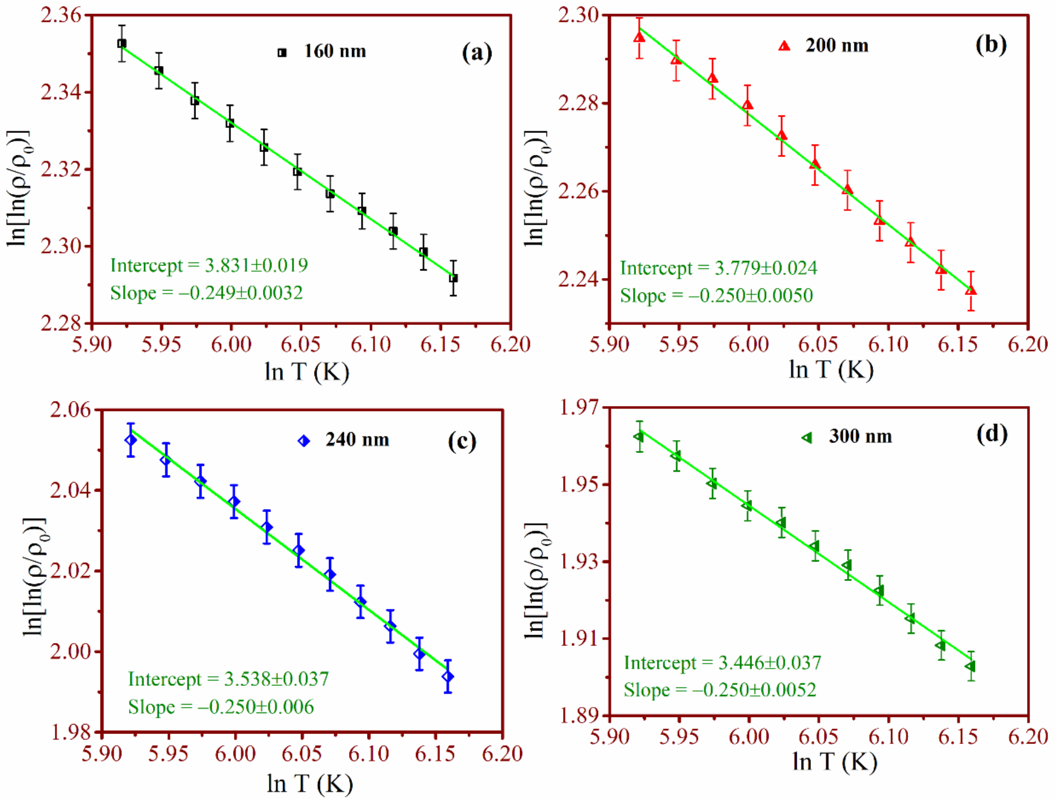

***Figure 5-23**. Variation ln[ln(ρ_{ac}/ρ_0)] as a function of ln(T) for all the LFO films.*

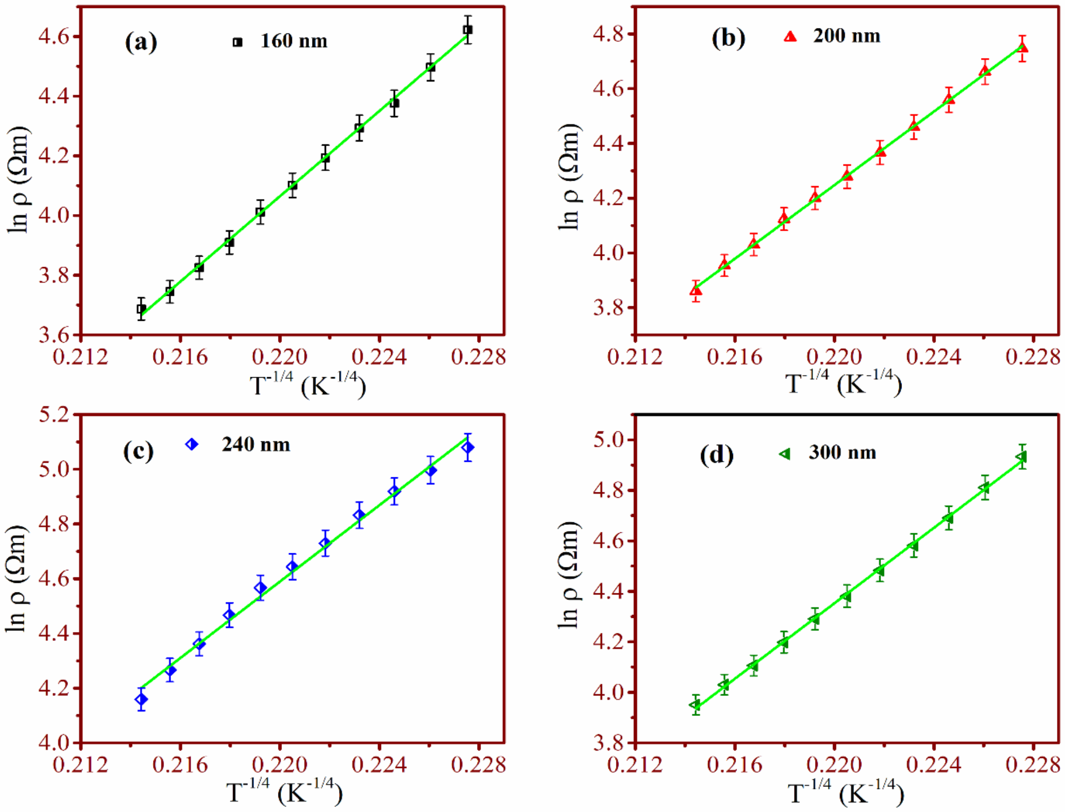

Figure 5-24. *Variation of ln (ρ_{ac}) vs. $T^{-1/4}$ for all the LDFO films.*

The slopes obtained from the linear plots are ~ -0.25. Similarly, the linear plot between ln (ρ_{ac}) vs. $T^{-1/4}$ and ln[ln(ρ_{ac}/ρ_0) vs. ln(T) for LDFO films are shown in **Figure 5-24** and **Figure 5-25**, respectively. Again, the density of the states of the films is calculated using the following:

$$N(E_f) = \frac{16\alpha^3}{k_B T_0} \qquad 5.3$$

Various literature is already available on where α is the inverse decay length of the localized wave function. For spinel FCC structure, the hopping length between ions at octahedral *B* and tetrahedral *A* site is given by $L_B = \frac{\sqrt{2}}{4}$ a, and $L_A = \frac{\sqrt{3}}{4}$ a, where a is the lattice constant. It is already reported that hopping between the B-B site is more favorable than A–A due to the smaller distance between ions. Again, hopping between A–B is very low in the normal condition.[255][252] So, L_B is chosen as a localized length where r = 1/α.

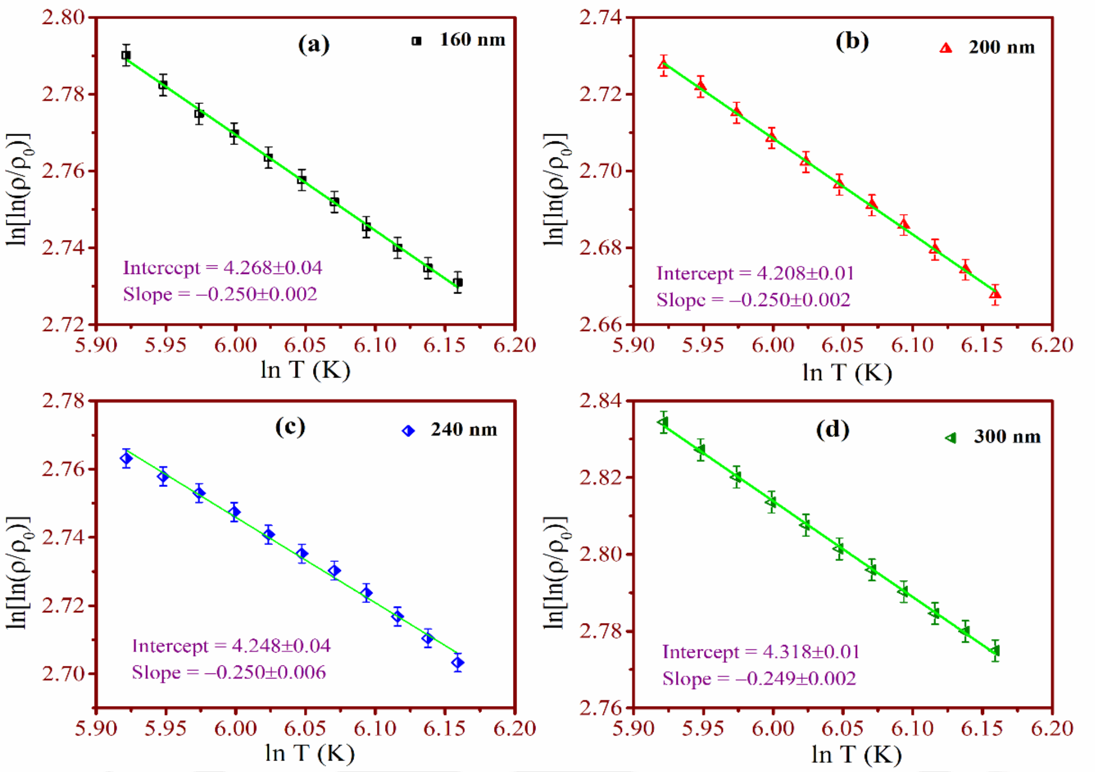

Figure 5-25. *Variation $ln[ln(\rho_{ac}/\rho_0)]$ as a function of ln(T) for all the LDFO films.*

The obtained values of density of states (DOS) for *LFO* films are 1.59 $\times10^{21}$, 1.98 $\times10^{21}$, 7.50 $\times10^{21}$, 5.22 $\times10^{21}$ eV^{-1} cm^{-3} for 160 nm, 200nm, and 240 nm, 300 nm, respectively. The deduced values of DOS for LDFO films are 1.76×10^{20}, 2.11×10^{20}, 2.69×10^{20}, and 2.32×10^{20} $eV^{-1}cm^{-3}$ for 160 nm, 200 nm, 240 nm, and 300 nm films, respectively. The highest DOS is observed for 240 nm thickness film, ascribed to the better packing density and crystallinity of the films with higher thickness. The other parameters such as hopping length (R_H) and hopping energy (W_H) are derived from VRH model using the provided equations.

$$R_H = 0.75\left[\frac{3}{2\pi\alpha N(E_f)k_BT}\right]^{\frac{1}{4}} \qquad 5.4$$

$$W_H = \frac{3}{4\pi R_H^3 N(E_f)} \qquad 5.5$$

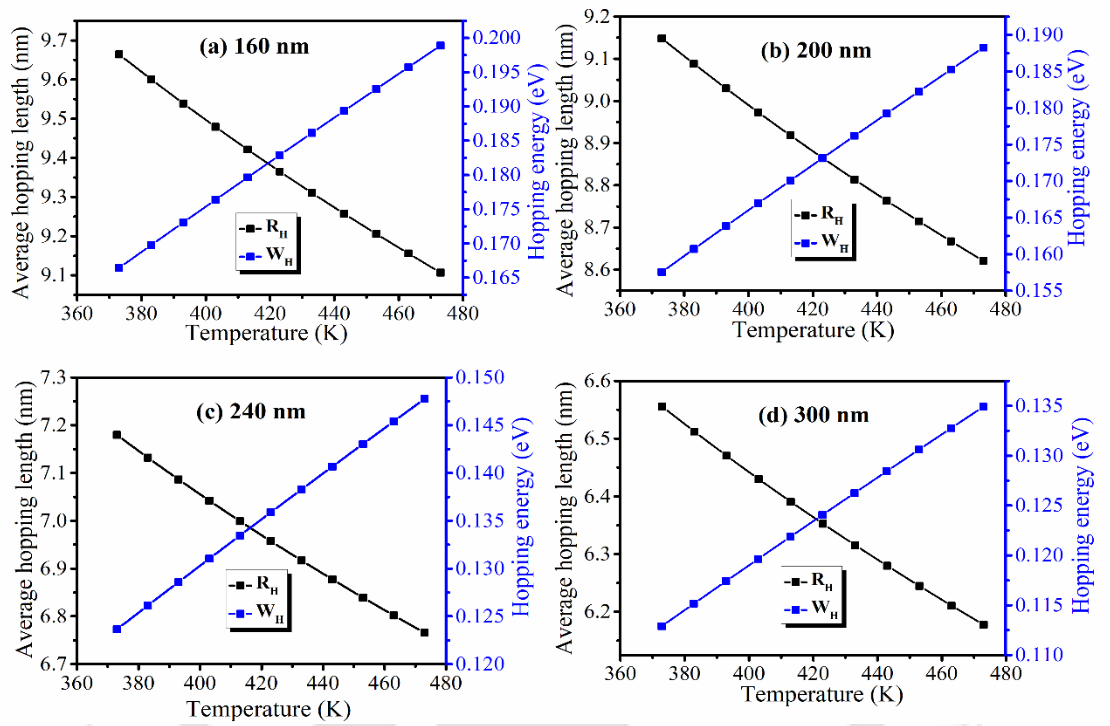

***Figure 5-26**. Variation of average hopping length and average hopping energy of all the LFO films.*

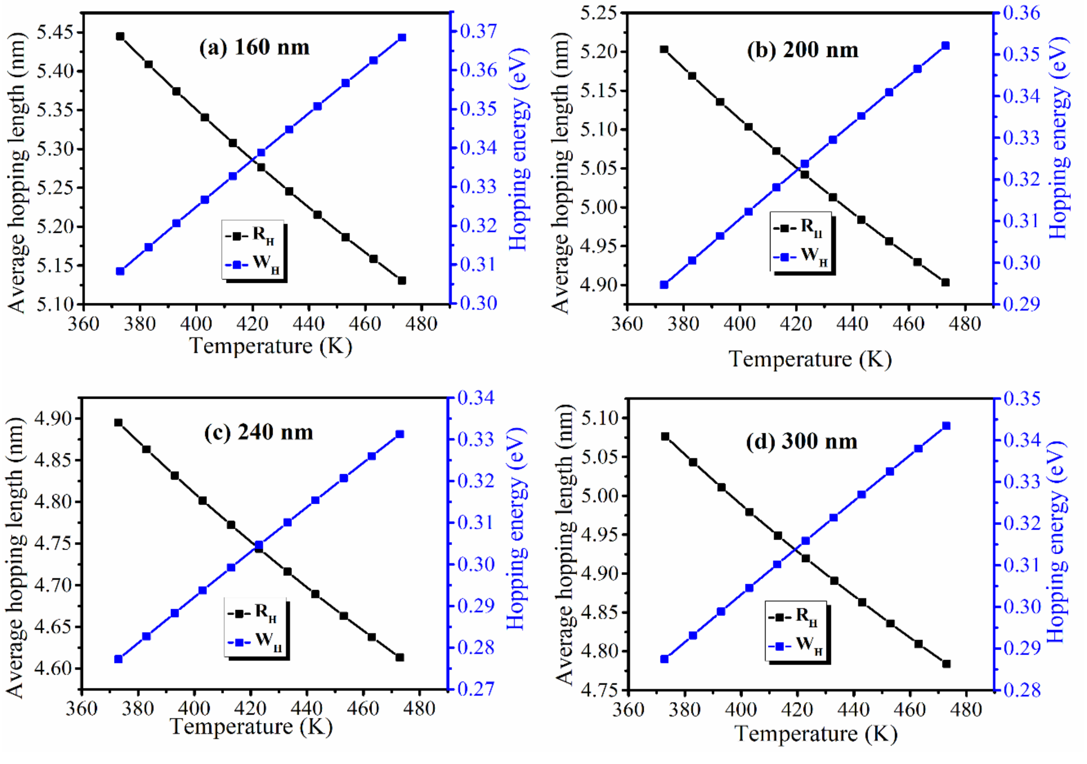

***Figure 5-27**. Variation of average hopping length and average hopping energy of all the LDFO films.*

The deduced values of R_H and W_H for *LFO* and *LDFO* films are depicted in **Figure 5-26** and **Figure 5-27**, respectively, as a function of temperature that obeys the condition for Mott's VRH, i.e., $W_H > k_BT$ and $\alpha R_H > 1$. The hopping length is decreased, whereas the Hopping energy increases with an increase in temperature, similar to barium titanate, Ni-Zn ferrite.[254][256] Above that, the R_H and W_H are decreased with the increase in film thickness.

5.4 Conclusions

The *LFO* and *LDFO* films are successfully deposited on Pt(111)/Ti/SiO_2/Si having a different thickness of 160 – 300 nm. The lattice constant is decreased, whereas the average grain size increased with the increase in thickness. The strain is found to be reduced with the film thickness, which is analyzed by employing the W-H plot. The uniform, compact grain growth is observed with the increase in thickness. The room temperature IP and OP magnetization decreased, whereas the coercivity enhanced with the film thickness. All the experimental parameters are correlated with each other, and film thickness (strain) played a significant role in tuning the physical properties of the films. The variation in the dielectric response is explained based on the electron hopping mechanism and the contribution of grain and grain boundaries. The contribution of grain and grain boundaries are investigated by employing an equivalent circuit model to the impedance spectra of different temperatures. Grains played a prominent role at higher thicknesses, whereas grain boundaries were at lower thicknesses. Apart from that, the involved conduction mechanism is interpreted by different models and observed to be suitably obeyed by Mott's VRH mechanism. This study concludes that controlling thickness effectively tunes the dielectric and magnetic properties to be used as magnetic oxide semiconductor.

Chapter 6 : Conclusions and future scope

This chapter contains the concluding remarks of the work carried out and discusses the possibility of the future scope of the work which can be carried out in this area.

6.1 Conclusions

A detailed study on the structural, microstructural, magnetic, dielectric, and electrical properties of LFO ceramics and Sr and Mg substituted LFO is carried out. A variation in the lattice parameters is observed with the substitution of Sr as well as Mg, as they possess different ionic radii as compared to Li and Fe. The average crystallite size and grain size are found to be decreased with the Sr concentration. All the substituted ceramics showed dense microstructure as compared to the pure LFO. The enhanced dielectric (ε_r = 5986 and tanδ = 1.17 @RT, 1 MHz) for x = 0.003) is observed for LSFO ceramics. Whereas in the case of LFMO ceramics, an excellent dielectric response (ε_r = 3034, tanδ = 0.001 at RT, 1 MHz) is observed for x = 0.005. The variations in the dielectric properties are explained based on the electron hopping mechanism and cationic distributions. AC conductivity enhanced with an increase in temperature as well as Mg^{2+} concentration due to the exchange of electrons among Fe^{2+} and Fe^{3+} ions. The highest saturation magnetization (M_S = 61 emu/g at RT and T_C = 883 K) for x = 0.007 is observed for LSFO ceramics. The LMFO with x = 0.007 exhibits the best permeability (μ_r = 29) and magnetic properties (M_s = 55 emu/g) at room temperature. The substitution of Sr enhanced both the dielectric as well as magnetic properties. The diffused transition exhibited a strong relaxor behavior. The variation in the magnetic behavior is explained by exchange interactions, cationic distribution, and Néel's two sub-lattice models. A combination of high dielectric constant, low loss tangent (order of 10^{-3}), high permeability, and magnetic properties of LMFO make x = 0.005 specimens a good candidate for microwave applications such as phase shifters and the circulator.

Looking into the demand for EMI-shielded material due to the advancement in the electronic and telecommunications industries, LFO-based ceramics composites with carbon black are synthesized. The structural, magnetic, and microstructural analysis is carried out for LFO with different wt% of CB, and Dy substituted LFO with 10 wt% of CB. Morphology, structure, magnetic, permittivity, permeability, and shielding efficiency is analyzed. The high electrical properties of CB-rich magnetic and dielectric properties of LFO contributed a crucial role in achieving high EMT shielding. The formation of phase and structural confirmation is carried out by Rietveld refinement analysis. The substitution of Dy affected the microstructural, magnetic, and dielectric responses. The lattice constant and volume initially decreased with an increase in Dy concentration. Though magnetic properties decreased with incorporating CB, high saturation magnetization is still observed. The maximum saturation magnetization is obtained for LD10FO/CB. The substitution of Dy affects the shielding efficiency due to absorption rather than reflection.

SE due to reflection as well as absorption enhanced with the incorporation of CB. A total SE of 28 dB is obtained for LFO/CB (20) at 18 GHz. Further, the maximum shielding effectiveness of 24 dB was obtained for LD10FO/CB ~ 17 – 18 GHz. The Dy substitution enhances the magnetic as well as dielectric loss. 99.68 % of A_{eff} is achieved with 20 wt % CB reinforcement in LFO. The permittivity and permeability loss increased with CB content in the composites. Also, it is observed that absorption is the dominant mechanism in EMI shielding. The maximum absorption efficiency of 99.6 % is obtained for LD10FO/CB ~ 17 – 18 GHz. The electron hopping mechanism explains the variation of permeability and permittivity. The synergic effect of dielectric and magnetic loss are the main contributors to the high SE. The above results suggest that LD10FO/CB can be used for EMI shielding applications.

Further, lithium ferrite and Dy substituted lithium ferrite in the form of a thin film is deposited on Pt(111)/Ti/SiO_2/Si substrate with different thicknesses (160, 200, 240, 300 nm). The lattice parameters, such as lattice constant, volume, and strain, are reduced to 240 nm with an enhancement in thickness. Raman spectra showed a shift towards lower wavenumber with the increase in thickness. The average grain size increased, the RMS roughness reduced with the film thickness up to 240 nm and suddenly enhanced for 300 nm. The IP and OP magnetization reduced, whereas coercivity enhanced with the thickness (maximum 177 and 122 emu/cc for IP and OP of 160 nm) for LFO film. In the case of LDFO, a similar response is observed. The variation in magnetization is explained based on lattice strain and the magnetoelastic energy density. The dielectric constant increases, whereas the dielectric loss decreases with the increase in film thickness. The dielectric constants obtained are 125 – 1120 and 320 – 1430 for LFO and LDFO films, respectively.

LFO films showed lower tanδ values as compared to LDFO films. The variation in the dielectric response is explained based on the electron hopping mechanism and the contribution of grain and grain boundaries. The contribution of grain and grain boundaries are investigated by employing an equivalent circuit model to the impedance spectra of different temperatures. Grains played a prominent role at higher thicknesses, whereas grain boundaries were at lower thicknesses. Apart from that, the involved conduction mechanism is interpreted by different models and observed to be suitably obeyed by Mott's VRH mechanism. All the experimental parameters are correlated with each other, and film thickness (strain) played a significant role in tuning the physical properties of the films. This study concludes that controlling thickness effectively tunes the dielectric and magnetic properties to be used as magnetic oxide semiconductors.

A comparison table of the dielectric and magnetic performances of the reported lithium ferrite-based ceramics and thin films with our present work is as follows:

***Table 6-1**: A comparison with the previously reported response with our work*

Composition	**Ms (emu/g)**	**ε_r**	**References**
$Li_{0.5}Fe_{2.5-x}In_xO_4$ ($x = 0.00–0.32$)	43 - 53	-	[116]
$Li_{0.49}Zn_{0.02}Mn_xFe_{2.49-x}O_4$	49-73	3,994 (0.1 MHZ)	[119]
$Li_{0.4}Fe_{2.4}Zn_{0.2}O_4$	60-67	58 (1MHz)	[120]
$Li_{0.5}Zr_xNi_xFe_{2.5-2x}O_4$ ($x = 0.0–0.4$)	11-19	3-6 (1MHz - 1GHz)	[122]
$Li_{1.2}Mg_{0.4}Gd_xFe_{(2-x)}O_4$ ($x = 0–0.10$)	30 - 36	-	[125]
$Li_{1.2}Co_{0.4}Ho_xFe_{2-x}O_4$ ($x = 0.00–0.15$)	55-68	2-4 (1MHz - 1GHz)	[126]
$Li_{1-x}Mg_{2x}Fe_{5-x}O_8$ ($x = 0– 0.01$)	55 -67	3834 (1MHz)	Our work
$Li_{1-x}Sr_{2x}Fe_{5-x}O_8$ ($x = 0– 0.01$)	55 -67	3063 (1MHz)	Our work
Thin films	**M_s (emu/cc)**	**ε_r**	**References**
Flexible lithium ferrite thin film	154 at 300 K	-	[128]
$LiFe_5O_8$ on MgO substrate	200 at 20 K	-	[132]
$LiFe_5O_8$ on $MgAl_2O_4$ substrate	150 at 300 K	-	[133]
$LiFe_5O_8$ on Pt(111)/Ti/SiO_2/Si substrate	180 at 300 K	1120 (10kHz)	Our work
$LiDy_{0.1}Fe_{4.9}O_8$ on Pt(111)/Ti/SiO_2/Si substrate	250 at 300 K	1430 (10kHz)	Our work

6.2 Scopes for future work

The studies on LFO and LFO-based ceramics showed an improved dielectric and magnetic response. This study opened many possibilities and frontiers to work in the future. Lithium ferrite's synergetic response is well explored for different purposes in the microwave frequency range. The future scopes derived from the present study are as follows:

- ✓ For the circulator and phase shifter, low-loss ferrites are required. In our case, we have worked with alkaline earth elements. Transition elements with comparable ionic radii can be substituted in a required concentration to decrease the dielectric and magnetic loss.
- ✓ The EMI shielding efficiency can be improved further by incorporating other carbon derivatives and nanomaterials of different structures, such as carbon nanotube, and reduced graphene oxide.
- ✓ In the case of thin films, bilayer and multilayer films with dielectric seed layers can be deposited on single crystal and conductive substrates, and the resistive behavior can be studied broadly. The temperature stability and the electrical response can be explored for terrestrial device application purposes.

References

[1] A.N. N Ponpandian, P Balaya, J. Phys. Condens. Matter 14 (2002) 3221–3237.

[2] V.L.M. Abdul Samee Fawzi, A.D. Sheikh, J. Alloys Compd. 502 (2010) 231–237.

[3] V.G. Harris, IEEE Trans. Magn. 48 (2012) 1075–1104.

[4] W. Hu, N. Qin, G. Wu, Y. Lin, S. Li, D. Bao, J. Am. Chem. Soc. 134 (2012) 14658–14661.

[5] T.T. B. Rajesh Babu, Mater. Chem. Phys. 207 (2018) 534–541.

[6] T.R.T. M.A. Ahmed, H.E. Hassan, M.M. Eltabey, K. Latka, Phys. B Phys. Condens. Matter 530 (2018) 195–200.

[7] B.Y. Chen, D. Chen, Z.T. Kang, Y.Z. Zhang, J. Alloys Compd. 618 (2015) 222–226.

[8] M. Verma, A.P. Singh, P. Sambyal, B.P. Singh, S.K. Dhawan, V. Choudhary, Phys. Chem. Chem. Phys. 17 (2015) 1610–1618.

[9] S. Dong, P. Hu, X. Li, C. Hong, X. Zhang, J. Han, Chem. Eng. J. 398 (2020) 125588.

[10] Y. Chen, P. Pötschke, J. Pionteck, B. Voit, H. Qi, ACS Appl. Mater. Interfaces 12 (2020) 22088–22098.

[11] Y.Y. Wang, Z.H. Zhou, C.G. Zhou, W.J. Sun, J.F. Gao, K. Dai, D.X. Yan, Z.M. Li, ACS Appl. Mater. Interfaces 12 (2020) 8704–8712.

[12] S.D. Xian Jian, Xiangyun Xiao, Longjiang Deng, Wei Tian, Xin Wang, Nasir Mahmood, ACS Appl. Mater. Interfaces 10 (2018) 9369–9378.

[13] V. Siegfried Hilpert, Verf, Reports Ger. Chem. Soc. 42 (1909) 2248–2261.

[14] Satoshi Sugimoto, History and Future of Soft and Hard Magnetic Materials, 2019.

[15] J.L. Snoek, Physica 3 (1936) 463–483.

[16] C. Yafet Y, Kittel, Phys. Rev. 87 (1952) 290–300.

[17] R. Dronskowski, Adv. Funtional Mater. 11 (2001) 27–29.

[18] A. Globus, P. Duplex, Phys. Status Solidi 31 (1969) 765–774.

[19] P. Taylor, D. Polder, Philos. Mag. Ser. 40 (1949) 99–115.

[20] M. Pardavi-Horvath, J. Magn. Magn. Mater. 215 (2000) 171–183.

[21] Ü. Özgür, Y. Alivov, H. Morkoç, Microwave Ferrites, Part 1: Fundamental Properties, 2009.

[22] J. Wang, A. Yang, Y. Chen, Z. Chen, A. Geiler, S.M. Gillette, V.G. Harris, C. Vittoria, IEEE Microw. Wirel. Components Lett. 21 (2011) 292–294.

[23] A.S. Dehlinger, M. Le Berre, E. Bènevent, H. Hassane, D. Givord, V. Larrey, D. Vincent, Mater. Sci. Eng. C 28 (2008) 755–758.

[24] T.-H. Chang, in: Electromagn. Mater. Devices, 2019, pp. 1–14.

[25] R.R. Romanofsky, in: Antenna Eng. Handb., New York: McGraw Hill, 2007, p. 23.

[26] J. Kulikowski, J. Magn. Magn. Mater. 41 (1984) 56–62.

[27] P. Chavan, L.R. Naik, P.B. Belavi, G. Chavan, C.K. Ramesha, R.K. Kotnala, J. Electron. Mater. 46 (2017) 188–198.

[28] T. Indrusiak, I.M. Pereira, A.P. Heitmann, J.G. Silva, Â.M.L. Denadai, B.G. Soares, J. Mater. Sci. Mater. Electron. 31 (2020) 13118–13130.

[29] P.J. Liu, Z.J. Yao, V.M.H. Ng, J.T. Zhou, Z.H. Yang, L.B. Kong, Acta Metall. Sin. (English Lett. 31 (2018) 171–179.

[30] Y. Liu, X. Liu, X. Wang, Adv. Appl. Ceram. 114 (2015) 82–86.

[31] J.Y. Shin, J.H. Oh, IEEE Trans. Magn. 29 (1993) 3437–3439.

[32] M.A. Almessiere, Y. Slimani, A. V. Trukhanov, A. Sadaqat, A.D. Korkmaz, N.A. Algarou, H. Aydın, A. Baykal, M.S. Toprak, Nano-Structures and Nano-Objects 26 (2021) 100728.

[33] A. Houbi, Z.A. Aldashevich, Y. Atassi, Z. Bagasharova Telmanovna, M. Saule, K. Kubanych, J. Magn. Magn. Mater. 529 (2021) 167839.

[34] X. Huang, J. Zhang, M. Lai, T. Sang, J. Alloys Compd. 627 (2015) 367–373.

[35] X. Ren, G. Xu, J. Magn. Magn. Mater. 354 (2014) 44–48.

[36] H. Li, L. Zheng, D. Deng, X. Yi, X. Zhang, X. Luo, Y. Wu, W. Luo, M. Zhang, J. Alloys Compd. 862 (2021) 158638.

[37] H.H. Nguyen, N. Tran, T.L. Phan, D.S. Yang, N.T. Dang, B.W. Lee, Ceram. Int. 46 (2020) 19506–19513.

[38] A. Hakeem, T. Alshahrani, H.M.T. Farid, A.R. Khan, M.H. Alhossainy, A. Laref, I. Ali, J. Mater. Sci. Mater. Electron. 32 (2021) 2557–2563.

[39] K.Y. Butt, S. Aman, A.A. AlObaid, T.I. Al-Muhimeed, A. Rehman, H.H. Hegazy, N. Ahmad, A.R. Khan, S.R. Ejaz, H.M.T. Farid, Appl. Phys. A Mater. Sci. Process. 127 (2021) 1–11.

[40] M. Arjmand, A.A. Moud, Y. Li, U. Sundararaj, RSC Adv. 5 (2015) 56590–56598.

[41] S.R. Dhakate, K.M. Subhedar, B.P. Singh, RSC Adv. 5 (2015) 43036–43057.

[42] C.Y.L. and X.G.Z. Che, R. C., C. Y. Zhi, Appl. Phys. Lett. 88 (2006) 033105.

[43] H. Lv, G. Ji, X.H. Liang, H. Zhang, Y. Du, J. Mater. Chem. C 3 (2015) 5056–5064.

[44] D.D.L. Chung, Mater. Chem. Phys. 255 (2020).

[45] F. Meng, H. Wang, F. Huang, Y. Guo, Z. Wang, D. Hui, Z. Zhou, Compos. Part B Eng. 137 (2018) 260–277.

[46] V. Shukla, Nanoscale Adv. 1 (2019) 1640–1671.

[47] P.P. Mohapatra, P. Dobbidi, Mater. Charact. 189 (2022) 111985.

[48] Y. Zhang, J. Gu, Nano-Micro Lett. 14 (2022).

[49] D. Wanasinghe, F. Aslani, G. Ma, D. Habibi, Nanomaterials 10 (2020).

[50] J. Kruželák, A. Kvasničáková, K. Hložeková, I. Hudec, Nanoscale Adv. 3 (2021) 123–172.

[51] S. Gupta, N.H. Tai, Carbon N. Y. 152 (2019) 159–187.

[52] Y. Huang, K. Yasuda, C. Wan, ACS Appl. Mater. Interfaces 12 (2020) 55148–55156.

[53] Y. Qing, H. Yao, Y. Li, F. Luo, J. Eur. Ceram. Soc. 41 (2021) 1071–1075.

[54] Y. Qing, L. Ma, X. Hu, F. Luo, W. Zhou, Ceram. Int. 44 (2018) 8706–8709.

[55] C.D.G. B. D. Cullity, Introduction to Magnetic Materials, 2nd ed., 2009.

[56] Stephen Blundell, Oxford Univ. Press (2001) 1–251.

[57] Moulson A.J. and Herbert J. M., Electroceramics: Materials,Properties,Applications, 2003.

[58] Y. Zhou, Q. Wen, Z. Ren, H. Xie, S. Tao, W. Zhou, J. Alloys Compd. 733 (2018) 33–39.

[59] S.K.S. Monika Saini, Rajni Shukla, J. Inorg. Org. Polym. Mater. 29 (2019) 2044–2053.

[60] W.M. Kadiyala Chandra Babu Naidu, Sirugudu Roopas Kiran, IEEE Trans. Magn.

53 (2017) 2900207.

[61] M.A. Dar, K. Majid, M. Hanief Najar, R.K. Kotnala, J. Shah, S.K. Dhawan, M. Farukh, Phys. Chem. Chem. Phys. 19 (2017) 10629–10643.

[62] V.N. Dhage, M.L. Mane, A.P. Keche, C.T. Birajdar, K.M. Jadhav, Phys. B Condens. Matter 406 (2011) 789–793.

[63] G. Albanese, A. Deriu, E. Lucchini, G. Slokar, Appl. Phys. A Solids Surfaces 26 (1981) 45–50.

[64] K.S. Martirosyan, E. Galstyan, S.M. Hossain, Y.J. Wang, D. Litvinov, Mater. Sci. Eng. B Solid-State Mater. Adv. Technol. 176 (2011) 8–13.

[65] R.E. El Shater, E.H. El-Ghazzawy, M.K. El-Nimr, J. Alloys Compd. 739 (2018) 327–334.

[66] Z.F. Zi, Q.C. Liu, J.M. Dai, Y.P. Sun, Solid State Commun. 152 (2012) 894–897.

[67] H. Nikmanesh, M. Moradi, G.H. Bordbar, R. Shams Alam, J. Alloys Compd. 708 (2017) 99–107.

[68] S.E. Shirsath, R.H. Kadam, K.M. Batoo, D. Wang, S. Li, J. Phys. D. Appl. Phys. 54 (2021).

[69] D.L. Wood, J.P. Remeika, J. Appl. Phys. 38 (1967) 1038–1045.

[70] Y. Sun, Y.Y. Song, H. Chang, M. Kabatek, M. Jantz, W. Schneider, M. Wu, H. Schultheiss, A. Hoffmann, Appl. Phys. Lett. 101 (2012).

[71] M.A. Musa, R.S. Azis, N.H. Osman, J. Hassan, T. Zangina, Results Phys. 7 (2017) 1135–1142.

[72] B. Rajeswaran, D. Sanyal, M. Chakrabarti, Y. Sundarayya, A. Sundaresan, C.N.R. Rao, Epl 101 (2013).

[73] Y.J. Ke, X.Q. Zhang, H. Ge, Y. Ma, Z.H. Cheng, Chinese Phys. B 24 (2015).

[74] A. Jaiswal, R. Das, T. Maity, P. Poddar, J. Appl. Phys. 110 (2011).

[75] K. Vijaya Kumar, A. Chandra Shekhar Reddy, D. Ravinder, J. Magn. Magn. Mater. 263 (2003) 121–126.

[76] K. Jalaiah, K. Vijaya Babu, J. Magn. Magn. Mater. 423 (2017) 275–280.

[77] S.B. Narang, K. Pubby, J. Magn. Magn. Mater. 519 (2021).

[78] H.L. Andersen, M. Saura-Múzquiz, C. Granados-Miralles, E. Canévet, N. Lock, M. Christensen, Nanoscale 10 (2018) 14902–14914.

[79] M. Mozaffari, M. Eghbali Arani, J. Amighian, J. Magn. Magn. Mater. 322 (2010) 3240–3244.

[80] S.E. Shirsath, S.S. Jadhav, B.G. Toksha, S.M. Patange, K.M. Jadhav, J. Appl. Phys. 110 (2011).

[81] K. Naz, J.K. Khan, M. Khalid, M.S. Akhtar, Z.A. Gilani, H.M. Noor ul Huda Khan Asghar, G.A.M. Mersal, M.M. Ibrahim, A. Muhammad, M.G.B. Ashiq, Mater. Chem. Phys. 285 (2022) 126091.

[82] X.H. Wu, L.Z. Li, B. Wu, X.X. Zhong, R. Wang, X.Q. Tu, L. He, C.Y. Zou, B.R. Hou, Ceram. Int. 47 (2021) 3720–3727.

[83] R. Qindeel, N.H. Alonizan, E.A. Alghamdi, M.A. Awad, J. Sol-Gel Sci. Technol. 97 (2021) 593–599.

[84] D.H. Kim, D.E. Nikles, C.S. Brazel, Materials (Basel). 3 (2010) 4051–4065.

[85] S. Güner, M. Amir, M. Geleri, M. Sertkol, A. Baykal, Ceram. Int. 41 (2015) 10915–10922.

[86] V.G. Harris, A. Geiler, Y. Chen, S.D. Yoon, M. Wu, A. Yang, Z. Chen, P. He, P. V. Parimi, X. Zuo, C.E. Patton, M. Abe, O. Acher, C. Vittoria, J. Magn. Magn. Mater. 321 (2009) 2035–2047.

[87] F. Ji, E.K.N. Yung, R.S. Chen, X.Q. Sheng, W. Bin Dou, J. Electromagn. Waves Appl. 17 (2003) 1631–1641.

[88] Y. Liu, Y. Li, H. Zhang, Q. Yang, J. Appl. Phys. 105 (2009) 1–4.

[89] G. V. Kurlyandskaya, S.M. Bhagat, S.E. Jacobo, J.C. Aphesteguy, N.N. Schegoleva, J. Phys. Chem. Solids 72 (2011) 276–285.

[90] M.N. Akhtar, M.A. Khan, M. Ahmad, M.S. Nazir, M. Imran, A. Ali, A. Sattar, G. Murtaza, J. Magn. Magn. Mater. 421 (2017) 260–268.

[91] P. Saha, S. Das, S. Sutradhar, J. Appl. Phys. 124 (2018).

[92] M.P. Reddy, A.M.A. Mohamed, M.V. Ramana, X.B. Zhou, Q. Huang, J. Magn. Magn. Mater. 395 (2015) 185–189.

[93] S. Hossein, A. Moghimi, M. Moloudi, Mater. Sci. Semicond. Process. 24 (2014) 272–277.

[94] L. Gong, G. Chen, J. Lv, M. Lu, J. Zhang, X. Wu, J. Wang, Appl. Surf. Sci. 565 (2021) 150532.

[95] A. Mishra, V. Sharma, T. Mohanty, B.K. Kuanr, J. Alloys Compd. 790 (2019) 983–991.

[96] J. Cao, W. Fu, H. Yang, Q. Yu, Y. Zhang, S. Liu, P. Sun, X. Zhou, Y. Leng, S. Wang, B. Liu, G. Zou, J. Phys. Chem. B 113 (2009) 4642–4647.

[97] N. Gandhi, K. Singh, A. Ohlan, D.P. Singh, S.K. Dhawan, Compos. Sci. Technol. 71 (2011) 1754–1760.

[98] R. Xu, D. Xu, Z. Zeng, D. Liu, Chem. Eng. J. 427 (2022) 130796.

[99] Y. Lin, J. Dong, H. Zong, B. Wen, H. Yang, ACS Sustain. Chem. Eng. 6 (2018) 10011–10020.

[100] F. Li, W. Zhan, Y. Su, S.H. Siyal, G. Bai, W. Xiao, A. Zhou, G. Sui, X. Yang, Compos. Part A Appl. Sci. Manuf. 133 (2020) 105866.

[101] S. Gupta, S. Kumar, D. Pradhan, N. Tai, Compos. Part A 123 (2019) 232–241.

[102] P.D.B. G. M. Argentina, IEEE Trans. Microw. Theory Tech. 22 (1974) 652–658.

[103] N.G. Jović, A.S. Masadeh, A.S. Kremenović, B. V. Antić, L.B. Jovan, D.C. Nikola, F.G. Gerardo, Marco Vittori Antisari, S.B. Emil, J. Phys. Chem. C 113 (2009) 20559–20567.

[104] M. Dasari, G. Gajula, R. Hanumantha, A. Chintabathini, S. Kurimella, B. Somayajula, Process. Appl. Ceram. 11 (2017) 7–12.

[105] N. Thomas, T. Shimna, P. V. Jithin, V.D. Sudheesh, H.K. Choudhary, B. Sahoo, S.S. Nair, N. Lakshmi, V. Sebastian, J. Magn. Magn. Mater. 462 (2018) 136–143.

[106] N. Rezlescu, C. Doroftei, E. Rezlescu, P.D. Popa, Sensors Actuators, B Chem. 133 (2008) 420–425.

[107] M. Shinkai, J. Biosci. Bioeng. 94 (2002) 606–613.

[108] V.K. Sankaranarayanan, O. Prakash, R.P. Pant, M. Islam, J. Magn. Magn. Mater. 252 (2002) 7–9.

[109] T. Collins, A.E. Brown, J. Appl. Phys. 41 (1971) 1351.

[110] N. Gupta, M.C. Dimri, S.C. Kashyap, D.C. Dube, Ceram. Int. 31 (2005) 171–176.

[111] E. Schloemann, J. Magn. Magn. Mater. 209 (2000) 15–20.

[112] S.A. Mazen, N.I. Abu-Elsaad, Ceram. Int. 40 (2014) 11229–11237.

[113] M. Srivastava, R.K. Mishra, J. Singh, N. Srivastava, N. Hoon, J. Hee, J. Alloys Compd. 645 (2015) 171–177.

[114] S. Verma, P.A. Joy, Mater. Res. Bull. 43 (2008) 3447–3456.

[115] P. Thakur, P. Sharma, J.L. Mattei, P. Queffelec, A. V. Trukhanov, S. V. Trukhanov, L. V. Panina, A. Thakur, J. Mater. Sci. Mater. Electron. 29 (2018) 16507–16515.

[116] M. Junaid, M.A. Khan, A. Majeed, H. Alkhaldi, M.S. Attia, M.A. Amin, M. Asif Iqbal, Ceram. Int. 48 (2022) 21651–21656.

[117] R. Cheruku, G. Govindaraj, L. Vijayan, Mater. Chem. Phys. 146 (2014) 389–398.

[118] R.H.K. D. R. Mane, Swati Patil, D. D. Birajdar, A. B. Kadam, Sagar E. Shirsath, Mater. Chem. Phys. 126 (2011) 755–760.

[119] Dipti, P. Kumar, J.K. Juneja, S. Singh, K.K. Raina, C. Prakash, Ceram. Int. 41 (2015) 3293–3297.

[120] A. V. Malyshev, E.N. Lysenko, V.A. Vlasov, Ceram. Int. 41 (2015) 13671–13675.

[121] K. Ding, J. Zhao, M. Zhao, Y. Chen, Y. Zhao, J. Zhou, Int. J. Electrochem. Sci. 11 (2016) 2513–2524.

[122] M. Junaid, I.A. Qazafi, M.A. Khan, S. Gulbadan, S.Z. Ilyas, H.H. Somaily, M.S. Attia, M.A. Amin, H.M. Noor ul Huda Khan Asghar, Ceram. Int. 48 (2022) 14307–14314.

[123] M.A. Ahmed, S.T. Bishay, J. Magn. Magn. Mater. 279 (2004) 178–183.

[124] V. Mohanty, R. Cheruku, L. Vijayan, G. Govindaraj, J. Mater. Sci. Technol. 30 (2014) 335–341.

[125] M. Asif Iqbal, M.U. Islam, M.N. Ashiq, I. Ali, A. Iftikhar, H.M. Khan, J. Alloys Compd. 579 (2013) 181–186.

[126] A. Manzoor, M.A. Khan, M. Shahid, M.F. Warsi, J. Alloys Compd. 710 (2017) 547–556.

[127] M. AsifIqbal, M.U. Islam, I. Ali, M.A. Khan, S.M. Ramay, M.H. Khan, M.K. Mehmood, J. Alloys Compd. 692 (2017) 322–331.

[128] G. Lan, L. Shen, L. Lu, C. Cao, C. Jiang, H. Fu, C. You, X. Lu, C. Ma, M. Liu, C.L. Jia, ACS Appl. Mater. Interfaces 10 (2018) 39422–39427.

[129] J.E.V. de Morais, A.J.N. de Castro, R.G.M. Oliveira, F.F. do Carmo, A.J.M. Sales, J.C. Sales, M.A.S. Silva, D.X. Gouveia, M.M. Costa, A.R. Rodrigues, A.S.B. Sombra, J. Electron. Mater. 47 (2018) 3829–3835.

[130] P. Paroli, C. Vittoria, S. Martellucci, G. Petrocelli, A. Tebano, IEEE Trans. Magn. 30 (1994) 4933–4935.

[131] F.J. Cadieu, R. Rani, W. Mendoza, B. Peng, S.A. Shaheen, M.J. Hurben, C.E. Patton, J. Appl. Phys. 81 (1997) 4801–4803.

[132] C. Boyraz, D. Mazumdar, M. Iliev, V. Marinova, J. Ma, G. Srinivasan, A. Gupta, Appl. Phys. Lett. 98 (2011) 10–13.

[133] R. Zhang, M. Liu, L. Lu, S.B. Mi, H. Wang, J. Mater. Chem. C 3 (2015) 5598–5602.

[134] R.R. Chilwar, A.R. Chavan, M.K. Babrekar, K.M. Jadhav, Phys. B Condens. Matter 566 (2019) 43–49.

[135] K. Liu, R. Zhang, L. Lu, S. Mi, M. Liu, H. Wang, S. Wu, C. Jia, J. Mater. Sci. Technol. 40 (2020) 31–38.

[136] C. B. D, Elements of X-Ray Diffraction, Second, 1978.

[137] S.R.C. Douglas A. Skoog, F. James Holler, Principles of Instrumental Methods of Analysis, 7 th, 2016.

[138] A.M. Nicolson, G.F. Ross, IEEE Trans. Instrum. Meas. 19 (1970) 377–382.

[139] W.B. Weir, Proc. IEEE 62 (1974) 33–36.

[140] I. Horcas, R. Fernández, J.M. Gómez-Rodríguez, J. Colchero, J. Gómez-Herrero, A.M. Baro, Rev. Sci. Instrum. 78 (2007).

[141] S.A. Mazen, N.I. Abu-Elsaad, Appl. Nanosci. 5 (2015) 105–114.

[142] A. V. Anupama, V. Kumaran, B. Sahoo, Soft Matter 14 (2018) 5407–5419.

[143] P. Vijaya Bhasker Reddy, B. Ramesh, C. Gopal Reddy, Phys. B Condens. Matter 405 (2010) 1852–1856.

[144] Y.T. Lee, C.S. Yoon, Y.S. Lee, Y.K. Sun, J. Power Sources 134 (2004) 88–94.

[145] S. Verma, J. Karande, A. Patidar, P.A. Joy, Mater. Lett. 59 (2005) 2630–2633.

[146] B. Li, Y. Xie, H. Su, Y. Qian, X. Liu, Solid State Ionics 120 (1999) 251–254.

[147] P.D. Baba, G.M. Argentina, W.E. Courtney, G.F. Dionne, D.H. Telmme, IEEE Trans. Magn. 8 (1972) 83–94.

[148] T. Das, B.K. Das, K. Parashar, R. Kumar, H.K. Choudhary, A. V. Anupama, B. Sahoo, P.K. Sahoo, S.K.S. Parashar, J. Mater. Sci. Mater. Electron. 28 (2017) 13587–13595.

[149] M.F. Al-Hilli, S. Li, K.S. Kassim, J. Magn. Magn. Mater. 324 (2012) 873–879.

[150] S.C. Watawe, U.A. Bamne, S.P. Gonbare, R.B. Tangsali, 103 (2007) 323–328.

[151] M.J. Iqbal, M.I. Haider, Mater. Chem. Phys. 140 (2013) 42–48.

[152] S.K. Gurav, S.E. Shirsath, R.H. Kadam, D.R. Mane, Powder Technol. 235 (2013)

485–492.

[153] M.G. El-Shaarawy, M.M. Rashad, N.M. Shash, M.H. Maklad, F.A. Afifi, J. Mater. Sci. Mater. Electron. 26 (2015) 6040–6050.

[154] Y.T. Prabhu, K.V. Rao, (2014) 21–28.

[155] M.M. Costa, R.S.T.M. Sohn, A.A.M. MacÊdo, S.E. Mazzetto, M.P.F. Graa, A.S.B. Sombra, J. Alloys Compd. 509 (2011) 9466–9471.

[156] V. Rathod, A. V. Anupama, R.V. Kumar, V.M. Jali, B. Sahoo, Vib. Spectrosc. 92 (2017) 267–272.

[157] O.F. Caltun, L. Spinu, 4 (2002) 337–340.

[158] M. Manjurul Haque, M. Huq, M.A. Hakim, J. Magn. Magn. Mater. 320 (2008) 2792–2799.

[159] M.A. Iqbal, M.U. Islam, I. Ali, M. Azhar, I. Sadiq, I. Ali, J. Alloys Compd. 586 (2014) 404–410.

[160] A.P. Surzhikov, A. V. Malyshev, E.N. Lysenko, V.A. Vlasov, A.N. Sokolovskiy, Ceram. Int. 43 (2017) 9778–9782.

[161] K.H. Maria, U.S. Akther, I.N. Esha, M.S. Hossain, M.N.I. Khan, J. Supercond. Nov. Magn. 33 (2020) 2133–2142.

[162] M.A. Dar, K.M. Batoo, V. Verma, W.A. Siddiqui, R.K. Kotnala, J. Alloys Compd. 493 (2010) 553–560.

[163] H. Du, W. Zhou, F. Luo, D. Zhu, S. Qu, Z. Pei, J. Appl. Phys. 105 (2009).

[164] P.R. Mandal, T.K. Nath, J. Alloys Compd. 628 (2015) 379–389.

[165] A.A. Kadam, S.S. Shinde, S.P. Yadav, P.S. Patil, K.Y. Rajpure, J. Magn. Magn.

Mater. 329 (2013) 59–64.

[166] L.C. S. S. Teixeira, M. P. F. Graca, Costa, M.A. Valente, 186 (2014) 83–88.

[167] V. Rathod, A. V. Anupama, V.M. Jali, V.A. Hiremath, B. Sahoo, Ceram. Int. 43 (2017) 14431–14440.

[168] L. Neel, Science (80-.). 174 (1971) 985–992.

[169] S.I. Hussein, A.S. Elkady, M.M. Rashad, A.G. Mostafa, R.M. Megahid, J. Magn. Magn. Mater. 379 (2015) 9–15.

[170] M.M. Rashad, M.I. Nasr, Electron. Mater. Lett. 8 (2012) 325–329.

[171] S. Verma, P.A. Joy, J. Appl. Phys. 98 (2005).

[172] M.N. Akhtar, M. Yousaf, S.N. Khan, M.S. Nazir, M. Ahmad, M.A. Khan, Ceram. Int. 43 (2017) 17032–17040.

[173] M. Niaz Akhtar, M. Azhar Khan, M. Ahmad, G. Murtaza, R. Raza, S.F. Shaukat, M.H. Asif, N. Nasir, G. Abbas, M.S. Nazir, M.R. Raza, J. Magn. Magn. Mater. 368 (2014) 393–400.

[174] J. Zhang, J. Li, G. Tan, R. Hu, J. Wang, C. Chang, X. Wang, ACS Appl. Mater. Interfaces 9 (2017) 42192–42199.

[175] Z. Zeng, M. Chen, H. Jin, W. Li, X. Xue, L. Zhou, Y. Pei, H. Zhang, Z. Zhang, Carbon N. Y. 96 (2016) 768–777.

[176] Y. Lin, J. Dai, H. Yang, L. Wang, F. Wang, Chem. Eng. J. 334 (2018) 1740–1748.

[177] B. Zhao, C. Zhao, R. Li, S.M. Hamidinejad, C.B. Park, ACS Appl. Mater. Interfaces 9 (2017) 20873–20884.

[178] A. Ameli, P.U. Jung, C.B. Park, Carbon N. Y. 60 (2013) 379–391.

[179] A. Ameli, P.U. Jung, C.B. Park, Compos. Sci. Technol. 76 (2013) 37–44.

[180] X. Shi, L. Chen, B. Liu, J. Long, Y. Xu, Y. Wang, Chinese Joulnal Polym. Sci. 36 (2018) 1357–1384.

[181] J.R. G. Haneczoka, R. Wroczynskib, P. Kwapulinskia, A. Chrobakc, Z. Stokłosaa, J. Mater. Process. Technol. 9 (2008) 2356–2360.

[182] A. Chrobak, A. Kaleta, M. Kubisztal, G. Haneczok, IEEE Trans. Magn. 48 (2012) 1512–1515.

[183] G. Sang, C. Wang, Y. Zhao, G. He, Q. Zhang, M. Yang, S. Zhao, P. Xu, X. Xi, J. Yang, ACS Appl. Mater. Interfaces 14 (2022) 4443–4455.

[184] Q. Yuchang, W. Qinlong, L. Fa, Z. Wancheng, Z. Dongmei, J. Mater. Chem. C 4 (2016) 371–375.

[185] D. Moitra, S. Dhole, B.K. Ghosh, M. Chandel, R.K. Jani, M.K. Patra, S.R. Vadera, N.N. Ghosh, J. Phys. Chem. C 121 (2017) 21290–21304.

[186] Z. HaiTao, M. RuiTing, Integr. Ferroelectr. 178 (2017) 79–87.

[187] G.L. and Y.W. Weimo Zhu, Lei Wang, Rui Zhao, Jiawen Ren, Nanosca 3 (2011) 2862–2864.

[188] V.A. Online, M. Fu, Q. Jiao, Y. Zhao, J. Mater. Chem. A 1 (2013) 5577–5586.

[189] M. Niaz, M. Yousaf, Y. Lu, M.A. Baqir, M. Azhar, M. Ahmad, A. Sarosh, M. Shahid, J. Magn. Magn. Mater. 537 (2021) 168232.

[190] K. Qian, Z. Yao, H. Lin, J. Zhou, A. Ali, T. Qi, W. Chen, X. Guo, Ceram. Int. 46 (2020) 227–235.

[191] C. Srinivas, K.N. Praveen, E.R. Kumar, S. Singh, S.S. Meena, P. Bhatt, T.V.C. Rao, D. Sarkar, B. Arun, K.C.J. Raj, D.L. Sastry, Ceram. Int. (2022).

[192] and R.H.K. G B Todkar, R A Kunale, R N Kamble, Khalid M Batoo, M F Ijaz, A Imran, M Hadi, E H Raslan, Sagar E Shirsath, J. Phys. D. Appl. Phys. 54 (2021) 294001.

[193] S. Jie, W.L. Б, X.U. Naicen, Z. Qitu, J. Rare Earths 28 (2010) 451–455.

[194] Y.-D.Y. Yen-Pe iFu, Dung-Shing Hung, Ceramics 35 (2009) 2179–2184.

[195] S. Joshi, M. Kumar, S. Chhoker, A. Kumar, M. Singh, J. Magn. Magn. Mater. 426 (2017) 252–263.

[196] S. Ikram, J. Jacob, K. Mahmood, K. Mehboob, M. Maheen, A. Ali, N. Amin, S. Hussain, F. Ashraf, S.Z. Ilyas, Ceram. Int. 46 (2020) 15943–15948.

[197] S.R. Kulal, S.S. Khetre, P.N. Jagdale, V.M. Gurame, D.P. Waghmode, G.B. Kolekar, S.R. Sabale, S.R. Bamane, Mater. Lett. 84 (2012) 169–172.

[198] M. Hashim, M. Raghasudha, S. Singh, J. Shah, S.E. Shirsath, S. Kumar, D. Ravinder, P. Bhatt, R. Kumar, R.K. Kotnala, J. Magn. Magn. Mater. 449 (2018) 319–327.

[199] K. V Zipare, S.S. Bandgar, G.S. Shahane, J. Rare Earths 36 (2018) 86–94.

[200] K.K. Bamzai, G. Kour, B. Kaur, S.D. Kulkarni, J. Magn. Magn. Mater. 327 (2013) 159–166.

[201] A.A.K.K.Y. Rajpure, J. Mater. Sci. Mater. Electron. 27 (2016) 10484–10496.

[202] M.M. Rashad, M.G. El-Shaarawy, N.M. Shash, M.H. Maklad, F.A. Afifi, J. Magn. Magn. Mater. 347 (2015) 495–501.

[203] Y. Melikhov, J.E. Snyder, D.C. Jiles, A.P. Ring, J.A. Paulsen, C.C.H. Lo, K.W. Dennis, J. Appl. Phys. 99 (2006) 97–100.

[204] Z.Y. Zhao, X.M. Wang, C. Fan, W. Tao, X.G. Liu, W.P. Ke, F.B. Zhang, X. Zhao, X.F. Sun, Phys. Rev. B 014414 (2011) 1–8.

[205] F. Meng, X. Shang, W. Zhang, Y. Zhang, Phys. B Phys. Condens. Matter 504 (2017) 69–73.

[206] A. Majumder, K. Ugendar, A.B.K. B, R.A. Mondal, G. Markandeyulu, in: Phys. Procedia, Elsevier B.V., 2015, pp. 238–244.

[207] S.L. Guiqin Wang, Xiaodong Chen, Yuping Duan, J. Alloys Compd. 454 (2006) 340–346.

[208] N. Jiang, Y. Yang, Y. Zhang, J. Zhou, P. Liu, J. Magn. Magn. Mater. 401 (2016) 370–377.

[209] C. Singh, S. Bindra Narang, I.S. Hudiara, K. Sudheendran, K.C. James Raju, J. Magn. Magn. Mater. 320 (2008) 1657–1665.

[210] T.K. Gupta, B.P. Singh, R.B. Mathur, S.R. Dhakate, Nanoscale 6 (2014) 842–851.

[211] J.P. Gogoi, N.S. Bhattacharyya, S. Bhattacharyya, Compos. Part B Eng. 58 (2014) 518–523.

[212] M. Junaid, M. Azhar, F. Iqbal, G. Murtaza, M. Niaz, M. Ahmad, I. Shakir, M. Farooq, J. Magn. Magn. Mater. 419 (2016) 338–344.

[213] B. Zhao, W. Zhao, G. Shao, B. Fan, R. Zhang, ACS Appl. Mater. Interfaces 7 (2015) 12951–12960.

[214] J.C. Sun, Z. He, W. Dong, W. Wu, G. Tong, J. Alloys Compd. 782 (2019) 193–202.

[215] N.N. Song, H.T. Yang, H.L. Liu, X. Ren, H.F. Ding, X.Q. Zhang, Z.H. Cheng, Sci. Rep. 3 (2013) 3–7.

[216] J.-E. Wegrowe, M.-C. Ciornei, Am. J. Phys. 80 (2012) 607–611.

[217] D. Fang, H. Kurebayashi, J. Wunderlich, K. Výborný, L.P. Zârbo, R.P. Campion, A. Casiraghi, B.L. Gallagher, T. Jungwirth, A.J. Ferguson, Nat. Nanotechnol. 6 (2011)

413–417.

[218] M.F. M. Abdullah Dar, Kowsar Majid, Mohd. Hanief Najar, R. K. Kotnala, Jyoti Shah, S. K. Dhawan, Phys. Chem. Chem. Phys. 19 (2017) 10629–10643.

[219] A. Ohlan, K. Singh, A. Chandra, S.K. Dhawan, Appl. Phys. Lett. 93 (2008) 12–14.

[220] R.K. Srivastava, P. Xavier, S.N. Gupta, G.P. Kar, S. Bose, A.K. Sood, ChemistrySelect 1 (2016) 5995–6003.

[221] S. Iqbal, H. Khatoon, R.K. Kotnala, S. Ahmad, Compos. Part B Eng. 175 (2019) 107143.

[222] N. Gulzar, K. Zubair, M.F. Shakir, M. Zahid, Y. Nawab, Z.A. Rehan, J. Supercond. Nov. Magn. 33 (2020) 3519–3524.

[223] M.M. Ismail, S.N. Rafeeq, J.M.A. Sulaiman, A. Mandal, Appl. Phys. A Mater. Sci. Process. 124 (2018) 1–12.

[224] and S.B.O. Vishal Thakare, Guozhong Xing, Haiyang Peng, Abhimanyu Rana, Onkar Game, P. Anil Kumar, Arun Banpurkar, Yesappa Kolekar, Kartik Ghosh, Tom Wu, D. D. Sarma, Appl. Phys. Lett. 172412 (2012) 0–4.

[225] A. V. Ramos, T.S. Santos, G.X. Miao, M.J. Guittet, J.B. Moussy, J.S. Moodera, Phys. Rev. B - Condens. Matter Mater. Phys. 78 (2008) 3–6.

[226] M. Lorenz, M. Brandt, K. Mexner, K. Brachwitz, M. Ziese, P. Esquinazi, H. Hochmuth, M. Grundmann, Phys. Status Solidi - Rapid Res. Lett. 5 (2011) 438–440.

[227] B.J. Chapman, E.I. Rosenthal, J. Kerckhoff, B.A. Moores, L.R. Vale, J.A.B. Mates, G.C. Hilton, K. Lalumière, A. Blais, K.W. Lehnert, Phys. Rev. X 7 (2017) 1–16.

[228] S.A. Wolf, D.D. Awschalom, R.A. Buhrman, J.M. Daughton, S. Von Molnár, M.L. Roukes, A.Y. Chtchelkanova, D.M. Treger, Science (80-.). 294 (2001) 1488–1495.

[229] B.M. and J.K. Chilwar Rahul R, Somvanshi Sandeep B, Chavan Apparao R, Kharat Prashant B, Int. Res. J. Sci. Eng. (2017) 73–76.

[230] M.M. Rashad, M.G. El-Shaarawy, N.M. Shash, M.H. Maklad, F.A. Afifi, J. Magn. Magn. Mater. 374 (2015) 495–501.

[231] D. Mukherjee, T. Dhakal, M.H. Phan, H. Srikanth, P. Mukherjee, S. Witanachchi, Phys. B Condens. Matter 406 (2011) 2663–2668.

[232] F. Eskandari, S.B. Porter, M. Venkatesan, P. Kameli, K. Rode, J.M.D. Coey, Phys. Rev. Mater. 1 (2017) 1–10.

[233] R. Zhang, M. Liu, L. Lu, S.B. Mi, H. Wang, CrystEngComm 17 (2015) 8256–8263.

[234] N.S. Sokolov, V. V. Fedorov, A.M. Korovin, S.M. Suturin, D.A. Baranov, S. V. Gastev, B.B. Krichevtsov, K.Y. Maksimova, A.I. Grunin, V.E. Bursian, L. V. Lutsev, M. Tabuchi, J. Appl. Phys. 119 (2016).

[235] A. Si, F. Lombardi, C. Vittoria, IEEE Sens. J. 19 (2019) 129–137.

[236] M. Oujja, L. Martín-García, E. Rebollar, A. Quesada, M.A. García, J.F. Fernández, J.F. Marco, J. de la Figuera, M. Castillejo, Appl. Surf. Sci. 452 (2018) 19–31.

[237] D.S. Rana, I. Kawayama, K. Mavani, K. Takahashi, H. Murakami, M. Tonouchi, Adv. Mater. 21 (2009) 2881–2885.

[238] S. Kale, S.M. Bhagat, S.E. Lofland, T. Scabarozi, S.B. Ogale, A. Orozco, S.R. Shinde, T. Venkatesan, B. Hannoyer, B. Mercey, W. Prellier, Phys. Rev. B - Condens. Matter Mater. Phys. 64 (2001) 1–9.

[239] M.N. Iliev, V.G. Ivanov, N.D. Todorov, V. Marinova, M. V. Abrashev, R. Petrova, Y.Q. Wang, A.P. Litvinchuk, Phys. Rev. B - Condens. Matter Mater. Phys. 83 (2011).

[240] P.P. Mohapatra, P. Dobbidi, J. Phys. Chem. C 125 (2021) 14014–14026.

[241] K.K. Jani, P.Y. Raval, N.H. Vasoya, M. Nehra, M. Singh, N. Jakhar, S. Kumar, K.B. Modi, D.K. Lim, R.K. Singhal, Ceram. Int. 48 (2022) 31843–31849.

[242] J.C.R. Aquino, F.F.H. Aragón, D.G. Pacheco-Salazar, J.A.H. Coaquira, J. Nanoparticle Res. 23 (2020).

[243] R. Tholkappiyan, K. Vishista, Appl. Surf. Sci. 351 (2015) 1016–1024.

[244] and D.T. Punam Silwal, Ludi Miao, Jin Hu, Leonard Spinu, Dae Ho Kim, J. Appl. Phys. 114 (2013) 103704.

[245] R.K. Subasa C. Sahoo, N. Venkataramani, Shiva Prasad, Murtaza Bohra, Appl. Phys. A 106 (2012) 931–935.

[246] J. Gil-Monsalve, J.E. Abrão, E. Santos, A. Ricalde, A. Azevedo, O. Arnache, Phys. Rev. B 105 (2022) 1–9.

[247] S. Riaz, S.M.H. Shah, A. Akbar, S. Atiq, S. Naseem, J. Sol-Gel Sci. Technol. 74 (2015) 329–339.

[248] James Clerk Maxwell, A Treatise on Electricity and Magnetism, Clarendon Press, 1873.

[249] K Wagner, Ann. Phys. 40 (1913) 817.

[250] A.R. West, D.C. Sinclair, N. Hirose, J. Electroceramics (1997) 65–71.

[251] K.B.R.V. C. Karthik, J. Phys. Chem. Solids 67 (2006) 2437–2441.

[252] L. Chauhan, S. Kumar, K. Sreenivas, A.K. Shukla, Mater. Chem. Phys. 259 (2021) 124135.

[253] T.T. Lin, S.L. Young, C.Y. Kung, H.Z. Chen, M.C. Kao, M.C. Chang, C.R. Ou,

IEEE Trans. Nanotechnol. 13 (2014) 425–430.

[254] H. Han, C. Davis, J.C. Nino, J. Phys. Chem. C 118 (2014) 9137–9142.

[255] T. Giannakopoulou, L. Kompotiatis, A. Kontogeorgakos, G. Kordas, J. Magn. Magn. Mater. 246 (2002) 360–365.

[256] N. Zn, F.O. Ceramic, H. Zheng, W. Weng, G. Han, P. Du, J. Phys. Chem. C 117 (2013) 12966–12972.